UNIVERSITY OF OKLAHOMA

GRADUATE COLLEGE

BEHAVIOR OF FLUIDS IN CLAY-HOSTED NANOPORES: INSIGHTS FROM MOLECULAR DYNAMICS

A DISSERTATION

SUBMITTED TO THE GRADUATE FACULTY

in partial fulfillment of the requirements for the

Degree of

DOCTOR OF PHILOSOPHY

By

HAO XIONG
Norman, Oklahoma
2021

BEHAVIOR OF FLUIDS IN CLAY-HOSTED NANOPORES: INSIGHTS FROM MOLECULAR DYNAMICS

A DISSERTATION APPROVED FOR THE
MEWBOURNE SCHOOL OF PETROLEUM AND GEOLOGICAL ENGINEERING

BY THE COMMITTEE CONSISTING OF

Dr. Deepak Devegowda, Chair

Dr. Liangliang Huang

Dr. Chandra S. Rai

Dr. Carl Sondergeld

Dr. Zulfiquar Reza

To my beloved parents and elder sister, thank you for your unceasing support

and unconditional love!!!

Acknowledgments

I would like to thank my parents for your reckless love and support, not just during the Ph.D., but in all the times beforehand. You have always respected my decisions and believed in me even in my weakest moments. You have been the constant in my life. Hong, my elder sister, thanks for your encouragement starting from my childhood and opening the door for me to leave the nest and fly away.

I would also like to express my greatest gratitude to my advisor, Dr. Deepak Devegowda. Thank you for giving me the freedom to explore the science that interests me the most. Thank you for inspiring me with new ideas and guiding me through the obstacles in researches. Thank you for helping me with how to make a fantastic presentation (although I am still on the way nowadays). Foremost, thank you for always being here when needed. I cannot reach so far without your support and supervision.

I want to thank my committee members one by one. To Dr. Liangliang Huang, I still remembered how excited I was in your multiscale modeling class. Thank you for teaching me, a petroleum engineer, a new skill to explore and understand the beauty of petroleum from a molecular scale. Thank you for your meaningful discussions, valuable advice, and even life guidance. To Dr. Carl Sondergeld, thank you for the challenges you threw at me during these years. Your wisdom and knowledge help me realize the weakness of my research and make me improve my works continuously. I will always remember your guidance and help over the past four years. To Dr. Chandra Rai, thank you for your valuable feedback in group research meetings. Even sometimes I was

under a serious lack of confidence and doubt myself, thank you for your encouragement to make me feel my work is still appreciated. To Dr. Zulfiquar Reza, not just for my research work, it was my honor and pleasure to be a teaching assistant in your class. Thank you for your hands-on guidance about various petroleum software. I truly enjoyed our brainstorms in your office.

To all my friends from the University of Oklahoma, Hao Li, Yaokun Wu, Na Yuan, Fu Jing, Kai Wang, Lei Han, Jianrong Lu, Qiao Qi, Guobin Zhou, Elena, Laura, and countless others, my life has been enriched by getting to know you all. To my friend and colleague, Dr. Felipe Perez, thank you for your technical and informative advice on molecular dynamics simulations. Your experience and sharing save me much time when exploring unknown areas. To my friend and colleague, Changjae Kim, thank you for spending an inordinate amount of time listening to my scientific and non-scientific mumbles. To the guys at the Integrated Core Characterization Center (IC^3), you were some of the best, most fun groupmates I could ever ask for. It was a great pleasure to spend four years with you all. My special thanks also go to Dr. Ali Tinni who provided instructive comments about my work.

Last but not the least, the computing for all the simulations was performed at the OU Supercomputing Center for Education & Research (OSCER) at the University of Oklahoma, which granted me hundreds of hours of simulation. Meanwhile, I want to appreciate the great human team at OSCER.

Boomer Sooner!!!

Table of Contents

Acknowledgments v

Table of Contents vii

List of Tables xii

List of Figures xiii

Abstract xxxvi

Chapter 1 Introduction 1

1.1 Literature Review 1

1.2 Research Motivations 9

1.3 Organization of the Dissertation 10

Chapter 2 EOR Solvent-Oil Interaction in Clay-Hosted Pores 15

2.1 Introduction 15

2.2 Construction of the Illite-fluid Systems 15

2.3 Molecular Dynamics Simulation Details 21

2.4 Results and Discussion 24

2.4.1 Swelling 24

2.4.2 Viscosity 30

2.4.3 Self-diffusion 35

2.5 Numerical Simulation 42

2.6 Final Remarks 47

2.7 Nomenclature 47

Chapter 3 Water Bridges in Clay Nanopores: Mechanisms of Formation and Impact on Hydrocarbon Transport 49
3.1 Introduction 49
3.2 Clay Slit Pore Models 49
3.3 Simulation Details 53
3.4 Results and Discussion 54
3.4.1 Distribution of Water and Hydrocarbon in P-H Nanopore 54
3.4.2 Mechanism of Formation of the Water Bridge 61
3.4.3 Self-diffusion 71
3.5 Final Remarks 76
Chapter 4 Oil-Water Transport in Clay-Hosted Nanopores: Effects of Long-Range Electrostatic Forces 78
4.1 Introduction 78
4.2 Models and Methodology 78
4.2.1 Structure of Illite and Charged Surface Chemistry 78
4.2.2 Simulation Details 79
4.3 Results and Discussion 82
4.3.1 Fluid Transport in H-H Nanopores 82
4.3.2 Fluid Transport in P-H Nanopores 85
4.4 Single-Phase Velocity Profile Comparison between H-H and P-H Pores 90
4.5 Mass Transport 94

4.6 Final Remarks 95

Chapter 5 Fluids Behavior in Clay-Hosted Pores as Salinity Varies 97

5.1 Introduction 97

5.2 The Story So Far 97

5.3 Simulation Models 98

5.4 Molecular Simulations 101

5.4.1 Force Field Details 101

5.4.2 Simulation Details 101

5.5 Results and Discussion 102

5.5.1 Fluid Distribution 102

5.5.2 Salinity Effect 107

5.5.3 Surface Electric Potential 110

5.6 Further Discussion 114

5.7 Final Remarks 116

Chapter 6 The Behavior of Surfactant Microemulsions in Clay-hosted Nanopores 118

6.1 Introduction 118

6.2 Computational Methodology 119

6.2.1 Force Field Details 119

6.2.2 Construction of Microemulsion with Varying Salinities in Bulk Conditions 121

6.2.3 Construction of Microemulsion in Clay-hosted Nanopore 124
6.3 Results and Discussion 125
6.3.1 Fluid Distribution in Bulk Condition 125
6.3.2 Fluid Distribution in Clay-hosted Nanopores 130
6.3.3 Surface Chemistry 135
6.3.4 Self-diffusion 138
6.4 Further Discussion 141
6.5 Final Remarks 142
Chapter 7 What Have We Learned? 143
7.1 Conclusions 143
7.2 Limitations 145
Reference 147
Appendix A 167
A-1 Temperature 167
A-2 Pressure 168
Appendix B-Supplementary Data 173
MD Simulation with Ions Randomly Distributed in Clay Nanopore 173
Results of NEMD Simulation 177
Effect of Acceleration 180
Equilibrium Result with Flexible Clay Structure 181
Unit Conversion of Electrostatic Force 182

Appendix C-LAMMPS Scripts 183

Solvent pdb File 183

Surfactant pdb File 184

Water pdb File 186

Salt pdb File 186

Input File 186

List of Tables

Table 2-1 Modeled atomic coordinates of the unit cell for the illite structure (Drits et al. 2009) 17

Table 2-2 Description of the models used in this paper 21

Table 2-3. Rock physical properties for CMG simulation model 43

Table 2-4. Fluid properties for CMG simulation model 43

Table 2-5 Summary of numerical simulation models 45

Table 3-1Description of the models used in chapter 3 52

Table 5-1 Description of simulation models used in this paper. 100

Table 5-2 Description of additional eight models 108

Table 5-3 Calculated decay length, surface charge density, and surface potential with different salinities, valid for both 10 and 20 nm models. 112

Table 6-1 Summarized models in bulk condition 123

Table 6-2 Summarized models in clay-hosted nanopores 125

List of Figures

Figure 1-2 (a) Surface charge map of kaolinite using high-resolution atomic force microscopy (Kumar et al. 2017), indicating the existence of heterogeneous surface charge. (b-g) Environmental Scanning Electron Microscopy micrographs of non-flat quartz surfaces show the variation of the contact angle due to the existence of heterogeneous surface charge (Kareem et al. 2016). (h-j) Frequency-modulation atomic force microscopy (FM-AFM) images of clinochlore indicate the existence of heterogeneous surface charges (Umeda et al. 2017).....5

Figure 2-1 Schematic representation of the illite supercell (10×2×1). The dimension is 6.4 nm×2.2 nm×1.0 nm. Panels a and b provide top and side views of the illite supercell. Panel C is the slit pore constructed with four parallel illite supercells. *d* is the pore width. Color codes: clay, grey; potassium ion K^+, light grey.....18

Figure 2-2 Snapshots showing the initial configuration of the four illite models containing fluids. Model 1 contains 100 dodecane molecules; Model 2 contains 100 dodecane and 400 methane molecules (20% C_{12} +80% C_1); Model 3 contains 100 dodecane and 400 ethane molecules (20% C_{12} +80% C_2); and Model 4 contains 100 dodecane, 400 ethane and 160 water molecules (20% C_{12} +80% C_2+water). The clay structure contains the same color codes as in Figure 2-1, while the color codes of fluid molecules are: ethane, light

green; dodecane, light blue; CH_4, cyan; and H_2O, red. Every simulation cell size is chosen to be sufficient to eliminate any finite-size effects. 19

Figure 2-3 Snapshots showing the initial fluid configuration in the four bulk fluid models. The fluids have the same color codes as in Figure 2-2. Model 5 contains 100 dodecane molecules; Model 5 contains 100 dodecane and 400 methane molecules (20% C_{12} +80% C_1); Model 7 contains 100 dodecane and 400 ethane molecules (20% C_{12} +80% C_2); and Model 8 contains 100 dodecane, 400 ethane and 160 water molecules (20% C_{12} +80% C_2+water). 20

Figure 2-4 Simulation results of pure dodecane without confinement (Model 5) in equilibrium stage at various temperatures. The green, red, yellow, black, and blue colors represent the temperature at 300K, 350K, 400K, 450K, and 500K, respectively. The densities after equilibrium stage are 0.75572 g/ml, 0.72044 g/ml, 0.69252 g/ml, 0.66114 g/ml, and 0.63404 g/ml, corresponding to temperature of 300K, 350K, 400K, 450K, and 500K, respectively. 24

Figure 2-5 Snapshots showing the four models of illite containing fluids after equilibrium at 350K and 300 atm. The figures have the same color codes as in Figure 2-2. Model 1 is set as a reference condition under illite confinement. Models 2, 3, and 4 show oil swelling when I inject solvents (C_1/C_2/C_2+water) into Model 1. Regions A and B in Model 2 show that some methane remains insoluble in the dodecane at the experimental pressure and temperature.

Model 4 shows that water molecules adsorb on the illite surface while the unabsorbed water forms a water bridge between the top and bottom of the pore (dodecane and ethane are treated by a transparent process). It should be noted that the illite is not fixed in these simulations, and the unbalanced distribution of water between the clay layers (Model 4) causes some warping of the clay plates in Model 4. I will discuss this phenomenon in detail in Chapter 3. 25

Figure 2-6 Snapshots showing the four models of fluids in bulk condition after equilibrium at 350K and 300 atm. The four simulation cells have the same color codes as in Figure 2-3. The hydrogen H is not shown in these snapshots. Model 5 is set as a reference condition for bulk fluids. Models 6, 7, and 8 show oil swelling after injection of solvent with the swelling more pronounced compared to Models 2, 3, and 4 at the same P and T and solvent and oil composition. There is no distinct gas phase indicating complete miscibility of methane with the oil in the bulk. 26

Figure 2-7 Phase envelope and molecular simulations for methane/dodecane at 350 K, 450 K, and 500 K respectively. At 350k, the mixture is just within the 2-phase region, while at 400k and 500K, the mixture is a single-phase liquid in bulk. However, looking at the figures above, methane remains only partly miscible with dodecane indicating that methane molecules have a higher solubility in the bulk than under illite confinement. 29

Figure 2-8 Calculated averaged running integral (Equation (2-4)) from 5 independent 10 ns long equilibrium MD trajectories and equilibrium densities for Model 5 at different temperatures. Panels a, b, c, d, and e correspond to the temperature at 300K, 350K, 400K, 450K, 500K, respectively. Red, green, and blue curves correspond to the average pressure tensor at *xy*, *xz*, and *yz* directions separately. In panel f, the green, red, yellow, black, and blue colors represent the temperature at 300K, 350K, 400K, 450K, and 500K, respectively. The densities after equilibrium stage are 0.75572 g/ml, 0.72044 g/ml, 0.69252 g/ml, 0.66114 g/ml, and 0.63404 g/ml, corresponding to temperature 300K, 350K, 400K, 450K, and 500K, respectively. 32

Figure 2-9 Calculated densities and viscosities as a function of temperature. The results show that the calculated densities (Model 5) agree with NIST densities very well. In Model 8, the calculated viscosities are lower than Model 7, since mixtures of water and hydrocarbons exhibit complex multiphase behavior at elevated temperatures and the water dissolution makes the liquid phase (hydrocarbons) viscosity lower in the simulation.....33

Figure 2-10 Calculated viscosities in Models 1-4 as a function of temperature. The results indicate that viscosities are decreased as solvents are injected. Ethane has a better performance than methane due to its solubility and stronger oil swelling. However, the viscosities in Model 4 increase a bit compared to Model 3. The reason is that water molecules are likely to adsorb on the illite

surface, which decreases the effective volume change for hydrocarbons. Another reason is that water molecules show less solubility than those in bulk density, as shown in Figure 2-8.....35

Figure 2-11 Mean square displacement as a function of observation time from reference (D. Keffer et al. 2001). Panel b is plotted on a log-log scale, which uses the same data from panel a. Panel b shows three regimes: I) free motion region; II) intermediate time regime, and III) long time behavior regime. We only use regime III to calculate the self-diffusion coefficient. 37

Figure 2-12 Mean square displacement as a function of observation time for Model 3 at temperature 350 K and pressure 300 atm. Panel b is on the log-log scale. The dashed lines are ethane in methane/dodecane mixture; The solid lines are ethane/dodecane mixture; The dashed dot lines are dodecane in ethane/dodecane mixture. 39

Figure 2-13 Calculated self-diffusion of fluids as a function of temperature. Panel a shows the calculated self-diffusions of dodecane from Models 1-4. Panel b shows the calculated self-diffusions of solvents from Models 2-4. Panel c and d show the calculated self-diffusions of mixtures from Models 1-8. The results indicate that illite confinement has a strong effect on self-diffusion, and injected solvents can enhance the self-diffusion of dodecane. Meanwhile, water molecules adsorbed on the illite surface will decrease the effective flow volume and finally lower the self-diffusion of dodecane. 41

Figure 2-14 Schematic of the base model from the top view.....43

Figure 2-15 Water and oil relative permeabilities (Sheng, 2017). 44

Figure 2-16 Self-diffusion coefficients of methane and ethane as a function of temperature in bulk condition. 45

Figure 2-17 Oil recovery and gas oil rate of 3 numerical simulations as a function of production time. The oil recovery factor of simulations 1 (green curve), 2 (red curve) and 3 (black curve) are about 27.5%, 12.5% and 5% respectively. Panel a indicates that huff-n-puff still acts a positive role in unconventional reservoir oil recovery according to Simulations 2 and 3. However, when I consider the confinement effects, the oil recovery decreases from 27.5% to 12.5% according to Simulations 1 and 2. This phenomenon might explain why previous numerical studies have a higher oil recovery than the field tests. Panel b demonstrates that miscibility is difficult to achieve in the unconventional reservoir. During the 'puff' process, a huge amount of undissolved gas comes out suddenly to form a GOR peak. Simulation 1 shows the lowest GOR, while Simulation 2 shows the highest. 46

Figure 3-1 Illustration of four illite slit-pore structures. P and H stand for potassium and hydroxyl. a) P-H pore has potassium ions on only one surface; b) is the H-H pore with no potassium ions; c) is the P-P pore with an equal number of potassium ions on both surfaces and d) is the structure that lies in between the P-H and H-H pore structures in terms of ion distribution. 51

Figure 3-2 Snapshots showing the initial configurations of the Models A1-A7 in slit pore of 5 nm, where Cw stands for the water concentration. The clay structure contains the same color codes as in Figure 3-1. The color codes of fluid molecules are ethane, green; dodecane, light blue; and H_2O, red. 53

Figure 3-3 Configurations and water number density profiles (in yellow curves) of different water concentrations at equilibrium at 350 K and 400 atm for a P-H nanopore. Illite structure is not presented for clarity. The higher density peaks adjacent to the hydroxyl surface indicate that water preferentially adsorbs on the hydroxyl and oxygen layer compared to the potassium layer. Liquid color codes: Oxygen in H_2O, red; Hydrogen, white; Carbon in dodecane, blue; Carbon in ethane, green. 56

Figure 3-4 Schematic diagram of calculated Van der Waals force near P-H surface. The calculated Van der Waals force confirms that water is more likely to adsorb on the hydroxyl layer than the potassium layer. 56

Figure 3-5 Configurations and water number density profiles (x-direction) of different water concentrations in pore width of 10 nm and 15 nm after the equilibrium in MD simulations at 350 K and pressure 400 atm. The illite structure is not shown for clarity. The blue lines are water number density profiles. The result illustrates that the distribution of water and dodecane-ethane in the nanopore, which are similar to that in Figure 3-3. 57

Figure 3-6 Equilibrium configurations and number density profiles (z-direction)

for different water concentrations in the 5 nm pore at 350 K and 400 atm for a P-H nanopore. Illite structure is not shown for clarity. The results illustrate that water solubility in the hydrocarbon is possible at a certain temperature and pressure conditions and the 'free' water molecules can disperse in the hydrocarbon to form water bridges. 59

Figure 3-7 Configurations of hydrocarbon and water distribution in the 5 nm P-H nanopore at the water concentration of 18.87%. The white line in panel a is the slice place. Panel b is the slice view for Fig. 6a. Panel b indicates that there is a water bridge formed in the P-H nanopore, but the bridge does not span the entire width in the y-direction. 59

Figure 3-8 Equilibrium configurations and number density profiles (z-direction) of water and hydrocarbon for different water concentrations in a P-H nanopore of width 10 nm at 350 K and 400 atm. Illite structure is not shown for clarity. 60

Figure 3-9 Equilibrium configurations and number density profiles (z-direction) of water and hydrocarbon for different water concentrations in a P-H nanopore of width 15 nm at 350 K and 400 atm. Illite structure is not shown for clarity. The results illustrate that the water bridge still exists even when the pore width increases from 5 nm to 10nm or 15 nm. 61

Figure 3-10 Configurations and number density profiles of water and oil in the hydroxyl-hydroxyl (H-H) surface clay slit pore of width 5 nm. Increasing the

water concentration promotes the formation of a water bridge. 62

Figure 3-11 Configurations and number density profiles of water and oil in the hydroxyl-hydroxyl (H-H) clay pore of width 10 nm. 62

Figure 3-12 Configurations and number density profiles of water and oil in the hydroxyl-hydroxyl (H-H) clay pore of width 15 nm. The results demonstrate that pore width will affect the formation of water bridge and the illite surface shows less effect on the water molecules at the pore center with the increasing the pore width. 63

Figure 3-13 Illustration of the process to calculate the electrostatic force. (a) 5 nm P-H system, and (b) 5 nm H-H system. 65

Figure 3-14 Calculated electric fields in different widths. Absolute values of the electric field strengths in P-H pores (left) are observed to be larger than those in H-H nanopores (right). Increases in pore width decrease the strength of the electric field in both pore systems. It should be noted that no fluid is considered when calculating the electric field. 66

Figure 3-15 Charge distribution of illite structure (the inset chart) and the surface charge density (the main chart) 66

Figure 3-16 In (a), V1 is the unit normal vector. V2 is the OH vector (OH bond angle). θ is the angle between two vectors. In (b), It shows the OH bond angle for all water molecules for different pore widths in H-H and P-H pores. In P-H pores, a dominant angle of 130° is observed while in H-H pores, the OH

bond angles are largely random with a weaker peak at 90°. The electric field of Figure 3-15 influences the orientation of water molecules in both pore systems. 68

Figure 3-17 Initial (left) and final (right) configurations for 15 nm P-H nanopore with water saturation of 38.46%. Note: the cutoff distance is 0.8 nm and hydrocarbon not shown in panel b. The periodic boundary in the z-direction is removed. 69

Figure 3-18 Thickness of water bridge at the water saturation of 71.43% in 5 nm H-H nanopore during the whole simulation time. 70

Figure 3-19 Calculated self-diffusion in P-H illite nanopores. The lines representing the self-diffusion of dodecane are in red, those for ethane are in black, water in green, and the mixture in blue. The results indicate that the self-diffusion coefficient increases initially with increasing water concentration probably because of the formation of a water film that promotes hydrocarbon transport. Subsequent increases lead to a water bridge that impedes hydrocarbon flow, leading to a decrease in the self-diffusion coefficient. Pore width also plays a role in dictating the effect of water adsorption on fluid transport. 72

Figure 3-20 Calculated self-diffusion coefficients in H-H nanopores. The results indicate that water adsorption promotes hydrocarbon flow sharing the same trend in P-H pores. Once the water bridges form, a drastic reduction in the

self-diffusion coefficients is seen. 74

Figure 3-21 Comparisons of self-diffusion between H-H and P-H in different pore widths. The results indicate that self-diffusion in P-H is lower than that in H-H, demonstrating that electric fields can influence the self-diffusion of hydrocarbon through the formation of the water bridge. 76

Figure 4-1 Initial configurations of the seven P-H slit pore models of 5 nm width with varying water concentration. Cw stands for water concentration. The color codes of clay are as in Figure 3-2. (a) the direction of the arrows indicates the direction of an imposed acceleration in subsequent sections of this paper. The fluid-color regimes: ethane (light green), H_2O (red), and dodecane (light blue) 79

Figure 4-2 Pressure and temperature as a function of simulation time. The setting temperature and pressure are 350K and 400atm. In the NEMD simulations, there is only a small increase in temperature. The average equilibrium of temperature is about 352K 81

Figure 4-3 Water and hydrocarbon velocity profiles at 0.0005 nm/ps2 in 5 nm H-H nanopore. Cw stands for water concentration. Water concentration is seen to strongly impact both water and hydrocarbon velocities. For the water and hydrocarbon velocities, the reader can refer to Figure B-1 in Appendix B. 83

Figure 4-4 Distribution of water molecules for various water concentrations. Hydrocarbon is not shown. On the left, Cw = 18.97% and on the right, Cw =

71.43%. Increases in water concentration increase the adsorbed layer thickness that in turn influences water and hydrocarbon velocities. 83

Figure 4-5 Water and hydrocarbon velocity profiles at 0.002 nm/ps2 in 15 nm H-H pores. The flow profiles for both phases appear more complex and simply correspond to the local phase densities within the pore.....84

Figure 4-6 Distribution of water at 0.002 nm/ps2 and Cw = 71.43% in 5nm, 10nm, 15nm H-H nanopores. The hydrocarbon molecules are not shown. The result indicates that at each pore width, the peaks and troughs in the velocity profiles correspond to the local density of each of the phases. The motion of the water elongates the droplets entrained in the hydrocarbon phase. 85

Figure 4-7 Water and hydrocarbon velocity profiles at the acceleration and water concentration of 0.002 nm/ps^2 and 71.43% respectively in different P-H nanopore widths. The result indicates that pore width impacts the velocity patterns. At 5nm, I observe a parabolic shape for the flow profiles which get progressively flattered as the pore width increases.....86

Figure 4-8 Molecular distribution and velocity profiles of water in P-H pores of different widths at a water concentration of 71.43%. The acceleration is 0.002 nm/ps2. Hydrocarbon is not shown for clarity. The red dots represent adsorbed water, and the yellow dots are those in the water bridge. In a 5 nm P-H nanopore, acceleration causes the adsorbed layer to exchange both mass and velocity with water at the pore center. Increasing the pore width to 10 nm

or 15 nm, no mass or velocity exchange occurs between the adsorbed layer and water in the bridge or pore center, as revealed by the flatter velocity profile, ... 88

Figure 4-9 Water and hydrocarbon velocity profiles at the acceleration of 0.002 nm/ps^2 in 10 nm P-H nanopore. The result indicates that water concentration can impact the flow pattern. 90

Figure 4-10 The bar errors of water-bridge thickness with different water concentrations. The minimum thickness of water bridges at a water concentration of 18.87%, 58.82%, 71.43%, and 80.00% is 0.94 nm, 1.24 nm, 1.60 nm, and 1.96 nm respectively. Increasing the water concentration creates thicker water bridges rather than increase the width of the adsorbed layer in P-H pores. 90

Figure 4-11 Comparison of single-phase (water and hydrocarbon) velocities between H-H and P-H nanopores of different widths. The self-generated electric field in P-H pores and the imposed acceleration dictate fluid transport in the center of the pore. For the same acceleration, the fluid velocity profile is flat in P-H pores and parabolic in H-H pores. 92

Figure 4-12 Water distribution in EMD and NEMD simulations in 5 nm P-H (left) and H-H (right) nanopore. Hydrocarbons are not presented for clearance. It indicates that the water bridge breaks down during flow in the NEMD simulation in the H-H nanopore, demonstrating that the strength of the

hydrogen bond is weak to persist the water bridge. However, in the P-H nanopore, with the assistance of the electric field, the water bridge persists in NEMD simulations. 93

Figure 4-13 (a) Illustration of the H bond. An H bond(Costa et al. 2005) occurs when the distance between oxygen and oxygen is less than 3.6 Å, the distance between hydrogen (donor) and oxygen (acceptor) is less than 2.4 Å, and the angle between V_{OO} and V_{OH} is less than 30° where V_{OO} is the vector starting from the oxygen to another oxygen and V_{OH} is the vector from the oxygen to hydrogen. (b) the distribution of H bond from the bottom to the top pore surface in P-H and H-H systems. 94

Figure 5-1 Previous works review (Xiong et al. 2020 and 2020b). (A-B) Illite structure from *xy* and *xz* projections. (C-D) Two different illite pore structures: P-H and H-H, where P-H and H-H represent the heterogeneous and homogeneous surface charges, respectively. (E) Water bridges in P-H nanopores. Hydrocarbon is not shown for clarity. (F) Adsorbed water in H-H nanopores. (G) Calculated electric fields across the whole P-H nanopore at different pore widths (5, 10, and 15 nm), where all the electric field strengths are larger than 1 V/nm, promoting the formation of a water bridge. (H) Weaker electric fields across the H-H nanopore lead to water existing as an adsorbed phase. Color codes: grey, clay; light grey, potassium (K^+); and red, water. 98

Figure 5-2 The initial configurations of the P-H models with varying salinities (pore width=10 nm, Cw= 70%). (A) 3200 ppm; (B) 37000 ppm; and (C) 100000 ppm. Color codes: grey, clay; light grey, potassium (K^+); red, water, light blue, oil; blue, Na^+; and yellow, Cl^-. 100

Figure 5-3 Fluid distribution in different salinities, water concentrations, and surface chemistries. The pore width is 10 nm and Oil is not shown for clarity. (A-C) Fluid distribution at a water concentration of 38% in P-H nanopore with different salinities. (D-F) Fluid distribution at a water concentration of 38% in H-H nanopore with different salinities. (G-I) Fluid distribution at a water concentration of 70% in P-H nanopore with different salinities. (J-L) Fluid distribution at a water concentration of 70% in H-H nanopore with different salinities. Color codes are the same as in Figure 5-2. 104

Figure 5-4 Water orientation and hydrogen bond. (A) Calculated possible orientation in P-H and H-H nanopores, data from Fig.3G and J. (B) Calculated number of H-bonds from the bottom to the top surface at the pore width of 10 nm. The H-bond has been described in Chapter 4..... 106

Figure 5-5 Fluid distribution in different salinities, water concentrations, and surface chemistries. The pore width is 20 nm and Oil is not shown for clarity. (A-C) Fluid distribution at a water concentration of 38% in P-H nanopore with different salinities. (D-F) Fluid distribution at a water concentration of 38% in H-H nanopore with different salinities. (G-I) Fluid distribution at a

water concentration of 70% in P-H nanopore with different salinities. (J-L) Fluid distribution at a water concentration of 70% in H-H nanopore with different salinities. Color codes same as Figure 5-2. 107

Figure 5-6 Fluid distribution in different salinities. Pore width is 10 nm, water saturation is 38%, surface chemistry is P-H and oil is not shown for clarity. (A) 8100 ppm; (B) 12400 ppm; (C) 16000 ppm; (D) 27000 ppm. The threshold value of salinity is between 8100 and 12400 ppm. In this model, the threshold value is about 8500 ppm, provided in the Supporting Information. Color codes same as Figure 5-2. 109

Figure 5-7 Fluid distribution in different salinities. Pore width is 20 nm, water saturation is 38%, surface chemistry is P-H and oil is not shown for clarity. (A) 8100 ppm; (B) 12400 ppm; (C) 16000 ppm; (D) 27000 ppm. Color codes same as Figure 5-2. 110

Figure 5-8 Calculated surface electric potentials in the z-direction. The pore width is 10 nm and the water concentration is 38%. The blue and orange curves are the surface potential of upper and lower surfaces, respectively. (A) 3200 ppm; (B) 8100 ppm; (C) 12400 ppm. The results indicate that the water-bridge phenomenon is attributed to the overlapping non-zero potentials from both surfaces. Increasing the salinity decreases the strength of surface potentials at the pore center to values close to zero. 112

Figure 5-9 Water number density profiles for different salinities in 10 nm

nanopores in the x-z plane (top panels) and along the z-axis (bottom panels). (A-B) Water bridges are observed; (C) A number density of zero indicates the absence of a water bridge. It indicates that water molecules are more inclined to be adsorbed on the lower surface than on the upper surface given the configuration used in my models with K^+ ions on the lower surface. This is expected given that hydroxyl groups and oxygen atoms on the top surface have larger van der Waals forces than potassium on the lower surface. Meanwhile, increasing the salinity will decrease the thickness of the water bridge (see panels A to B). 113

Figure 5-10 Calculated self-diffusion coefficients in nine models with different salinities in the 10nm pores. When the salinity is below 8500ppm, the presence of a water bridge impedes fluid flow. However, when the salinity is higher than 12400ppm, the formation of ionic aggregates is the primary factor to impede flow. Therefore, there exists an optimal range of salinity (8500-12400ppm, grey region) where the mobility of oil and water is the highest in clay pores. 114

Figure 5-11 Calculated self-diffusion coefficients in seven models with different salinities in the 20nm pores..... 115

Figure 6-1 Schematic illustration showing how the microemulsion droplet can squeeze itself through the nanopore and recover its original structure (Bui et al. 2017). 119

Figure 6-2 Schematic configuration of d-limonene (a) and $C_{12}E_7$ (b). Color code: pink, carbon in solvent; brown, carbon in surfactant; red, oxygen; and white, hydrogen. 120

Figure 6-3 (a) Initial configuration of the simulation box containing random placement of water (red), solvent (pink), and surfactant (brown). (b) Equilibrium configuration of the simulation box containing a stable microemulsion. (c) Microemulsion extracted from panel b. The diameter of the microemulsion is about 6.5 nm and the scale is not the same as panel b. The total simulation time is 50 ns. 122

Figure 6-4 Initial Configuration of models in bulk condition with varying salinities. The color code follows in Figure 6-2. The color codes of salt are Na, red, and Cl, yellow. 123

Figure 6-5 Initial Configuration of models in clay-hosted nanopore with varying salinities. The fluid color code follows in Figure 6-3. Grey color is the clay, and light grey is potassium (K^+). The pore width is 11 nm. The surface chemistry in M11-M14 is P-H while in M15-M18 is H-H. 125

Figure 6-6 Equilibrium configuration of Models 2-10 after 50 ns. The color code is the same as Figure 6-4. 126

Figure 6-7 The shape of microemulsions in Models 2-10. The microemulsion surface is rendered as a light grey surface. The color code is the same as Figure 6-4. 127

Figure 6-8 Projection on the *xy*- plane of microemulsion after the simulation time of 50 ns. 128

Figure 6-9 Projection on the *xz*- plane of microemulsion after the simulation time of 50 ns illustrating that they are stable at all salinities 129

Figure 6-10 Calculated surfaces of microemulsions at varying salinities. It indicates that by increasing the salinity, the microemulsion surface will correspondingly increase. Meanwhile, the surface areas of the microemulsions with varying salinity range from 9152 to 9487 A^2 with a standard deviation of 111 A^2 illustrating microemulsions are stable at all salinities. 129

Figure 6-11 Fluid distribution in P-H clay-hosted nanopores as the function of simulation time (in the vertical direction) and salinity (in the horizontal direction). Remembered that the salinities of M11-M14 are 0, 3000, 10000, and 100000 ppm, respectively. Water molecules are not shown for clarity. It indicates the behavior of the microemulsion is a function of salinity and increasing the salinity to a certain value (i.e., 10000 ppm) can enhance the stability of the microemulsion in P-H clay-hosted nanopores. 132

Figure 6-12 Density plot of M11-M14 in *xy*- projection at the simulation time of 50 ns in P-H clay-hosted nanopores. High-density numbers correspond to red colors and low-density numbers to blue colors. The calculated method follows the same process described in Section 6.3.1. 133

Figure 6-13 (Upper four panels) Fluid distribution in H-H clay-hosted nanopores as the function of salinity where water molecules are not shown for clarity. (Bottom four panels) Extracted microemulsions from the corresponding models. It indicates that irrespective of the salinity, the microemulsions are stable keeping the shape as a sphere in H-H clay-hosted nanopores. 134

Figure 6-14 Density plot of M15-M18 in *xy*- projection at the simulation time of 50 ns in H-H clay-hosted nanopores. High-density numbers correspond to red colors and low-density numbers to blue colors. The calculated method follows the same process described in Section 6.3.1. 135

Figure 6-15 Calculated electric fields as the function of salinity and surface chemistry. Remembered that the surface chemistry of M11-M14 is P-H and M15-M18 H-H. The average electric fields in M11-M18 are 7.77, 4.94, 1.13. 0.41, 0.51, 0.39, 0.35 and 0.26 V/nm respectively. 136

Figure 6-16 Behavior of microemulsion at the only presence of electric field as the function of simulation time. Color code refers to Figure 6-2. 137

Figure 6-17 (a-b) Behavior of microemulsion at the only presence of clay surface as the function of simulation time. (c-d) Density plots on *xz* and *xy* projections respectively. High-density numbers correspond to red colors and low-density numbers to blue colors. The calculated method follows the same process described in Section 6.3.1. 138

Figure 6-18 Calculated self-diffusions of water, solvent, and surfactant in M1-M18.

.....139

Figure 6-19 Equilibrium configuration of the model at the salinity of 11000 ppm in different projections. The simulation time is 50 ns. The color code refers to Figure 6-4.....142

Figure A-1 Schematic of a cubic box.....167

Figure A- 2 Schematic of external pressure.....170

Figure B-1 (a) Initial model where potassium ions are randomly distributed in clay nanopore, the pore width is 5 nm and water saturation 38%. (b) An initial model where oil and water are not shown. (c-g) Equilibrium results after 20 ns starting from the same model but with 5 different initial velocities. The numbers in panels c to g are the number of potassium ions corresponding to upper and bottom surfaces. Color codes: clay, grey; potassium, light grey; water, red; and oil, blue.....174

Figure B-2 (Upper three figures) initial configuration of models with different pore widths (1, 2, and 5 nm). (a-c) Equilibrium results after 20 ns where potassium ions are handled by a transparent process (transparency is 0.8) and green lines are the trajectories of potassium ions. Color codes refer to Figure B-1. ...176

Figure B-3 Water and hydrocarbon velocity profiles at the acceleration of 0.0005 nm/ps^2 ,0.001 $nm/ps^{2,}$ and 0.002 nm/ps^2 in a 5 nm H-H nanopore. Cw stands for water concentration. Water concentration is seen to strongly impact both water and hydrocarbon velocities. 177

Figure B-4 Water and hydrocarbon velocity profiles at the acceleration of 0.002 nm/ps^2 in 10 nm and 15 nm H-H nanopores. Increasing the pore width causes a more complex and disturbed flow pattern. The peaks and troughs in the velocity profiles correspond to local phase density variations. 178

Figure B-5 Hydrocarbon velocity profiles from all 54 NEMD simulations for P-H pores, where the effects of acceleration, pore width, and water concentration are analyzed. The results indicate that at increasing water concentrations, hydrocarbon velocity decreases. An increase in pore width and acceleration also increases the velocities. The flat velocity profile is more pronounced at larger pore widths because of the decreasing interaction between hydrocarbon molecules and clay surface. 179

Figure B-6 Water velocity profiles for 54 NEMD simulations in P-H nanopore. The results indicate that increasing water concentrations will decrease water velocity. An increase in pore width and acceleration also increases the velocities. The flat velocity profile is more pronounced at larger pore widths because of the decreasing interaction between water molecules and the clay surface. 180

Figure B-7 Water velocity profiles at different accelerations and 100% water concentration in 15 nm P-H nanopore. The result indicates that a flatter velocity profile is observed when the acceleration is dominant and any other wall effects are less significant'. 181

Figure B- 8 Equilibrium Result with a flexible clay structure. In the presence of a strong electric field, even when I allow the clay structure to move, the distance between upper and lower surfaces is still not changed. 181

Abstract

Our understanding of fluid behavior and transport in shales, especially in organic or kerogen pore systems, has grown rapidly over the last few years. Yet, given the prevalence of inorganic material that often hosts the organics in shales, little attention has been devoted to how fluids move and distribute themselves in clay-hosted pores. In this work, I use classical molecular dynamics simulations to investigate fluid behavior and transport in charged clay-hosted nanopores. I focus on mixtures of brines and hydrocarbon confined in clay slit pores and consider two different surface charges. A very important constraint I impose on the models is rigidity to avoid clay swelling behavior. My initial set of simulations focuses on oil-solvent mixtures in clay pores and the conditions under which they become miscible, and the impact of confinement on the self-diffusion of hydrocarbon as well as viscosity. At specific pore widths and water saturations, water is shown to bridge across the pore from one clay surface to the other, and not merely be adsorbed. My work discusses the conditions under which these bridges form and their impact on fluid movement. I show that increasing brine salinities can dissipate the water bridges which motivates me to discuss optimizing salinity for waterfloods or hydraulic fracturing fluids when clays are predominant. The final discussion is the effect of varying salinity on the shape and stability of surfactant-solvent microemulsions in clay pores.

Chapter 1 Introduction

1.1 Literature Review

The U.S. Energy Information Administration (EIA et al. 2019) reports that the proven oil and natural gas reserves in US shale plays are 23.2 trillion barrels and 353.1 trillion cubic feet respectively, underscoring their significance to the US energy mix.

However, these plays are characterized by an ultra-low permeability (in the range of nanodarcies[1], six orders of magnitude below the permeability in conventional reservoirs) and a very low porosity where the pore width ranges from a few to hundreds of nanometers in diameter (Nelson et al. 2009; Curtis et al. 2010; Kuila et al. 2013). In these extremely small pores, the pore surface can significantly impact the phase behavior and transport of hydrocarbon molecules (Singh et al. 2009; Jin et al. 2016a; Singh et al. 2018). Therefore, understanding fluid behavior under confinement in shale nanopores is a necessary prerequisite to quantifying both primary and enhanced recovery in these tight rocks. There have been several complementary approaches to address the complex behavior of fluids in these pore systems: computational approaches (Hu et al. 2016; Wang et al. 2016a; Khoa Bui et al. 2017; L. Huang et al. 2018; Perez et al. 2020), bench-top experiments (Sheng et al. 2014 and 2015; Sharma et al. 2017; Dang et al. 2019; Mamoudou et al. 2020), and field tests (Hoffman et al. 2016; Sheng et al. 2015a, 2015b and 2017). This dissertation belongs to the first group and specifically focuses on molecular dynamics (MD) simulations.

[1] $1\ Darcy\ \approx 1 \times 10^{-12} m^2$

Hydrocarbons in organic-rich shales are largely understood to be stored within organic nanopores, specifically within organic matter known as kerogen (Curtis et al. 2010 and 2011; Perez et al. 2020 and 2020a). Earlier studies of shales relied on molecular proxies for kerogen, such as planar graphene slit pores, in MD simulations (Plathe et al. 1997; Wongkoblap et al. 2008; Campos et al. 2009; Mosher et al. 2013; Akkutlu et al. 2014; Hu et al. 2015 and 2016; Wang et al. 2016). While these models are instructive, they do not represent the complex pore surface chemistry and structure seen in kerogen (Gouth et al. 2013; Kazemi et al. 2016; Perez et al. 2020). Ungerer et al. (2015) and Bousige et al. (2016) laid the foundations for several subsequent modeling studies (Pathak et al. 2016; Borujeni et al. 2019; Perez et al. 2019a; Gong et al. 2020; Perez et al. 2020a and 2020b) that rely on the use of more realistic molecular models of kerogen. Recent studies have expanded to modeling enhanced oil recovery (EOR) in unconventional reservoirs (Perez et al. 2020a and 2020b) and show results consistent with lab observations (Dang et al. 2019; Mamoudou et al. 2020) and field pilots (Wang et al. 2010; Hoffman et al. 2016; Sheng et al. 2017).

However, clay minerals and other inorganic material account for 70-90% volume fraction in shales (Heidari et al. 2011; Zhai et al. 2014; Zhang et al. 2016a; Chen et al. 2016; Zhang et al. 2016b; Hao et al. 2018; Szczerba et al. 2020) and play a significant role in fluid behavior and transport (Geramian et al. 2016; Lara et al. 2017; Katti et al. 2017; Liu et al. 2018; Eveline et al. 2018; Rahromostaqim et al. 2018). FIB-SEM (Focused Ion Beam-Scanning Electron Microscopy) images also suggest that the

organics are typically hosted in an inorganic background and the fluids are likely driven from organic pore systems to inorganic pores and eventually to the fracture systems (Sondergeld et al. 2010).

Clay minerals are layer-type aluminosilicates (Sposito et al. 1999), ubiquitous in geological deposits (Pevear et al. 1999; Tombácz et al. 2004; Katti et al. 2017; Hao et al. 2019b). The crystal structures of clay minerals are usually classified as 1:1 or T:O type, typified by kaolinite (T and O stand for one tetrahedral silicate sheet and one octahedral hydroxide sheet separately) and 2:1 or T:O:T type, typified by illite (Galán et al. 2013). Clay minerals generally are thought to have negatively charged surfaces due to the existence of oxygen and hydroxyl groups on the local surface (Pevear et al. 1999; Tombácz et al. 2004; Katti et al. 2017; Hao et al. 2019b). Experimental results also show that cation substitutions (isomorphic replacement of tetrahedral Si^{4+} by Al^{3+}, or octahedral Al^{3+} by Mg^{2+} and Fe^{2+}) can often happen in tetrahedral and octahedral sheets in clays (Mueller et al. 2014). For example, smaller cations tend to occur in tetrahedral sheets (such as Si^{4+}) while larger cations tend to occur in octahedral sheets (such as Mg^{2+} and Fe^{2+}) and cations with intermediate size can occur in either sheet (such as Al^{3+}, Fe^{3+}). These cation substitutions lead to a negative structural charge. This negatively charged structure is balanced by adsorbing counterions such as Na^{+}, $Ca^{2+,}$ and K^{+} nearby. The largest counterions must enter into the interlayer spaces because neither octahedral nor tetrahedral sites have enough space to hold them (Mueller et al. 2014).

During cation substitutions, unbalanced surface charges can occur. For instance, Tombácz et al. (2006) and Kumar et al. (2017) use experiments to prove that 2:1 type montmorillonite and 1:1 type kaolinite can carry a heterogeneous surface charge as shown in Figure 1-1a, and the distribution of charge is the function of the crystal structure of clay particles, pH and dissolved electrolytes. Kareem et al. (2016) further suggest that surface charge heterogeneities can likely explain varying contact angle measurements locally on clays as shown in Figure 1-1b to Figure 1-1g. Later, Umeda et al. (2017) use ultra-low noise frequency-modulation atomic force microscopy (FM-AFM) to image clinochlore as shown in Figure 1-1h and observe a heterogeneous surface charge distribution where T denotes negatively charged surfaces and B positively charged. The experimental observations enable reconstruction of the structure of clinochlore as shown in Figure 1-1i, and the calculated electric potential along the surface is shown in Figure 1-1g where the highest and lowest electric potentials are 20 and -20V respectively. More interestingly, Fan et al. (2018) observe voltage enhancement when a NaCl-based electrolyte flows over this specially charged surface. Recently, Hao et al. (2019a) also show that illite might possess an internally unbalanced electrical charge due to the heterogeneous distribution of potassium (K^+). Clay flocculation can also occur with heterogeneously charged surfaces (Nguyen et al. 2009; Sakhawoth et al. 2017).

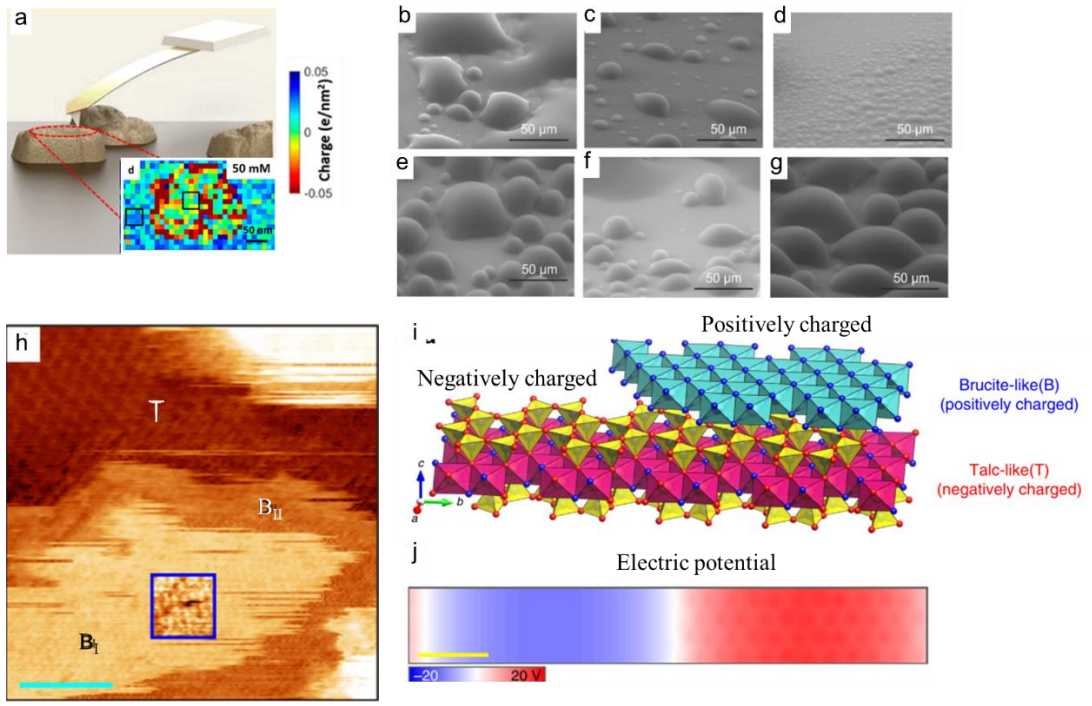

Figure 1-1 (a) Surface charge map of kaolinite using high-resolution atomic force microscopy (Kumar et al. 2017), indicating the existence of heterogeneous surface charge. (b-g) Environmental Scanning Electron Microscopy micrographs of non-flat quartz surfaces show the variation of the contact angle due to the existence of heterogeneous surface charge (Kareem et al. 2016). (h-j) Frequency-modulation atomic force microscopy (FM-AFM) images of clinochlore indicate the existence of heterogeneous surface charges (Umeda et al. 2017).

These heterogeneous surface charges in clay minerals make clay-water interaction quite complex (Lockhart et al. 1980; Smalley et al. 1994; Saarenketo et al. 1998; Vlachy et al. 2001; Prakash et al. 2015). Current research on clay-water interaction can be broadly classified into five different areas: hydration, dispersion, flocculation, deflocculation, and aggregation (Low et al. 1961). Hydration refers to the adsorption of water and subsequent swelling (Loring et al. 2013). Dispersion, on the other hand, occurs when clay platelets disperse as water forces the platelets apart (Czyż et al. 2015). Flocculation begins when previously dispersed platelets come together due to the attractive force of oppositely charged surfaces on the platelets (Shakeel et al. 2020).

Deflocculation typically occurs with a chemical deflocculant that reduces the surface and edge charges to eventually impair the forces of attraction (Orton et al. 1906). Aggregation is a slightly different phenomenon where the hydrational layer around clay platelets is altered by removal of the deflocculant from the positive edge charges allowing platelets to assume a face-to-face structure (Guichet et al. 2008).

This work focuses solely on the hydration issue that occurs as clays absorb water but do not consider swelling. My dissertation is focused on the behavior of fluids within the pore systems. Traditional MD work has focused on adsorption in clay pores (Hensen et al. 2002; Zen et al. 2016; Underwood et al. 2016; Yi et al. 2018; Hwang et al. 2019), but a growing body of work on clay-water hydration reports the formation of a water bridge in hydrated clay minerals (Osipov et al. 2012; Yanagihara et al. 2013; Striolo et al. 2015; Zhang et al. 2016; Liu et al. 2016; Liu et al. 2018; Xiong et al. 2019a;). This phenomenon is commonly accepted as 'capillary condensation' or 'capillary bridge' (Yamashita et al. 2013; et al. 2015; Coasne et al. 2010; Monson et al. 2012; Ho et al. 2015; Dörmann et al. 2015; Leroch et al. 2013; Giner et al. 2019).

However, clay minerals typically carry negatively charged surfaces and nonbonded positive cations (sometimes even with heterogeneous surface charge) (Hensen et al. 2002; Kuila et al. 2013). Therefore, the formation of water bridges might not solely occur due to 'capillary condensation' but due to preferential orientation of water thereby influencing its structure (Rigo et al. 2019). There is also strong evidence that the water bridge can significantly impact fluid transport in clay nanopores (Liu et

al. 2018).

It is also important to consider the effect of salinity in clay-rich formations where the formation of brine salinity can reach as high as 100,000 ppm (Sheng et al. 2014). Fracturing fluids, meanwhile, are typically low salinity formulations to mitigate the effect of clay swelling (Hensen et al. 2002; Yi et al. 2018; Snosy et al. 2020). The underlying mechanism of clay swelling is by repulsion between clay layers (induced by the formation of electric double layers) (Hensen et al. 2002). The low salinity formulation of fracturing fluids decreases the thickness of the double layer (compared with freshwater) and in turn mitigates clay swelling (Bennion et al. 1998). In the electric double layer, all ions are hydrated to some extent (Tombácz et al. 2006; Howard et al. 2010; Fang et al. 2020) but are associated with different hydrated radii. Consequently, Na^+ (hydration radius of 450 pm) and K^+ (hydration radius of 300 pm) (Bennett et al. 2015) have different impacts on clay swelling (Ahmed et al. 2016) with KCl often used as a clay stabilizer to mitigate swelling (Sameni et al. 2015).

There is however no discussion of optimal salinity levels for clays. While pure water promotes swelling (Hensen et al. 2002), higher salinities can also cause other problems such as ionic aggregation (Koleini et al. 2019a) and formation damage (Galliano et al. 2000). The optimal salinity for hydraulic fracturing is analogous to considerations for low salinity waterflooding (Tang et al. 1997; Galliano et al. 2000; Lager et al. 2008; Denney et al. 2009; Alotaibi et al. 2011; Kadoura et al. 2016). In this dissertation, I also attempt to provide optimal salinity values for hydraulic fracturing

fluids and/or waterflooding when clays are present.

Surfactant flooding is widely used in conventional reservoirs to enhance oil recovery by reducing the interfacial tension between oil and water, thus increasing the displacement efficiency (Schramm et al. 1992). For ultra-low permeability unconventional shales, water-based EOR has traditionally been limited in scope. However, a few recent successful experiments show increased well productivity in response to microemulsion additives in water-based hydraulic fracturing fluids (Champagne et al. 2011; Penny et al. 2012). Microemulsions are clear, thermodynamically stable isotropic liquid mixtures of oil, water, and surfactant, frequently in combination with a cosurfactant (Kahl et al. 2002).

Bui et al. (2015a, 2015b, 2016, and 2018) use MD simulations to systematically study the behavior of the microemulsions within kerogen, including the penetration behavior of microemulsions in shale nanopores, microemulsion effects on oil recovery from kerogen, and the mobilization of oil using microemulsions. However, there is little to no consideration of the stability of the microemulsions (Eastoe et al. 1990; Klier et al. 2000; He et al. 2004; Lee et al. 2018; Ma et al. 2019) in response to changes in temperature, pressure, salinity, surfactant-solvent (cosurfactant) ratio, and surface interactions. While the impact of varying temperatures, pressures, salinities, and surfactant-solvent ratios are more effectively determined using benchtop experiments, probing the behavior of microemulsions confined in clay or organic nanopores necessitates the use of MD. In this work, I study the stability of microemulsions at

varying salinity conditions when confined in clay slit-pores. This is important because the delivery of the microemulsion to target organic pores will require the microemulsion to traverse and interact with clay surfaces.

Finally, I would also like to mention that there is a growing body of work in organic pores while this dissertation focuses on inorganic, clay pores, thereby laying the foundation to understand fluid storage and transport in mixed-wet pore systems (Kim et al. 2020).

1.2 Research Motivations

This dissertation is a computational study into the fluid behavior in clay-hosted nanopores. Interactions between clay mineral surfaces, oil components, brine solutions, or microemulsions have been modeled using classical atomistic molecular dynamics. The emphasis of this study is on understanding how the clay-hosted nanopores change the behavior of water, oil, brine solutions, or microemulsions at an atomic level. The main motivations of the dissertation are:

1. To understand solvent-oil interactions in clay-hosted pores: *Do clays impact the mobility of hydrocarbons or water? Does the distribution of these fluids impact the relative mobility of the phases? Are these considerations absent from traditional reservoir simulation tools?*
2. To interpret the role of charged clay surfaces on the behavior and transport of water and hydrocarbon: *Does the distribution of water depend on the type of*

clay surface or charge distribution? What are the impacts of fluid-clay interactions on the relative phase mobility?

3. To understand the effect of varying salinity on the fluid distribution in the clay-hosted nanopore: *Is there an optimal range of salinity for fracturing fluids or low-salinity waterfloods ?*
4. To probe the behavior of microemulsion in clay-hosted nanopores with varying salinity: *To describe the stability of microemulsions in clay pores under different salinity conditions. Can clay pores deliver microemulsions to organic pores?*

1.3 Organization of the Dissertation

With these aims in mind, the dissertation is broken down into several chapters. Each chapter has been written with forethought of being submitted for publication in the future (Chapter 6) or has already been published in peer-reviewed journals (Chapters 2, 3, and 4) or conference papers (Chapter 5, ready to transfer to peer-reviewed journal). A brief description of each chapter is as follows:

Chapter 2: EOR Solvent-Oil Interaction in Clay-Hosted Pores

This chapter has previously been published in *Fuel*:

Reprinted (adapted) with permission from *(Hao Xiong, Deepak Devegowda, Liangliang Huang. EOR Solvent-Oil Interaction in Clay-Hosted Pores: Insights from Molecular Dynamics Simulations. Fuel, 2019,249:233-251. DOI:*

https://doi.org/10.1016/j.fuel.2019.03.104). **Copyright (2019) Elsevier Ltd.**

This chapter introduces the concept of using atomistic simulations to model solvent-oil interactions in clay-hosted nanopores which has not been addressed previously. I use illite to represent clays and compare fluid behavior (i.e., diffusion, miscibility, viscosity, and oil swelling) between bulk and confined[2] conditions. I show that recovery estimates using commercially available simulators can be overly optimistic because they neglect the effect of confinement on viscosity and self-diffusion of the resulting mixtures.

Chapter 3: Water Bridges in Clay Nanopores: Mechanisms of Formation and Impact on Hydrocarbon Transport

This chapter has previously been published in *Langmuir*:

Reprinted (adapted) with permission from *(Hao Xiong, Deepak Devegowda, Liangliang Huang. Water Bridges in Clay Nanopores: Mechanisms of Formation and Impact on Hydrocarbon Transport. Langmuir. 2020, 36(03): 723-733. DOI: https://doi.org/10.1021/acs.langmuir.9b03244).* **Copyright (2020) American Chemical Society.**

This chapter has an in-depth analysis of the formation mechanisms of water bridges in clay-hosted nanopore using equilibrium MD simulations and their impact on hydrocarbon transport. I use two different basal illite surface chemistries: potassium-

[2] Confinement refers to situations where the pore walls exert an influence on fluid molecules altering their phase behavior or other properties.

hydroxyl (P-H) and hydroxyl-hydroxyl (H-H) structures. Results show that pore width and water concentration control the formation of water bridges in addition to the degree of charge imbalance between adjacent clay plates. My results also indicate that heterogeneous surface charges can induce local electric fields, favoring the formation of water bridge.

Chapter 4 Oil-Water Transport in Clay-Hosted Nanopores: Effects of Long-Range Electrostatic Forces

This chapter has previously been published in *AIChE Journal*:

Reprinted (adapted) with permission from *(Hao Xiong, Deepak Devegowda, Liangliang Huang. Oil-Water Transport in Clay-Hosted Nanopores: Effects of Long-Range Electrostatic Forces. AIChE Journal.2020, 66(08):1-16. DOI: https://doi.org/10.1002/aic.16276).* **Copyright (2020) American Institute of Chemical Engineers (License Number: 5021010431821).**

Chapter 4 is an extension of the work done in Chapter 3. This chapter aims to understand the effect of long-range electric fields on oil-water transport using non-equilibrium MD (NEMD) simulations. My NEMD results show complex two-phase hydrocarbon and water flow patterns in H-H nanopores. In contrast, flow patterns in P-H nanopores are more organized because of the presence of an electric field that creates a water bridge. Water bridges in H-H nanopore are less stable and break down during fluid transport but the presence of an electric field in the P-H nanopore maintains the water bridge under more severe conditions.

Chapter 5 Fluids Behavior in Clay-Hosted Pores as Salinity Varies

This chapter has previously been published in two conference papers:

The main aim of this chapter is to understand the impact of salinity on fluid behavior in clay nanopores to determine optimal fracturing fluid salinity (or low salinity waterflooding applications). I use a wide range of concentrations (0-100000ppm NaCl) in these pores and quantify the fluid spatial distribution, surface electric potentials, and self-diffusion to model the interaction between clays, water, oil, and salts. I show that there is an optimal range of salinity for the pore surface chemistry and pore widths under consideration where the mobility of the oil phase is the highest.

Chapter 6 The Behavior of Surfactant Microemulsion in Clay-hosted Nanopore

This chapter considers the stability of microemulsion in clay-hosted nanopores at different salinities. The microemulsion includes d-limonene (solvent) and dodecanol heptaethyl ether (C12E7, nonionic surfactant). I compare the stability of the microemulsion in bulk and under confinement with two different clay surface charges. Although stable in the bulk under various conditions of salinity, I show that with a strong charge imbalance and at low salinities, the microemulsion is unstable. My work demonstrates an optimal salinity exists that can weaken the effect of charged clay surface and keep the microemulsion stable and therefore, deliver the microemulsion to the target kerogen more effectively.

Chapter 7 Conclusions

This chapter highlights the key conclusions of the dissertation. It presents the overall successes of the work and discusses additional opportunities for examining fluid behavior in clay-hosted nanopores using atomistic simulations.

Chapter 2 EOR Solvent-Oil Interaction in Clay-Hosted Pores

2.1 Introduction

Despite the tremendous progress in horizontal well technology and hydraulic fracturing (Sheng et al. 2015a), the expected recovery from unconventional shales is often below 10% of the original oil-in-place (Hoffman et al. 2013; Salahshoor et al. 2018). Enhanced oil recovery (EOR) has been shown to be promising using benchtop experiments (Sheng et al. 2017; Dang et al. 2019; Mamoudou et al. 2020) and field pilots (Wang et al. 2010; Hoffman et al. 2016). Huff-n-puff miscible-gas injection (Gamadi et al. 2013; Tovar et al. 2014; Sheng et al. 2015a; Kazemi et al. 2019; Zhu et al. 2020) is the current area of interest at the time of writing this paper; however, there is also a growing interest in chemical EOR (Deshpande et al. 1999; Bui et al. 2018; Sheng et al. 2018; Chen et al. 2021).

Although our understanding of EOR processes in organic or kerogen pore systems has grown rapidly over the last few years (Dang et al. 2019; Perez et al. 2020a; Mamoudou et al. 2020), there has been little to no focus on solvent-oil interactions in inorganic pore systems, specifically in clays that form a large percentage of the shale matrix and that may host pores that deliver fluids from the organics to the fractures.

2.2 Construction of the Illite-fluid Systems

Clay minerals are ubiquitous accounting for more than 50% by volume in most shales (Yang et al. 2016). The most common clay minerals are kaolinite, illite, chlorite, and

smectite (Gualtieri et al. 2008). I focus on illite-hosted pores because illite is the most common diagenetic product in shales (Galán et al. 2013).

Illite comprises Al-centered octahedral (O) layers sandwiched between two Si-centered tetrahedral layers (T) as a 2:1 clay mineral (TOT) (Drits et al. 1993). In this study, I use the composition of $K_x[Si_{(8-x)}Al_x](Al_4)O_{20}(OH)_4$ (x=1) and isomorphic substitutions are made by replacing one Si^{4+} by one Al^{3+} in every replicated unit cell (Zhang et al. 2016b). I follow Loewenstein's rule for ion substitution in clay minerals which states that the locations of two substitution sites are not adjacent to each other (Loewenstein et al. 1954). Interlayer counter cations (potassium cations, K^+) are distributed randomly in the illite interlayer space to counterbalance the electrostatic charges induced by the isomorphic substitutions in the illite layers. The K^+ cations can move in the interlayer space. Material Studio™ is used to build an illite model (Accelrys et al. 2016). The unit cell has the parameters of space group: C2/m, a=5.193 Å, b=8.994 Å, C=10.204 Å, α=90°, β=101.77° and γ=90° (Drits et al. 2006), where the parameters *a*, *b* and *c* are dimensions of the unit cell, and parameters α, β, and γ are the angles of the unit cell. The modeled atomic coordinates of the unit cell for the illite structure are shown in Table 2-1.

Table 2-1 Modeled atomic coordinates of the unit cell for the illite structure (Drits et al. 2009)

Sample Atom	*x*	*y*	*z*
K	0.0000	0.5000	0.5000
Al	0.5000	0.1667	0.0000
Si	0.4191	0.3280	0.2688
O1	0.3487	0.3100	0.1063
O2	0.4984	0.5000	0.3131
O3	0.6715	0.2246	0.3350
OH	0.4191	0.0000	0.1006

The simulation cell contains 20 clay unit cells (10×2×1 supercell) resulting in a clay model of 6.4 nm×2.2 nm×1.0 nm (*x*-, *y*- and *z*-direction) as shown in Figure 2-1a and Figure 2-1b. The slit pore is constructed with four parallel illite layers confined in a three-dimensional simulation cell with the *xz* plane shown in Figure 2-1c. I use a slit pore following Rao et al. (2013), Sun et al. (2015), Underwood et al. (2016), and Hao et al. (2018) and because slit pores are the most prevalent pore shape in clays (Adeyeri et al. 2019).

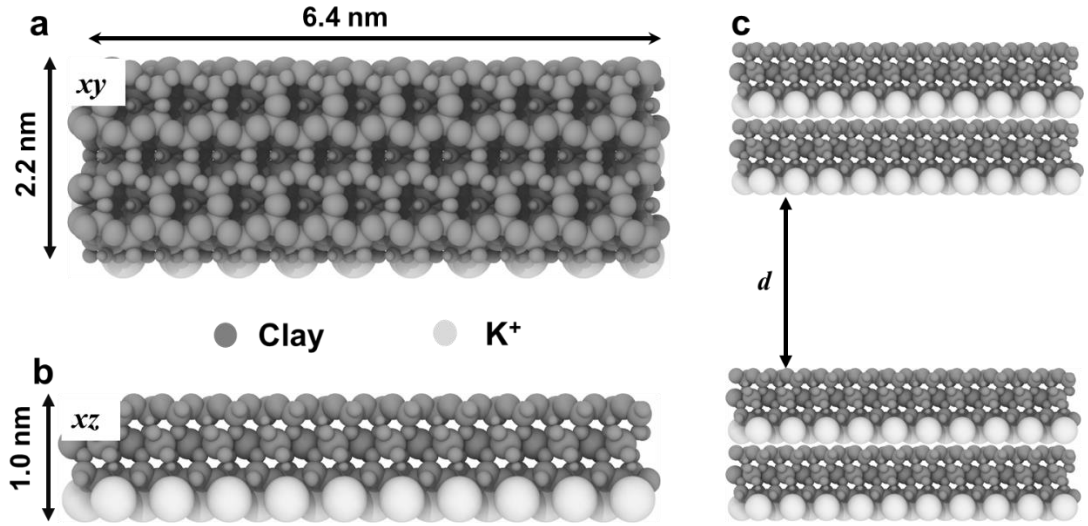

Figure 2-1 Schematic representation of the illite supercell (10×2×1). The dimension is 6.4 nm×2.2 nm×1.0 nm. Panels a and b provide top and side views of the illite supercell. Panel C is the slit pore constructed with four parallel illite supercells. *d* is the pore width. Color codes: clay, grey; potassium ion K^+, light grey.

I consider four different fluid mixtures that are randomly placed in the illite slit pore using the Packmol package (Martínez et al. 2003). Models 1-4 focus on illite-confined behavior of pure dodecane, methane/dodecane, ethane/dodecane, and ethane/dodecane/water respectively. Model 1 contains 100 dodecane molecules in a slit pore of width 5nm as shown in Figure 2-2a. Model 2 contains 100 dodecane and 400 methane molecules (20% C_{12} +80% C_1) in a slit pore of width 6nm as shown in Figure 2-2b. Model 3 contains 100 dodecane and 400 ethane molecules (20% C_{12} +80% C_2) in a slit pore of width 6nm as shown in Figure 2-2c. Model 4 contains 100 dodecanes, 400 ethane, and 160 water molecules (20% C_{12} +80% C_2+water) in a slit pore of width 9 nm as shown in Figure 2-2d.

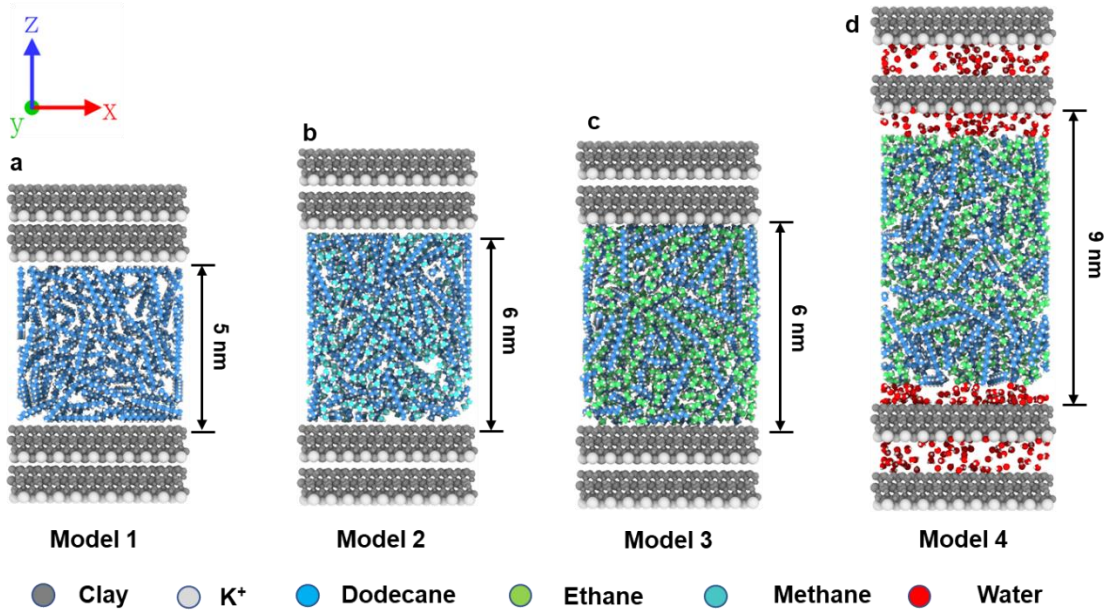

Figure 2-2 Snapshots showing the initial configuration of the four illite models containing fluids. Model 1 contains 100 dodecane molecules; Model 2 contains 100 dodecane and 400 methane molecules (20% C_{12} +80% C_1); Model 3 contains 100 dodecane and 400 ethane molecules (20% C_{12} +80% C_2); and Model 4 contains 100 dodecane, 400 ethane and 160 water molecules (20% C_{12} +80% C_2+water). The clay structure contains the same color codes as in Figure 2-1, while the color codes of fluid molecules are: ethane, light green; dodecane, light blue; CH_4, cyan; and H_2O, red. Every simulation cell size is chosen to be sufficient to eliminate any finite-size effects.

I also construct four other simulation cells to study solvent-oil mixture behavior in the bulk condition as shown in Figure 2-3. Model 5 contains 100 dodecane molecules as shown in Figure 2-3a; Model 6 contains 100 dodecane and 400 methane molecules (20% C_{12} +80% C_1) as shown in Figure 2-3b; Model 7 contains 100 dodecane and 400 ethane molecules (20% C_{12} +80% C_2) as shown in Figure 2-3c; and Model 8 contains 100 dodecanes, 400 ethane and 160 water molecules (20% C_{12} +80% C_2+water) as shown in Figure 2-3d. I add a 1 Å wide area in all three directions to eliminate boundary effects (Collell et al. 2015; Liu et al. 2017). All models can freely expand along the *z*-axis. Table 2-2 describes my models.

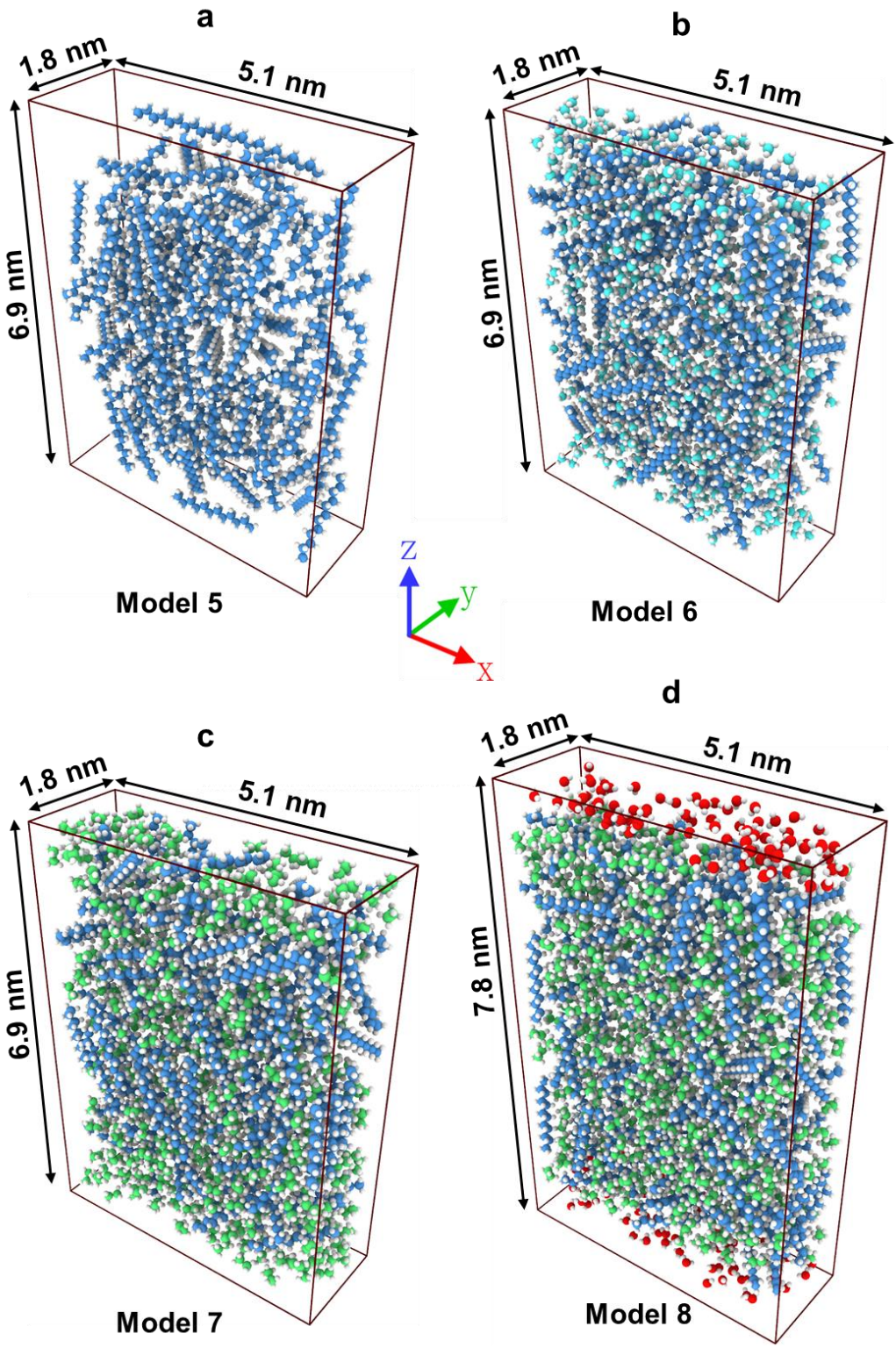

Figure 2-3 Snapshots showing the initial fluid configuration in the four bulk fluid models. The fluids have the same color codes as in Figure 2-2. Model 5 contains 100 dodecane molecules; Model 5 contains 100 dodecane and 400 methane molecules (20% C_{12} +80% C_1); Model 7 contains 100 dodecane and 400 ethane molecules (20% C_{12} +80% C_2); and Model 8 contains 100 dodecane, 400 ethane and 160 water molecules (20% C_{12} +80% C_2+water).

Table 2-2 Description of the models used in this paper

Model types	Fluid components	Illite confinement
1	100 dodecane molecules	Yes
2	100 dodecane and 400 methane molecules	Yes
3	100 dodecane and 400 ethane molecules	Yes
4	100 dodecane, 400 ethane and 160 water molecules	Yes
5	100 dodecane molecules	No
6	100 dodecane and 400 methane molecules	No
7	100 dodecane and 400 ethane molecules	No
8	100 dodecane, 400 ethane and 160 water molecules	No

2.3 Molecular Dynamics Simulation Details

All MD simulations were performed using a Large-scale Atomic/Molecular Massively Parallel Simulator (LAMMPS) (Version 11 Aug 2017) (Plimpton et al. 1995). The interatomic interactions for the T-O-T clay structure and the cations are described using the ClayFF force field (Cygan et al. 2004), which is widely used in clay interfacial simulations (Underwood et al. 2016; Zen et al. 2016). Water molecules are described using a flexible SPC model and the shake algorithm is used to make two O-H bonds and the H-O-H angle rigid (Berendsen et al. 1981). According to the ClayFF the total interaction energy *E* of the material is given by Equation (2-1):

$$\mathrm{E} = \sum_{bonds} k_1\left(r_{ij} - r_0\right)^2 + \sum_{angle} k_2\left(\theta_{ijk} - \theta_0\right)^2 + \sum_{ij} \epsilon_{ij}\left[\left(\frac{\sigma_{ij}}{r_{ij}}\right)^{12} - 2\left(\frac{\sigma_{ij}}{r_{ij}}\right)^{6}\right] + \frac{e^2}{4\pi\varepsilon_0}\sum_{i,j}\frac{q_i q_j}{r_{ij}} \quad (2\text{-}1)$$

Where, k_1 and k_2 are force constants; θ_{ijk} is the angle between bond *ij* and *jk*; *e* is the electron charge; q_i is the partial charge of atom *i*; ε_0 is the dielectric permittivity

of vacuum ($8.85419 \times 10^{-12}\mathrm{F/m}$); r_0 and θ_0 are the equilibrium values of the corresponding quantities; and ϵ_i and σ_i are the usual Lennard-Jones (LJ) energy and size parameters. The Lorentz-Berthelot mixing rules are used to calculate the interaction parameters between the unlike atoms *ij* (Cygan et al. 2004) as shown below in Equation(2-2) and Equation(2-3) :

$$\sigma_{ij} = \frac{1}{2}(\sigma_i + \sigma_j) \tag{2-2}$$

$$\epsilon_{ij} = \sqrt{\epsilon_i \epsilon_j} \tag{2-3}$$

Organic compounds such as methane, ethane, and dodecane are represented using the OPLS All-Atom force field (Jorgensen et al. 1996). It is worth noting that the mixing rules of ClayFF force field and OPLS All-Atom are different. The OPLS All-Atom force field uses a geometric mixing rule to obtain the Lennard-Jones interaction parameters between unlike atoms, while the Lorentz-Berthelot mixing rule is used for the ClayFF force field. For the interaction parameters between clay and organic materials, the use of the Lorentz-Berthelot mixing rule has been documented in Sun et al. (2018), Zhao et al. (2018), and Li et al. (2019). for methane adsorption in clay minerals and is also applied in my study. Meanwhile, Ye et al. (2013) state that although the scaling factor of 0.5 (default) for the 1-4 intramolecular interactions in OPLS-AA is appropriate for linear alkane chains with less than 10 carbon atoms, it yields quasi-crystalline structures when the alkane chain has 12 or more carbon atoms. I, therefore, use a scaling factor of 0.3 for the 1-4 intramolecular interactions in all dodecane molecules.

Periodic boundary conditions (PBCs) are used in all 3 directions and the short-

range interactions are represented by a Lennard-Jones (LJ) 12-6 term (Lennard-Jones et al. 1924). The cutoff distance for the short-range nonbonded van der Waals interactions is 8 Å following the rule that cutoff distance cannot be larger than half of the minimum box size. The long-range electrostatic interactions are calculated by the Fourier-based Ewald summation method (Toukmaji et al. 1996) - the particle-particle/particle-mesh (PPPM) method with a precision value of 10^{-6} (Eastwood et al. 1984). The simulations were initially carried out at 350K using an isobaric-isothermal (NPT) ensemble. The pressure was fixed at 300 atm with volume fluctuation only in the z-direction. I also later assess the impact of temperature by varying it from 300K to 400K, 450K, and 500K. The motivation for varying the temperature is to assess the impact of high-temperature solvents to increase shale oil recovery. A time step of 0.01 fs was used for 100ps, after which it was increased to 1 fs for 10 ns when the simulations reached equilibrium. The pressure was controlled by the Parrinello-Rahman barostat (Parrinello et al. 1981) while the temperature was controlled by the Nose Hoover thermostat (Nosé et al. 1984). With equilibrium in the NPT ensemble, I switch to the microcanonical (NVE) ensemble and continue the simulation for another 10 ns. The equilibrium results of Model 5 at different temperatures are shown in Figure 2-4, demonstrating my simulation time is enough to reach the equilibrium. All snapshots of simulation trajectories are created using OVITO 3.0.0 (Stukowski et al. 2010) and VMD 1.9.3 is used to produce the LAMMPS input file (Humphrey et al. 1996).

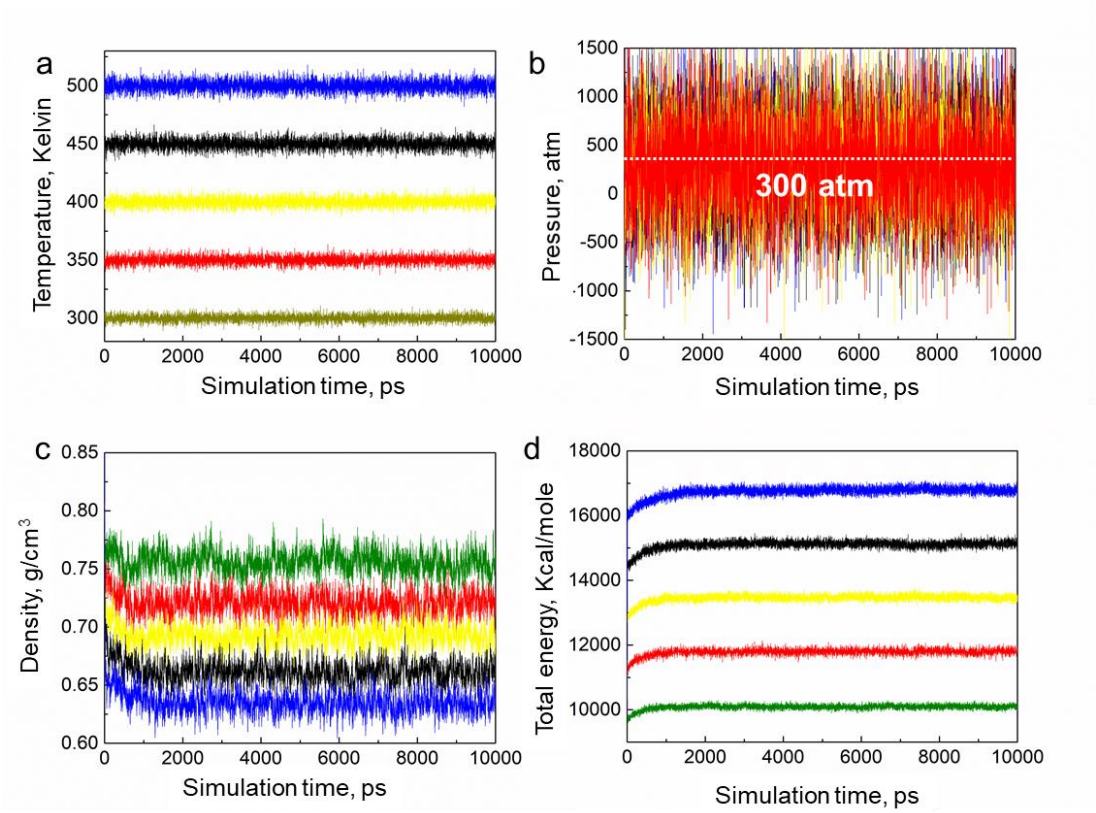

Figure 2-4 Simulation results of pure dodecane without confinement (Model 5) in equilibrium stage at various temperatures. The green, red, yellow, black, and blue colors represent the temperature at 300K, 350K, 400K, 450K, and 500K, respectively. The densities after equilibrium stage are 0.75572 g/ml, 0.72044 g/ml, 0.69252 g/ml, 0.66114 g/ml, and 0.63404 g/ml, corresponding to temperature of 300K, 350K, 400K, 450K, and 500K, respectively.

2.4 Results and Discussion

2.4.1 Swelling

When solvents are injected into oil-bearing reservoirs above miscible conditions, one of the mechanisms promoting oil recovery is oil volume swelling (Li et al. 2013; Zheng et al. 2016). In my study, Models 1-4 quantify oil swelling under illite confinement, and Models 5-8 focus on oil swelling in the bulk. The equilibrium results at T=350 K and P=300 atm are shown in Figure 2-5 and Figure 2-6.

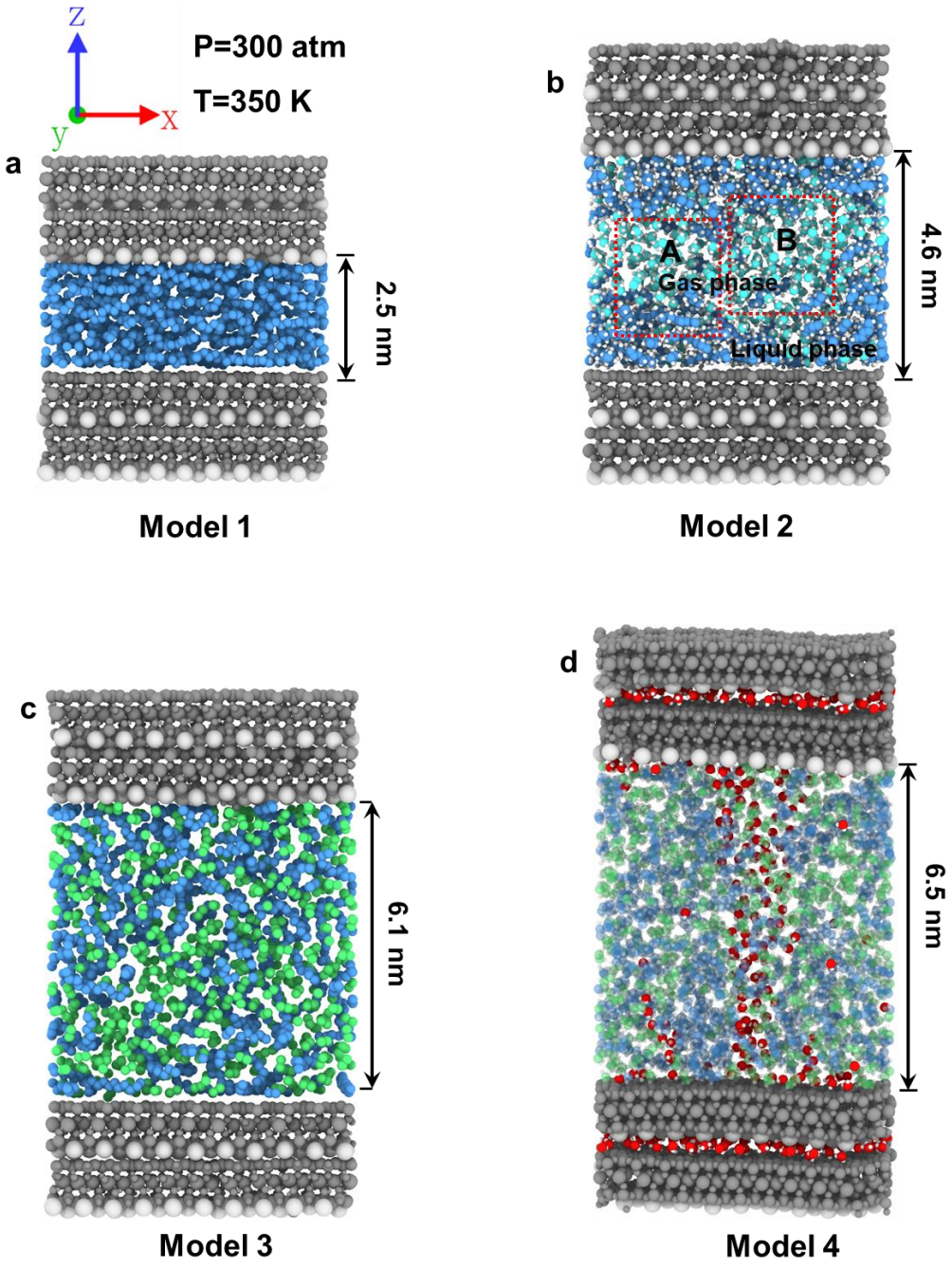

Figure 2-5 Snapshots showing the four models of illite containing fluids after equilibrium at 350K and 300 atm. The figures have the same color codes as in Figure 2-2. Model 1 is set as a reference condition under illite confinement. Models 2, 3, and 4 show oil swelling when I inject solvents (C_1/C_2/C_2+water) into Model 1. Regions A and B in Model 2 show that some methane remains insoluble in the dodecane at the experimental pressure and temperature. Model 4 shows that water molecules adsorb on the illite surface while the unabsorbed water forms a water bridge between the top and bottom of the pore (dodecane and ethane are treated by a transparent process). It should be noted that the illite is not fixed in these simulations, and the unbalanced distribution of water between the clay layers (Model 4) causes some warping of the clay plates in Model 4. I will discuss this phenomenon in detail in Chapter 3.

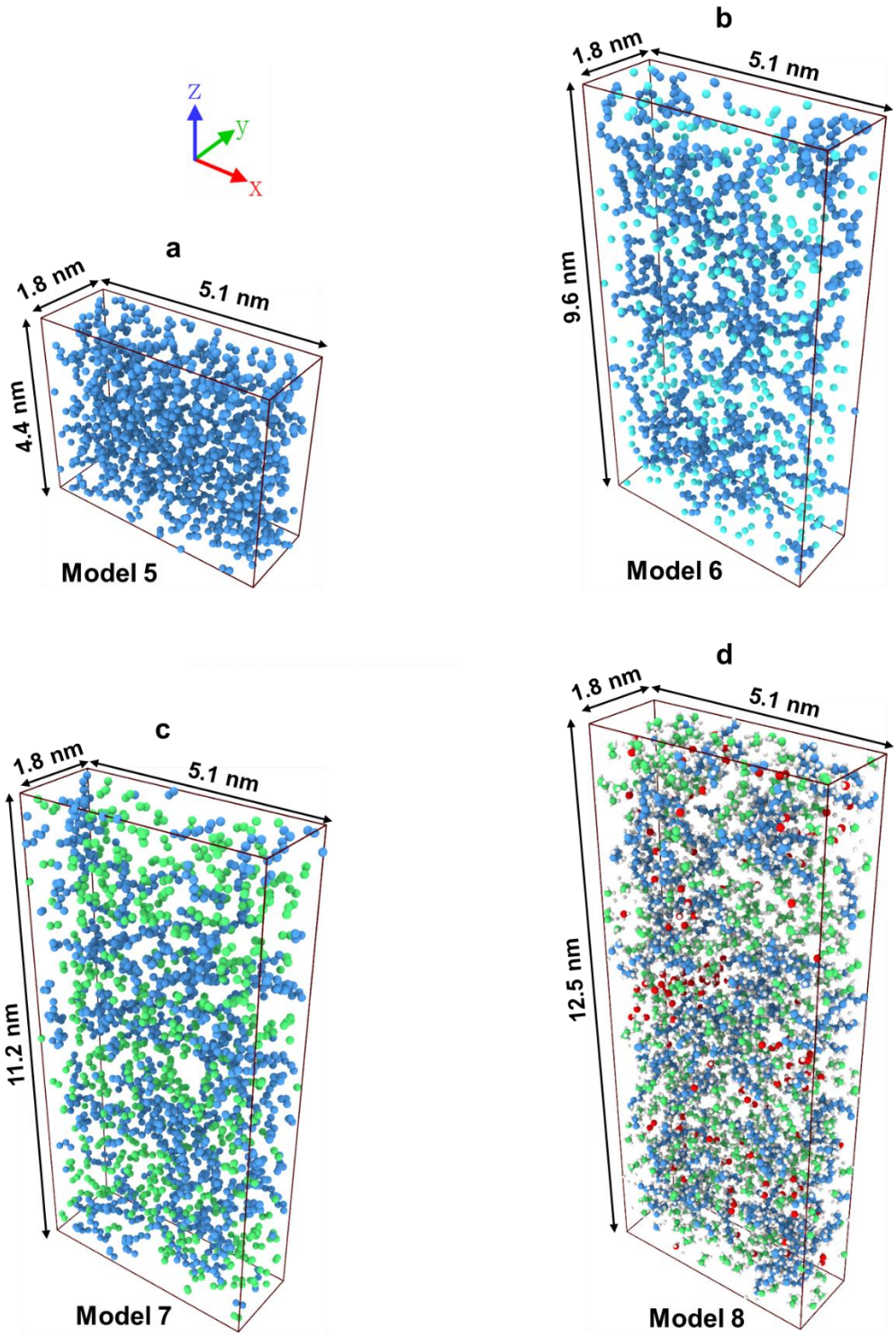

Figure 2-6 Snapshots showing the four models of fluids in bulk condition after equilibrium at 350K and 300 atm. The four simulation cells have the same color codes as in Figure 2-3. The hydrogen H is not shown in these snapshots. Model 5 is set as a reference condition for bulk fluids. Models 6, 7, and 8 show oil swelling after injection of solvent with the swelling more pronounced compared to Models 2, 3, and 4 at the same P and T and solvent and oil composition. There is no distinct gas phase indicating complete miscibility of methane with the oil in the bulk.

After equilibrium, the slit pore width of Model 1 is 2.5 nm as shown in Figure 2-5a. Model 1 is set as the reference condition for illite confinement at T=350K and P=300 atm. When solvent (methane/ethane/ethane+water) is introduced into Model 1, the slit pore widths of Models 2, 3, and 4 increase to 4.6 nm, 6.1 nm, and 6.5 nm resulting in 1.84 times, 2.42 times, and 2.61 times the slit pore width of Model 1 as shown in Figure 2-5b to Figure 2-5d. It should be noted that illite is not fixed in these simulations, and the unbalanced distribution of water between clay layers (in Model 4) causes some warping of the clay plates.

Model 5 is set as the reference condition for bulk fluid behavior at T=350K and P=300 atm. After equilibrium, the height of Model 5 is 4.4 nm as shown in Figure 2-6a. Adding solvent to Model 1 results in the simulation cells of Models 6, 7, and 8 having heights of 9.6 nm, 11.2 nm, and 12.5 nm respectively resulting in 2.15 times, 2.52 times, and 2.80 times the height of Model 5 as shown in Figure 2-6b to Figure 2-6d.

At the same pressure and temperature, the volume of dodecane in the bulk (Model 5) is 1.54 times the volume of confined dodecane in Model 1. Confinement appears to negatively impact oil swelling with the swelling in bulk being about 1.78, 1.59, and 1.64 times the swelling under confinement when comparing Models 2 and 6, Models 3 and 7, and Models 4 and 8, respectively.

Additionally, Figure 2-5b shows that methane appears partly immiscible with dodecane at the pressure and temperature of the experiment and forms a distinct gas phase while in Figure 2-6b (methane and dodecane in the bulk), the methane is almost

completely miscible in the oil phase at the conditions just below the saturation pressure (The phase envelope of the mixture in Figure 2-6b is provided in Figure 2-7a). This result indicates that methane molecules have a higher solubility in the bulk condition than under illite confinement. I also show the immiscibility of methane at other values of pressure and temperature as seen in Figure 2-7c to Figure 2-7d. Figure 2-6d also presents an interesting phenomenon where water molecules coalesce to form a water bridge, not water droplets. I will discuss this phenomenon in detail in Chapter 3.

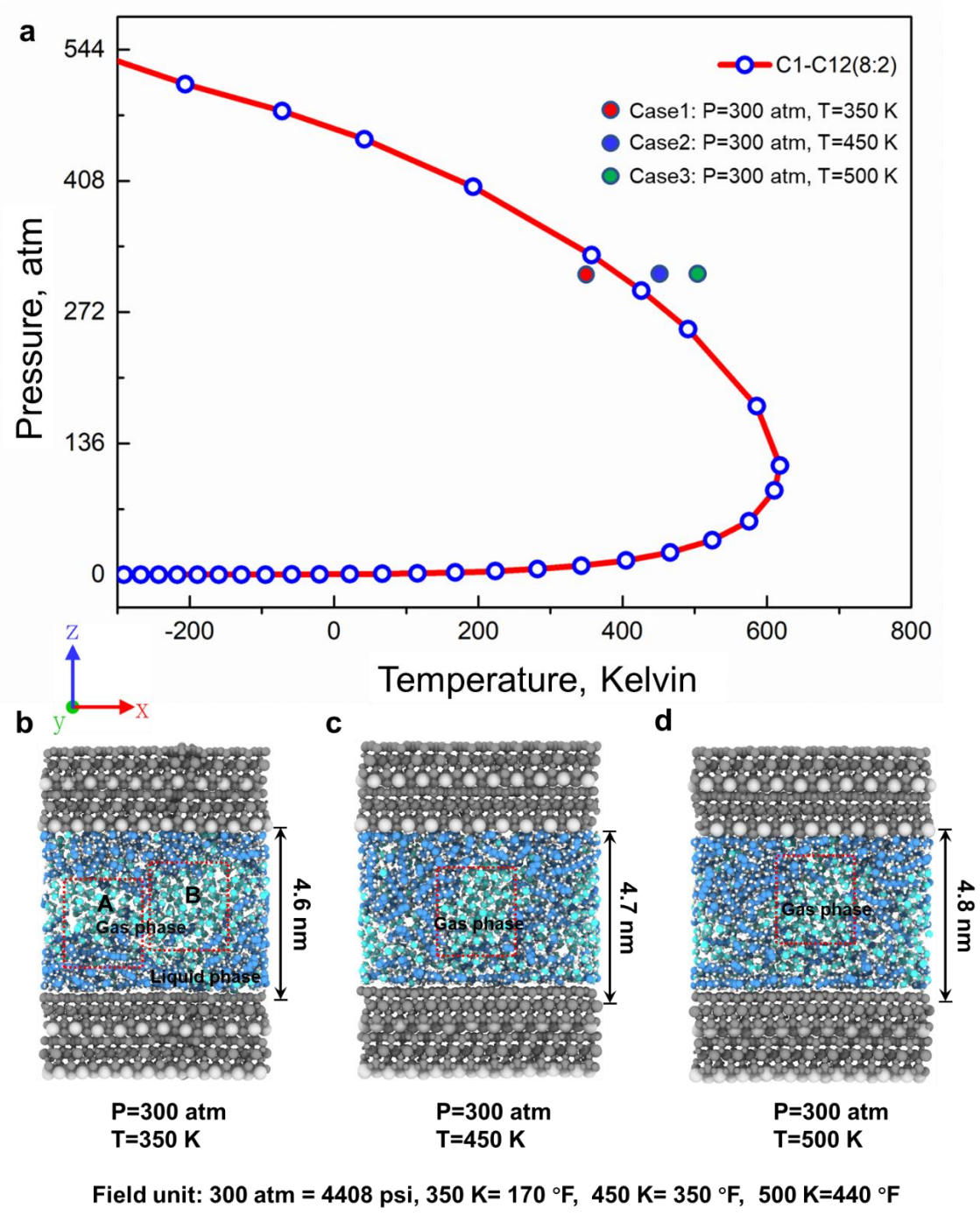

Figure 2-7 Phase envelope and molecular simulations for methane/dodecane at 350 K, 450 K, and 500 K respectively. At 350k, the mixture is just within the 2-phase region, while at 400k and 500K, the mixture is a single-phase liquid in bulk. However, looking at the figures above, methane remains only partly miscible with dodecane indicating that methane molecules have a higher solubility in the bulk than under illite confinement.

2.4.2 Viscosity

There are at least five different atomistic simulation methods developed for computing the shear viscosity of liquids such as moving a wall to shear the fluid between two walls (Denis et al. 1984), using fixed viscosity and the Muller-Plathe method (Plathe et al. 1997) or using the Green-Kubo method (Green et al. 1954), etc. Due to its simplicity, the Green−Kubo relation based on equilibrium molecular dynamics (MD) simulations is perhaps the most widely used method (Allen et al. 1988). In the Green−Kubo approach, the shear viscosity is calculated from an integral over time of the pressure tensor autocorrelation function as shown in Equation (2-4):

$$\eta = \frac{V}{k_B T}\int_0^{\infty} \langle P_{\alpha\beta}(t) \cdot P_{\alpha\beta}(0)\rangle dt \qquad (2\text{-}4)$$

where V is the system volume, k_B is the Boltzmann constant, T is the temperature, $P_{\alpha\beta}$ denotes the element $\alpha\beta$ of the pressure tensor ($\alpha\beta = xy, xz, yx, yz, zx, \text{ or } zy$), and the bracket indicates the ensemble average. Theoretically, the pressure tensor autocorrelation function decays to zero in the long-time limit and the integral in Equation (2-4) reaches a constant value, which corresponds to the calculated shear viscosity. In practice, however, it is very time-consuming to run the simulations long enough to obtain accurate viscosities. An alternative strategy is to run multiple independent simulations and taking the average of the running time integrals (Mouas et al. 2012; Mondal et al. 2014). This method is computationally tractable, less time-intensive, and provides reliable results (Zhang et al. 2015).

To calculate the viscosity at different temperatures (300K, 350K, 400K, 450K, and

500K), I ran 200 simulations from 5 independent trajectories starting at the same configuration but a different initial velocity assignment, which is obtained from a random seed. Each trajectory is 20 ns long with the first 10 ns (equilibrium time) ignored in the viscosity calculation. Meanwhile, the elements of pressure tensor ($\alpha\beta = xy, xz, yz$) are calculated at different temperatures. The average viscosities and equilibrium densities of Model 5 at different temperatures are shown in Figure 2-8. Alphabets a, b, c, d, and e in Figure 2-8 correspond to the temperatures at 300K, 350K, 400K, 450K, 500K respectively. Red, green, and blue curves correspond to the average pressure tensors at *xy*, *xz*, and *yz* directions separately. Figure 2-8a-e indicates that after 4 ns, the curves become smooth, and the fluctuations are small. Therefore, I can conclude that 10 ns production time is long enough to reach the long-time limit since the integral converges to a constant value. Then I average the viscosity over three directions $\left(\mu = \frac{\mu_{xy}+\mu_{xz}+\mu_{yz}}{3}\right)$ to calculate the fluid viscosity. NIST data for dodecane is used to verify the accuracy of the MD simulations. Meanwhile, the final calculated viscosities and NIST data are shown in Figure 2-9a.

Figure 2-8f presents the equilibrium densities of Model 5 for 10 ns at different temperatures. In Figure 2-8f, the green, red, yellow, black, and blue curves represent the densities at 300K, 350K, 400K, 450K, and 500K respectively. The densities obtained after equilibrium are 0.75572 g/ml, 0.72044 g/ml, 0.69252 g/ml, 0.66114 g/ml, and 0.63404 g/ml corresponding to the temperature of 300K, 350K, 400K, 450K, and 500K respectively. The densities at different temperatures are compared between Model

5 and NIST data, as shown in Figure 2-9b. Figure 2-9 demonstrates that the calculated results have an excellent agreement with NIST data.

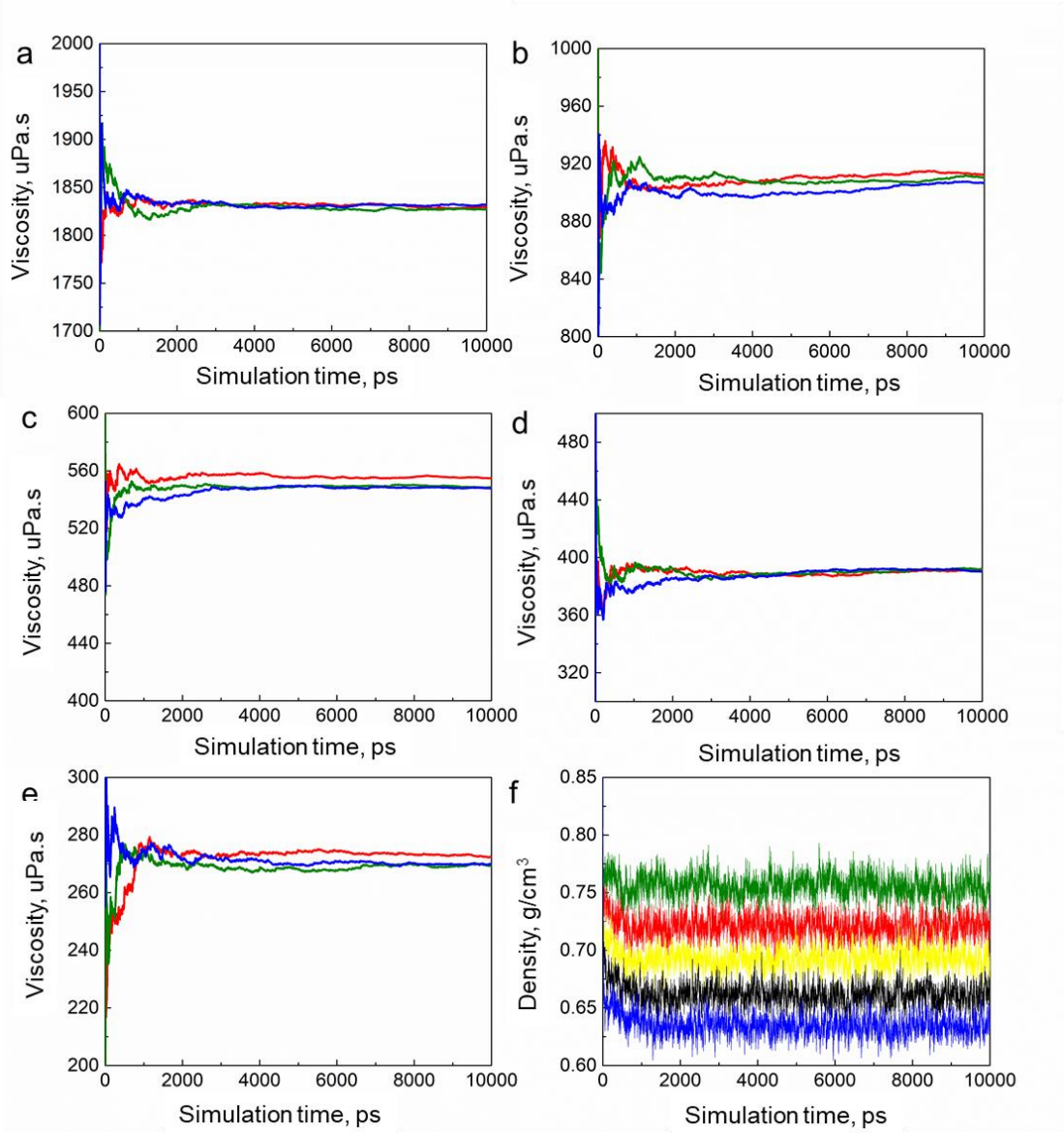

Figure 2-8 Calculated averaged running integral (Equation (2-4)) from 5 independent 10 ns long equilibrium MD trajectories and equilibrium densities for Model 5 at different temperatures. Panels a, b, c, d, and e correspond to the temperature at 300K, 350K, 400K, 450K, 500K, respectively. Red, green, and blue curves correspond to the average pressure tensor at *xy*, *xz*, and *yz* directions separately. In panel f, the green, red, yellow, black, and blue colors represent the temperature at 300K, 350K, 400K, 450K, and 500K, respectively. The densities after equilibrium stage are 0.75572 g/ml, 0.72044 g/ml, 0.69252 g/ml, 0.66114 g/ml, and 0.63404 g/ml, corresponding to temperature 300K, 350K, 400K, 450K, and 500K, respectively.

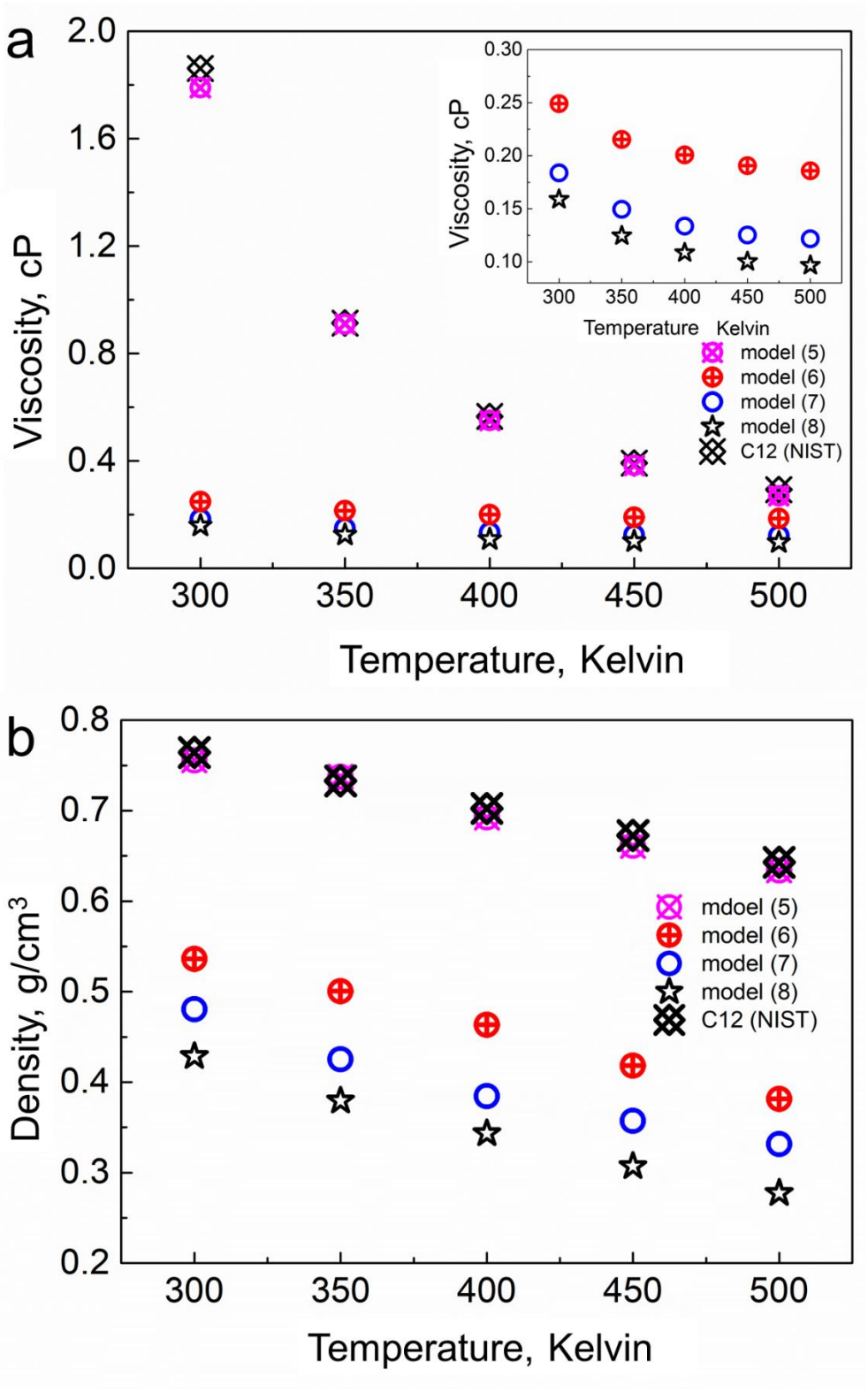

Figure 2-9 Calculated densities and viscosities as a function of temperature. The results show that the calculated densities (Model 5) agree with NIST densities very well. In Model 8, the calculated viscosities are lower than Model 7, since mixtures of water and hydrocarbons exhibit complex multiphase behavior at elevated temperatures and the water dissolution makes the liquid phase (hydrocarbons) viscosity lower in the simulation

I also calculate the viscosities for Models 6-8 (fluid in the bulk) and the results are shown in Figure 2-9 with the expected decrease in density and viscosity with temperature increases. The density and viscosity of the mixtures also decrease with solvent injection. Model 8 (with water in an ethane/dodecane mixture) has a lower viscosity than Model 7 without water. In some cases, water can act as a solvent to further lower the viscosity and lowering liquid viscosity (Huang et al. 2016; Yang et al. 2017; Xiong et al. 2019) which appears to be the case here.

Figure 2-10 shows the calculated viscosities of Models 1-4 (confined mixtures) as a function of temperature. The viscosities of the confined fluids in Models 1-4 are much higher than those of Models 5-8 as shown in Figure 2-10 and Figure 2-9a. The confined fluid viscosities are in fact up to 2 orders of magnitude higher compared to the fluids in bulk demonstrating the strong impact of illite confinement on fluid properties. A few previous papers also allude to similar results (Klein et al. 1998; Cui et al. 2001) indicating that a strong surface-fluid interaction causes increases in fluid viscosity through a phase transition region from liquid-like to solid-like behavior.

Additionally, water dissolution leads to slight decreases in viscosity in Model 8 (compared to Model 7) while in Model 4, the viscosity increases in comparison to Model 3 with no water. The unabsorbed water molecules form a bridge that is likely to increase the viscosity of the mixture.

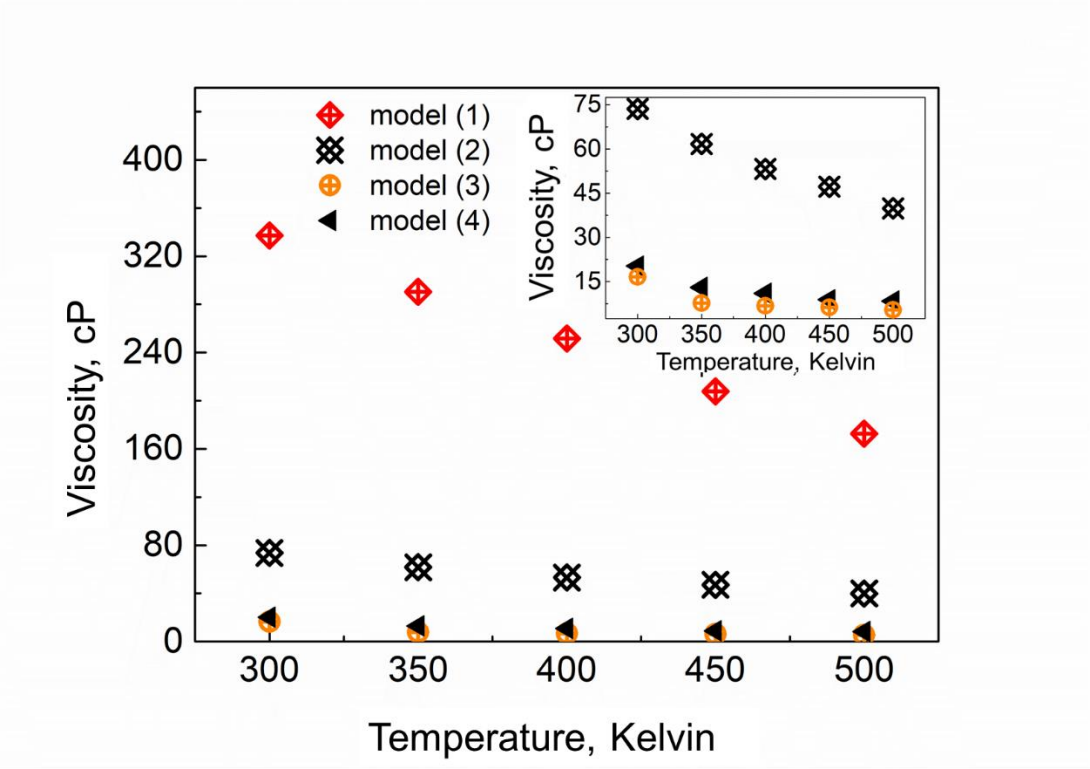

Figure 2-10 Calculated viscosities in Models 1-4 as a function of temperature. The results indicate that viscosities are decreased as solvents are injected. Ethane has a better performance than methane due to its solubility and stronger oil swelling. However, the viscosities in Model 4 increase a bit compared to Model 3. The reason is that water molecules are likely to adsorb on the illite surface, which decreases the effective volume change for hydrocarbons. Another reason is that water molecules show less solubility than those in bulk density.

2.4.3 Self-diffusion

There are two common ways to obtain the self-diffusion coefficient (Keffer et al. 2004). The Einstein method relates the mean square displacement (MSD) to the observation time (Frenkel et al. 2002). The second method uses the velocity auto-correlation function in a Green-Kubo relation (Allen et al. 1988). Theoretically, both methods should yield the same results. However, Keffer et al. (2001) concluded that there was a 'long-time' tail in the Green-Kubo relation that might result in numerical problems

necessitating long simulation times for reliable self-diffusivity from velocities rather than from the positions. Therefore, in this study, I will obtain self-diffusion coefficients from position data. The MSD is defined as Equation (2-5):

$$MSD = \langle (x - x_0)^2 \rangle = \frac{1}{N} \sum_{n=1}^{N} \left(x_n(t) - x_n(0) \right)^2 \quad (2\text{-}5)$$

Where N is the number of particles to be averaged, $x_n(t) = x_0$ is the reference position of each particle, and $x_n(t)$ is the position of each particle in determined *t*. The self-diffusion coefficient is related to the mean square displacement of a particle as a function of observation time (Keffer et al. 2004) allowing us to get the self-diffusion coefficient from the mean square displacement. The self-diffusion coefficient is defined as Equation (2-6):

$$D = \frac{1}{2d} \lim_{t \to \infty} \frac{\langle (x - x_0)^2 \rangle}{t} \quad (2\text{-}6)$$

where D is the self-diffusion coefficient, and *d* is the dimensionality of the system. It should be noted that when we use MD simulation to calculate the self-diffusion, it is necessary to know whether the mean square displacement behavior is satisfactorily close to the long-time limit. Keffer (2001) provides us a method to solve this problem by plotting the mean square displacement *vs* elapsed time as shown in Figure 2-11a on a cartesian scale and a log-log scale as shown in Figure 2-11b. There are usually three regimes as shown in Figure 2-11b. Regime I is 'collision-free motion', which occurs at very short observation times. Regime II is the 'intermediate time regime'. Regime III is the long-time behavior where the mean square displacement is proportional to the observation time. We only use region III to determine the self-diffusion coefficient. If

there is no region three, the simulation time is not long enough to approximate long-time behavior.

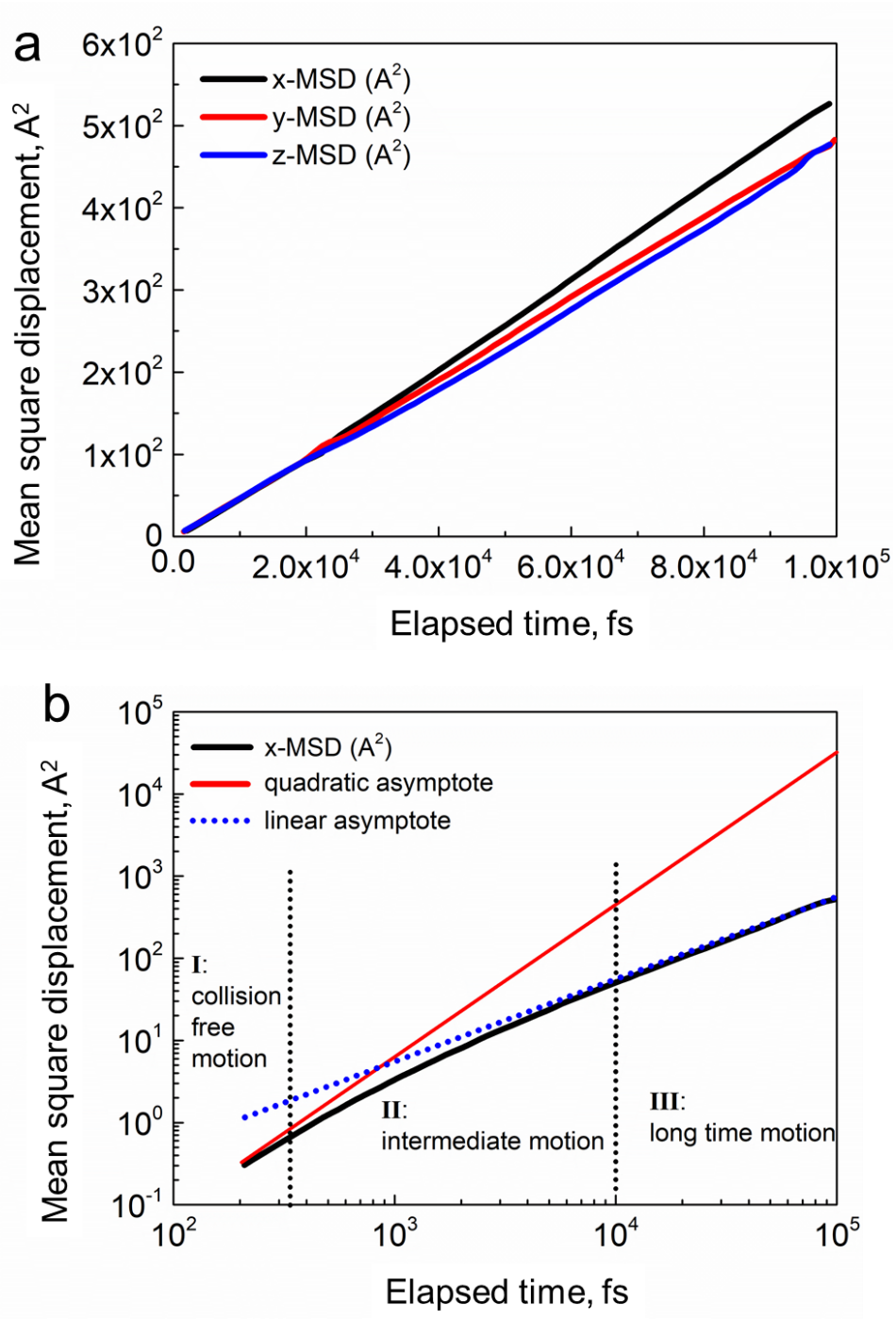

Figure 2-11 Mean square displacement as a function of observation time from reference (D. Keffer et al. 2001). Panel b is plotted on a log-log scale, which uses the same data from panel a. Panel b shows three regimes: I) free motion region; II) intermediate time regime, and III) long time behavior regime. We only use regime III to calculate the self-diffusion coefficient.

To make the results more reliable, 4 independent trajectories are generated starting from the same configuration but a different random seed for initial velocity assignment for each model to obtain mean square displacement. The results of Model 3 at temperature 350 K and pressure 300 atm are shown in Figure 2-12. Remembered that Model 3 contains 100 dodecane and 400 ethane molecules. All of them are under illite confinement. In Model 3, the mean square displacements (MSD) of dodecane, solvents (methane/ethane), and their mixtures are calculated as shown in Figure 2-12a. Figure 2-12b indicates that simulation time of 10 ns is long enough to reach the long-time limit since all the MSD plots show a linear relationship with observation time on a log-log scale.

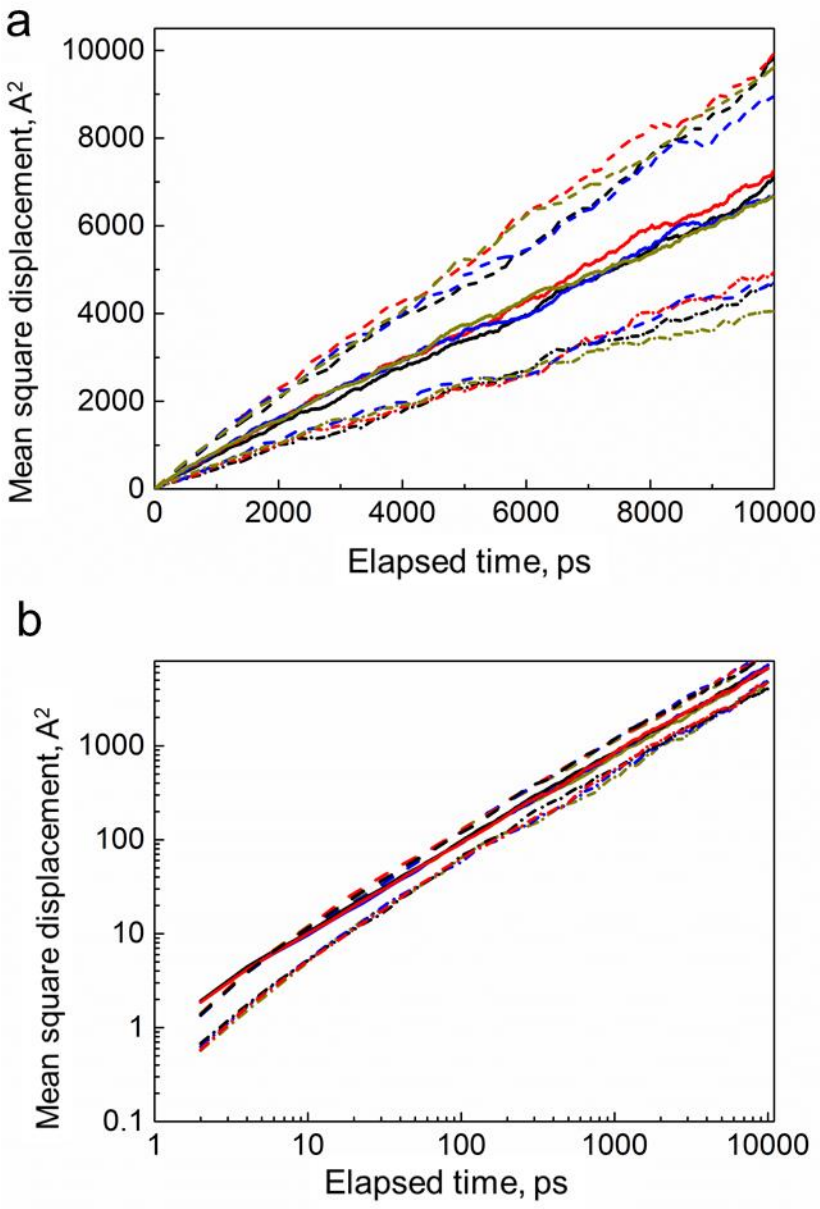

Figure 2-12 Mean square displacement as a function of observation time for Model 3 at temperature 350 K and pressure 300 atm. Panel b is on the log-log scale. The dashed lines are ethane in methane/dodecane mixture; The solid lines are ethane/dodecane mixture; The dashed dot lines are dodecane in ethane/dodecane mixture.

Figure 2-13 shows the calculated self-diffusion of fluids as a function of temperature. Figure 2-13a indicates that injected solvents can enhance the self-diffusion of dodecane by comparing Model 1 to Models 2-4. Figure 2-13a-b also demonstrates that the self-diffusion of dodecane and ethane in Model 3 is larger than that in Model 4

and is likely because of the presence of water in Model 4. Figure 2-13c-d shows the calculated self-diffusion from Models 1-8. The results indicate that illite confinement has a strong effect on self-diffusion. The self-diffusions of fluids in the bulk are almost 3 times the self-diffusion coefficient of fluids under illite confinement.

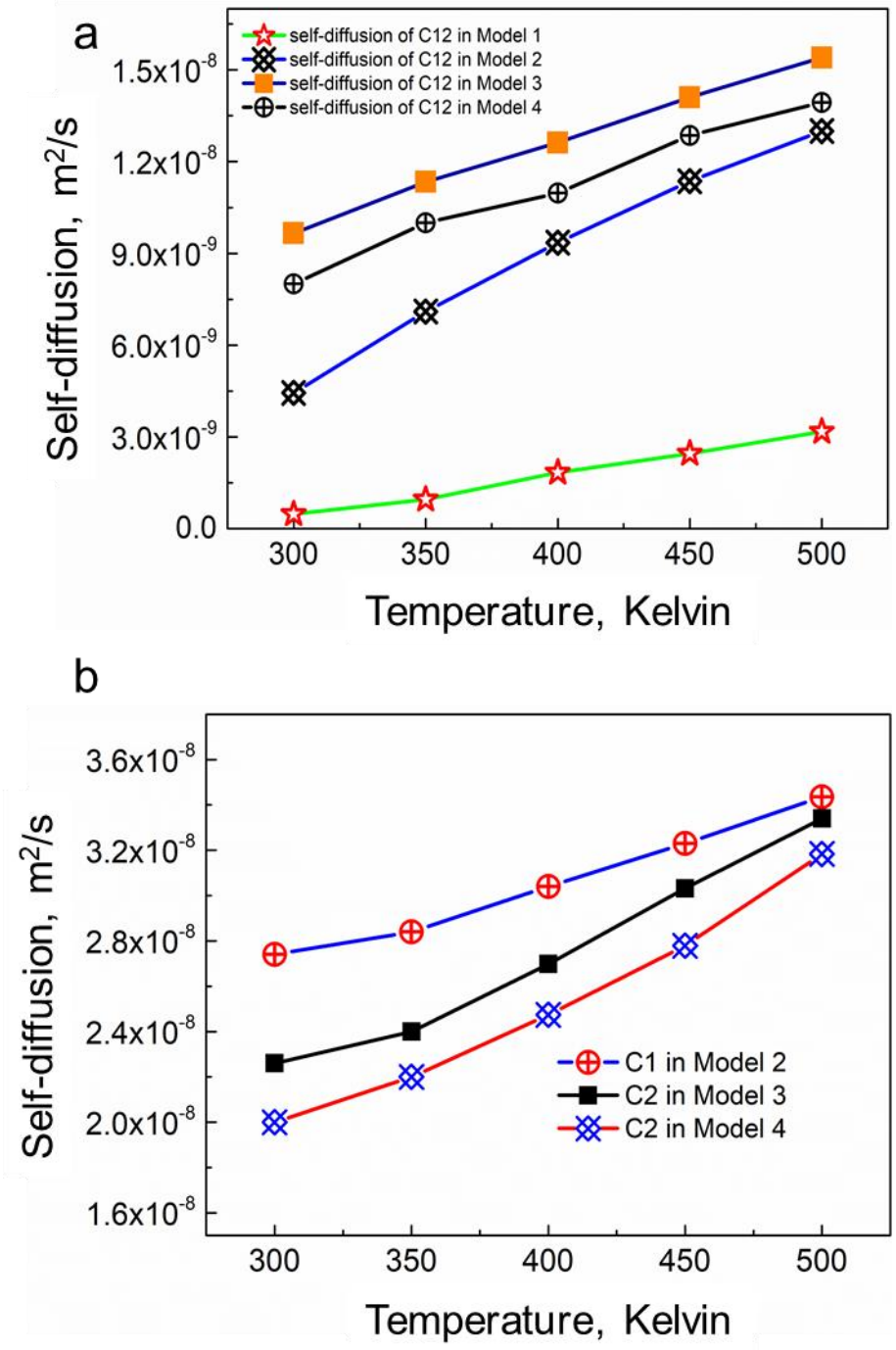

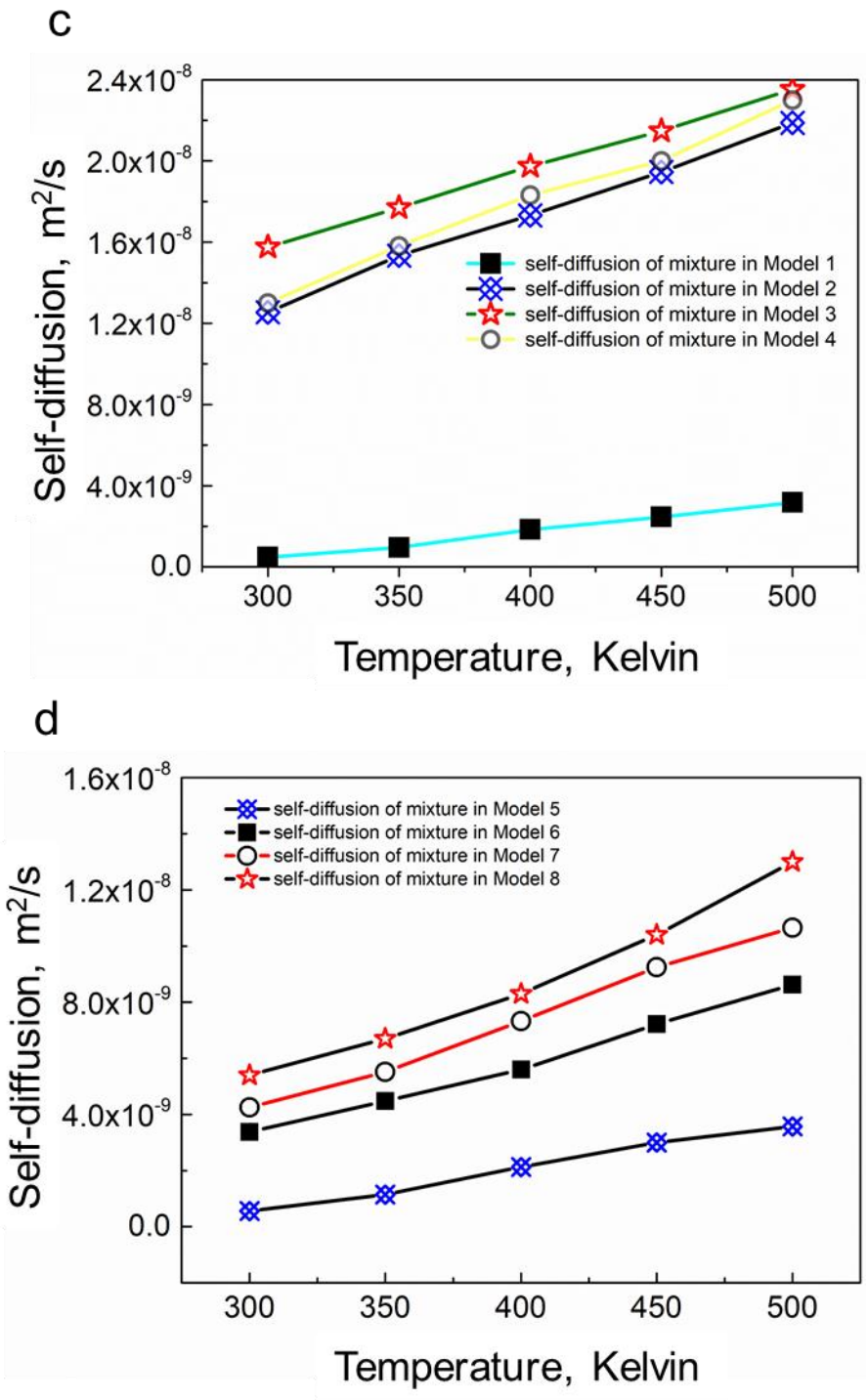

Figure 2-13 Calculated self-diffusion of fluids as a function of temperature. Panel a shows the calculated self-diffusions of dodecane from Models 1-4. Panel b shows the calculated self-diffusions of solvents from Models 2-4. Panel c and d show the calculated self-diffusions of mixtures from Models 1-8. The results indicate that illite confinement has a strong effect on self-diffusion, and injected solvents can enhance the self-diffusion of dodecane. Meanwhile, water molecules adsorbed on the illite surface will decrease the effective flow volume and finally lower the self-diffusion of dodecane.

2.5 Numerical Simulation

3 numerical simulation models are constructed to investigate the effects of confinement in shale oil recovery using the CMG GEM simulator. The model consists of 25×25×5 (I×J×K) blocks. The grid sizes along I and J directions are 50 ft. In the K direction, it is 25, 20, 15, 20, and 30 ft respectively. The schematic is shown in Figure 2-14. The initial oil saturation is 0.76. The aqueous (W) phase initially exists at its irreducible saturation of 0.24. A dual permeability model is used to simulate the matrix and hydraulically fracture. The reservoir temperature and pressure are 350K and 300 atm respectively. Table 2-3 summarizes the rock physical used in the numerical simulations (Sheng, 2017). Table 2-4 summarizes fluid composition and the Peng-Robinson EOS parameters. The primary production time is 30 months. The injection time is 3 months. Shut-in time is 1 month. The time of the 'Puff' process is 13 months. There are 3 cycles in Simulations 1 and 2. The relative permeability curves for CMG simulations are given in Figure 2-15 (Sheng, 2017). It is important to mention that this simulation is a very idealized simulation with a single-component fluid and only considers one pore size. The results shown here are indicative of the impact of confinement on fluid mobility but the numbers should not be used for anything other than instructional purposes.

Table 2-3. Rock physical properties for CMG simulation model

Rock physical property	Value
Reservoir depth	10500 ft
Matrix porosity	0.056
Fracture porosity	0.0056
Matrix permeability	0.0003 mD
Fracture permeability	0.022 mD
Rock compressibility of fracture	1e-5
Rock compressibility of matrix	1e-6
Reference pressure of rock compressibility determination	300 atm
Injected solvent	C_2H_6

Table 2-4. Fluid properties for CMG simulation model

Component	Initial mole fraction	Pc (atm)	Tc (K)	Vc (L/mole)	Acentric Factor	MW (g/mole)
C_2H_6 (injection gas)	0	45.4	190.6	0.099	0.008	16.04
$C_{12}H_{26}$ (reservoir oil)	1	21.6	663.9	0.626	0.5222	161

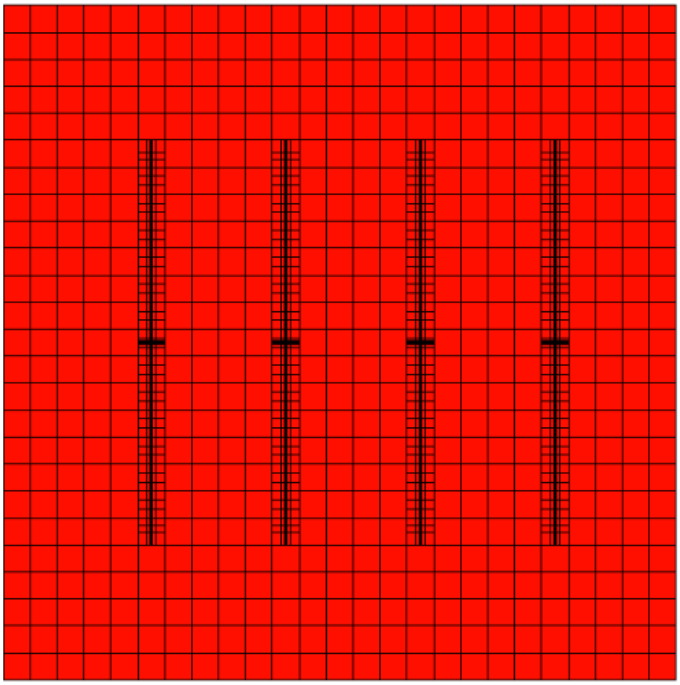

Figure 2-14 Schematic of the base model from the top view.

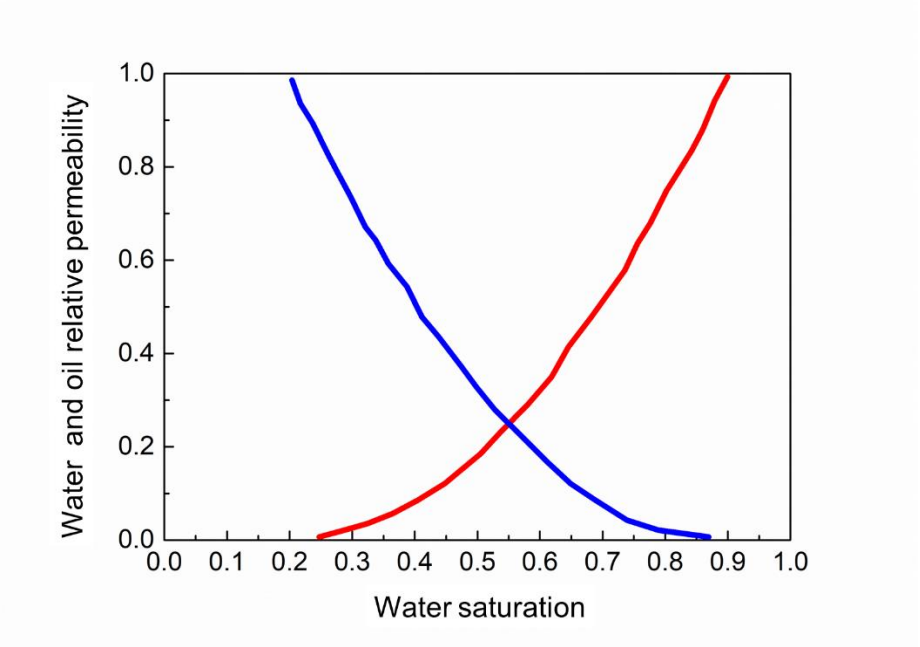

Figure 2-15 Water and oil relative permeabilities (Sheng, 2017).

I assume that the formation is homogenous and comprised of a single pore throat size allowing me to assume that the viscosity of the oil-solvent mixture increases by a factor of 300 and the diffusion coefficient decreases by a factor of 3 under confinement as shown in Figure 2-9a, and Figure 2-10. Simulation 1 shows oil recovery for bulk oil, solvent, and mixture properties while Simulation 2 shows oil recovery under confinement for huff-n-puff enhanced oil recovery. Simulation 3 shows primary oil recovery under confinement. Simulations 1 and 2 have 3 cycles during the huff-n-puff process. A summary of 3 numerical simulations is provided in Table 2-5. Note: The number of 2.4×10^{-8} cm^2/s is obtained from molecular dynamics, as shown in Figure 2-13b. The number of 8×10^{-8} cm^2/s is also calculated from molecular dynamics, as shown in Figure 2-16, where I provide the diffusion coefficients of methane and ethane as a function of temperature in bulk conditions.

Table 2-5 Summary of numerical simulation models

Simulation types	Diffusivity of ethane ($x10^{-8}$ m^2/s)	Huff-n-puff	Confinement
1	8.0	Yes	No
2	2.4	Yes	Yes
3	2.4	No	Yes

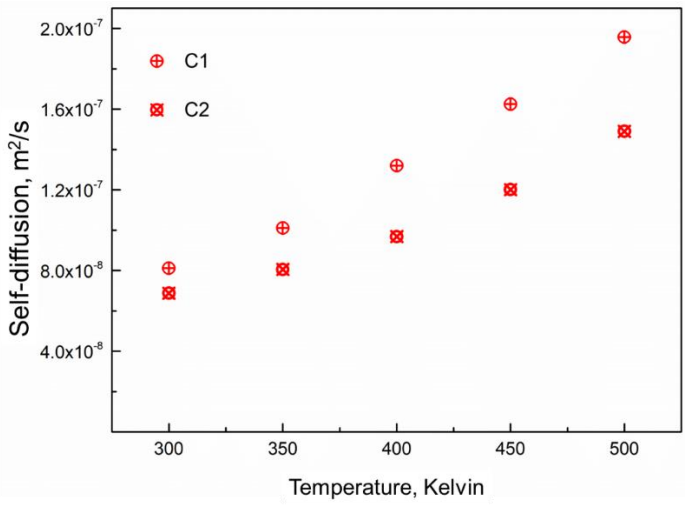

Figure 2-16 Self-diffusion coefficients of methane and ethane as a function of temperature in bulk condition.

The results of oil recovery of 3 numerical simulations are shown in Figure 2-17a with Simulations 1 (green curve), 2 (red curve), and 3 (black curve) having oil recoveries of 27.5%, 12.5%, and 5% respectively. Comparing Simulations 2 and 3, huff-n-puff miscible gas injection is promising for unconventional reservoir enhanced oil recovery even if confinement effects compromise the benefits that would have been possible with fluids in the bulk. In addition to the surface area arguments, the effect of confinement can help explain why field tests perhaps do not show as high of recovery compared to numerical and experimental studies.

The gas-oil ratio is shown in Figure 2-17b. showing that the produced GOR is higher

when confinement effects dominate. This is because of the slower diffusion coefficients as well as the higher oil viscosities which compromise gas solubility and oil production rates.

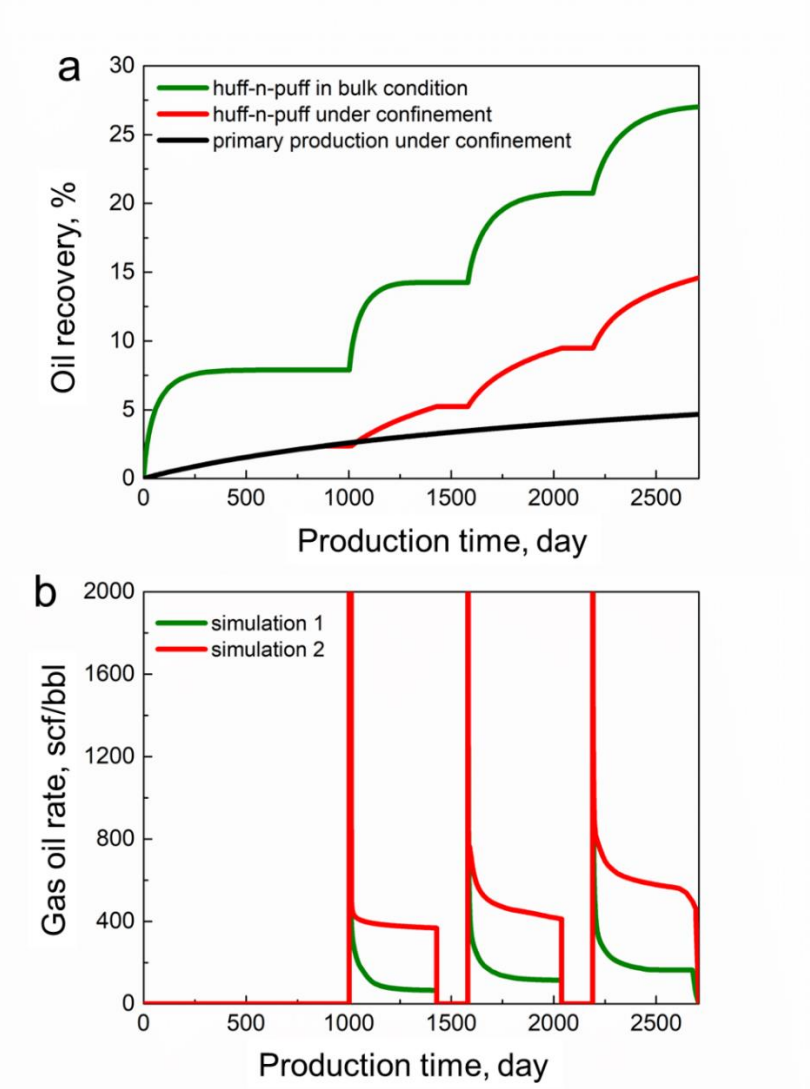

Figure 2-17 Oil recovery and gas oil rate of 3 numerical simulations as a function of production time. The oil recovery factor of simulations 1 (green curve), 2 (red curve) and 3 (black curve) are about 27.5%, 12.5% and 5% respectively. Panel a indicates that huff-n-puff still acts a positive role in unconventional reservoir oil recovery according to Simulations 2 and 3. However, when I consider the confinement effects, the oil recovery decreases from 27.5% to 12.5% according to Simulations 1 and 2. This phenomenon might explain why previous numerical studies have a higher oil recovery than the field tests. Panel b demonstrates that miscibility is difficult to achieve in the unconventional reservoir. During the 'puff' process, a huge amount of undissolved gas comes out suddenly to form a GOR peak. Simulation 1 shows the lowest GOR, while Simulation 2 shows the highest.

2.6 Final Remarks

In this chapter, I have conducted a series of molecular dynamics and numerical simulations to study solvent-oil mixtures in clay minerals, specifically within illite. I demonstrate that oil swelling, viscosity, and self-diffusion coefficients as well as the behavior of water are impacted by illite confinement. The key observations of this study are summarized as follows:

- The illite confinement hinders gas solubility and under the same conditions, methane is seen to be only partly miscible under confinement while being fully miscible with dodecane in the bulk.
- The solvent-oil mixture viscosity under confinement is higher by about two orders of magnitude compared to the fluid in bulk condition compromising liquid production.
- The self-diffusion coefficients of fluids in bulk condition are almost 3 times their value under confinement illustrating that confinement can negatively impact liquid production.

2.7 Nomenclature

k_1 and k_2 = force constants, kcal/mol Å^2

θ_{ijk} = the angle between bond *ij* and *jk* , degree

e = the electron's charge, *e*

q_i = the partial charge of an atom *I, e*

ε_0= the dielectric permittivity of vacuum (8.85419×10^{-12}), F/m

r_0 and θ_0 = the equilibrium values of the corresponding quantities. Å and degree

ϵ_i = the usual Lennard-Jones (LJ) energy parameters, kcal/mol

σ_i = the usual Lennard-Jones (LJ) size parameters, Å

V = the system volume, nm^3

k_B = the Boltzmann constant

T = the temperature, Kelvin

P=the pressure, atm

$P_{\alpha\beta}$ = the element $\alpha\beta$ of the pressure tensor ($\alpha\beta = xy, xz, yx, yz, zx, \ or \ zy$)

N = the number of particles to be averaged

x_0 = the reference position of each particle

$x_n(t)$ = the position of each particle in determined *t*

D = the self-diffusion coefficient, cm^2/s

d = the dimensionality of the system

μ_{xy}=the viscosity from *xy* direction.

μ_{xz}=the viscosity from *xz* direction.

μ_{yz}=the viscosity from *yz* direction.

Chapter 3 Water Bridges in Clay Nanopores: Mechanisms of Formation and Impact on Hydrocarbon Transport

3.1 Introduction

Chapter 2 showed the formation of a water bridge alongside adsorption in clay pores. In this chapter, I take a closer look at the formation mechanisms of this water bridge and its impact on hydrocarbon transport.

3.2 Clay Slit Pore Models

The clay model is created using the illite structure described in Chapter 2 and illustrated in Figure 2-1. Here I discuss different clay surface chemistries to investigate their effect on fluid distribution.

There are generally four illite slit pore structures discussed in literature based on the charged clay surface chemistry: potassium-hydroxyl (P-H) (Hao et al. 2018) which is also presented in Chapter 2, hydroxyl-hydroxyl (H-H) (Jin et al. 2013), potassium-potassium (P-P) (Zhang et al. 2016a), and a structure between the P-H and H-H pore systems (Jin et al. 2014), as shown in Figure 3-1.

In the P-H model, all the potassium ions are adjacent to the upper surface leading to a charge imbalance and these ions can move freely in the interlayer space as shown in Figure 3-1a. In the H-H model, as shown in Figure 3-1b, there are no ions on the clay surface and the charges are balanced. In the P-P model (Figure 3-1c), the upper and lower surfaces have an equal number of potassium ions. In Figure 3-1d, the potassium ions are randomly distributed in the clay nanopores which leads to a clay structure that

lies in between the P-H and H-H structures (Jin et al. 2014) following an equilibrium MD simulation. The unbalanced ionic distribution on the clay surfaces is also consistent with Jin et al.(2013 and 2014) and detailed results are provided in Appendix B.

Clay minerals consist of asymmetrically distorted Si-tetrahedra and Al-octahedra sheets (Richard et al. 2019), which might change ion distribution and consequently, the electrical properties of the clays. For instance, during cation substitutions, an unbalanced surface charge might occur (Tombácz et al. 2006; Kumar et al. 2017; Umeda et al. 2017; Fan et al. 2018; Hao et al. 2019a). Therefore, these four different illite-slit pore structures can also be classified by the ion distribution: unbalanced (Figure 3-1a and Figure 3-1d) and balanced (Figure 3-1b and Figure 3-1c). To simplify my study and following extensive published work in this area (Jin et al. 2013 and 2014; Sun et al. 2015; Zhang et al. 2016b; Lara et al. 2017; Hao et al. 2018 and 2019b; Xiong et al. 2019b;). I choose P-H and H-H structures to represent clay surfaces with unbalanced and balanced ionic distributions throughout the remainder of this dissertation. Since the fluid behavior within the P-P structure is similar to that in the H-H structure the interested reader can refer to Kim et al. (2020).

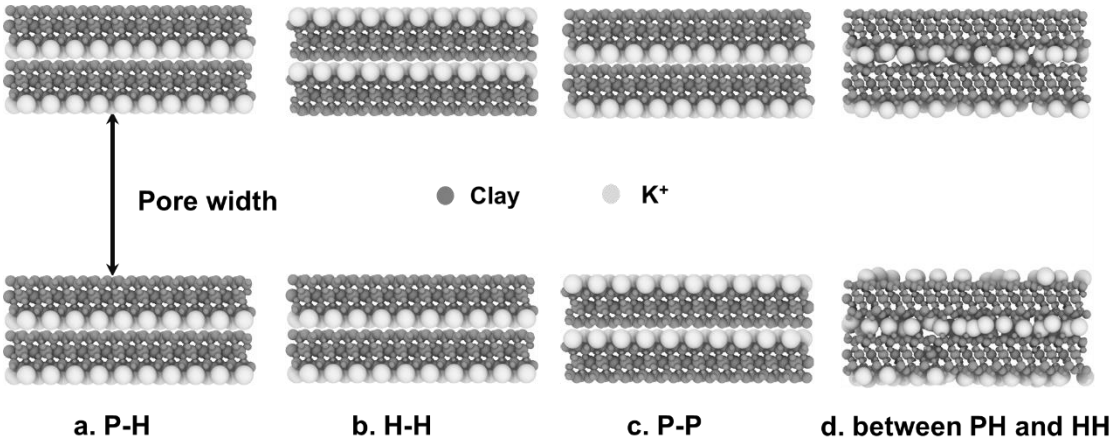

Figure 3-1 Illustration of four illite slit-pore structures. P and H stand for potassium and hydroxyl. a) P-H pore has potassium ions on only one surface; b) is the H-H pore with no potassium ions; c) is the P-P pore with an equal number of potassium ions on both surfaces and d) is the structure that lies in between the P-H and H-H pore structures in terms of ion distribution.

Kuila et al. (2013) use N_2 gas-adsorption and mercury intrusion porosimetry (MIP) showing that clays are associated with multiple scales of pore structures (~3-100 nm). Therefore, in my study, three different basal spacings (5nm, 10nm, and 15nm) are constructed for each illite pore model.

To study the effect of water concentration on fluid transport, I construct seven models with different concentrations for each slit pore width. Dodecane and ethane are chosen to represent hydrocarbon (oil-solvent) following Chapter 2. The number of fluid components is determined by the Peng-Robinson equation to guarantee the target pressure and temperature (Peng et al. 1976). Models A1-A7, B1-B7, and C1-C7 contain different water concentrations in the P-H nanopore of width 5, 10, and 15 nm respectively. Table 3-1 summarizes all the 21 P-H models. Another 21 MD models with the H-H configuration are constructed and they share the same fluid composition as listed in Table 3-1. Initial configurations of Models A1-A7 are shown in Figure 3-2. To

keep the temperature and pressure constant at 350 K and 400 atm respectively, when the hydrocarbon concentration decreases as the water concentration increases.

Table 3-1Description of the models used in chapter 3

Slit pore width, nm	P-H/H-H Models		Number of molecules			Water concentration (Cw), mol %
			Water	Dodecane	Ethane	
5	A	1	0	90	360	0.00
		2	100	86	344	18.87
		3	250	80	320	38.46
		4	500	70	280	58.82
		5	750	60	240	71.43
		6	1000	50	200	80.00
		7	2000	0	0	100.00
10	B	1	0	180	720	0.00
		2	200	172	688	18.87
		3	500	160	640	38.46
		4	1000	140	560	58.82
		5	1500	120	480	71.43
		6	2000	100	400	80.00
		7	4000	0	0	100.00
15	C	1	0	270	1080	0.00
		2	300	258	1032	18.87
		3	750	240	960	38.46
		4	1500	210	840	58.82
		5	2250	180	720	71.43
		6	3000	150	600	80.00
		7	6000	0	0	100.00

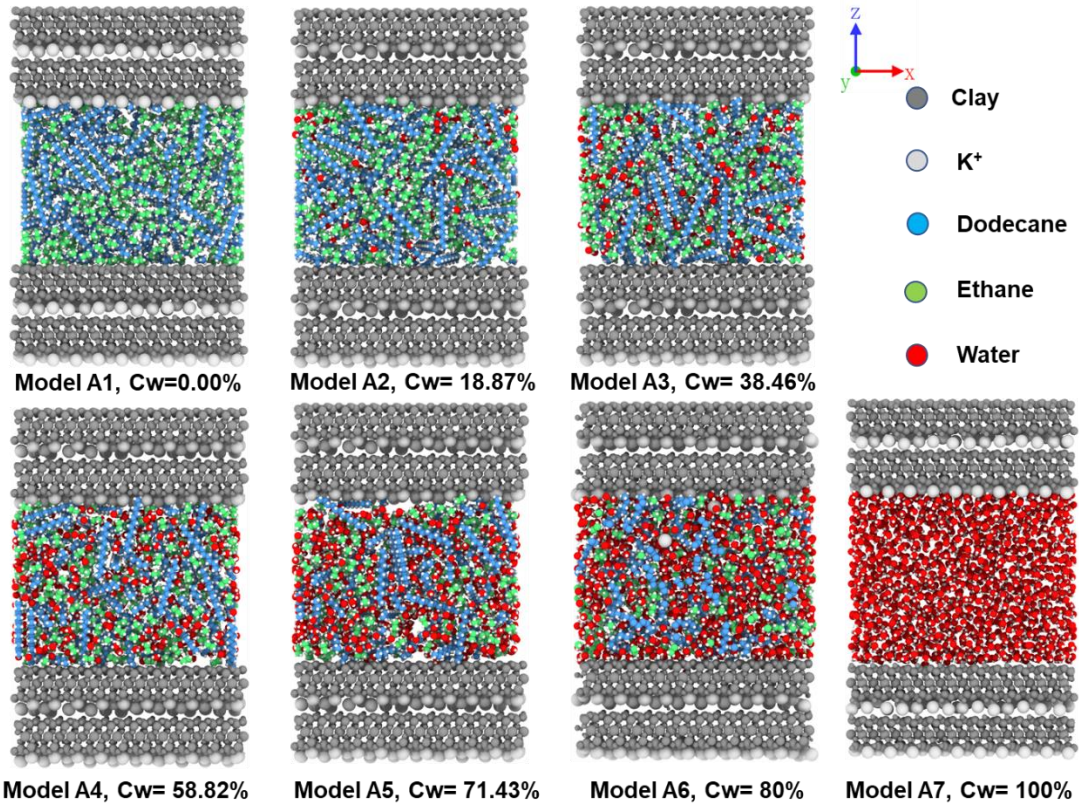

Figure 3-2 Snapshots showing the initial configurations of the Models A1-A7 in slit pore of 5 nm, where Cw stands for the water concentration. The clay structure contains the same color codes as in Figure 3-1. The color codes of fluid molecules are ethane, green; dodecane, light blue; and H_2O, red.

3.3 Simulation Details

The simulation process followed is similar to that described in Section 2.3, starting with the random placement of dodecane, ethane, and water in the slit nanopore using the Packmol package (Martínez et al. 2003). ClayFF force field is applied to describe the interatomic interactions for illite structure and the cations (Cygan et al. 2004). Water molecules are described using a flexible SPC model and the shake algorithm is used to make two O-H bonds and the H-O-H angle rigid (Berendsen et al. 1981). OPLS All-Atom force field is employed to represent the organic components such as ethane and dodecane (Jorgensen et al. 1996). Periodic boundary conditions (PBCs) are used in all

three directions and the cutoff distance for the short-range nonbonded van der Waals interactions is 8 Å. The long-range electrostatic interactions are calculated by the particle-particle/particle-mesh (PPPM) method with a precision value of 10^{-6} (Eastwood et al. 1984). The illite-structural atoms (Al, Si, and O) are kept rigid to their crystal lattice sites, except that H^+ in hydroxyl and the cation K^+ are mobile with thermal motion (Hao et al. 2018).

The initial step involves running an NVT ensemble MD simulation with a time step of 0.01 fs for a total time of 100ps, after which it is increased to 1 fs for a time of 10 ns. The temperature is held at 350 K by the Nose-Hoover thermostat (Nosé et al. 1984). All snapshots of simulation trajectories are created using OVITO 3.0.0 (Stukowski et al. 2010) and VMD 1.9.3 is used to produce the LAMMPS input file (Humphrey et al. 1996).

3.4 Results and Discussion

3.4.1 Distribution of Water and Hydrocarbon in P-H Nanopore

Figure 3-3 shows the equilibrium configurations and water number density profiles (in the *x*-direction) for different water concentrations (Cw) in a 5 nm pore. The illite structure is not presented for clarity. Unsurprisingly, Figure 3-3 indicates that water molecules preferentially adsorb onto the clay surface with one distinct peak in the number density profile indicating a single adsorption layer. This is attributed to the strong electrostatic interactions between water and clay surface (Phan et al. 2012), and

the hydrogen bond between water and surface hydroxyl and oxygen groups (Bourg et al. 2012).

Another observation is that more water molecules are adsorbed on the surface hydroxyl layer than the potassium layer as shown in Figure 3-3a, which agrees with previous reports (Osipov et al. 2012; Rao et al. 2013; Hao et al. 2018) and is because the hydration energy of oxygen and hydroxyls on the clay surface is comparable or even slightly higher than the hydration energy of potassium cations (Sposito et al. 2006). Additionally, adsorption between water and oxygen atoms and hydroxyl groups due to hydrogen bonds are stronger than the electrostatic interaction between water and potassium (Méring et al. 1967). Also when cations interact with a mineral surface, their hydration weakens naturally during adsorption (Osipov et al. 2012), therefore the water adsorption on the potassium layer in my simulations is relatively weak. I also calculate the Van der Waals force of one water molecule in a P-H nanopore as shown in Figure 3-4. It indicates that the absolute value of van der Waals force near the hydroxyl layer is about 0.65 Kcal/mol/Å, which is higher than that near potassium layer (absolute value is about 0.3 Kcal/mol/Å). Thus, the calculated result confirms that water is more likely to adsorb on the hydroxyl layer than the potassium layer. The configuration and water number density profiles (*x*-direction) of different concentrations in pore widths of 10 nm and 15 nm are provided in Figure 3-5 showing the distributions of water in the nanopore, which are like the trends in Figure 3-3.

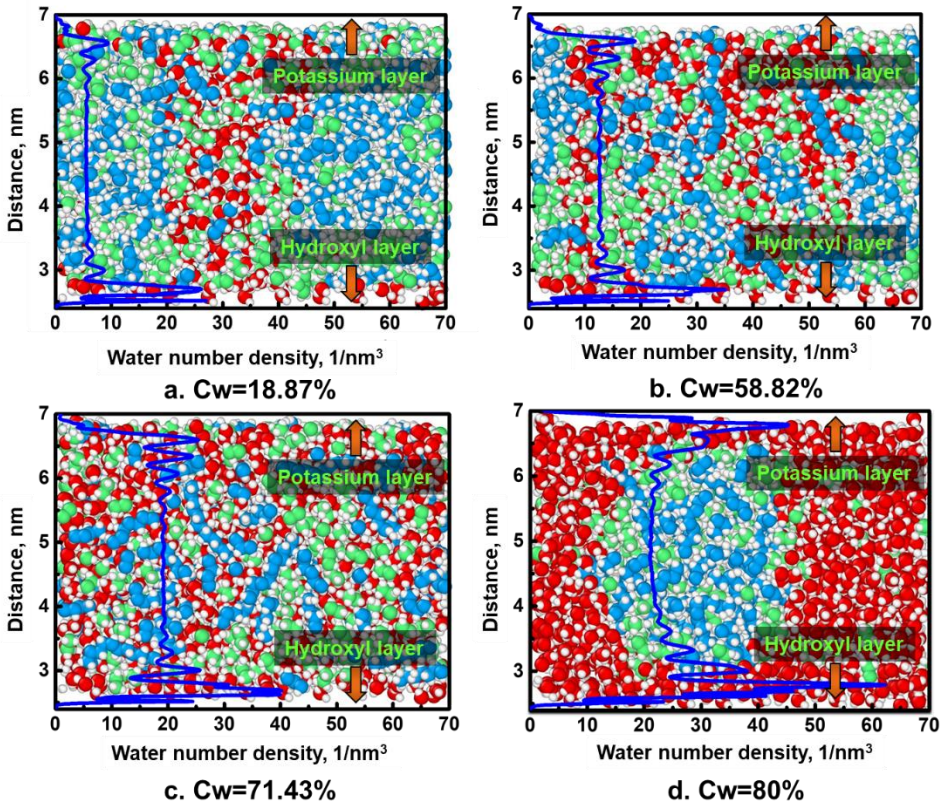

Figure 3-3 Configurations and water number density profiles (in yellow curves) of different water concentrations at equilibrium at 350 K and 400 atm for a P-H nanopore. Illite structure is not presented for clarity. The higher density peaks adjacent to the hydroxyl surface indicate that water preferentially adsorbs on the hydroxyl and oxygen layer compared to the potassium layer. Liquid color codes: Oxygen in H_2O, red; Hydrogen, white; Carbon in dodecane, blue; Carbon in ethane, green.

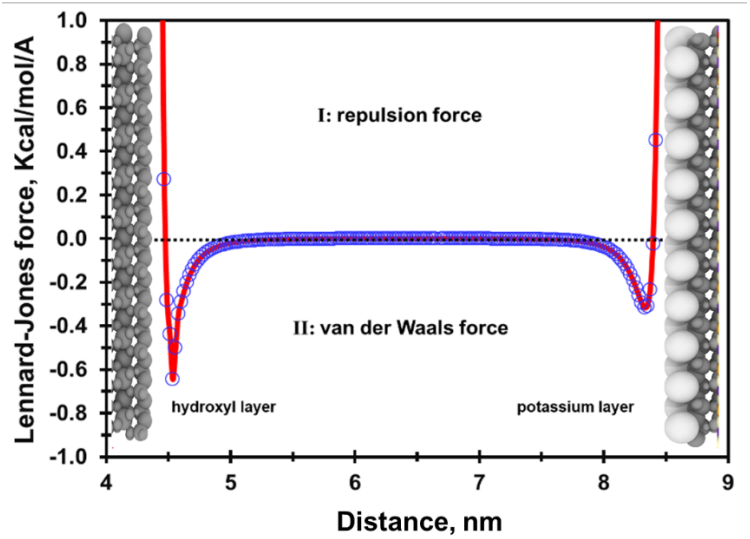

Figure 3-4 Schematic diagram of calculated Van der Waals force near P-H surface. The calculated Van der Waals force confirms that water is more likely to adsorb on the hydroxyl layer than the potassium layer.

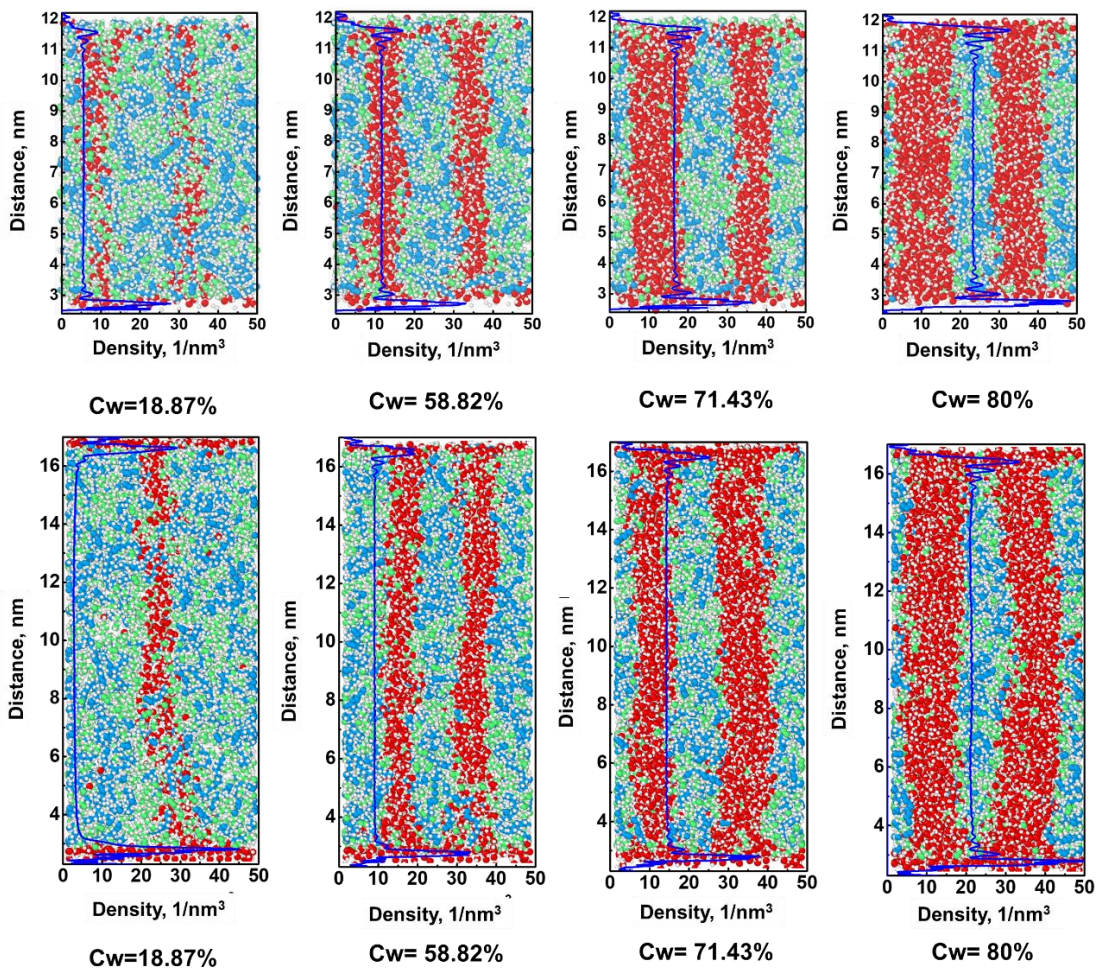

Figure 3-5 Configurations and water number density profiles (x-direction) of different water concentrations in pore width of 10 nm and 15 nm after the equilibrium in MD simulations at 350 K and pressure 400 atm. The illite structure is not shown for clarity. The blue lines are water number density profiles. The result illustrates that the distribution of water and dodecane-ethane in the nanopore, which are similar to that in Figure 3-3.

Figure 3-6 shows the structures and number density profiles (z-direction) of water and the hydrocarbon mixture at different water concentrations for a pore width of 5 nm for a P-H nanopore. The illite structure is not presented and the hydrocarbons are rendered translucent for the ease of observation. Figure 3-6a indicates that when the water concentration is 18.87 %, the water film connects across the pore in the form of a water bridge at 350K and 400 atm. The number density profile of hydrocarbon is non-zero because the bridge does not span the entire width in the y-direction (The side view

of hydrocarbon and water for Figure 3-6a is provided in Figure 3-7).

Figure 3-6b demonstrates that when water concentration is increased to 58.82 %, two water bridges form as interpreted from two peaks of the water density profile. Figure 3-6c (front view) and Figure 3-6e (side view taken at 2 nm from the left) are the simulation results at a water concentration of 71.43%. According to the number density profiles of water and hydrocarbon in Figure 3-6c, the water and hydrocarbon are almost equally distributed along the *x*-direction in an x-z film with a minimum thickness of 12.4 Å. However, from the side view, as shown in Figure 3-6e, it shows that the water film connects across the whole slit pore. Figure 3-6c also illustrates that both water and hydrocarbon are continuous phases at a water concentration of 71.43%. When the water concentration is further increased to 80%, the hydrocarbon mixture forms a droplet in between 2 water films as seen in Figure 3-6d. It should be noted that the fluctuation in the number density profiles in Figure 3-6 mainly comes from the periodical arrangement of hydroxyl groups and oxygen on the clay surfaces (Liu et al. 2017).

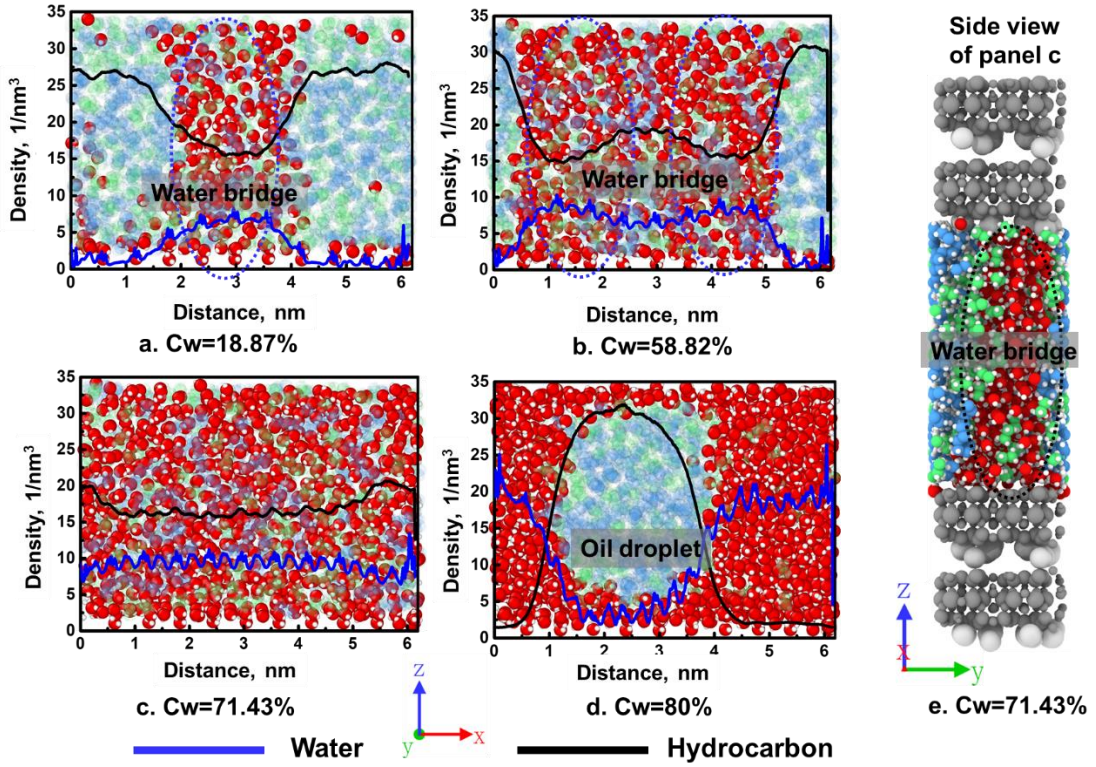

Figure 3-6 Equilibrium configurations and number density profiles (z-direction) for different water concentrations in the 5 nm pore at 350 K and 400 atm for a P-H nanopore. Illite structure is not shown for clarity. The results illustrate that water solubility in the hydrocarbon is possible at a certain temperature and pressure conditions and the 'free' water molecules can disperse in the hydrocarbon to form water bridges.

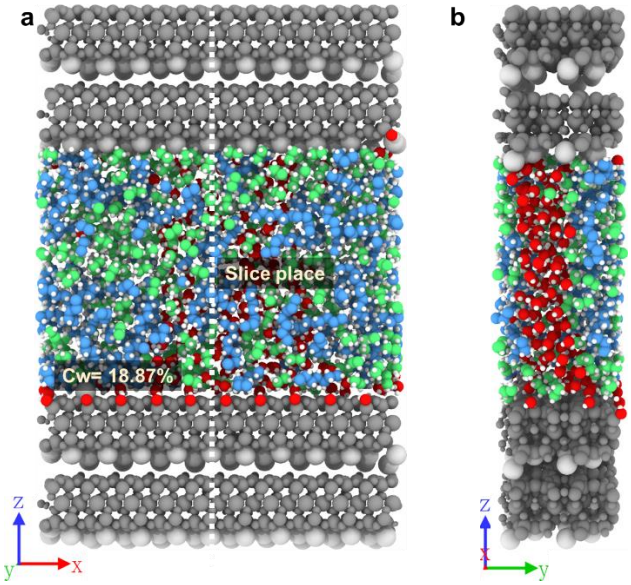

Figure 3-7 Configurations of hydrocarbon and water distribution in the 5 nm P-H nanopore at the water concentration of 18.87%. The white line in panel a is the slice place. Panel b is the slice view for Fig. 6a. Panel b indicates that there is a water bridge formed in the P-H nanopore, but the bridge does not span the entire width in the y-direction.

In Chapter 2, I report that water adsorbs onto the clay surface till fully saturated, and then the excess water molecules subsequently form a water bridge. Other researchers also report similar 'water bridges' in inorganic nanopores (Yanagihara et al. 2013; Yamashita et al. 2015; Li et al. 2016; Liu et al. 2018), and refer to them as 'capillary bridges' or 'capillary condensation' (Yamashita et al. 2013; Tan et al. 2015; Danov et al. 2018). It is worth noting that the 'capillary condensation' often occurs when two adsorbed water films are adequately close to each other (Li et al. 2016). In this study, the water bridge persists in P-H nanopores at even 10 or 15 nm pore width as shown in Figure 3-8 and Figure 3-9. Thus, the water bridges observed in this work are not solely due to 'capillary condensation'. In the next section, I discuss the formation mechanism of the water bridge.

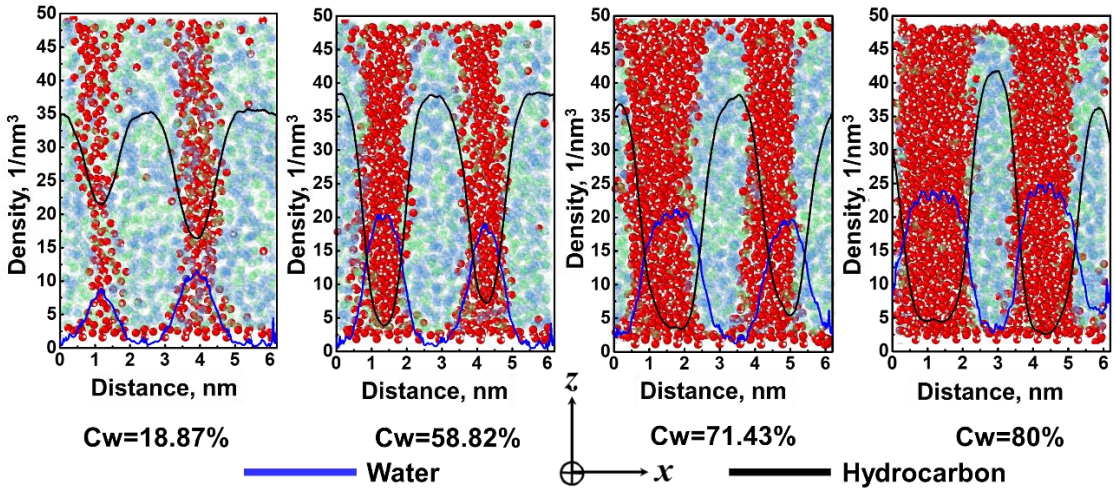

Figure 3-8 Equilibrium configurations and number density profiles (z-direction) of water and hydrocarbon for different water concentrations in a P-H nanopore of width 10 nm at 350 K and 400 atm. Illite structure is not shown for clarity.

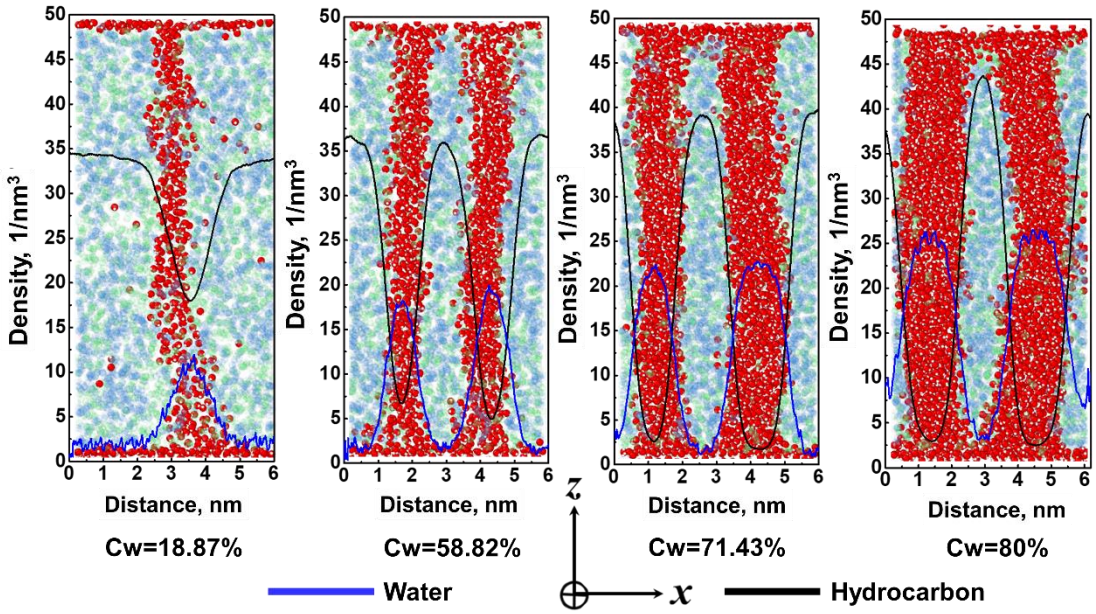

Figure 3-9 Equilibrium configurations and number density profiles (z-direction) of water and hydrocarbon for different water concentrations in a P-H nanopore of width 15 nm at 350 K and 400 atm. Illite structure is not shown for clarity. The results illustrate that the water bridge still exists even when the pore width increases from 5 nm to 10nm or 15 nm.

3.4.2 Mechanism of Formation of the Water Bridge

In this section, I will describe the conditions (partial charge, water concentration, and pore width) for the formation of the water bridge. Figure 3-10, Figure 3-11, and Figure 3-12 present the configurations and number density profiles (z-direction) of hydrocarbon and water in H-H slit pores of width 5, 10, and 15 nm in respectively, where the illite structure is not shown and hydrocarbons are shown as translucent particles for clarity.

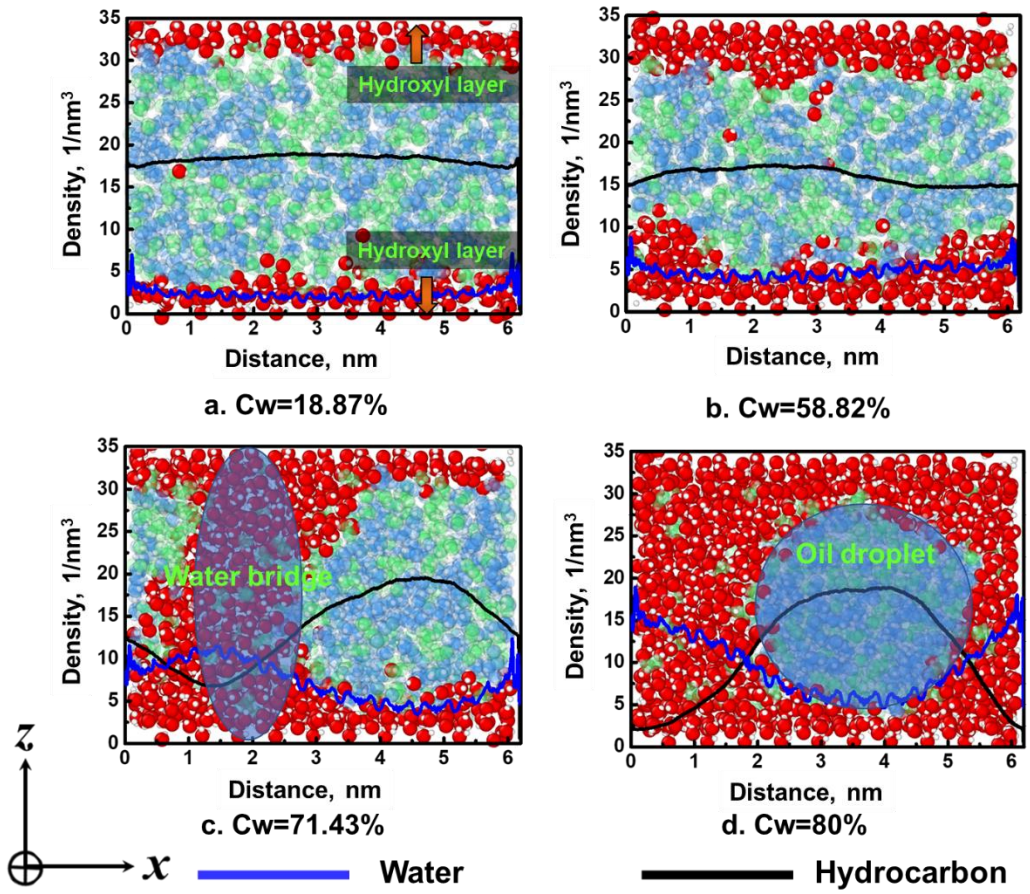

Figure 3-10 Configurations and number density profiles of water and oil in the hydroxyl-hydroxyl (H-H) surface clay slit pore of width 5 nm. Increasing the water concentration promotes the formation of a water bridge.

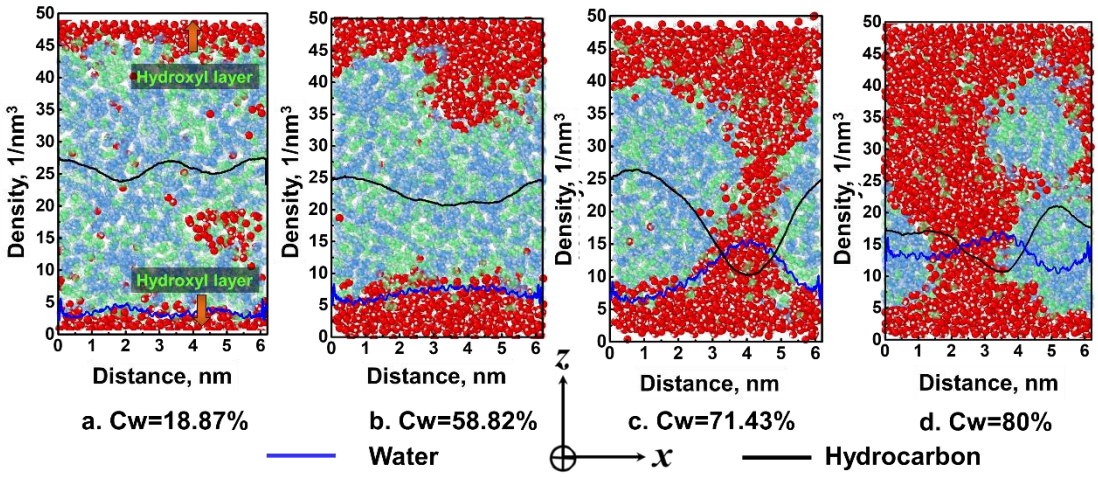

Figure 3-11 Configurations and number density profiles of water and oil in the hydroxyl-hydroxyl (H-H) clay pore of width 10 nm.

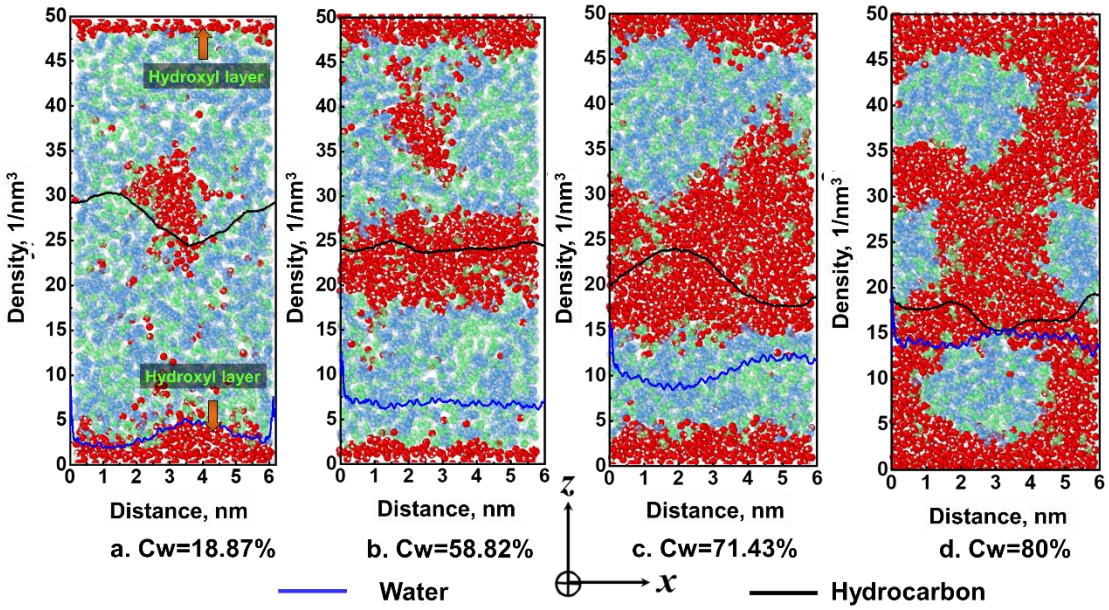

Figure 3-12 Configurations and number density profiles of water and oil in the hydroxyl-hydroxyl (H-H) clay pore of width 15 nm. The results demonstrate that pore width will affect the formation of water bridge and the illite surface shows less effect on the water molecules at the pore center with the increasing the pore width.

1) Partial charge

Figure 3-10a and Figure 3-10b indicate that there is no water bridge formed in the H-H slit pore structure at water concentrations of 18.87% and 58.82% with almost all water molecules adsorbed on the hydroxyl surfaces. Figure 3-11a, Figure 3-11b, Figure 3-12a, and Figure 3-12b are similar as well. However, Figure 3-6a and Figure 3-6b show a water bridge in P-H slit pores for the same concentration of water.

Inspired by the work of Zhang et al.(2019), Namin et al.(2013), Fuchs et al. (2007 and 2008), Ponterio et al. (2010), and Chen et al. (2016) who indicate that an electric field can change the OH stretching band and water distribution, I hypothesize that the positive potassium cations and negative surface in clay nanopores might produce a local electric field that influences the structure of water. To validate this hypothesis, I calculate the electric field of P-H and H-H pore systems by computing the electrostatic

force on a test atom with charge e.

This is done by measuring a cross-section of the pores devoid of any fluid. I first calculate the electric field of P-H and H-H pore systems by computing the electrostatic force on a test atom with charge e. As shown in Equation (3-1), the electrostatic force, F is the product of the electric field, E and the charge, e:

$$F = Ee \tag{3-1}$$

Because I use a test atom with charge e, the electrostatic force is equal to the electric field. In MD simulations, there are 5 force fields: bond, angle, dihedral, van der Waals and electrostatic forces. To calculate the electrostatic forces, I ignore the other forces. It should be noted that in my LAMMPS script, the measured force is in the units of *Kcal/mol/Angstrom*, where 1 *Kcal/mol*=0.043eV. e is the electron and V is the volt. After a simple unit conversion, $\frac{F}{e} = E = 0.43\frac{V}{nm}$. Due to the complexity of the clay structure and the small distance (< 10 nm), it is possible to have such a high magnitude electric field as shown in Appendix B. Taking the 5 nm P-H (Figure 3-13a) and H-H nanopores (Figure 3-13b) as an example, I move a charge e (shown in the red circle) along the black curve from the bottom to the top surface of the pore. In LAMMPS simulations, I can manually move the charge e along the black curve by changing its coordinate step-by-step and recording the corresponding electrostatic force.

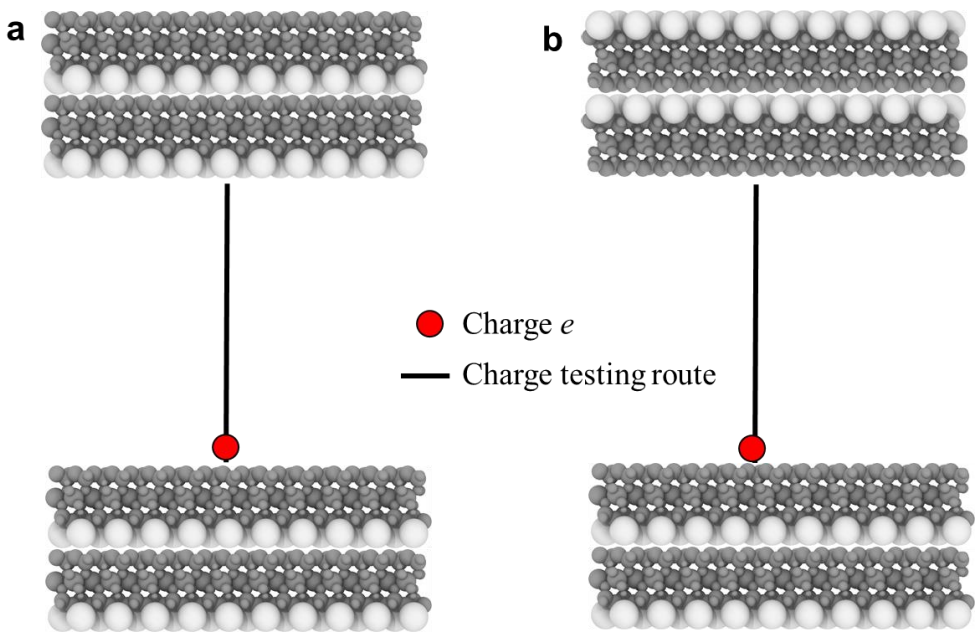

Figure 3-13 Illustration of the process to calculate the electrostatic force. (a) 5 nm P-H system, and (b) 5 nm H-H system.

Figure 3-14 shows the calculated electric field in 5 nm, 10 nm, and 15 nm P-H and H-H pores. The average strengths of the electric field in 5 nm, 10 nm, and 15 nm P-H pores, as shown in Figure 3-14a, are 12.92 V/nm, 8.72 V/nm, 6.56 V/nm with a standard deviation of 0.51, 0.39, and 0.44 V/nm respectively. While in theory, the electric field should be uniform (Barrachina et al. 2011), non-uniformly distributed charges in the clay minerals cause variations in the electric field near the clay surface. The calculated charge distribution of illite is provided in Figure 3-15. In the inset chart of Figure 3-15, it shows the non-uniform charge distribution on the illite structure. Although the whole illite model is electrically neutral, the main chart shows that the surfaces have heterogeneous charge distributions with the average upper and lower charge densities of 0.97 and -4.02 c/m^2, which can influence fluid distributions.

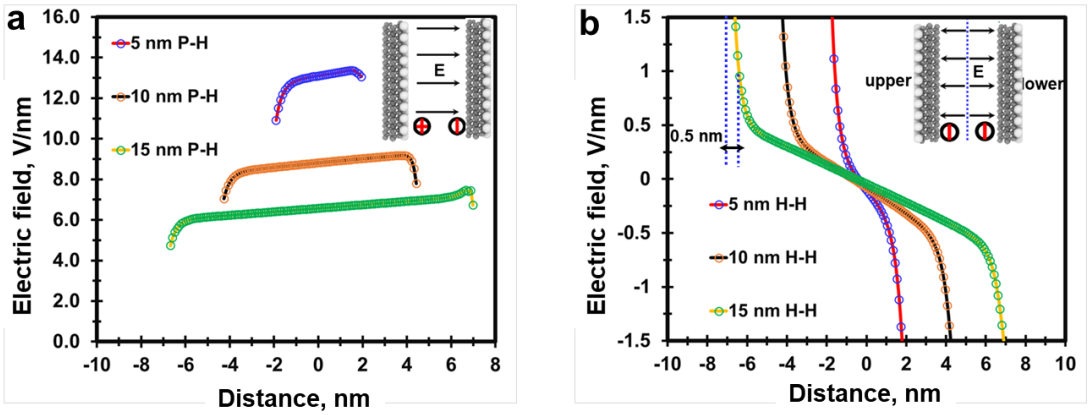

Figure 3-14 Calculated electric fields in different widths. Absolute values of the electric field strengths in P-H pores (left) are observed to be larger than those in H-H nanopores (right). Increases in pore width decrease the strength of the electric field in both pore systems. It should be noted that no fluid is considered when calculating the electric field.

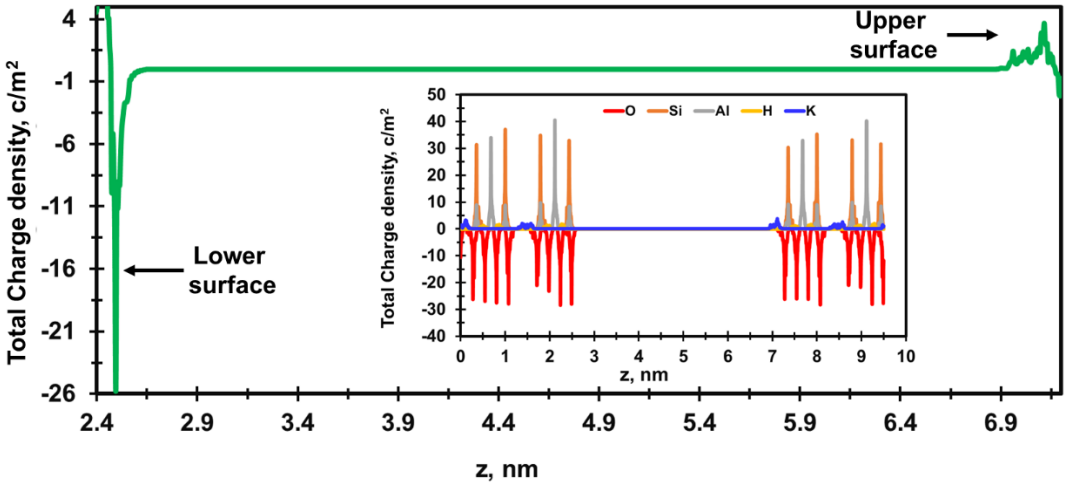

Figure 3-15 Charge distribution of illite structure (the inset chart) and the surface charge density (the main chart)

Figure 3-14b shows the calculated electric field in 5 nm, 10 nm, and 15 nm H-H pores which range from -1.5 V/nm and 1.5 V/nm. In Figure 3-14b, near the upper surface, the strength of the electric field is about 1.5 V/nm. Moving across the pore, the field strength decreases to zero, and its absolute value increases again (with an accompanying change in direction). Such electric fields have also been observed to

occur naturally in zeolite cavities because they have an electrical surface charge (Barrachin et al. 1986; Liu et al. 2014; Chen et al. 2015). In both pore systems, an increase in pore width is accompanied by a decrease in electric field strength, an observation that is consistent with Bueno et al. (2011).

Skinner et al.(2012), Cramer et al.(2008), and Hao et al.(2019a) also indicate that electric field strengths larger than 1 V/nm change the structure of water. A comparison of the electric fields in Figure 3-14 suggests that P-H pores exhibit stronger and more long-range fields in comparison to H-H pores. In the H-H pore, the electric field is greater than 1V/nm for only less than 0.5 nm from the pore surface as shown in Figure 3-14b. In the P-H nanopore, a strong electric field extends across the entire pore width promoting the formation of water bridges.

In Figure 3-16, I discuss the orientation of the water molecules at a concentration of 58.82% in both pore systems. The water orientational direction is defined as the angle between V_1 and V_2 vectors (Figure 3-16a), where V_1 is a unit vector normal to the surface and V_2 is the OH vector. Figure 3-16b shows one sharp peak in the P-H pore at 130° indicating that the two OH bonds are aligned with the direction of the electric field. These results are similar to those presented in Skinner et al. (2012). The OH bond orientation in H-H pores is more heterogeneous with a relatively weaker peak at 90°, which is consistent with Cramer et al. (2008). Figure 3-14 and Figure 3-16 confirm that the existence of the electric field influences the orientation of water molecules within the pore.

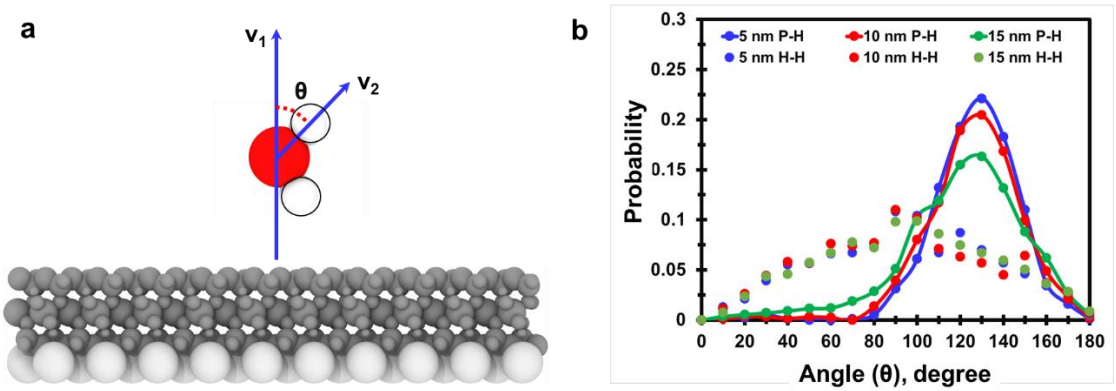

Figure 3-16 In (a), V1 is the unit normal vector. V2 is the OH vector (OH bond angle). θ is the angle between two vectors. In (b), It shows the OH bond angle for all water molecules for different pore widths in H-H and P-H pores. In P-H pores, a dominant angle of 130° is observed while in H-H pores, the OH bond angles are largely random with a weaker peak at 90°. The electric field of Figure 3-15 influences the orientation of water molecules in both pore systems.

Ossowska et al. (2013) report that dipole moments in crystal slabs can induce an electric field. When I use periodic boundary conditions in all three directions, there is a possibility that the surface and image surface in the z-direction can generate a large dipole moment favoring the formation of a water bridge. To eliminate this effect, I remove periodic boundary in the z-direction (normal to the surface) and the water bridge persists in a 15nm P-H pore as shown in Figure 3-17. This confirms that the formation of the water bridge is caused by the electric field induced in the illite nanopore, not the dipole moment generated by the surface and image surface.

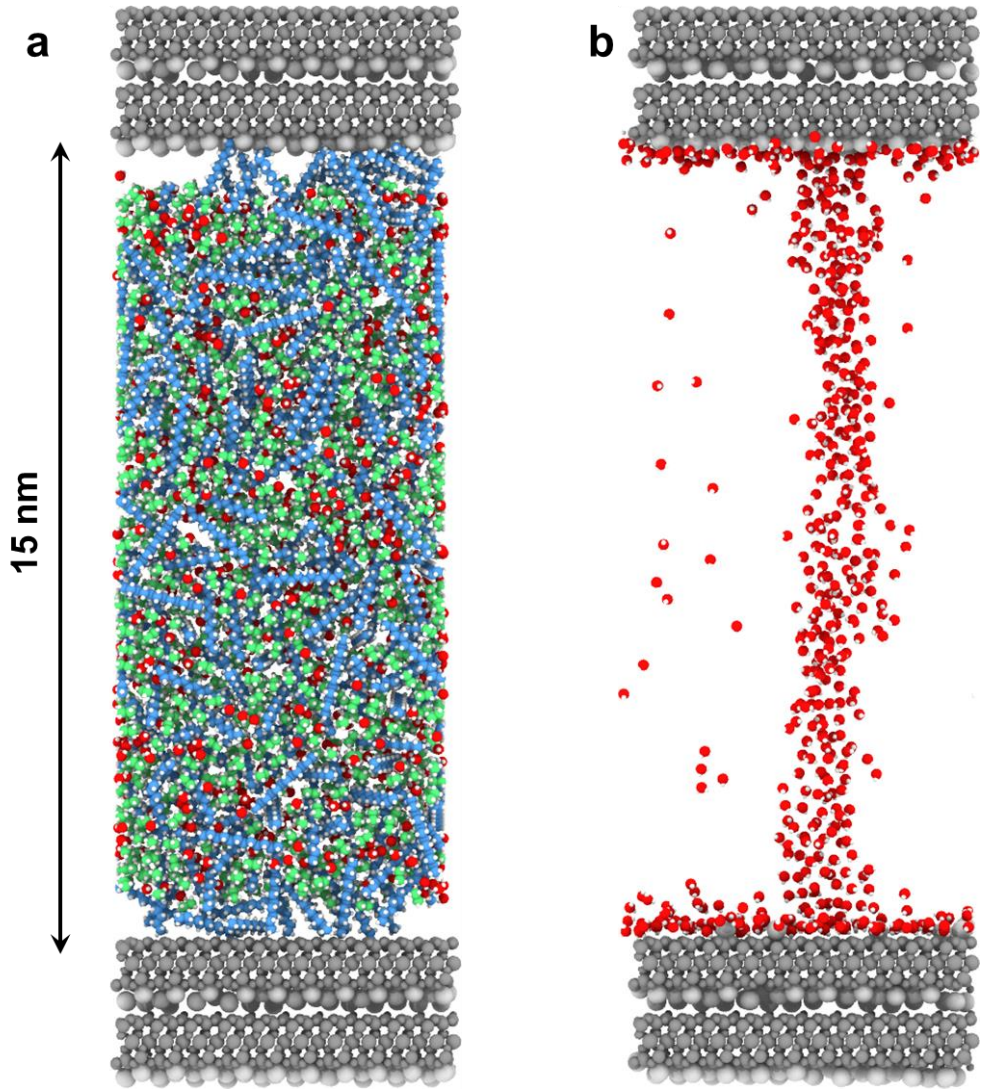

Figure 3-17 Initial (left) and final (right) configurations for 15 nm P-H nanopore with water saturation of 38.46%. Note: the cutoff distance is 0.8 nm and hydrocarbon not shown in panel b. The periodic boundary in the z-direction is removed.

2) Water concentration

Figure 3-10 indicates that the water concentration can also influence the formation of water bridges even in H-H nanopores. At low water concentrations such as 18.87% and 58.82%, almost all water molecules are adsorbed onto the illite surface and no water bridges are observed as shown in Figure 3-10a and Figure 3-10b. When the water concentration increases to 71.43%, a water bridge is formed as shown in Figure 3-10c.

For the last 2 ns, the average minimum thickness of the water bridge in the *x*-direction is 2.1 nm with a variance of 0.08 nm as shown in Figure 3-18. It should be noted that even though Figure 3-10c shows a water bridge at high-water concentration, the oil phase is not continuous in contrast to Figure 3-6c (for a P-H nanopore) where both oil and water are continuous phases. Finally, at a water concentration of 80%, a small oil droplet forms as shown in Figure 3-10d which is similar to Figure 3-6d and the results presented in Liu et al. (2018). Figure 3-11 and Figure 3-12 show the results for pore widths of 10 and 15 nm.

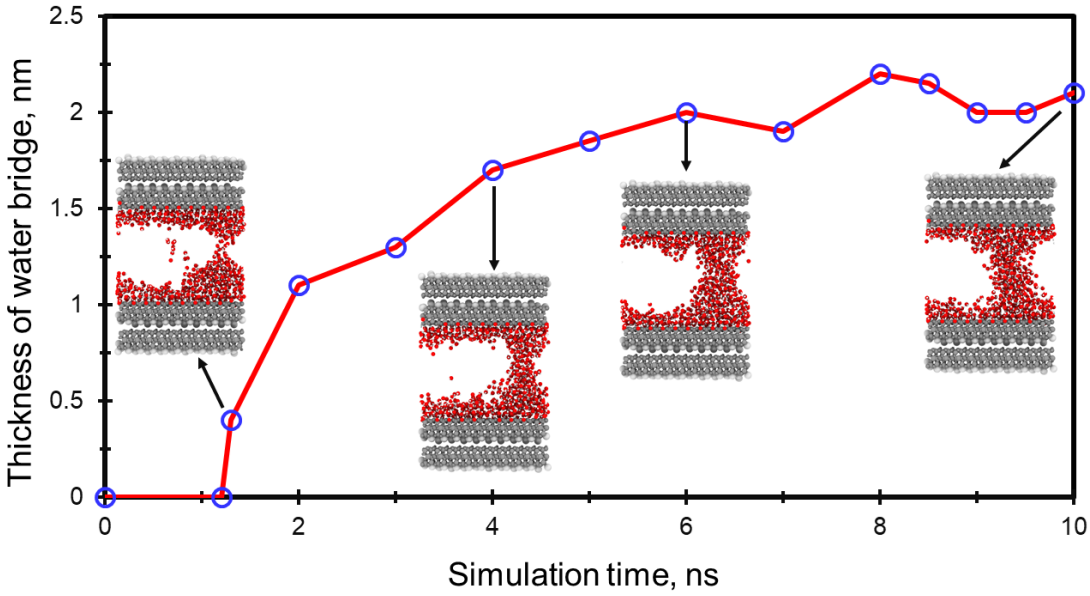

Figure 3-18 Thickness of water bridge at the water saturation of 71.43% in 5 nm H-H nanopore during the whole simulation time.

3) Pore width

Figure 3-10, Figure 3-11, and Figure 3-12 demonstrate that pore width also affects the formation of a water bridge. Figure 3-10c indicates that the water bridge is formed in 5 nm H-H nanopore with a minimum thickness of 2.1 nm in the *x*-direction. Increasing

the pore width to 10 nm as shown in Figure 3-11c, the thickness of the water bridge decreases to 0.7 nm. Further increasing to 15 nm, there is no water bridge as shown in Figure 3-12c. That is, at the same water concentration, the water bridge is more inclined to form in smaller pores. Meanwhile, comparing Figure 3-11a/Figure 3-12a and Figure 3-11b/Figure 3-12b, we can see that increasing the pore width reduces the influence of the illite pore surface on the water, leading to the formation of small water droplets in the middle of the pore as shown in Figure 3-12a and Figure 3-12b. This phenomenon is similar to capillary condensation as reported in Yamashita et al. (2013), Tan et al. (2015), and Li et al. (2016).

3.4.3 Self-diffusion

The self-diffusion coefficient is obtained following the procedure described in Section 2.4.3 in Chapter 2. The calculated self-diffusions of the different fluid molecules in P-H and H-H nanopores are shown in Figure 3-19 and Figure 3-20 respectively as a function of the water concentration. Figure 3-19a to Figure 3-19c show the calculated self-diffusion of P-H illite nanopores as the function of water concentration in the pore width of 5, 10, and 15 nm respectively.

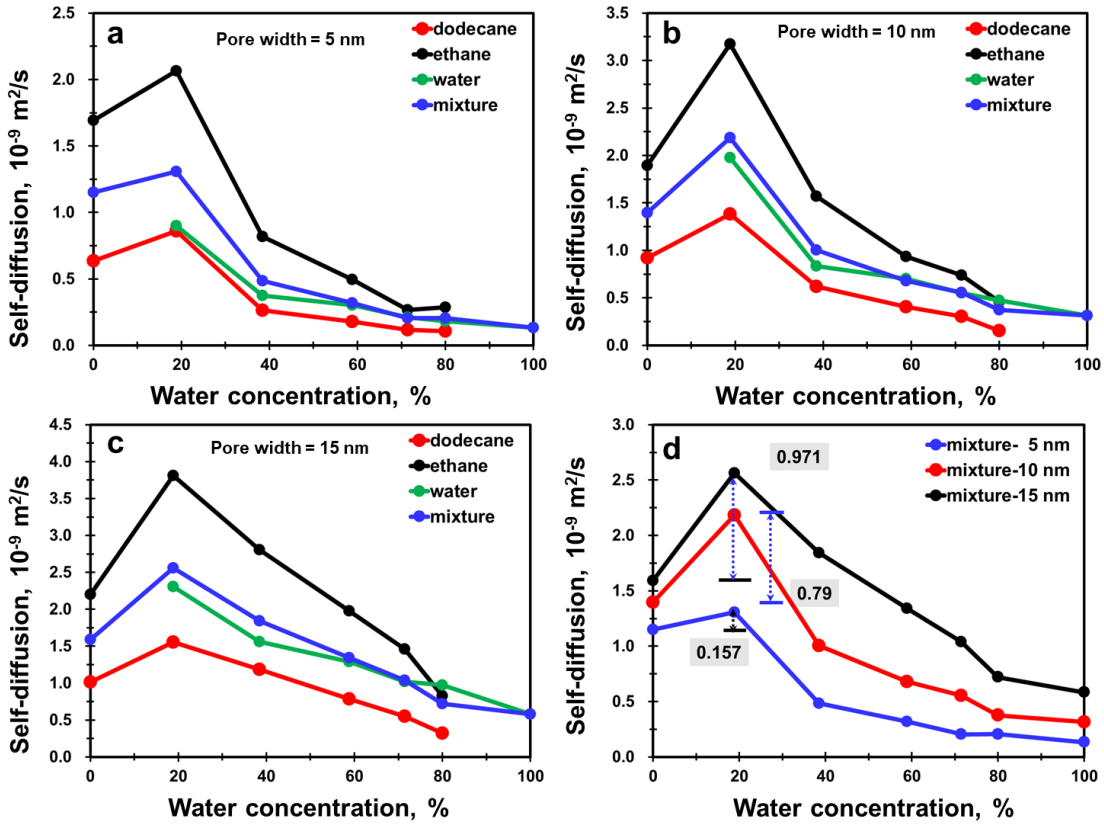

Figure 3-19 Calculated self-diffusion in P-H illite nanopores. The lines representing the self-diffusion of dodecane are in red, those for ethane are in black, water in green, and the mixture in blue. The results indicate that the self-diffusion coefficient increases initially with increasing water concentration probably because of the formation of a water film that promotes hydrocarbon transport. Subsequent increases lead to a water bridge that impedes hydrocarbon flow, leading to a decrease in the self-diffusion coefficient. Pore width also plays a role in dictating the effect of water adsorption on fluid transport.

The results indicate that initial increases in the water concentration enhance the self-diffusion of hydrocarbon because of the creation of water films that create a smooth surface for hydrocarbon transport (Liu et al. 2018). At higher concentrations (for example, above 18.87% in P-H) the formation of water bridges impedes the hydrocarbon flow. Further increasing the water concentration leads to strong reductions in the self-diffusion coefficients.

Figure 3-19a to Figure 3-19c also indicate that at a water concentration of 18.87%,

despite the formation of water bridges in the pores of 5, 10, and 15 nm, the negative effects of the water-bridge effect are counterbalanced by the smooth adsorption walls, leading to an increase in the self-diffusion coefficients. Therefore, I can conclude that in P-H illite nanopores the fluid behavior is initially dominated by the water adsorption film and later by the formation of a water bridge.

Figure 3-19d shows the calculated self-diffusions of the mixture (averaged self-diffusion from water-dodecane-ethane) in P-H nanopores as the function of water concentration in pores of width 5, 10, and 15 nm respectively. It indicates that the pore width has an impact on self-diffusion. The calculated self-diffusions in the pore width of 15 nm are the largest compared to that in pore widths of 5 and 10 nm. The smaller the pore width is, the lower the self-diffusion coefficient. Figure 3-19d also demonstrates that the smooth effect of water adsorption film is affected by the pore width. When the water concentration increases to 18.87%, the increased self-diffusions in the pore widths of 5, 10, and 15 nm are 0.157×10^{-9} m^2/s, 0.79×10^{-9} m^2/s, and 0.971×10^{-9} m^2/s, respectively. In the pore width of 5 nm, although the water adsorption film will promote the hydrocarbon flow, the decreased effective flow radius due to water adsorption film will compromise this positive effect. However, such a negative effect contributes less to larger pores of 10 and 15 nm. Therefore, the increased degree of self-diffusion is more apparent in the studied 10 and 15 nm pores.

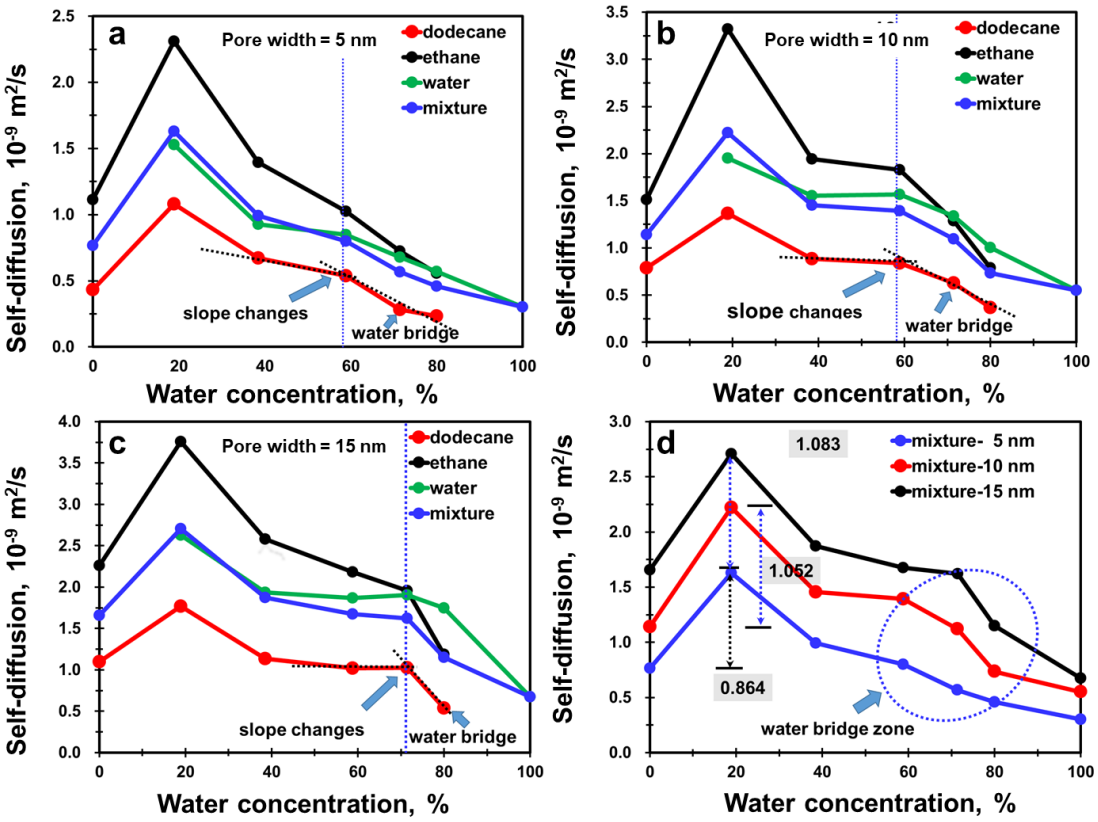

Figure 3-20 Calculated self-diffusion coefficients in H-H nanopores. The results indicate that water adsorption promotes hydrocarbon flow sharing the same trend in P-H pores. Once the water bridges form, a drastic reduction in the self-diffusion coefficients is seen.

Figure 3-20a to Figure 3-20c show the calculated self-diffusion in H-H illite nanopores as a function of water concentration in pores of width 5, 10, and 15 nm respectively. The results show the same trends as in the P-H nanopores. However, because the water bridge does not form until higher concentrations of water (in the absence of an electric field in H-H nanopores), I observe a self-diffusion plateau for intermediate values of water concentrations. Increasing the water concentration beyond ~58% leads to the formation of a water bridge (as shown in Figure 3-10c and Figure 3-11c). For the 15nm pore in Figure 3-20c, the slope change happens at the water concentration of 71.43% at which a water bridge is observed as seen in Figure 3-12d.

Figure 3-20d is the calculated self-diffusion coefficients of the mixture in H-H illite nanopores as a function of water concentration in the pores of 5, 10, and 15 nm respectively. The results confirm that the self-diffusion coefficient varies with the pore width. These values are higher than the corresponding values in a P-H nanopore because of the absence of a water bridge. However, we can notice that when the water concentration increases to 18.87%, the increased self-diffusions in the pore widths of 5, 10, and 15 nm are 0.864×10^{-9} m^2/s, 1.052×10^{-9} m^2/s, and 1.083×10^{-9} m^2/s respectively, which are larger than the results in P-H illite nanopores. This is because, in P-H nanopores, the water bridges are formed as shown in Figure 3-6, Figure 3-8, and Figure 3-9. But in H-H illite nanopores, there are no water bridges as shown in Figure 3-10 and Figure 3-11. Therefore, the formation of the water bridge will compromise the smooth effect of water adsorption film.

Figure 3-21 is the comparison of the self-diffusion coefficients of the mixture, dodecane, ethane, and water in both H-H and P-H nanopores. Figure 3-21a indicates that because of the water bridge, the self-diffusion of the mixture in the 5nm H-H nanopore (red curve) is higher than that in the P-H nanopore (black curve) except for the initial point where water concentration is 0%. More importantly, the self-diffusion coefficient of the mixture in the P-H nanopore at a pore width of 10 nm (brown curve) is still lower than the one in a 5nm H-H nanopore (black curve) indicating that water bridges have a strong impact on hydrocarbon flow and increasing the pore width may not be able to overcome this negative effect. Figure 3-21b-d provides the same insights

as Figure 3-21a.

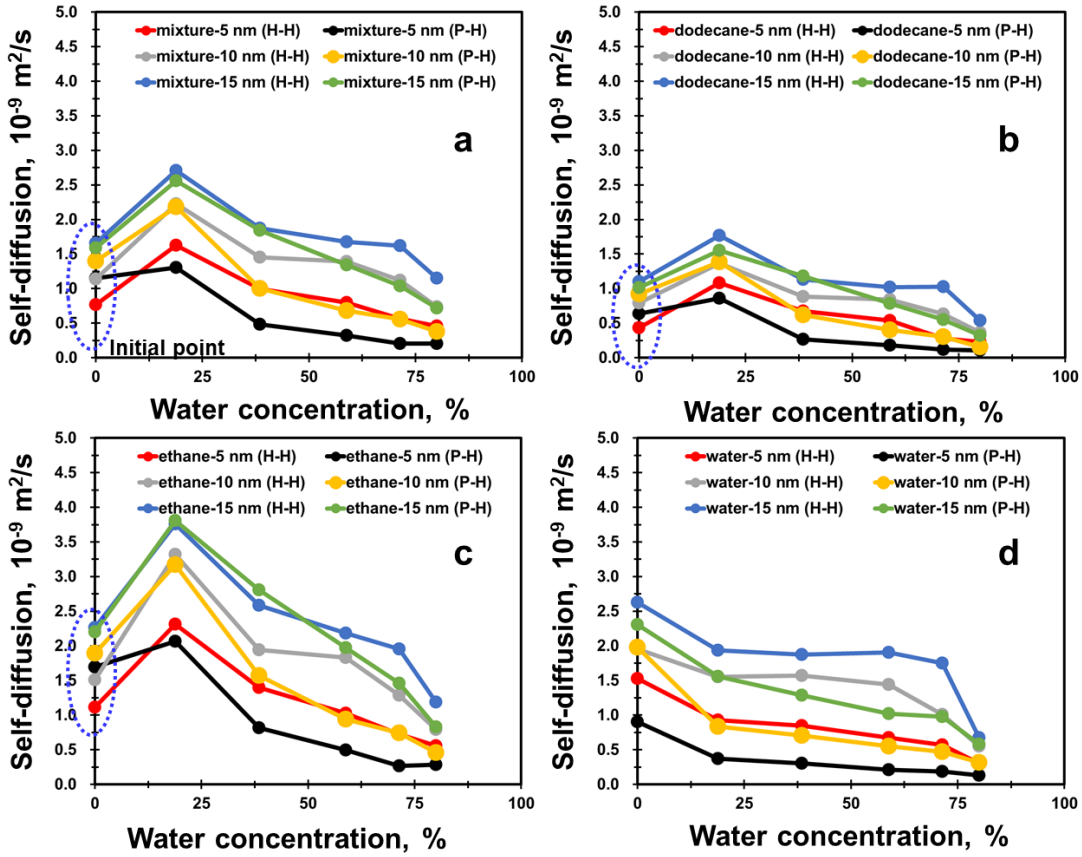

Figure 3-21 Comparisons of self-diffusion between H-H and P-H in different pore widths. The results indicate that self-diffusion in P-H is lower than that in H-H, demonstrating that electric fields can influence the self-diffusion of hydrocarbon through the formation of the water bridge.

3.5 Final Remarks

This chapter uses MD simulations to investigate the formation of water bridges and their influence on fluid transport in clay nanopores through a discussion of spatial molecule distribution and self-diffusion. The positive potassium layers and negative hydroxyl groups in the P-H illite structure can induce local electric fields which can favor the formation of the water bridge. The formation of a water bridge is influenced by the concentration of water. In P-H nanopores, water bridges appear at relatively low

water concentrations (In my study, as low as 18.87%). In H-H nanopores, water bridge only happens at high water concentration (as high as 71.43%). The formation of a water bridge is also influenced by pore width. For a given concentration of water, smaller pore widths promote the formation of a water bridge. In both P-H and H-H nanopores, the initial formation of an adsorbed water film creates a smooth surface to promote the hydrocarbon flow, leading to an increase in the self-diffusion coefficient. However, increasing water concentration promotes the formation of water bridges that impede hydrocarbon flow, leading to a decrease in self-diffusion coefficients. Because of the presence of water bridges, the self-diffusion coefficients in P-H nanopores are lower than that in H-H nanopores except where water concentration is 0%. However, it can also favor the formation of the water bridge in an aqueous environment to impede the hydrocarbon flow. Future work is needed to investigate the minimum water concentration to form the water bridge in both P-H and H-H nanopores.

Chapter 4 Oil-Water Transport in Clay-Hosted Nanopores: Effects of Long-Range Electrostatic Forces

4.1 Introduction

In this chapter, I continue with the studies of Chapter 3 and use non-equilibrium MD simulation to investigate transport and the stability of water bridges in clay pores.

4.2 Models and Methodology

4.2.1 Structure of Illite and Charged Surface Chemistry

The illite structure used here is the same as in Section 3.2 with two different surface chemistries (P-H and H-H) following Chapter 3. I consider seven different values of water concentrations (Cw) for each of the three slit pore widths (5, 10, and 15 nm). All the simulation models are the same as in Section 3.2 and summarized in Table 3-1. In the interests of space, I only show the initial configurations of the P-H models with a pore width of 5 nm in Figure 4-1. The temperature and pressure are kept constant at 350 K (170 °F) and 400 atm (5878 psi). To keep pressure conditions similar across all models, an increase in water concentration is accompanied by a decrease in the number of hydrocarbon molecules.

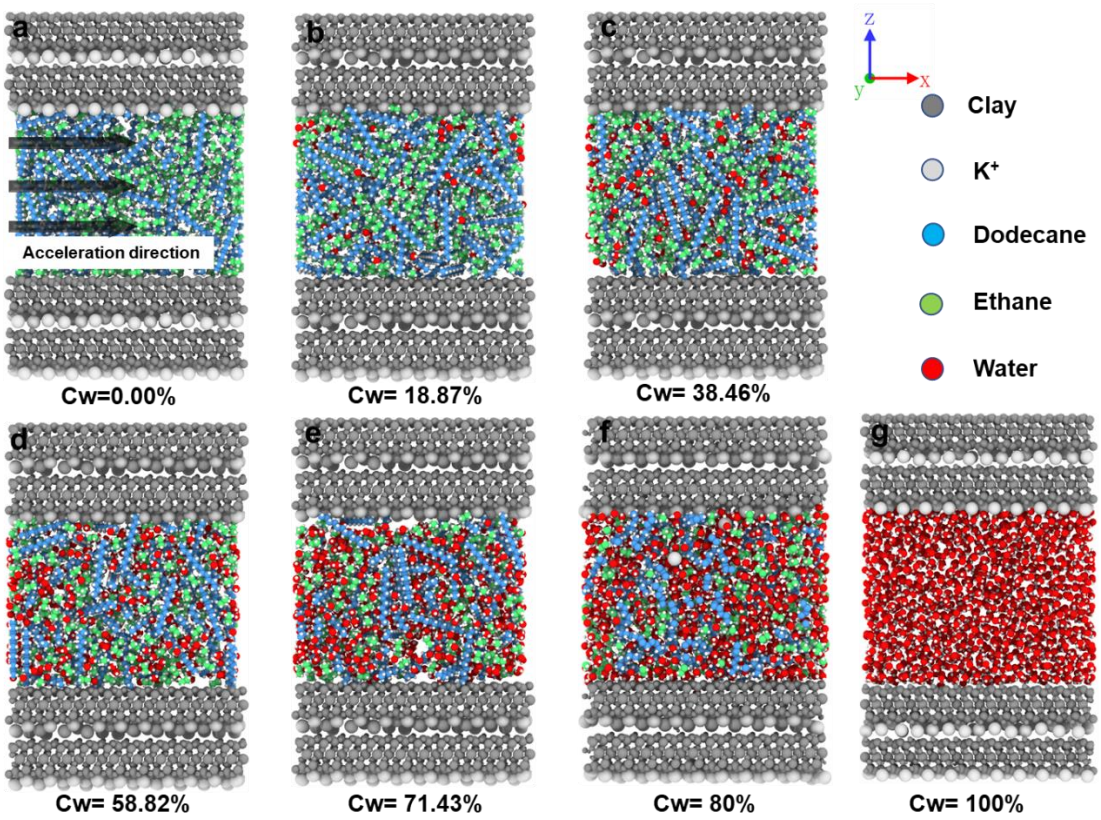

Figure 4-1 Initial configurations of the seven P-H slit pore models of 5 nm width with varying water concentration. Cw stands for water concentration. The color codes of clay are as in Figure 3-2. (a) the direction of the arrows indicates the direction of an imposed acceleration in subsequent sections of this paper. The fluid-color regimes: ethane (light green), H_2O (red), and dodecane (light blue).

4.2.2 Simulation Details

My modeling relies on the use of the ClayFF and OPLS All-Atom force field to describe illite (Underwood et al. 2016; Zen et al. 2016) and organic components (Jorgensen et al. 1996) respectively, while the flexible SPC model and the shake algorithm are applied to model water. Lorentz-Berthelot mixing rules describe the interactions between different atoms. I use LAMMPS (Large-scale Atomic/Molecular Massively Parallel Simulator) (Plimpton et al. 1995) with periodic boundary conditions applied in 3 directions.

My workflow is as follows: In the initial set-up, the number of fluid components is determined by the Peng-Robinson equation to guarantee the target pressure and temperature (Peng et al. 1976), and the fluid molecules are placed randomly between the slit pore using the Packmol package (Martínez et al. 2003). The illite-structural atoms (Al, Si, and O) are kept rigid to their crystal lattice sites, except that H^+ in hydroxyl and the cation K^+ are mobile with thermal motion (Hao et al. 2018). I then run the equilibrium MD (EMD) simulations using an NVT ensemble for 10 ns. During NVT, the pore surfaces are partially flexible where H+ in hydroxyl and the cation K+ are mobile with thermal motion. Temperature is maintained at 350 K using Nose Hoover thermostat (Nosé et al. 1984).

After EMD simulations, non-equilibrium MD (NEMD) simulations are performed for another 10 ns to mimic hydrocarbon-water transport. Several methods exist for inducing flow in molecular dynamics, such as forced (Malevanets et al. 1999 and 2000; Lamura et al. 2001), surface-induced, pressure difference (Thomas et al. 2009), osmotic pressure (Kalra et al. 2003), and gravitational approaches (Nikoubashman et al. 2010 and 2013; Allahyarov et al. 2002). In my simulations, I adopt the gravitational technique because other methods have been known to distort the velocity-field and density profile along with the flow direction (Allahyarov et al. 2002; Liu et al. 2016; Liu et al. 2018). A uniform gravity-like force (F, along the x-direction as shown in Figure 4-1), is imposed on all molecules inside the illite nanopores (Falk et al. 2012; Wang et al. 2016). The Published literature suggests applying large accelerations in simulations can

produce a sudden velocity jump, therefore, using small accelerations on the order of 10^{-4} to 10^{-3} nm/ps^2 (Wang et al. 2016b; Zhao et al. 2017) is a must to ensure a linear response in the system. In my study, the acceleration ranges from 0.0005 to 0.002 nm/ps^2.

It should be noted that in MD simulations, fluid temperature is calculated from the kinetic energy($KE = \frac{1}{2}mv^2$) (Wang et al. 2016a) where KE is the kinetic energy, m is the mass of the molecule and v is the velocity. More detailed information about temperature calculation can refer to Appendix A-1. However, in NEMD simulations, since I have added an external force, in the x-direction the molecule velocities consist of both thermal velocities and the imposed center-of-mass velocity. To ensure the temperature is maintained and not raised, fluid temperature calculations do not include the imposed center-of-mass velocity (Liu et al. 2018). The temperature and pressure during the NEMD simulations are shown in Figure 4-2.

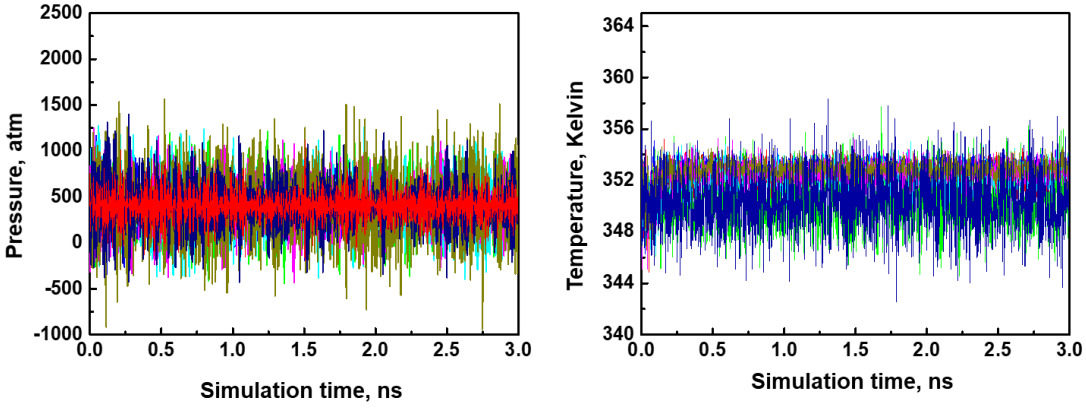

Figure 4-2 Pressure and temperature as a function of simulation time. The setting temperature and pressure are 350K and 400atm. In the NEMD simulations, there is only a small increase in temperature. The average equilibrium of temperature is about 352K

4.3 Results and Discussion

4.3.1 Fluid Transport in H-H Nanopores

In Chapter 3, I discussed the fluid distribution using equilibrium MD simulation. In this section, I report on the hydrocarbon and water velocity profiles with different accelerations (0.0005, 0.001, and 0.002 nm/ps^2) at 350 K and 400 atm. This would be analogous to imposing advective flow on the fluid confined within the pores. The velocity profile is obtained applying the bin method (Hansen et al. 2011). The slit pore is divided into *N* bins in the *z*-direction. The bin size is equal to 0.5 Å. For each bin, the center of mass velocity of water and hydrocarbon is extracted from time step t_n to t_m, and the velocity calculated as shown in Equation (4-1).

$$v_{bin} = \frac{\sum_{t_n}^{t_m} \sum_i m_i v_{iy,t}}{\sum_i m_i} \tag{4-1}$$

Where m_i is the mass of the particle *i* in the bin, v_{iy} is the component velocity of the particle *i* at the time step t in the bin.

I present the water (Figure 4-3a) and hydrocarbon (Figure 4-3b) velocity profiles at 0.0005 nm/ps^2 in the 5 nm H-H nanopore. Because the hydrocarbon and water velocity profiles at the acceleration of 0.001 nm/ps^2 and 0.002 nm/ps^2 show similar trends with that of 0.0005 nm/ps^2, they are not shown here and provided in Figure B-3 in Appendix B.

Figure 4-3a indicates that the water velocity changes with water concentration. At 100% water, I observe the classical parabolic signature of liquid flow in slit-pores.

Figure 4-3b indicates that increasing water concentration promotes hydrocarbon

flow up to a point. The initial increase has been attributed to the creation of smooth surfaces following the adsorption of water (Liu et al. 2018). Subsequent increases in the concentration of water decrease the effective flow radius, as shown in Figure 4-4, leading to a decline of hydrocarbon velocity.

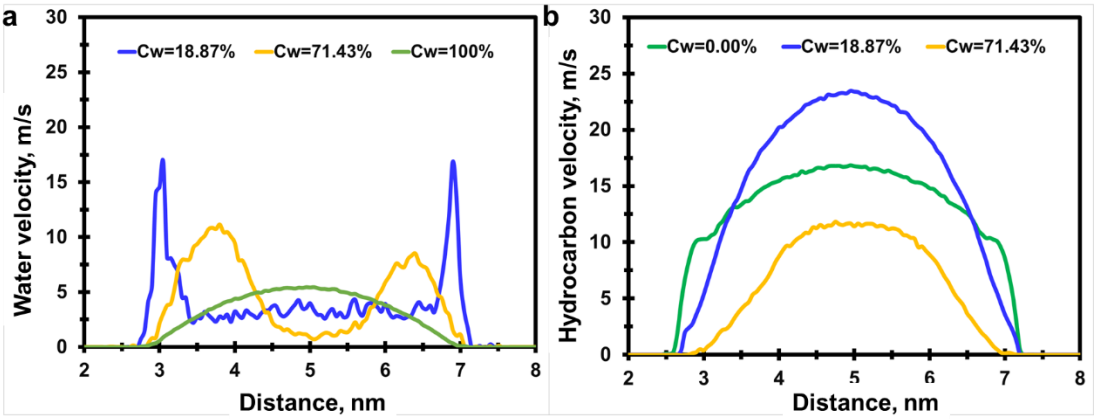

Figure 4-3 Water and hydrocarbon velocity profiles at 0.0005 nm/ps2 in 5 nm H-H nanopore. Cw stands for water concentration. Water concentration is seen to strongly impact both water and hydrocarbon velocities. For the water and hydrocarbon velocities, the reader can refer to Figure B-3 in Appendix B.

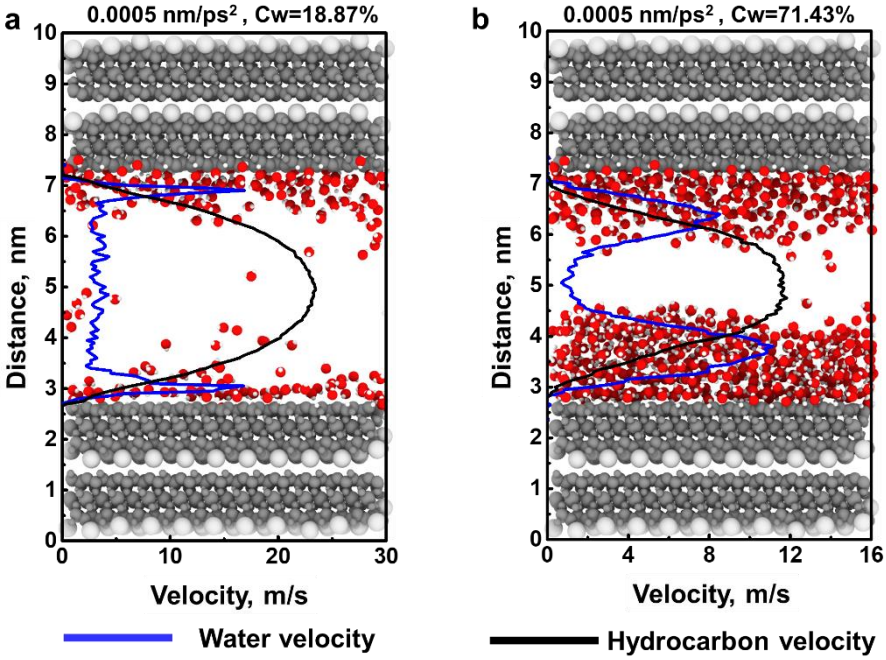

Figure 4-4 Distribution of water molecules for various water concentrations. Hydrocarbon is not shown. On the left, Cw = 18.97% and on the right, Cw = 71.43%. Increases in water concentration increase the adsorbed layer thickness that in turn influences water and hydrocarbon velocities.

Figure 4-5 shows the water and hydrocarbon velocity profiles at a higher value of the acceleration of 0.002 nm/ps^2 in a larger 15 nm H-H nanopore (velocity profiles for the 10 nm H-H nanopore are provided in Figure B-4 in Appendix B). The flow profiles are observed to be more complex at all values of saturation and are a function of the location of the respective phases within the pore.

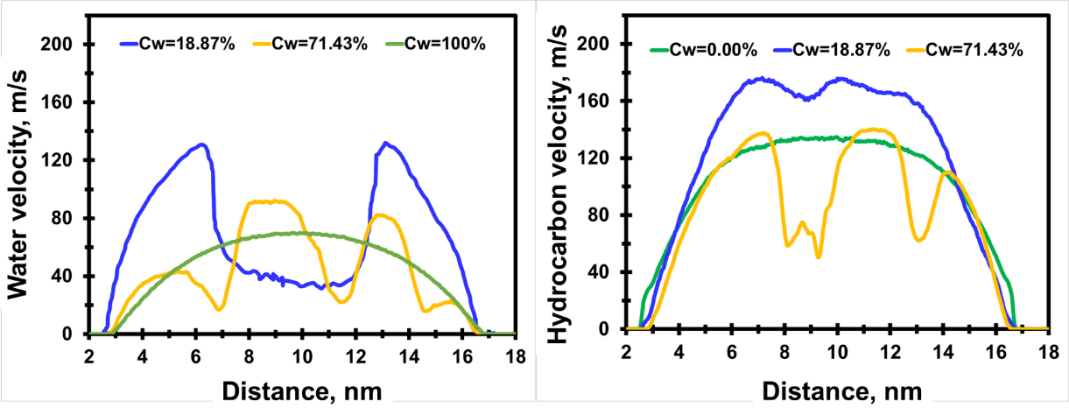

Figure 4-5 Water and hydrocarbon velocity profiles at 0.002 nm/ps2 in 15 nm H-H pores. The flow profiles for both phases appear more complex and simply correspond to the local phase densities within the pore.

Figure 4-6 shows the velocity profiles in 5 nm, 10nm, and 15nm H-H nanopores with a water concentration of 71.43%. The peaks and the troughs in the velocity profiles correspond to the local density of the water and hydrocarbon phases within the pore. Figure 4-6a indicates that in a 5nm nanopore, most of the water molecules are adsorbed and expected velocity profiles are observed. However, with larger pore widths, a more disordered flow pattern emerges. Unabsorbed water molecules form water droplets that elongate under the imposed acceleration as shown in Figure 4-6b and Figure 4-6c, making both the hydrocarbon and water phases discontinuous. Therefore, the velocity profiles of water and hydrocarbon in the 10 and 15 nm nanopores are asymmetric. I will

now discuss transport in P-H clay nanopores.

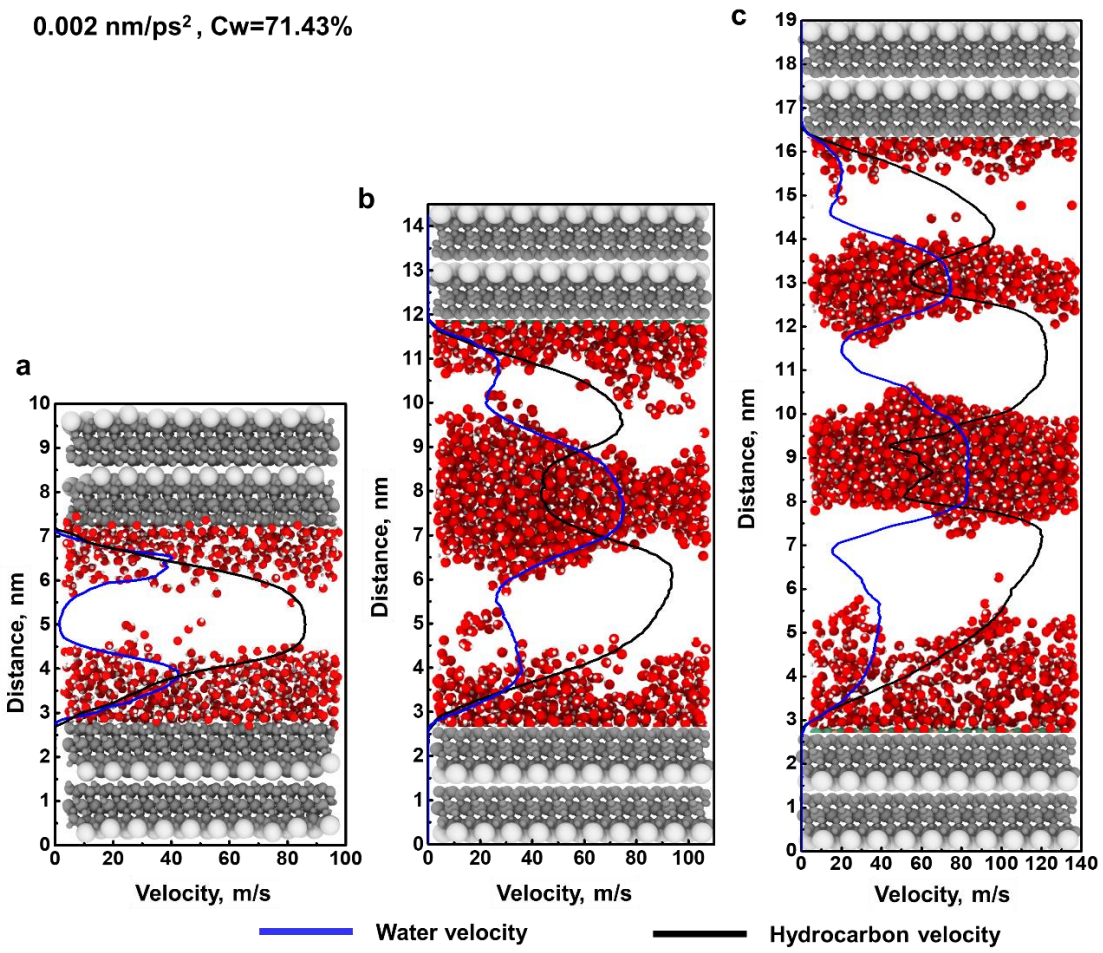

Figure 4-6 Distribution of water at 0.002 nm/ps2 and Cw = 71.43% in 5nm, 10nm, 15nm H-H nanopores. The hydrocarbon molecules are not shown. The result indicates that at each pore width, the peaks and troughs in the velocity profiles correspond to the local density of each of the phases. The motion of the water elongates the droplets entrained in the hydrocarbon phase.

4.3.2 Fluid Transport in P-H Nanopores

In the previous section, I reviewed the transport of water and hydrocarbon in H-H pore systems where water bridges are largely absent. In this section, I present the corresponding results for P-H pores where water bridges are prevalent across multiple pore widths and water concentrations.

The hydrocarbon and water velocity profiles for 54 NEMD simulations in P-H nanopore are provided in Figure B-5 and Figure B-6 in Appendix B. In this section, I only analyze a few representative hydrocarbon-water velocity profiles in P-H nanopores and address the effects of pore width, water concentration. The effect of the local electric field is important and discussed in Section 5.

1) Effect of Pore width

Figure 4-7 shows the water (Figure 4-7a) and hydrocarbon (Figure 4-7b) velocity profiles at an acceleration and water concentration of 0.002 nm/ps^2 and 71.43% respectively in different P-H nanopore widths. Water and hydrocarbon velocities increase with an increase of pore width which is in agreement with Liu et al.(2017). Additionally, water and hydrocarbon velocity profiles are parabolic in the 5 nm P-H nanopore and show flatter profiles for the 10nm and 15nm pores with increasing distance from the pore walls and the accompanying decrease in fluid-pore wall interactions.

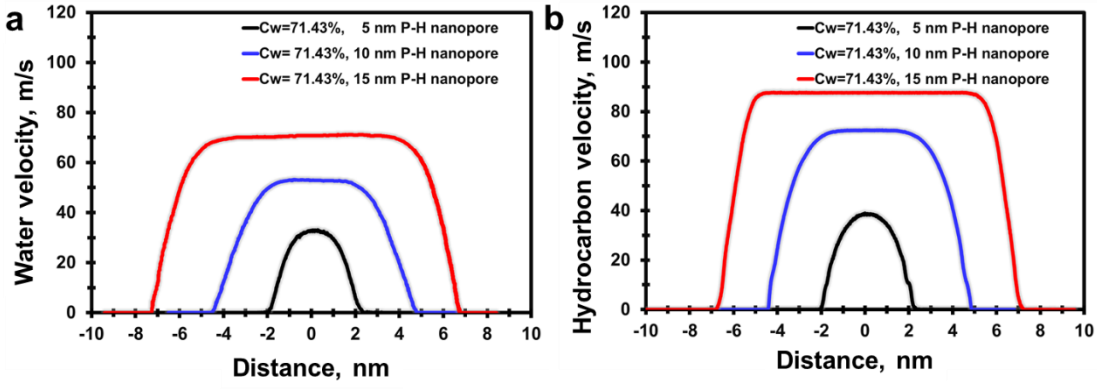

Figure 4-7 Water and hydrocarbon velocity profiles at the acceleration and water concentration of 0.002 nm/ps^2 and 71.43% respectively in different P-H nanopore widths. The result indicates that pore width impacts the velocity patterns. At 5nm, I observe a parabolic shape for the flow profiles which get progressively flattered as the pore width increases.

In Figure 4-8, I take a closer look at the water bridges present in the P-H pores at a water concentration of 71.43%. Hydrocarbon molecules are not shown for clarity. The red-colored water molecules are those adjacent to the pore surface and the yellow-colored water molecules are those present in the water bridge. Figure 4-8a shows the distribution of water in a 5nm P-H pore obtained from my equilibrium MD (EMD simulations) on top and under an imposed acceleration of 0.002 nm/ps^2 on the bottom. The water bridge in Figure 4-8a is essentially a sheet extending across the entire x-direction in the 5nm P-H nanopore.

Figure 4-8b and Figure 4-8c show the corresponding information for 10nm and 15nm pore widths. The intermingling of adsorbed water and water from within the bridge causes the velocity profile in Figure 4-8a (shown in a blue line). However, when pore widths increase to 10 nm or 15 nm, there is limited or no exchange of water molecules between the film and the bridge. The combination of constant acceleration and no exchange contributes to the flat velocity profiles observed in Figure 4-8b and Figure 4-8c. It is important to mention that under the imposed acceleration, the bridges remain intact.

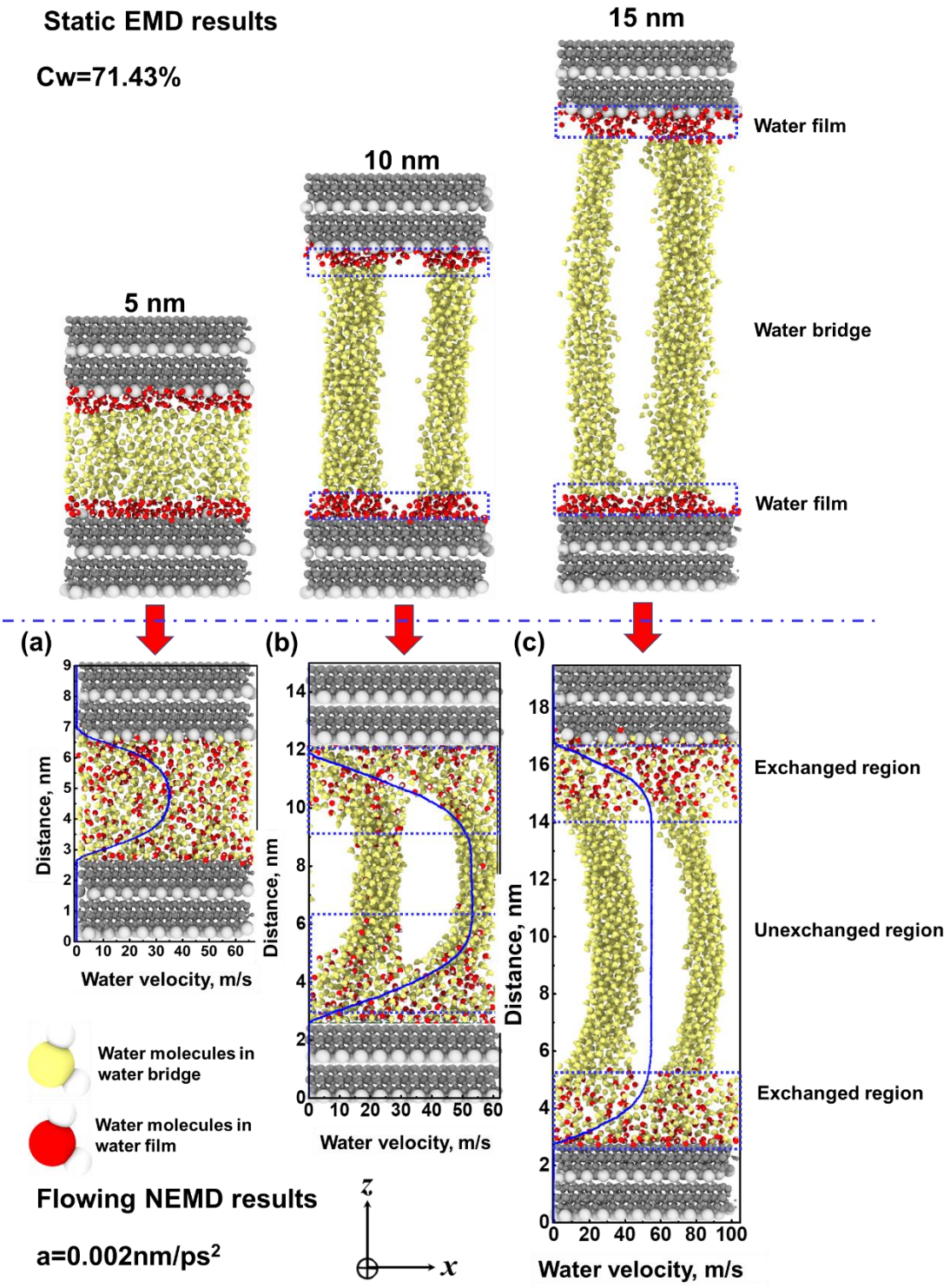

Figure 4-8 Molecular distribution and velocity profiles of water in P-H pores of different widths at a water concentration of 71.43%. The acceleration is 0.002 nm/ps2. Hydrocarbon is not shown for clarity. The red dots represent adsorbed water, and the yellow dots are those in the water bridge. In a 5 nm P-H nanopore, acceleration causes the adsorbed layer to exchange both mass and velocity with water at the pore center. Increasing the pore width to 10 nm or 15 nm, no mass or velocity exchange occurs between the adsorbed layer and water in the bridge or pore center, as revealed by the flatter velocity profile,

2) Effect of Water Concentration

Figure 4-9 shows the water (Figure 4-9a) and hydrocarbon (Figure 4-9b) velocity profiles at 0.002 nm/ps^2 in a 10 nm P-H nanopore for different values of water concentration. The velocity of water decreases with increasing water concentration (Figure 4-9a) because of the increased thickness of the water bridge. The minimum thickness (averaged over the last 2 ns) of the water bridge at water concentrations of 18.87%, 58.82%, 71.43%, and 80.00% is 0.94 nm, 1.24 nm, 1.60 nm, and 1.96 nm respectively. Figure 4-10 shows a boxplot of the bridge thickness over the last 2 ns of simulation time.

Figure 4-9b shows an increased hydrocarbon velocity for an initial increase in the water concentration which has been attributed to the creation of smoother surfaces for hydrocarbon flow (Liu et al. 2018). However, when the water concentration is increased, the width of the water bridge progressively increases (shown in Figure 4-10), thereby hampering hydrocarbon flow.

Figure 4-9 shows flat velocity profiles for both the oil and water phases. Because of the hydrophilic surface, hydrocarbon molecules are responding to the acceleration and are not strongly influenced by the pore surfaces, leading to a flatter velocity profile. The effect of acceleration on velocity profile is provided in Appendix B.

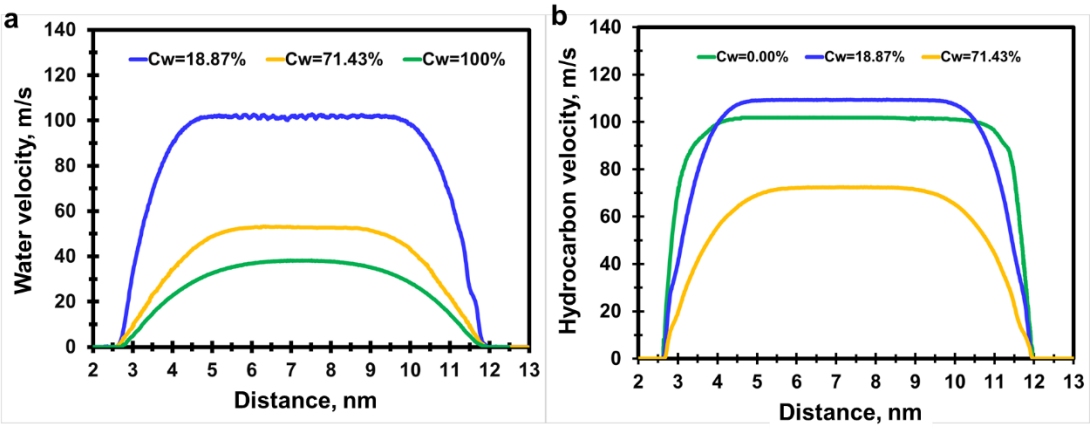

Figure 4-9 Water and hydrocarbon velocity profiles at the acceleration of 0.002 nm/ps^2 in 10 nm P-H nanopore. The result indicates that water concentration can impact the flow pattern.

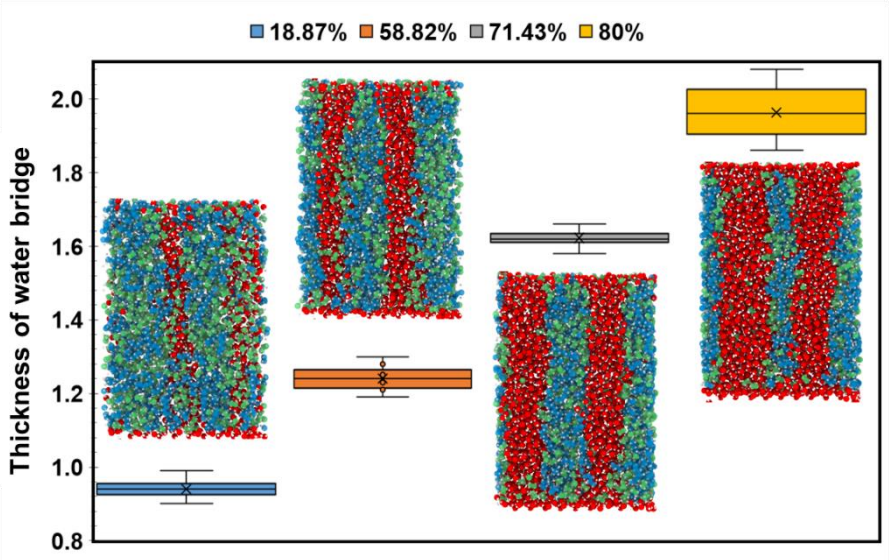

Figure 4-10 The bar errors of water-bridge thickness with different water concentrations. The minimum thickness of water bridges at a water concentration of 18.87%, 58.82%, 71.43%, and 80.00% is 0.94 nm, 1.24 nm, 1.60 nm, and 1.96 nm respectively. Increasing the water concentration creates thicker water bridges rather than increase the width of the adsorbed layer in P-H pores.

4.4 Single-Phase Velocity Profile Comparison between H-H and P-H Pores

This section focuses on single-phase velocities for different pore widths at a fixed acceleration of 0.002 nm/ps^2 in P-H and H-H pores. The results are shown in Figure 4-11 indicating that the P-H nanopore exhibits flatter flow profiles at the pore center

due to the presence of the electric field as shown in Figure 3-14.

Normally, adsorption is the result of van der Waals forces, covalent bonding, and electrostatic attraction (Ferrari et al. 2010). In this work, I do not consider covalent bonding (Huber et al. 2019). Therefore, in my study, adsorption is solely due to the van der Waals force and electrostatic attraction. Adjacent to the surface, these forces impact fluid transport. However, van der Waals force quickly diminishes for increasing distances from the pore surface (Autumn et al. 2002), while the influence of the electrostatic interaction force can extend more than 10 nanometers (Hao et al. 2019a).

Therefore, in the P-H pore, fluid transport is controlled by the electric field and imposed acceleration, leading to a flat pattern as shown in Figure 4-11a and Figure 4-11b. Increasing pore widths for P-H pores increases the width of the flat pattern as shown in Figure 4-11c and Figure 4-11d because of the increase in the width of the zone dominated by the electric field. However, in H-H pores with a negligible electric field, I observe classical parabolic velocity patterns as shown in Figure 4-11.

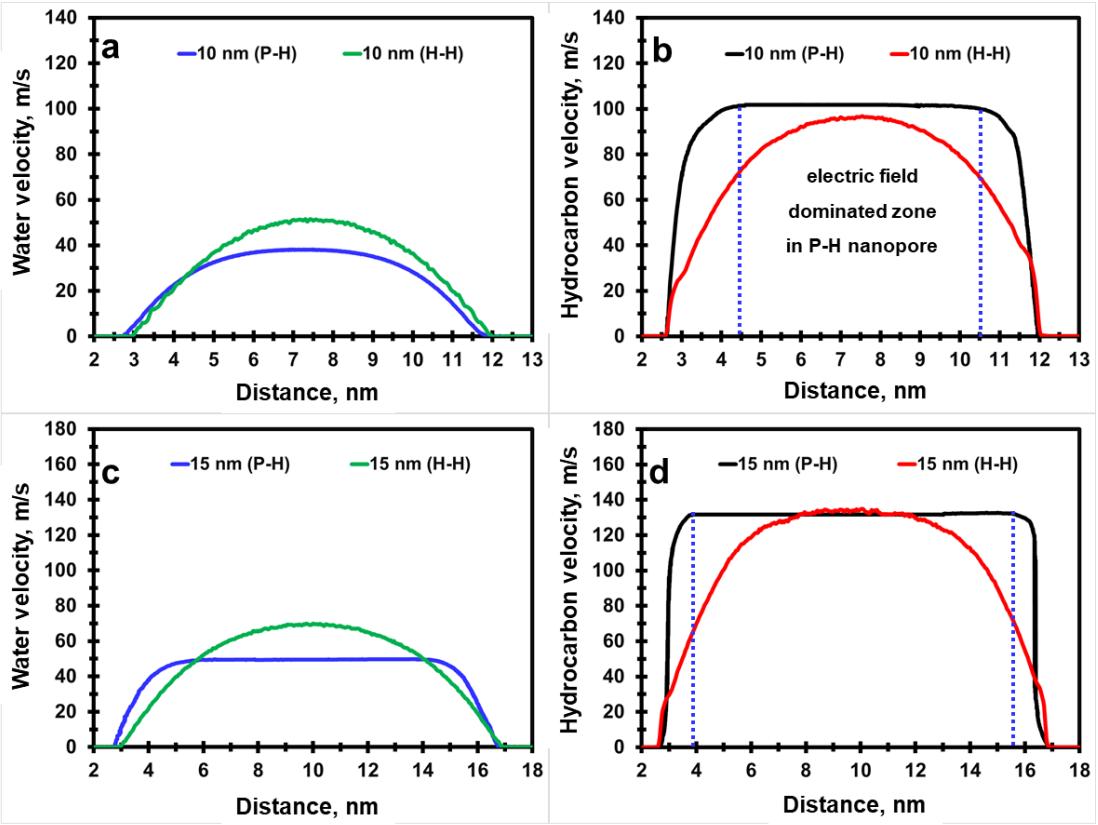

Figure 4-11 Comparison of single-phase (water and hydrocarbon) velocities between H-H and P-H nanopores of different widths. The self-generated electric field in P-H pores and the imposed acceleration dictate fluid transport in the center of the pore. For the same acceleration, the fluid velocity profile is flat in P-H pores and parabolic in H-H pores.

Figure 4-12 shows the distribution of water in 5 nm P-H and H-H pores. Hydrocarbon is not shown for clarity and water concentration is 80%. Figure 4-12a and Figure 4-12b are the EMD results for P-H and H-H nanopores respectively and Figure 4-12c and Figure 4-12d are the NEMD results for P-H and H-H nanopores respectively. During transport, water bridges persist in P-H pores as shown in Figure 4-12c. However, the water bridge of the H-H nanopore breaks down as shown in Figure 4-12d.

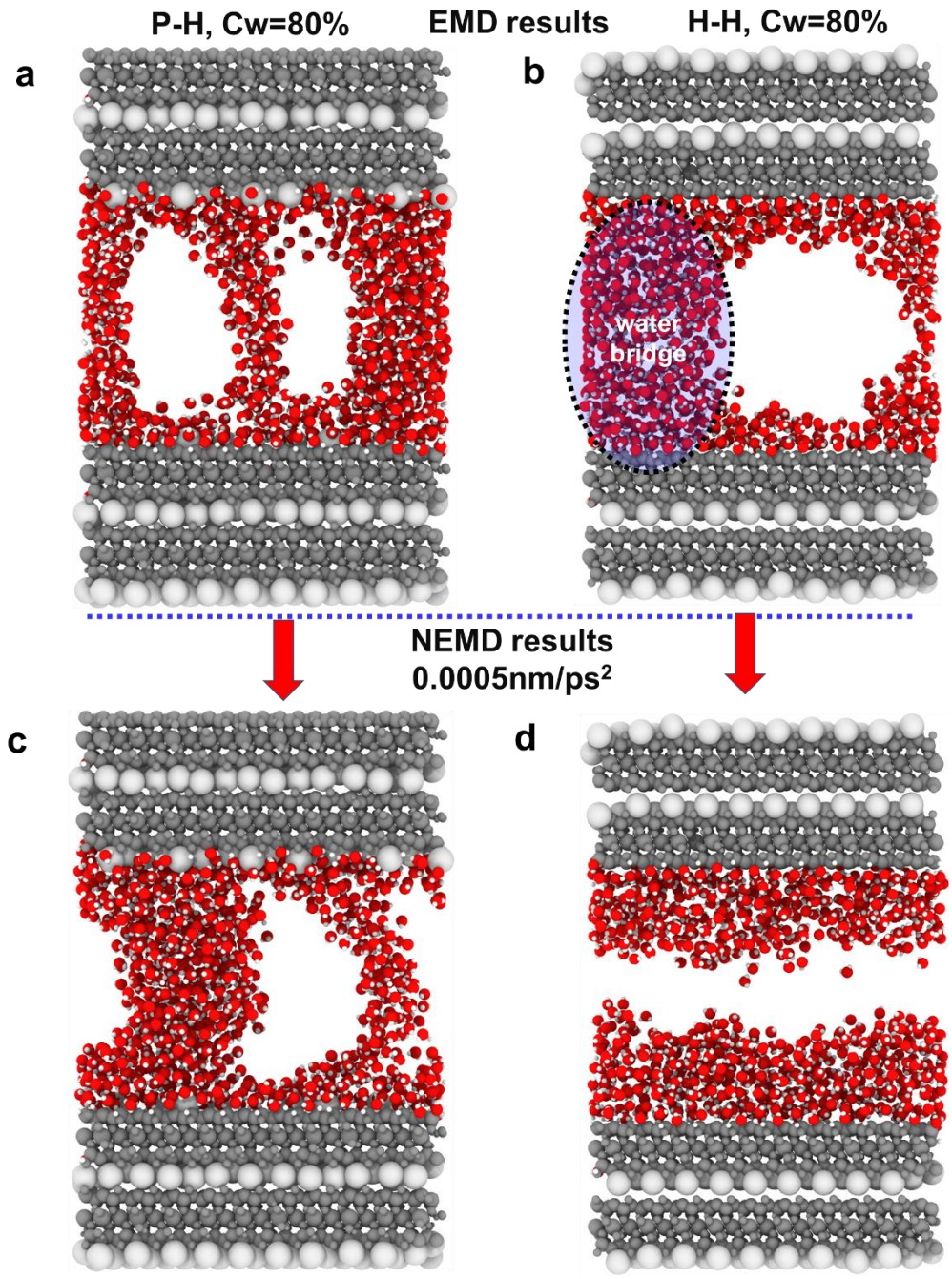

Figure 4-12 Water distribution in EMD and NEMD simulations in 5 nm P-H (left) and H-H (right) nanopore. Hydrocarbons are not presented for clearance. It indicates that the water bridge breaks down during flow in the NEMD simulation in the H-H nanopore, demonstrating that the strength of the hydrogen bond is weak to persist the water bridge. However, in the P-H nanopore, with the assistance of the electric field, the water bridge persists in NEMD simulations.

I will now discuss the observations of Figure 4-13 in the context of H-bonds. Figure 4-13a shows the definition of H-bond (Costa et al. 2005) while Figure 4-13

shows the number of H-bonds calculated from Figure 4-12a and Figure 4-12b. In an H-bond, the distance between 2 oxygen atoms is less than 3.6 Å, the distance between hydrogen (donor) and oxygen (acceptor) is less than 2.4 Å, and the angle between V_{OO} and V_{OH} is less than 30° where V_{OO} is the vector starting from the oxygen to another oxygen and V_{OH} is the vector from the oxygen to hydrogen. The total numbers of H-bonds in P-H and H-H nanopores are 148 and 77 respectively. In the P-H system, the local electric field promotes the occurrence of an H-bond which leads to the stability of the water bridge under an imposed acceleration.

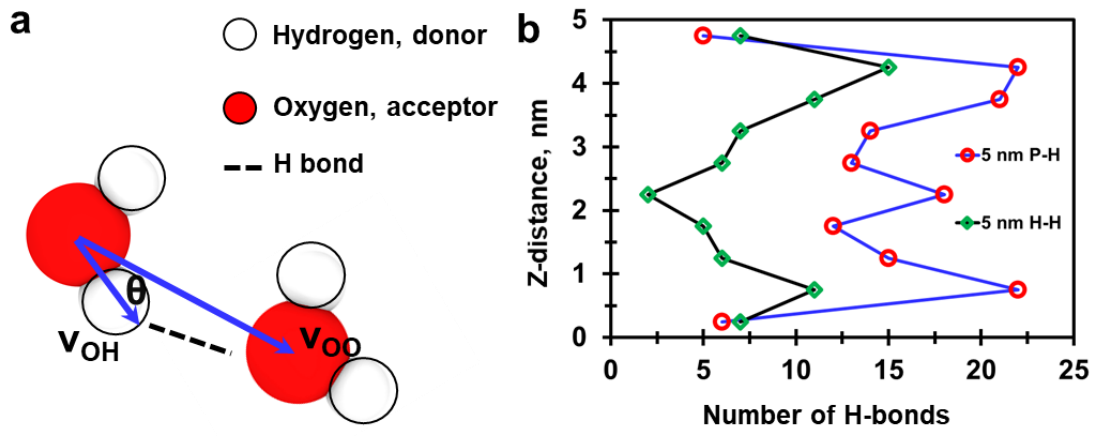

Figure 4-13 (a) Illustration of the H bond. An H bond(Costa et al. 2005) occurs when the distance between oxygen and oxygen is less than 3.6 Å, the distance between hydrogen (donor) and oxygen (acceptor) is less than 2.4 Å, and the angle between V_{OO} and V_{OH} is less than 30° where V_{OO} is the vector starting from the oxygen to another oxygen and V_{OH} is the vector from the oxygen to hydrogen. (b) the distribution of H bond from the bottom to the top pore surface in P-H and H-H systems.

4.5 Mass Transport

Over the past two chapters, I discuss differences between the behavior of fluids in P-H

and H-H nanopores. The differences are considerable in terms of the structure of water present in these systems. These differences also result in varying flow patterns that appear to influence mass transport through these different pores. In this section, I show that although the flow patterns are distinctly separate, the overall mass transport is not all that different.

I consider a pore size of 10 nm, water saturation of 71.43%, and acceleration of 0.002 nm/ps^2 as shown in Figure 4-6b and Figure 4-7. The velocity profile and flow area are used to characterize the mass transport. The calculated mass transports of water and oil in H-H nanopore are $\sim 8.9 \times 10^{-16}\, m^3/s$ and $13.2 \times 10^{-16}\, m^3/s$ respectively. For the P-H nanopore, they are $\sim 8.1 \times 10^{-16}\, m^3/s$ and $11.9 \times 10^{-16}\, m^3/s$ respectively. From the point of view of transport, the differences are less than 10%, although the storage modes and flow patterns are different. This calculation is essential to demonstrate that flow experiments will likely not be sensitive enough to detect these differences. Given the extremely narrow pore widths under consideration, it may also be impossible to visualize the different structures of water even with the most advanced forms of microscopy. This is also likely the reason for the absence of a discussion of water bridges in clays although the literature is rich with experimental observations of clay hydration.

4.6 Final Remarks

This chapter focuses on the use of Non-equilibrium MD (NEMD) simulations to

investigate hydrocarbon-water interactions, structure, and transport in clay-hosted nanopores with two different charged clay surface chemistries (H-H and P-H nanopores). With an imposed acceleration, the velocity profiles in H-H and P-H clay pores are different. Water preferentially flows adjacent to the pore surface for H-H pores with hydrocarbon occupying the center of the pore. With P-H pores, the water bridge persists under acceleration and a different velocity profile is observed irrespective of pore width.

As mentioned earlier, in H-H pores, water bridges can form under specific conditions but dissipate during flow. However, in P-H nanopores, the water bridges persist under flowing conditions.

Chapter 5 Fluids Behavior in Clay-Hosted Pores as Salinity Varies

5.1 Introduction

In Chapters 3 and 4, I focus on the behavior of pure water in clay pores. This chapter considers the effect of salinity on fluid behavior.

5.2 The Story So Far

As described earlier, Figure 5-1 recaps the findings of the previous chapters. Figure 5-1(A-B) shows illite structure from *xy* and *xz* projections, respectively. The slit pore is constructed with four parallel illite layers and two different illite-slit pore structures are constructed: potassium-hydroxyl (P-H) and hydroxyl-hydroxyl (H-H) to study the impacts of surface charge, as illustrated in Figure 5-1(C-D). Different pore widths and water concentrations (Cw) are considered. Dodecane is chosen to represent the oil phase. With no zwitterionic molecules in the hydrocarbon, they do not impact the charged clay surface (Underwood et al. 2015). Polar hydrocarbon components are outside the scope of the current study.

Figure 5-1(E-F) shows adsorbed water in H-H nanopore (Figure 5-1F) while at the same concentration, water bridges form in P-H nanopores (Figure 5-1E). Hydrocarbon is not shown for clarity in Figure 5-1 (E-F). The calculated electric fields across the whole nanopore in different pore widths are shown in Figure 5-1(G-H), occurring because of a charge imbalance in the P-H nanopore (Figure 5-1G) leading to the formation of a water bridge. The electric field in the H-H nanopore (Figure 5-1H)

weaker and most of the water is solely adsorbed.

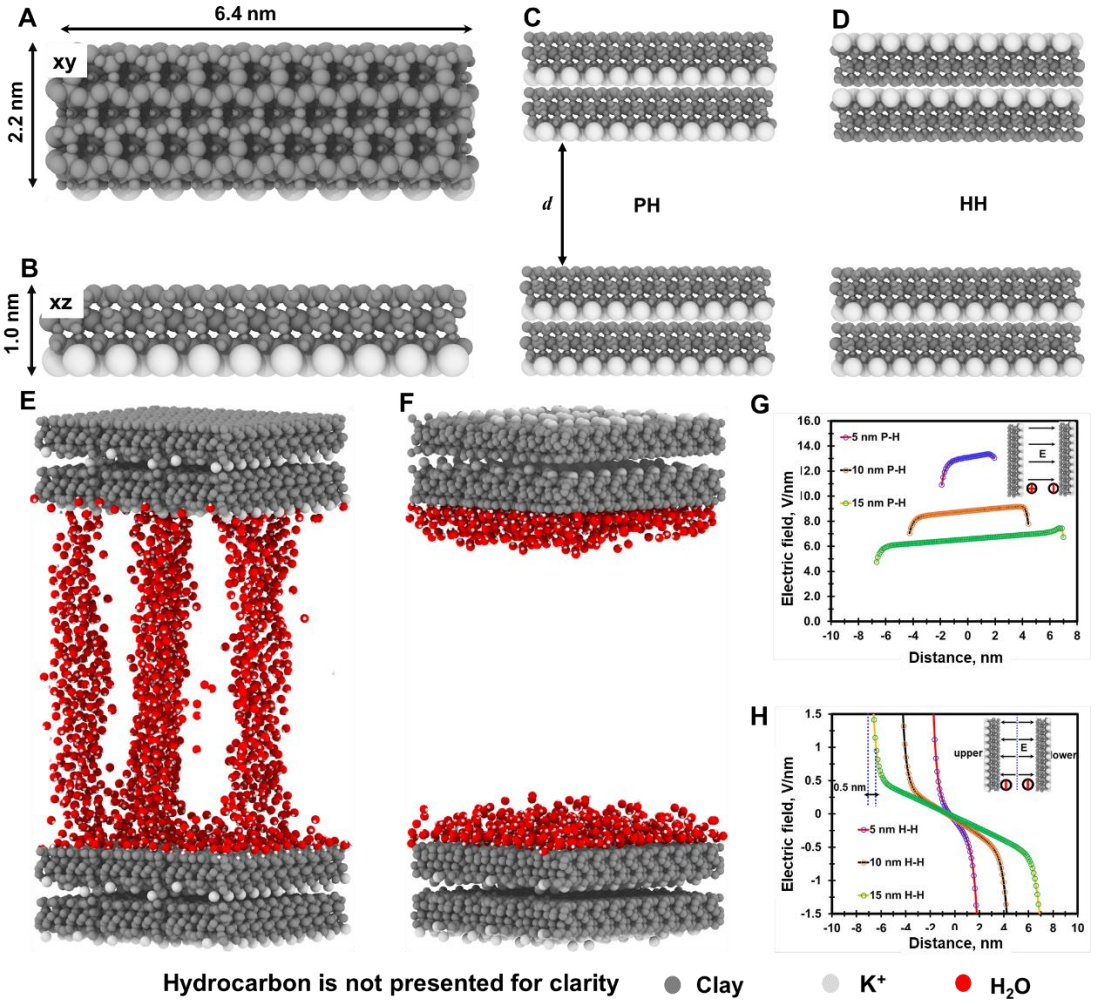

Figure 5-1 Previous works review (Xiong et al. 2020 and 2020b). (A-B) Illite structure from *xy* and *xz* projections. (C-D) Two different illite pore structures: P-H and H-H, where P-H and H-H represent the heterogeneous and homogeneous surface charges, respectively. (E) Water bridges in P-H nanopores. Hydrocarbon is not shown for clarity. (F) Adsorbed water in H-H nanopores. (G) Calculated electric fields across the whole P-H nanopore at different pore widths (5, 10, and 15 nm), where all the electric field strengths are larger than 1 V/nm, promoting the formation of a water bridge. (H) Weaker electric fields across the H-H nanopore lead to water existing as an adsorbed phase. Color codes: grey, clay; light grey, potassium (K^+); and red, water.

5.3 Simulation Models

In this chapter, I consider two different water concentrations (Cw, 38% and 70%), two

surface chemistries (P-H and H-H), two different pore widths (10 and 20 nm), and three different salinities of 3200, 37000, and 100,000 ppm representing low, middle and high salinities, respectively. The 24 models are shown in Table 5-1.

I only consider NaCl in my work and no other salts such as KCl or $CaCl_2$ or $CaCO_3$ because I can observe ion adsorption and the formation of electric double layers as reported in Moučka et al. (2017), Svoboda et al. (2018), Underwood et al. (2018) and Hamidian et al. (2019). Additionally, I am not investigating ion exchange capacity in clay minerals (Carroll et al. 1959).

I initially populate my models to achieve the target pressure and temperature using the Peng-Robinson EOS (Peng et al. 1976) with oil, water, and NaCl randomly placed in the clay pores via the Packmol package (Martínez et al. 2003). In the interests of brevity, I only show the initial configurations of P-H models with varying salinities at the pore width of 10 nm and water concentration of 70% in Figure 5-2.

Table 5-1 Description of simulation models used in this paper.

Model	Cw	Surface Chemistry	Pore Width, nm	ppm	Model	Cw	Surface Chemistry	Pore Width, nm	ppm
1	38%	PH	10	3200	13	38%	HH	10	3200
2	70%	PH	10	3200	14	70%	HH	10	3200
3	38%	PH	10	37000	15	38%	HH	10	37000
4	70%	PH	10	37000	16	70%	HH	10	37000
5	38%	PH	10	100000	17	38%	HH	10	100000
6	70%	PH	10	100000	18	70%	HH	10	100000
7	38%	PH	20	3200	19	38%	HH	20	3200
8	70%	PH	20	3200	20	70%	HH	20	3200
9	38%	PH	20	37000	21	38%	HH	20	37000
10	70%	PH	20	37000	22	70%	HH	20	37000
11	38%	PH	20	100000	23	38%	HH	20	100000
12	70%	PH	20	100000	24	70%	HH	20	100000

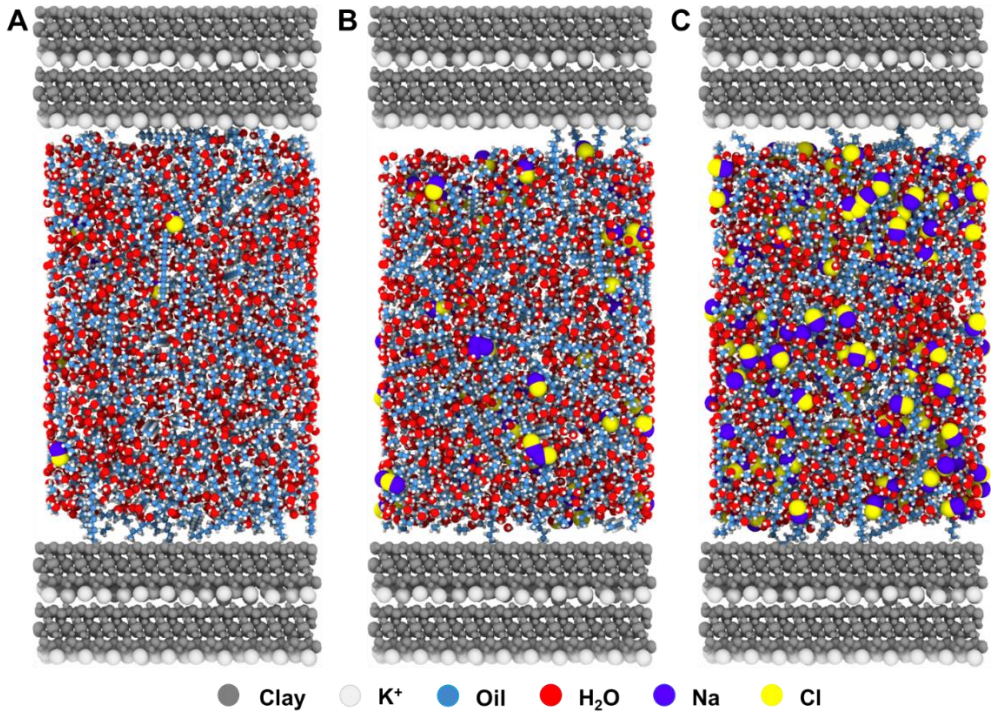

Figure 5-2 The initial configurations of the P-H models with varying salinities (pore width=10 nm, Cw= 70%). (A) 3200 ppm; (B) 37000 ppm; and (C) 100000 ppm. Color codes: grey, clay; light grey, potassium (K^+); red, water, light blue, oil; blue, Na^+; and yellow, Cl^-.

5.4 Molecular Simulations

5.4.1 Force Field Details

In this work, I use the CLAYFF force field (Cygan et al. 2004) to simulate clay minerals and NaCl. Water molecules are simulated using the rigid SPC/E force field (Berendsen et al. 1987) where the SHAKE algorithm (Ryckaert et al. 1977) is used to keep the water molecules rigid throughout the whole simulation. The parameters to describe the oil molecules are taken from OPLS-AA and updated values of torsional energy contribution to the total energy (Price et al. 2001) are used in my model. Lorentz-Berthelot mixing rules are used to compute the interactions between nonbonded atoms in clay mineral and NaCl (followed by the CLAYFF force field) and geometric mixing rules for all the other nonbonded interactions (Perez et al. 2020c).

5.4.2 Simulation Details

LAMMPS (Large-scale Atomic/Molecular Massively Parallel Simulator) (Plimpton et al. 1995) is applied to do the simulations. Periodic boundary conditions are used to produce a series of parallel clay nanopores that are kept rigid and forbids clay swelling due to adsorption/desorption/EDL (Sposito et al. 1999). Lennard-Jones (LJ) 12-6 term (Lennard-Jones et al. 1924) is used to describe the short-range interactions and the cutoff distance is 8 Å following the rule that cutoff distance cannot be larger than half of the minimum box size. Although a cutoff distance of 12 Å is usually used in the OPLS-AA force field, my previous works (Xiong et al. 2020) show that a cutoff

distance of 8 Å is valid. The particle-particle/particle-mesh (PPPM) method with a precision value of 10^{-6} (Eastwood et al. 1984) is adopted to estimate long-range electrostatic interactions.

I use the PR-EOS to determine an appropriate number of fluid molecules to achieve the target pressure (400 atm) and temperature (350K). Then simulations are carried out at 350K using a canonical NVT ensemble, where the temperature is controlled by the Nose Hoover thermostat (Nosé et al. 1984). First, a time step of 0.1 fs was used for 100ps, after which it is increased to 1 fs for 10 ns when the simulations reach equilibrium followed by another 10ns for data analyses. Snapshots of simulation trajectories are created using OVITO (Stukowski et al. 2010) and rendered with Tachyon (Stone et al. 1998).

5.5 Results and Discussion

5.5.1 Fluid Distribution

Figure 5-3 shows the equilibrated systems of fluid distribution in different salinities, water concentrations, and surface chemistries. The pore width is 10 nm and oil is not shown for clarity.

Figure 5-3 (A-C) illustrates the fluid distribution at a water concentration of 38% in P-H nanopore with different salinities. It shows that at a salinity of 3200 ppm (Figure 5-3A), the formation of a water bridge is observed that spans the pore width and connects the upper and lower pore surfaces. However, as I increase the salinity to 37000 ppm and 100000 ppm (Figure 5-3B-C), the water bridge disappears and ionic

aggregates form at the salinity of 100000 ppm, highlighted by a circle (Figure 5-3C).

I hypothesize that the adsorption of Na^+ and Cl^- ions onto the clay surface will influence the clay surface charge, modifying the electric field, leading to the breakage of the water bridge. To confirm this, I employ a test atom with charge *e* in the clay nanopore and measure the electrostatic force on this atom from one surface of the pore to the other to measure the electric field. I perform this exercise with only the Na^+ and Cl^- ions and no fluid molecules (Hao et al. 2019b). The calculated electric fields at the pore center for different salinity values (3200, 37000, and 100000 ppm) are 4.58, 0.53, and 0.51 V/nm, respectively. At a salinity of 0 ppm, Chapter 3 showed the electric field strength to be 8.84 V/nm. Salinity, therefore, influences the local electric field through the adsorption of the Na^+ and Cl^- ions. As reported in Skinner et al.(2012), Cramer et al.(2008), Hao et al.(2019a), Zhang et al.(2019), Namin et al.(2013), Fuchs et al. (2007 and 2008), Ponterio et al. (2010), and Chen et al. (2016), an electric field strength larger than 1 V/nm can change the structure of water and at 3200 ppm, at 4.58 V/nm we observe a water bridge (Figure 5-3A). However, at the salinity of 37000 and 100000 ppm (Figure 5-3B and Figure 5-3C), both the electric fields are lower than 1 V/nm and a water bridge is absent.

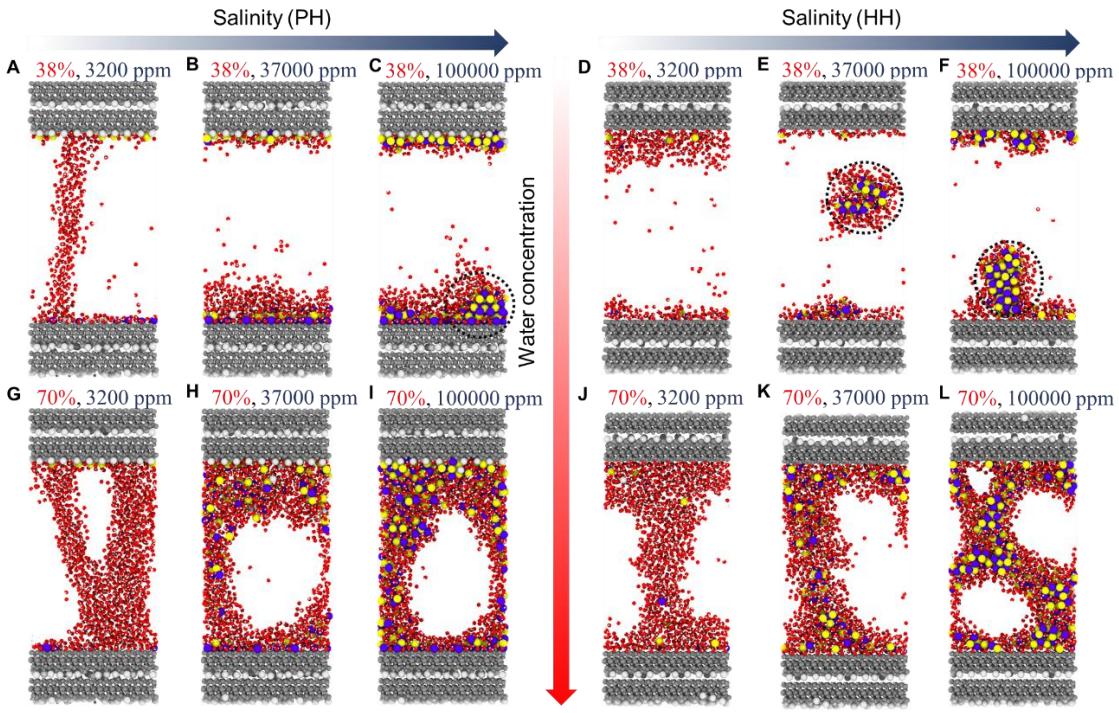

Figure 5-3 Fluid distribution in different salinities, water concentrations, and surface chemistries. The pore width is 10 nm and Oil is not shown for clarity. (A-C) Fluid distribution at a water concentration of 38% in P-H nanopore with different salinities. (D-F) Fluid distribution at a water concentration of 38% in H-H nanopore with different salinities. (G-I) Fluid distribution at a water concentration of 70% in P-H nanopore with different salinities. (J-L) Fluid distribution at a water concentration of 70% in H-H nanopore with different salinities. Color codes are the same as in Figure 5-2.

Figure 5-3 (D to F) presents the fluid distribution at a water concentration of 38% in H-H nanopore with different salinities. Unsurprisingly, as reported in previous chapters, there are no water bridges. Instead, at 37000 ppm and 100000 ppm salinity (Figure 5-3E and Figure 5-3F), ionic aggregates are also observed, shown in the circles. In P-H pores, Na^+ and Cl^- ions are largely adsorbed as shown in Figure 5-3B and Figure 5-3C, however in H-H pores as seen in Figure 5-3E and Figure 5-3F, they form clusters and are partially adsorbed. This is largely because of the presence of an electric field and not due to the occurrence of rare events during the MD sampling process (Noé et al. 2018). I confirm this by running another six independent systems with different

initial velocity distributions and arrive at the same conclusion.

Figure 5-3 (G to I) and Figure 5-3 (J to L) present the fluid distribution at a water concentration of 70% in P-H and H-H nanopores with different salinities, respectively. We can see that the formation of water bridges is observed irrespective of salinity and surface chemistry. The reason is that the formation mechanism of a water bridge is mainly dependent on three factors (pore width, surface chemistry, and water concentration), reported in Chapter 3 (Xiong et al. 2020b). In this work, high water concentration (70%) makes water continuous phase with suspended oil droplets. This observation of water bridge at high water concentration is also consistent with Yamashita's et. al. (2013 and 2015) and Ho's et al.(2015) works.

Although Figure 5-3 (G to I, for P-H pores) and Figure 5-3 (J to L, for H-H pores) appear similar, there are differences in the occurrence of H-bonds. The orientation and number of hydrogen bonds at a water saturation of 70% and salinity of 3200 ppm are shown in Figure 5-4A and Figure 5-4B, respectively. The H-bond has been described in Chapter 4.

Figure 5-4A indicates that in a small electric field, the orientation of water molecules is randomly distributed as shown by the Gaussian distribution of orientation for water shown in blue, which is consistent with Cramer et al.(2008) and Hao et al.(2019b). However, in a stronger electric field (black), the orientation of water molecules aligns with the direction of the electric field (at 130°) to produce a phenomenon called orientational polarizability (Harder et al. 2005). Figure 5-4B is the

calculated number of H-bonds from the bottom to the top surface at the pore width of 10 nm, demonstrating that the strong electric field in the P-H system increases the number of H-bonds (191) compared to the H-H system (119). This finding is important because the high number of H-bonds in the P-H system will enhance the strength of water bridges, thus needing more energy to break them (refer to Figure 4-12 in Chapter 4). Therefore, increasing the salinity to decrease the electric field in the P-H nanopore is a good way to impair the formation of H-bonds (or water bridge) and to improve fluid mobility.

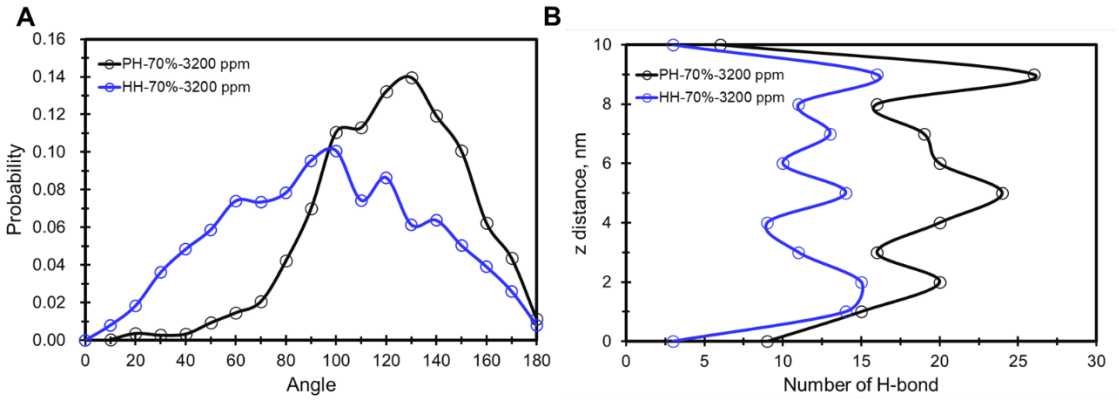

Figure 5-4 Water orientation and hydrogen bond. (A) Calculated possible orientation in P-H and H-H nanopores, data from Figure 5-3G and J. (B) Calculated number of H-bonds from the bottom to the top surface at the pore width of 10 nm. The H-bond has been described in Chapter 4.

The equilibrated systems of fluid distribution at the pore width of 20 nm as shown in Figure 5-5 are similar to that in a 10nm pore (Figure 5-3). At 3200 ppm, we still observe the presence of water (Figure 5-5A) while at higher salinities Na^+ and Cl^- form ionic aggregates in the pore center.

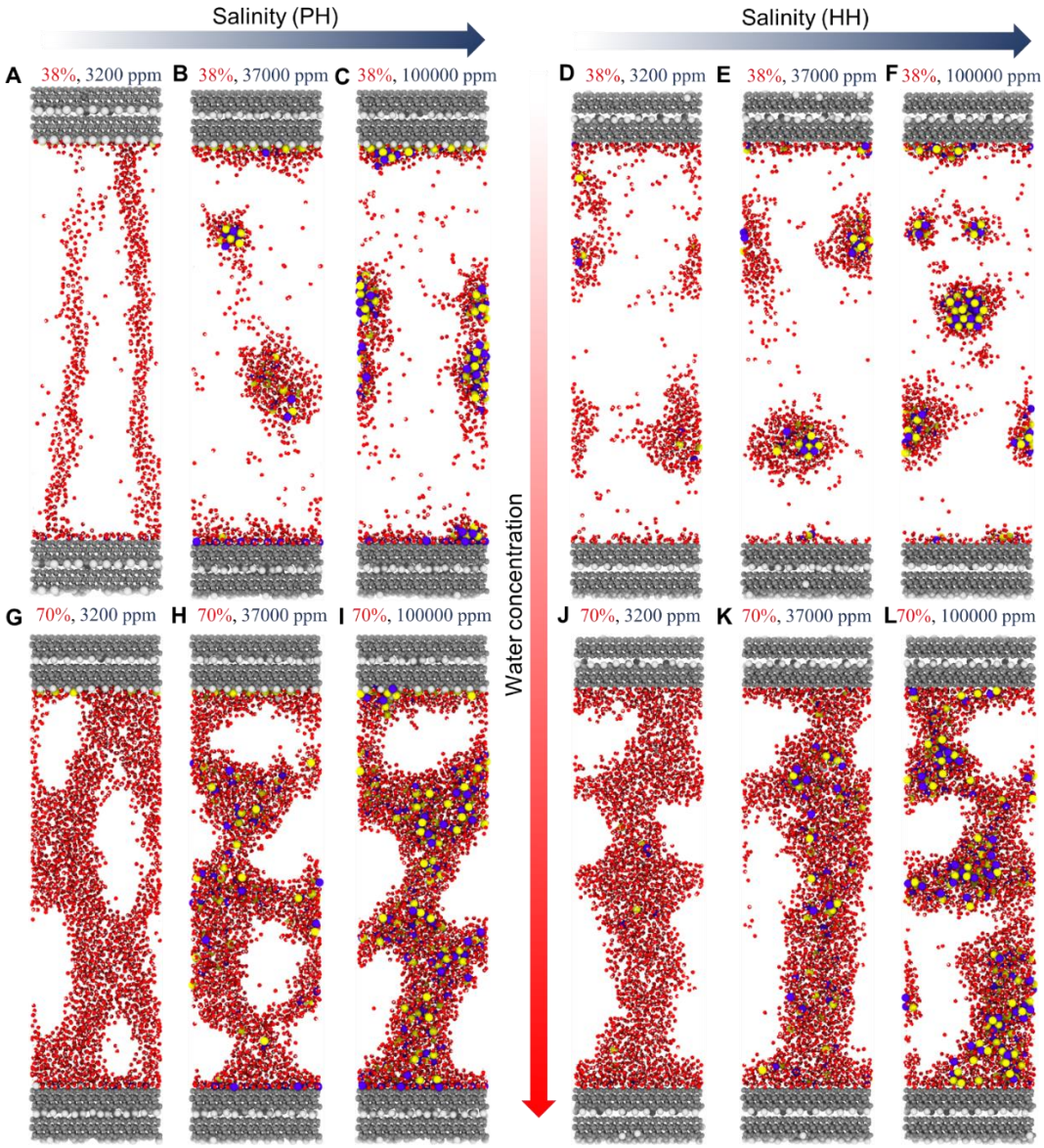

Figure 5-5 Fluid distribution in different salinities, water concentrations, and surface chemistries. The pore width is 20 nm and Oil is not shown for clarity. (A-C) Fluid distribution at a water concentration of 38% in P-H nanopore with different salinities. (D-F) Fluid distribution at a water concentration of 38% in H-H nanopore with different salinities. (G-I) Fluid distribution at a water concentration of 70% in P-H nanopore with different salinities. (J-L) Fluid distribution at a water concentration of 70% in H-H nanopore with different salinities. Color codes same as Figure 5-2.

5.5.2 Salinity Effect

At this point, my results show that high salinity values disrupt the formation of water bridges and high salinities lead to the formation of ionic aggregates. To establish a

complete understanding of the salinity effect, I construct another 8 with intermediate values of salinity as shown in Table 5-2.

Table 5-2 Description of additional eight models

Model	Cw	Surface Chemistry	Pore Width, nm	ppm	Model	Cw	Surface Chemistry	Pore Width, nm	ppm
1	38%	PH	10	8100	5	38%	PH	20	8100
2	38%	PH	10	12400	6	38%	PH	20	12400
3	38%	PH	10	16000	7	38%	PH	20	16000
4	38%	PH	10	27000	8	38%	PH	20	27000

Figure 5-6 shows the equilibrated systems of fluid distribution in different salinities. Pore width is 10 nm, water concentration is 38%, and oil is not shown for clarity. Figure 5-6A indicates at the salinity of 8100 ppm; the formation of the water bridge is still observed. However, when the salinity is higher than or equal to 12400 ppm (Figure 5-6B to Figure 5-6D), there are no water bridges. The calculated electric fields at the salinity of 8100, 12400, 16000, and 27000 ppm are 1.06, 0.56, 0.54, and 0.55 V/nm respectively. The threshold value of salinity that disrupts the formation of a water bridge is between 8100 and 12400 ppm. Figure 5-6D shows ionic aggregate at the salinity of 27000 ppm.

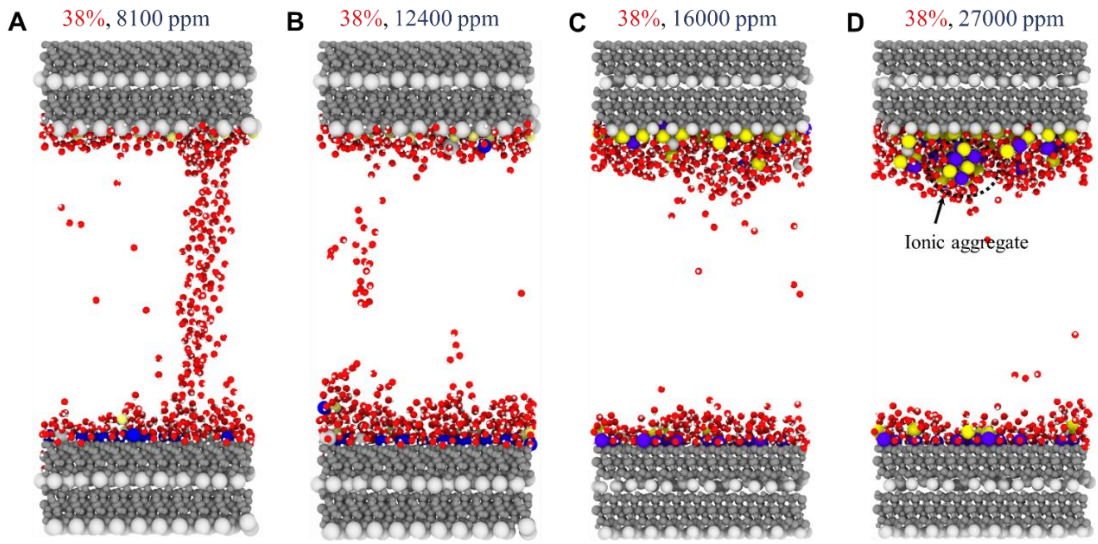

Figure 5-6 Fluid distribution in different salinities. Pore width is 10 nm, water saturation is 38%, surface chemistry is P-H and oil is not shown for clarity. (A) 8100 ppm; (B) 12400 ppm; (C) 16000 ppm; (D) 27000 ppm. The threshold value of salinity is between 8100 and 12400 ppm. In this model, the threshold value is about 8500 ppm, provided in the Supporting Information. Color codes same as Figure 5-2.

The equilibrated systems of fluid distribution at the pore width of 20 nm are shown in Figure 5-7. With an increased pore width, the calculated electric fields at the salinities of 8100, 12400, 16000, and 27000 are 0.52, 0.27, 0.26, and 0.23 V/nm, respectively and the water bridge is absent.

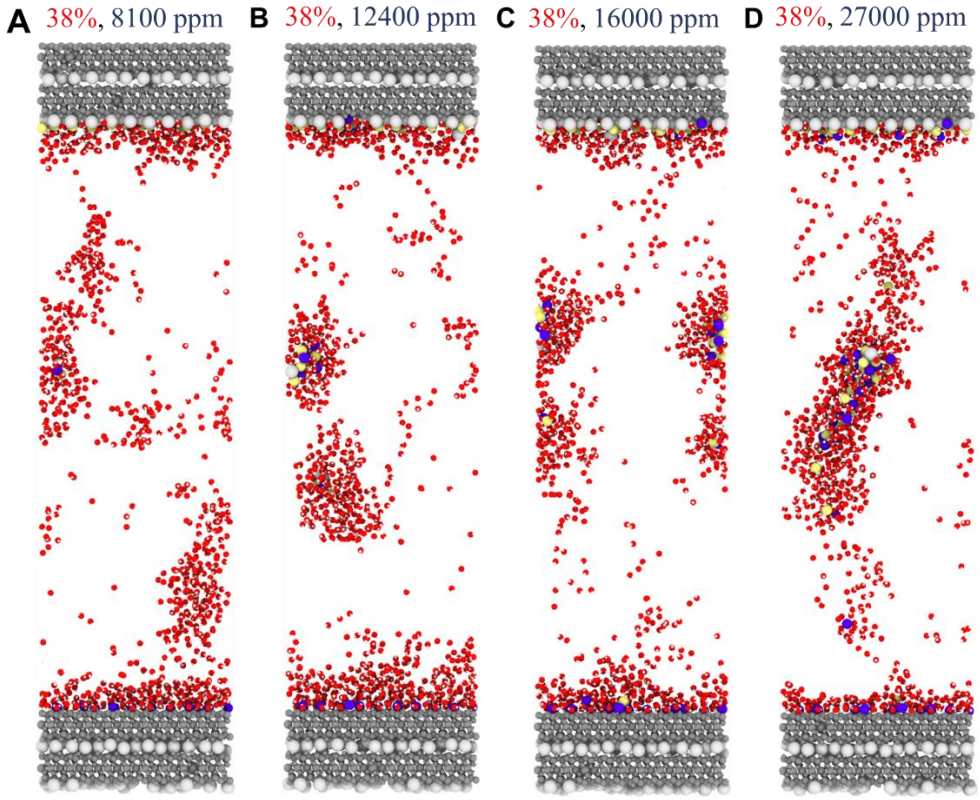

Figure 5-7 Fluid distribution in different salinities. Pore width is 20 nm, water saturation is 38%, surface chemistry is P-H and oil is not shown for clarity. (A) 8100 ppm; (B) 12400 ppm; (C) 16000 ppm; (D) 27000 ppm. Color codes same as Figure 5-2.

5.5.3 Surface Electric Potential

In this section, I explain the effect of salinity using the concept of surface electric potential.

The distribution of surface electric potential ψ as the function of distance (x, y, z) is given by the Poisson equation (Kappl et al. 2003). Here, I only consider the distribution of surface electric potential in the z-direction, which is calculated from Gouy-Chapman's theory (Kappl et al. 2003) in Equation (5-1).

$$\psi(z) = \frac{2k_BT}{e} ln\left(\frac{1+\alpha(\psi_0)\mathrm{e}^{-\kappa z}}{1-\alpha(\psi_0)\mathrm{e}^{-\kappa z}}\right) \quad (5\text{-}1)$$

Where $\psi(z)$ is the distribution of surface electric potential in the z-direction, k_B is

the Boltzmann constant in J/K, T is the temperature in K, e is the charge of the electron, $\alpha = tanh\,(\frac{e\psi_0}{4k_BT})$ with ψ_0 where the surface electric potential is at z=0. κ is the inverse of the decay length λ_D (Leike et al. 2002). and can be expressed as Equation (5-2):

$$\kappa = {\lambda_D}^{-1} = \sqrt{\frac{2c_0e^2}{\varepsilon\varepsilon_0k_BT}} \qquad (5\text{-}2)$$

Where c_0 is the bulk ion concentration in 1/m^3; ε and ε_0 are the permittivity of water and vacuum in c^2/ (J m) that can be obtained from Malmberg's et. al. work (Malmberg et al. 1956).

Therefore, the only unknown parameter in Equation (5-1) is the surface electric potential, ψ_0. The Grahame equation (Kappl et al. 2003) provides the relationship between surface charge density ($\sigma\ in\frac{C}{m^2}$) and surface electric potential ($\psi_0\ in\ mv$), expressed in Equation (5-3):

$$\sigma = \sqrt{8c_0\varepsilon\varepsilon_0k_BT}\cdot sinh\,(\frac{e\psi_0}{2k_BT}) \qquad (5\text{-}3)$$

The surface charge densities (σ) for the lower and upper surfaces are directly calculated from MD simulations (Figure 3-15) The average charge densities on the upper and lower surfaces are 0.97 c/m^2 and -4.02 c/m^2.Table 5-3 summarizes the main parameters to calculate the distribution of surface electric potential in the z-direction.

Table 5-3 Calculated decay length, surface charge density, and surface potential with different salinities, valid for both 10 and 20 nm models.

Salinity, ppm	Decay (Debye) length, λ_D (A)	Ƙ, (1/A)	Partial charge density, σ(c/m2)	Surface potential, ψ_0 (mV)	α
Upper surface					
3200	12.43	0.08	0.97	256.15	0.9718
8100	7.86	0.13	0.97	228.54	0.9557
12400	6.35	0.16	0.97	215.66	0.9455
Lower surface					
3200	12.43	0.08	-4.02	-344.58	-0.9934
8100	7.86	0.13	-4.02	-316.95	-0.9896
12400	6.35	0.16	-4.02	-304.05	-0.9871

Figure 5-8 shows the calculated surface potential in z-direction using Equation (5-1) with the parameters listed in Table 5-3. From Figure 5-8A at the salinity of 3200ppm, the surface potentials of both upper and lower surfaces have non-zero values at the pore center (black dash line) thereby promoting the formation of a water-bridge.

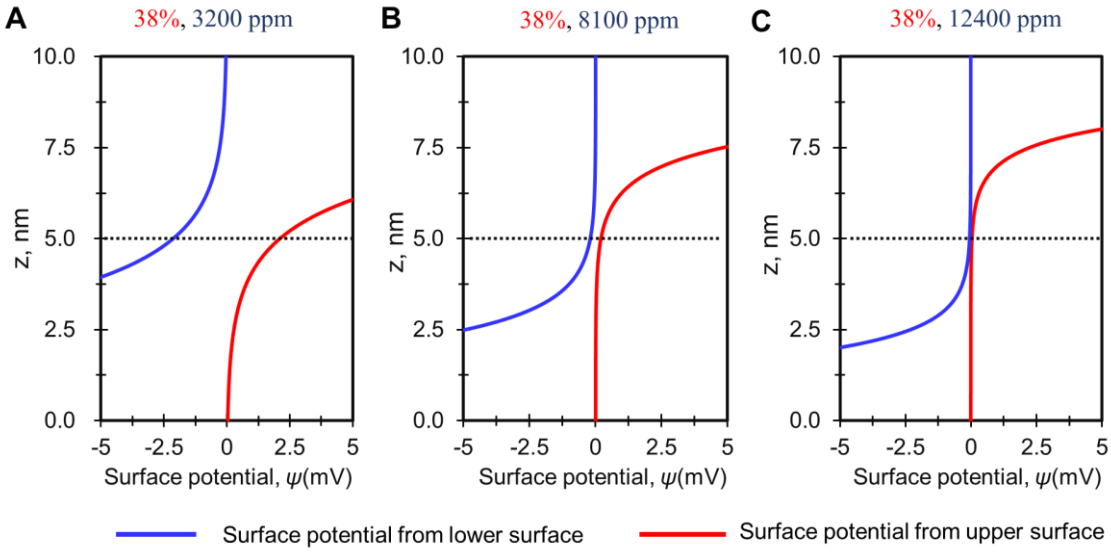

Figure 5-8 Calculated surface electric potentials in the z-direction. The pore width is 10 nm and the water concentration is 38%. The blue and orange curves are the surface potential of upper and lower surfaces, respectively. (A) 3200 ppm; (B) 8100 ppm; (C) 12400 ppm. The results indicate that the water-bridge phenomenon is attributed to the overlapping non-zero potentials from both surfaces. Increasing the salinity decreases the strength of surface potentials at the pore center to values close to zero.

When the salinity increases to 8100ppm, the decay length decreases to 7.86 Å (Table 5-3) and the potentials drop to a small, non-zero value at the pore center (Figure 5-8B). Both pore surfaces continue to exert an influence on the behavior of water at the pore center but with a reduction in magnitude leading to a water bridge with a lower thickness as shown in Figure 5-9.

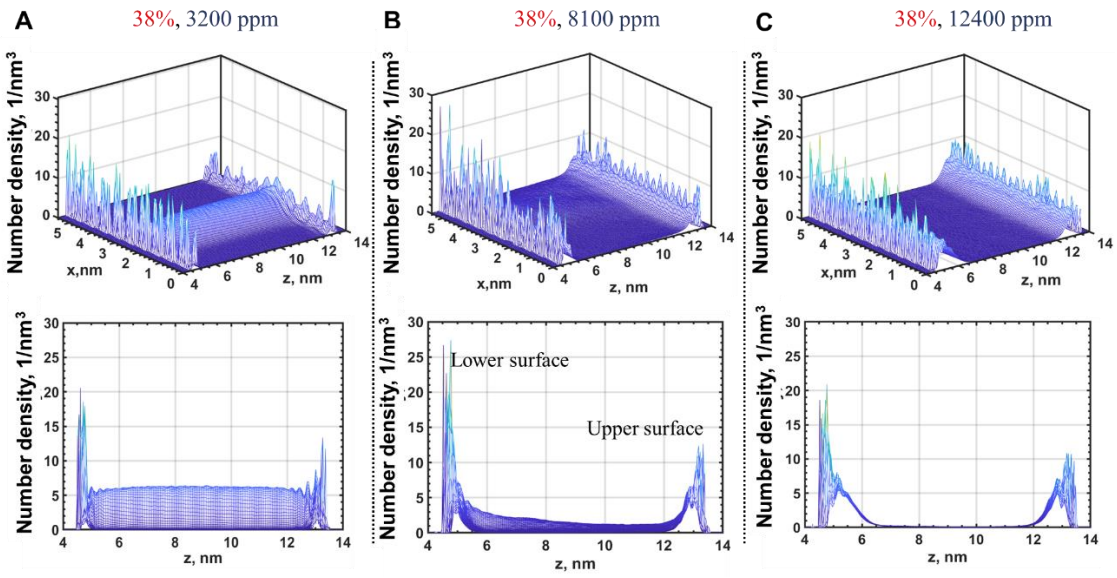

Figure 5-9 Water number density profiles for different salinities in 10 nm nanopores in the x-z plane (top panels) and along the z-axis (bottom panels). (A-B) Water bridges are observed; (C) A number density of zero indicates the absence of a water bridge. It indicates that water molecules are more inclined to be adsorbed on the lower surface than on the upper surface given the configuration used in my models with K^+ ions on the lower surface. This is expected given that hydroxyl groups and oxygen atoms on the top surface have larger van der Waals forces than potassium on the lower surface. Meanwhile, increasing the salinity will decrease the thickness of the water bridge (see panels A to B).

At the salinity of 12400ppm (Figure 5-8C), the high salinity leads to a further decrease of decay length (6.35 Å) and both surface potentials are zero at the pore center leading to the absence of a water bridge (Figure 5-8B).

5.6 Further Discussion

Given the results of the previous discussion, we can expect that the presence of water bridges at low salinities and ionic aggregates at high salinities might impede fluid flow. To verify this hypothesis, I calculate the self-diffusion coefficients of oil and water in the 10 and 20 nm P-H pores across all salinity ranges using the concept of MSD (mean square displacement), and the result is shown in Figure 5-10 and Figure 5-11. The procedure follows the discussion provided in Chapter 2 in section 2.4.3. The calculated self-diffusion at the pore width of 20 nm shows trends similar to the 10 nm pore (Figure 5-10). Intuitively, increasing the pore width increases the self-diffusion coefficients

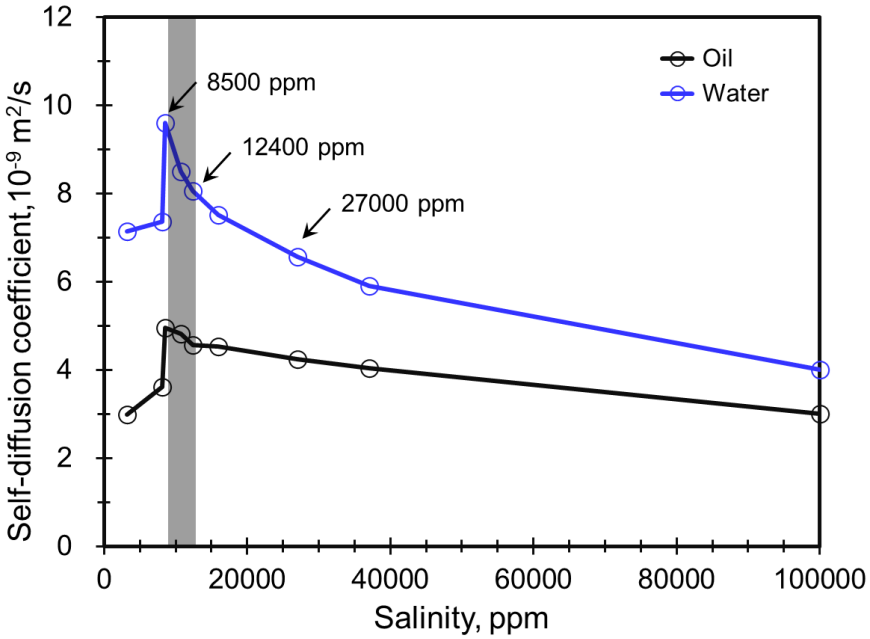

Figure 5-10 Calculated self-diffusion coefficients in nine models with different salinities in the 10nm pores. When the salinity is below 8500ppm, the presence of a water bridge impedes fluid flow. However, when the salinity is higher than 12400ppm, the formation of ionic aggregates is the primary factor to impede flow. Therefore, there exists an optimal range of salinity (8500-12400ppm, grey region) where the mobility of oil and water is the highest in clay pores.

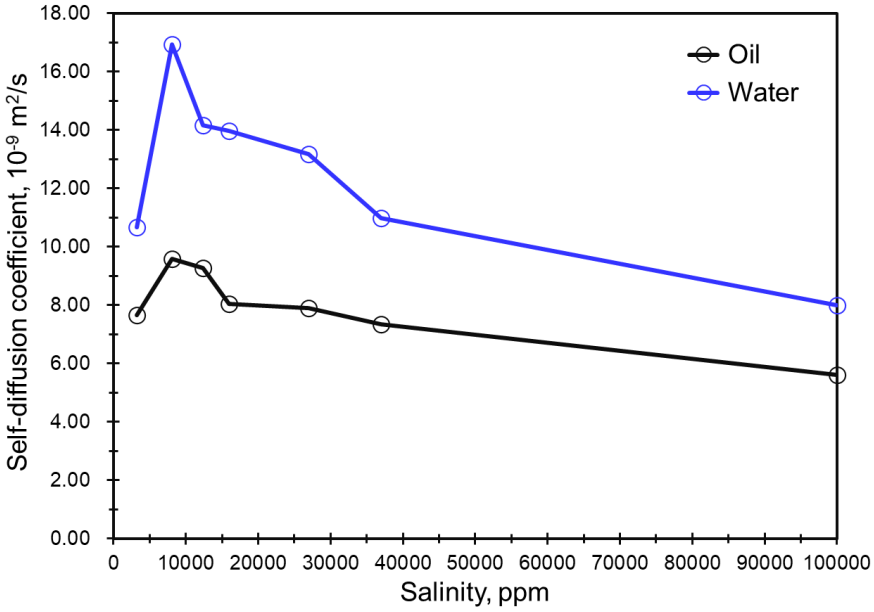

Figure 5-11 Calculated self-diffusion coefficients in seven models with different salinities in the 20nm pores.

Figure 5-10 shows that initially increasing the salinity will increase the fluid self-diffusion. However, once it increases to a certain point (8500 ppm), further increases in salinity lead to moderate decreases in fluid self-diffusion. Denney et al (2009) also report that an initial increase in salinity promotes oil recovery with a subsequent decrease for further increases in salinity. Morrow et al. (2011) also report that high salinity reduces recovery for waterflooding.

If the water salinity is too low (below 8500ppm in this section), water bridges can form (see Figure 5-3A and Figure 5-6A) and lead to low oil/water diffusion coefficients hampering the transport of both water and oil. If the salinity is too high, Na^+ and Cl^- ions adsorb on the clay surface due to the charge screening effect, and the excessed unabsorbed Na^+ and Cl^- ions appear as aggregates (see Figure 5-3C and Figure 5-6D),

which also impede the fluid flow. Therefore, the optimal salinity value should create a condition where both ionic aggregates and water bridges are largely absent. It should be noted the optimal salinity value is likely to be a function of pore size and my results should be considered as valid strictly only for the pore width of 10 and 20 nm considered in this work.

Although different pore widths and water concentrations can influence the optimal range of salinity, we can generalize my findings to hypothesize that if the salinity of formation water is extremely high such as 100,000 ppm, we can inject low salinity fluid to lower the formation salinity to more optimal ranges to disrupt the formation of ionic aggregates. On the other hand, in the hypothetical situation where the formation water is extremely fresh, injection of a moderately saline brine may perhaps not compromise productivity as it disrupts the formation of water bridges. An analogous argument can be made for adjusting the salinity of waterflooding in response to the formation of water salinity.

5.7 Final Remarks

This chapter extends my understanding of the effect of salinity variations on fluid distribution and its impact on oil transport in clay pores and demonstrates that there exists an optimal range of salinity that promotes oil recovery. The main conclusions are listed as follows:

1. Salinity shows a dramatic impact on the distribution of water molecules.

a. At low salinities, a water bridge exists within the clay pores. Increasing the salinity reduces the thickness of the water bridge until it finally disappears. Water then exists mostly in the adsorbed phase.
b. Further increasing the salinity (> 124000ppm) leads to ionic aggregates that impede oil recovery moderately.

2. An optimal range of salinity for low salinity waterflooding corresponds to the absence of ionic aggregates or ion hydration shells and the prevalence of adsorbed water over water bridging. Under these conditions, the mobility of the oil phase is the highest.
3. The water-bridge phenomenon occurs because of the local electric field and surface potentials in clay nanopores. Increasing the salinity weakens the strength of the electric field due to the charge screening effect of the counterions, leading to a decrease of surface potentials in the interior region of the pore.

Chapter 6 The Behavior of Surfactant Microemulsions in Clay-hosted Nanopores

6.1 Introduction

The successful use of microemulsions during hydraulic fracturing and subsequent shut-in periods in enhancing oil production from shale reservoirs is documented in numerous studies (Champagne et al. 2011; Penny et al. 2012). But the mechanisms describing the process for improved oil recovery using microemulsions are still not fully understood.

Recently, Bui et al. (2016) investigate improved recovery using microemulsions in an ideal graphene slit pore using molecular dynamics. They conclude that the surfactants (carried by microemulsions) act as a linker between oil and water surface reducing the slippage of water at the oil/water interface, and finally dragging oil with the aqueous phase. Meanwhile, the solvents (carried by microemulsions) dissolve into the oil and modify its rheological properties. Later, Bui et al. (2017) demonstrate that the penetration of microemulsions in shale nanopores depends on the pore surface and size. When the pore width is less than 4.5 nm, a microemulsion with a diameter of 6.5 nm is shown to be unable to enter the pore. However, when the pore width is 5.4 nm, deformation of the microemulsion allows penetration as shown in Figure 6-1. Most recently, Bui et al. (2019) use realistic kerogen models with different pore widths (4.3 nm- 6.9 nm) demonstrating that the effectiveness of microemulsions on oil recovery highly dependent on pore width. When the largest pore width is less than 4.3 nm, the microemulsion simply adsorbs on the pore surface with little penetration. However. with a pore width of ~6.5 nm, a 22.6% increase in oil recovery is observed.

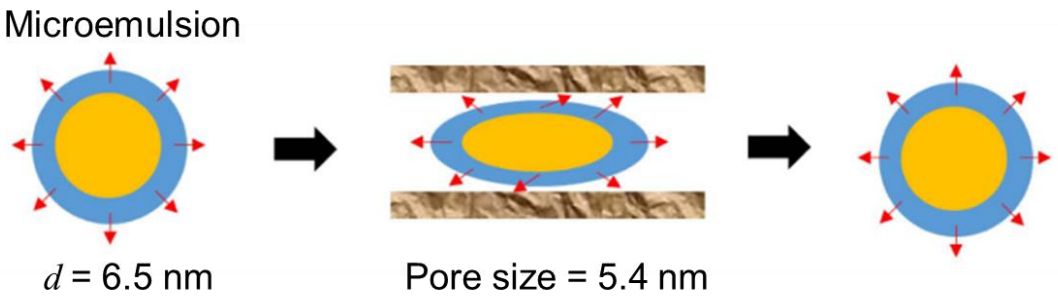

Figure 6-1 Schematic illustration showing how the microemulsion droplet can squeeze itself through the nanopore and recover its original structure (Bui et al. 2017).

Although these three papers reveal important aspects of microemulsion behavior in shales, the question of whether these microemulsions can penetrate deeper into the formation remains unanswered. For deeper infiltration, the microemulsion will have to traverse both organic and inorganic pore networks. Given that clay minerals account for more than 50% of the volume in shale reservoirs (Yang et al. 2016), it is essential to understand the behavior (stability) of microemulsions in clay-hosted pores and the answers to this question forms the basis of the current chapter.

6.2 Computational Methodology

6.2.1 Force Field Details

I use LAMMPS (Large-scale Atomic/Molecular Massively Parallel Simulator) (Plimpton et al. 1995) with periodic boundary conditions in all simulations. Following Bui et al. (2017 and 2019), the microemulsion comprises molecular models of d-limonene (solvent, Figure 6-2a) and dodecanol heptaethyl ether ($C_{12}E_7$, nonionic surfactant, Figure 6-2b). The molecule of $C_{12}E_7$ contains one hydrophobic tail of 12 alkyl groups and one hydrophilic head of seven ethylene oxide groups and one terminal

hydroxyl group. I use the OPLS-AA force field to describe d-limonene and $C_{12}E_7$ following a similar process as described in Section 5.4.1. I also use the SPC/E force field (Berendsen et al. 1987) to simulate water molecules where the SHAKE algorithm (Ryckaert et al. 1977) is used to keep the water molecules rigid throughout the whole simulation.

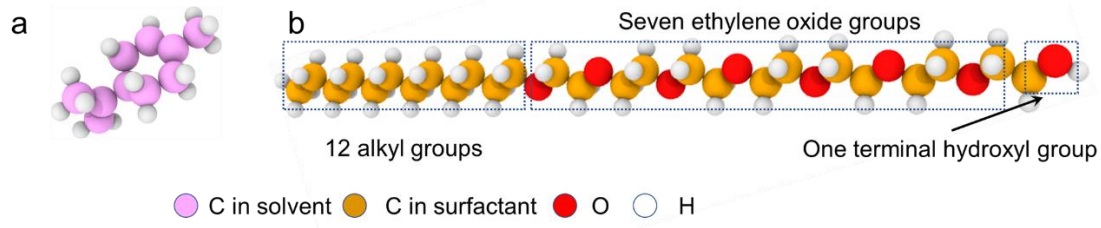

Figure 6-2 Schematic configuration of d-limonene (a) and $C_{12}E_7$ (b). Color code: pink, carbon in solvent; brown, carbon in surfactant; red, oxygen; and white, hydrogen.

I use the clay structure (illite) described in earlier chapters with the ClayFF force field (Cygan et al. 2004) to describe the interatomic interactions for the clay structure and the cations. I also use the Lennard-Jones (LJ) 12-6 term (Lennard-Jones et al. 1924) to describe the short-range interactions with a cutoff distance of 15 Å and the particle-particle/particle-mesh (PPPM) method with a precision value of 10^{-6} (Eastwood et al. 1984) to estimate long-range electrostatic interactions. I also use Lorentz-Berthelot mixing rules to compute the interactions between nonbonded atoms in clay minerals (followed by the CLAYFF force field) and geometric mixing rules for all the other nonbonded interactions (Perez et al. 2020c).

6.2.2 Construction of Microemulsion with Varying Salinities in Bulk Conditions

Initially, water, solvent, and surfactant are randomly distributed in a cubic box with a length of 50 nm using Packmol package (Martínez et al. 2003), as shown in Figure 6-3a. The number of water (in red), solvent (in pink), and surfactant (in brown) molecules are 42000, 86, and 55 respectively following Bui's et al. (2018) work. It should be noted that to distinguish solvent and surfactant easily, the oxygen atoms in surfactant are also colored brown in the remainder of this chapter. I run the equilibrium MD (EMD) simulations using an NPT ensemble to obtain a stable microemulsion. Temperature and pressure are maintained at 400 atm (5878 psi) and 380 K (224 °F) using Parrinello-Rahman barostat (Parrinello et al. 1981) and Nose Hoover thermostat (Nosé et al. 1984) respectively.

Figure 6-3b shows the equilibrium configuration of the simulation box containing a stable microemulsion droplet where the total simulation time is 50 ns. The length of the simulation box after equilibrium is about 11 nm and the diameter of the microemulsion is about 6.5 nm (Figure 6-3c), both of which are consistent with Bui's et al. (2018) work.

I then create another 9 models with varying salinities (M2-M10) as shown in Table 6-1 to model microemulsion behavior under bulk conditions. The salinity variation is in a range of 3,000-500,000 ppm. First, I use the Packmol package (Martínez et al. 2003) to fix the microemulsion at the center of a cubic box with a length of 11 nm (same size in Figure 6-3b). Second, water and NaCl are randomly distributed around the

microemulsion and salinity is increased by adding a greater number of Na^+ and Cl^- ions.

M1 is treated as a reference model where salinity is not considered. The 9 remaining models are categorized into three groups: low (3000-8000 ppm), mid (10000-40000 ppm), and high (100000-500000 ppm) salinity. The initial configurations are shown in Figure 6-4. These 9 models are equilibrated using an NPT ensemble through the whole simulation process. First, a time step of 0.1 fs is used for 100ps, after which it is increased to 1 fs for 10 ns when the simulations reached equilibrium. Then another 40 ns of simulations are carried out for the analysis in this chapter.

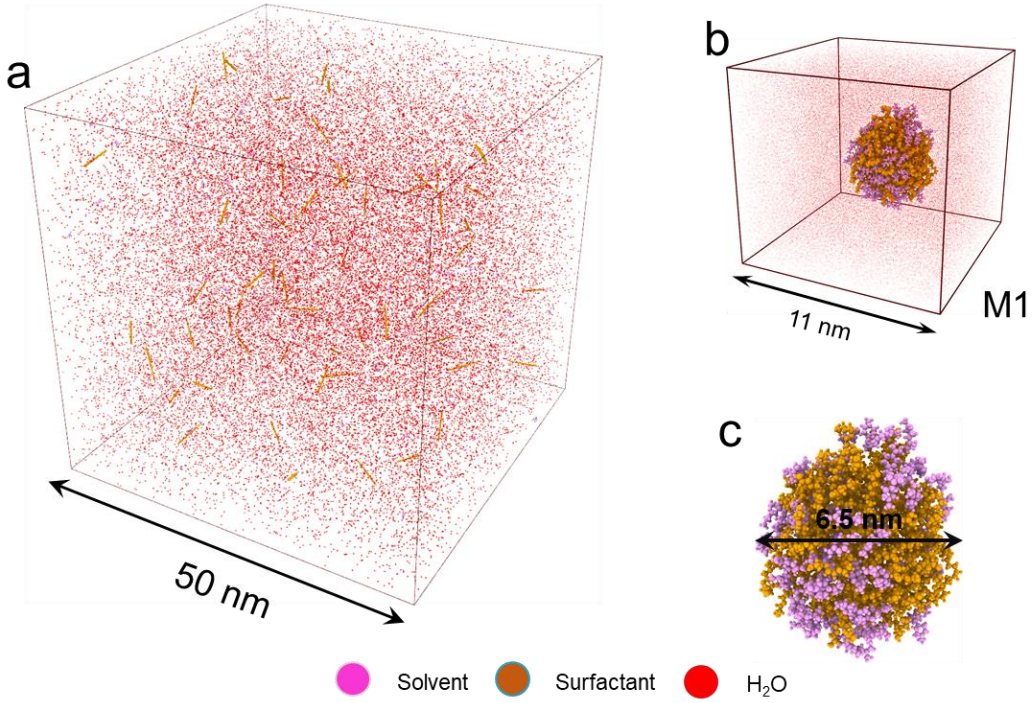

Figure 6-3 (a) Initial configuration of the simulation box containing random placement of water (red), solvent (pink), and surfactant (brown). (b) Equilibrium configuration of the simulation box containing a stable microemulsion. (c) Microemulsion extracted from panel b. The diameter of the microemulsion is about 6.5 nm and the scale is not the same as panel b. The total simulation time is 50 ns.

Table 6-1 Summarized models in bulk condition

	Model	ppm
Reference model	M1	0
Low salinity	M2	3000
	M3	5000
	M4	8000
Mid salinity	M5	10000
	M6	20000
	M7	40000
High salinity	M8	100000
	M9	300000
	M10	500000

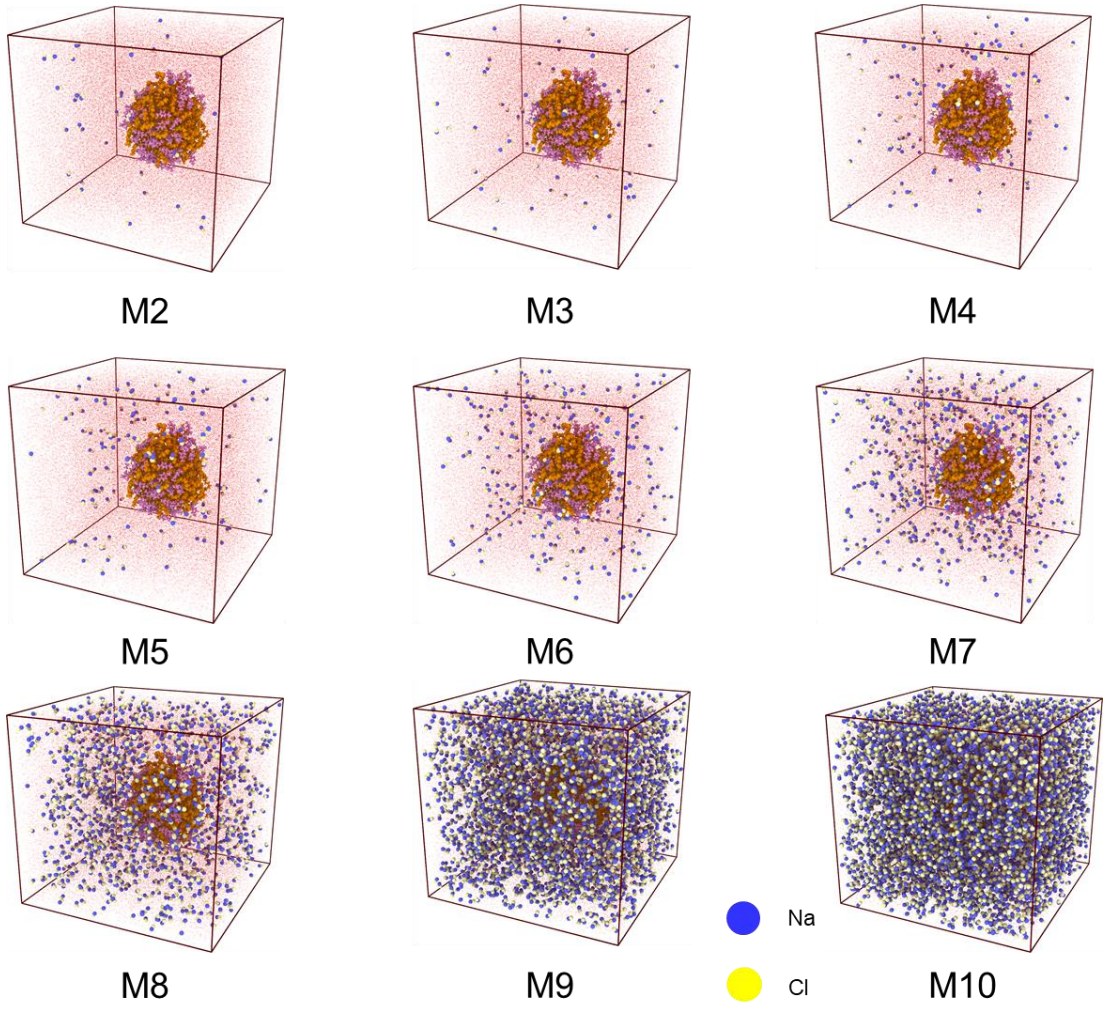

Figure 6-4 Initial Configuration of models in bulk condition with varying salinities. The color code follows in Figure 6-3. The color codes of salt are Na, red, and Cl, yellow.

6.2.3 Construction of Microemulsion in Clay-hosted Nanopore

I choose the salinities of 3000, 10000, and 100000 ppm representing low, mid, and high salinity, respectively from Table 6-1. Zero salinity is chosen as a reference model. Different clay surface chemistries (P-H and H-H structures) are also considered in this work following Chapter 3. All models are summarized in Table 6-2. Initial configurations are shown in Figure 6-5. The pore width is 11 nm. The surface chemistry in M11-M14 is P-H while in M15-M18 is H-H, where P and H stand for potassium and hydroxyl respectively following the convention in Chapter 3.

The clay structure is kept rigid throughout the simulations, except that H^+ in hydroxyl and cation K^+ are mobile with thermal motion (Hao et al. 2018). This choice forbids the geochemical study of clay swelling due to adsorption/desorption/EDL (Sposito et al. 1999). All 8 simulations are carried out at 380K using a canonical NVT ensemble, where the temperature is controlled by the Nose Hoover thermostat (Nosé et al. 1984). It should be noted that the volume of the simulation box is primarily determined in M1 with the pressure of 400 atm, and is the same in M2-M10 that includes NaCl, consistent with the observations of Koleini et al. (2019b). Models M11-M18 also have the same pressure during the NVT ensemble simulations.

Table 6-2 Summarized models in clay-hosted nanopores

Model	ppm	Surface chemistry	Model	ppm	Surface chemistry
M11	0	PH	M15	0	HH
M12	3000	PH	M16	3000	HH
M13	10000	PH	M17	10000	HH
M14	100000	PH	M18	100000	HH

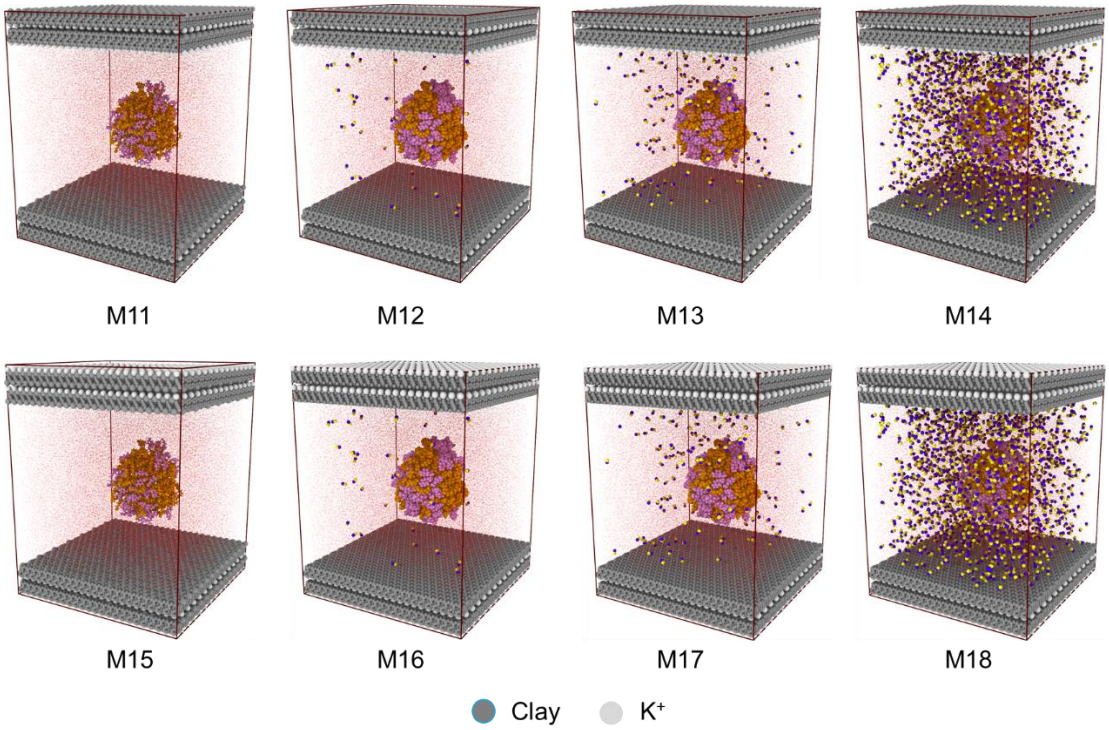

Figure 6-5 Initial Configuration of models in clay-hosted nanopore with varying salinities. The fluid color code follows in Figure 6-4. Grey color is the clay, and light grey is potassium (K^+). The pore width is 11 nm. The surface chemistry in M11-M14 is P-H while in M15-M18 is H-H.

6.3 Results and Discussion

6.3.1 Fluid Distribution in Bulk Condition

Figure 6-6 shows the fluid distribution in models M2-M10 in bulk condition after 50 ns of simulation. I also render the microemulsion surfaces in gray in Figure 6-7 using OVITO (Stukowski et al. 2010). Figure 6-7 indicates that the shape of the

microemulsions remains spherical at all salinities underscoring its stability under these conditions. To further validate this conclusion, I calculate the density profiles in *x*-*y* and *x*-*z* directions, as shown in Figure 6-8 and Figure 6-9 respectively. High-density numbers correspond to red colors and low-density numbers to blue colors. The density plots use $100 \times 100 \times 100$ bins in the simulation box to count particle numbers spatially.

These results underscore the stability of the microemulsions under varying salinities. The high density within the microemulsion shows a centered solvent surrounded by the surfactant.

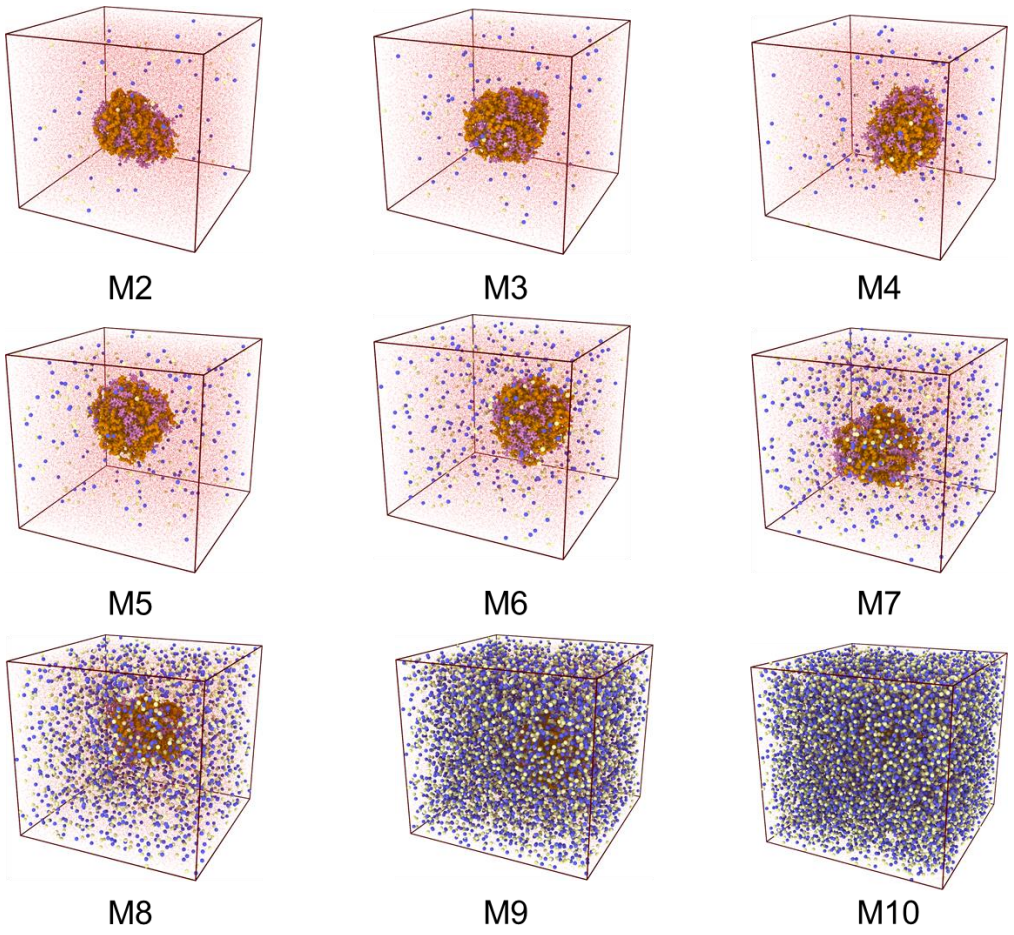

Figure 6-6 Equilibrium configuration of Models 2-10 after 50 ns. The color code is the same as Figure 6-4.

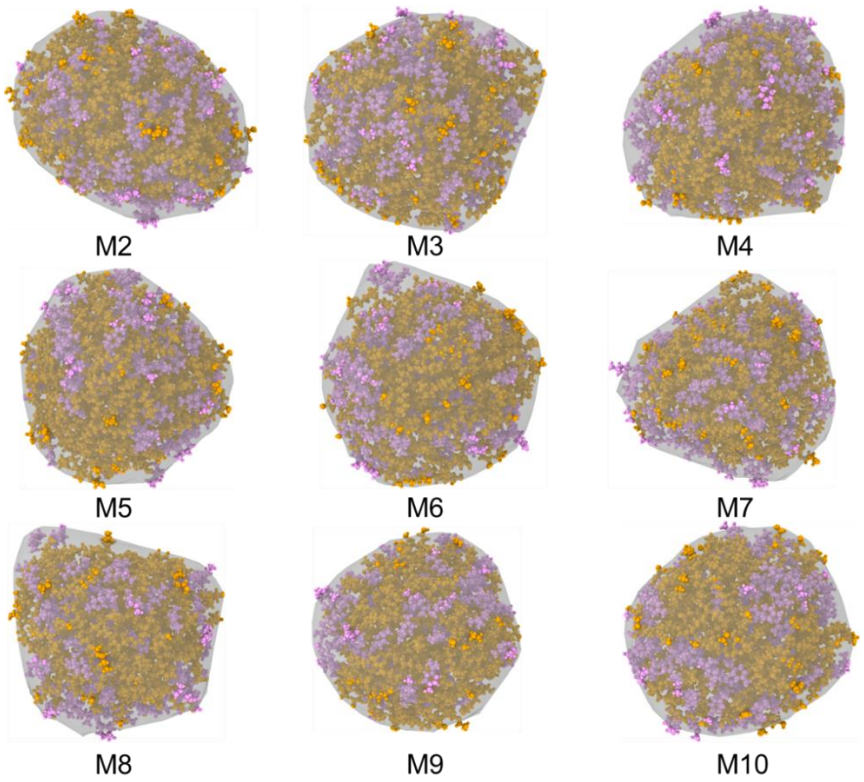

Figure 6-7 The shape of microemulsions in Models 2-10. The microemulsion surface is rendered as a light grey surface. The color code is the same as Figure 6-4.

Microemulsions tend to show different behavior with variations in salinity, temperature, and pressure (Eastoe et al. 1990; Bera et al. 2015). In this work, the calculated microemulsion surface areas (light grey surfaces in Figure 6-7) as a function of salinity are shown in Figure 6-10 indicating that with increasing salinity, the microemulsion surface area correspondingly increases, which agrees with Bera et al. (2015) and Torrealba et al. (2019).

Although, I do not observe a change in the microemulsion stability with respect to salinity, it is important to note that, in reality, the type of microemulsion will change from Winsor Type I (oil-in-water) to Type III (bicontinuous) to Type II (water-in-oil) with increases in salinity. This however only occurs if oil and water are present in

approximately equal quantities (Yuan et al. 2018). In this work, I chose a large percentage of water compared to oil to consider only the effect of salinity on the microemulsion. My simulation also allows comparison to the work by Bui et al. (2019) where the oil-water ratio is similar to this work.

Here, I use two definitions of '*stability*'. If the microemulsion is largely spherical, the microemulsion is considered to be *'highly stable'*. If the shape changes and becomes more ellipsoidal, it is considered as '*moderately stable'*. Otherwise, I refer to it as '*unstable*'. Therefore, the stability of microemulsions in M1-M10 is *highly stable*.

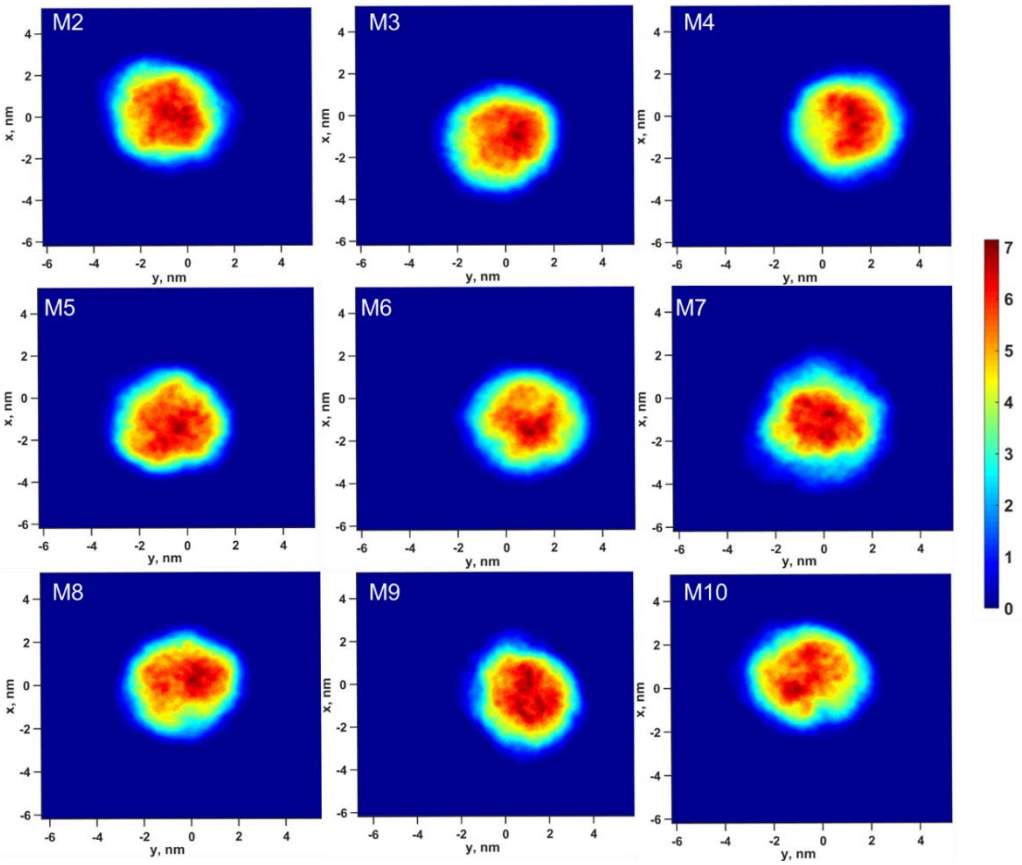

Figure 6-8 Projection on the *xy*- plane of microemulsion after the simulation time of 50 ns.

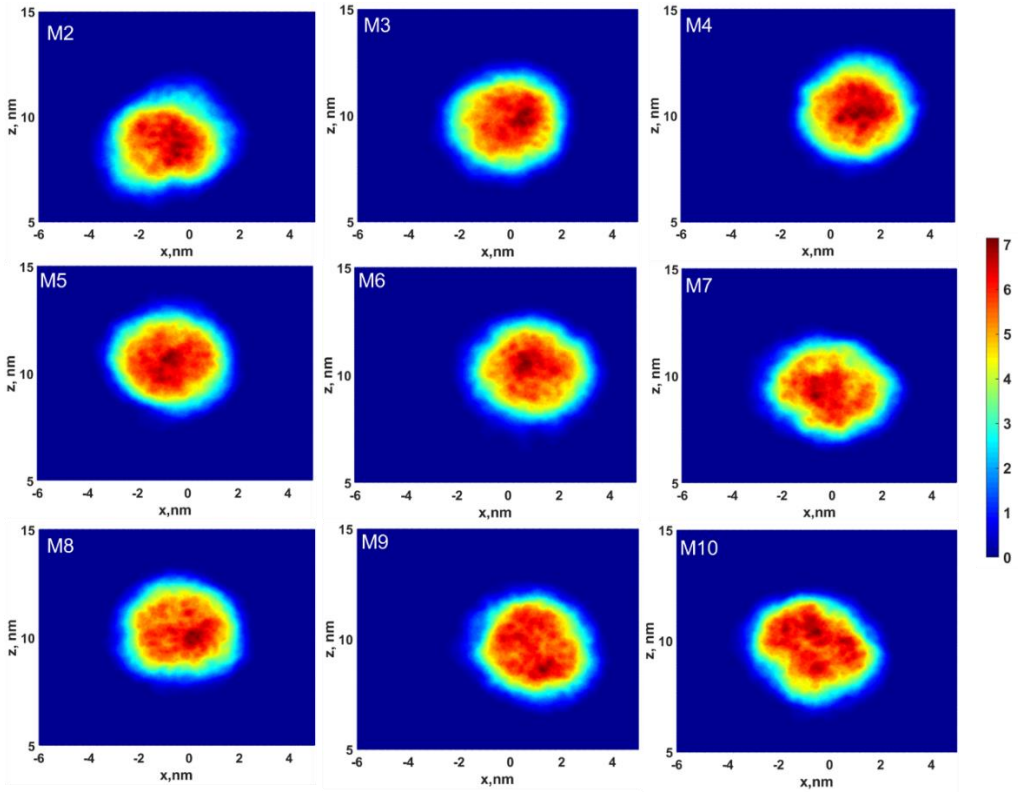

Figure 6-9 Projection on the *xz*- plane of microemulsion after the simulation time of 50 ns illustrating that they are stable at all salinities

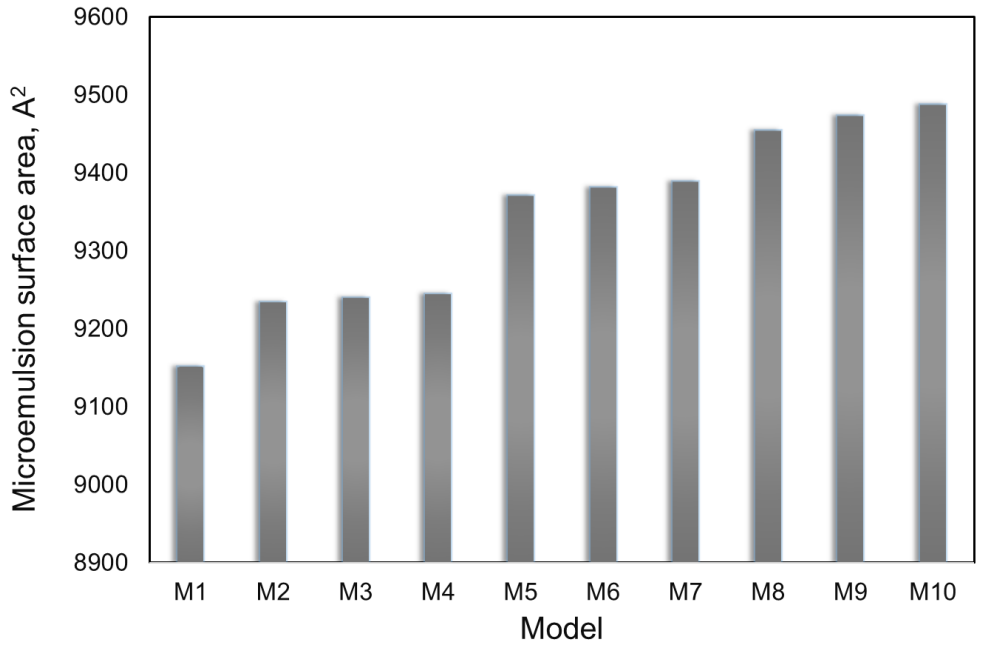

Figure 6-10 Calculated surfaces of microemulsions at varying salinities. It indicates that by increasing the salinity, the microemulsion surface will correspondingly increase. Meanwhile, the surface areas of the microemulsions with varying salinity range from 9152 to 9487 A^2 with a standard deviation of 111 A^2 illustrating microemulsions are stable at all salinities.

6.3.2 Fluid Distribution in Clay-hosted Nanopores

Figure 6-11 shows the fluid distribution in P-H clay-hosted nanopores as a function of simulation time (in the vertical direction) and salinity (in the horizontal direction). The salinities of M11-M14 are 0, 3000, 10000, and 100000 ppm, respectively. Water molecules are not shown for clarity. Figure 6-12 shows the density plot of M11-M14 in *xy*-projection at the simulation time of 50 ns. High-density numbers correspond to red colors and low-density numbers to blue colors.

In M11, at a simulation time of 10 ns, the microemulsion moves toward the clay surface and appears to wet the surface. As simulation time progresses, the droplet continues to wet the surface and finally breaks up at around 40ns. At 50ns, the microemulsion simply covers the lower clay surface. I show the same result in the calculated density of Figure 6-12a. Note that the upper and bottom parts in Figure 6-12a are linked together due to the periodic boundary condition.

Increasing the salinity to 3000 ppm (Figure 6-11, M12), the microemulsion shows some degree of affinity to the clay surface (20-50 ns). Figure 6-12b also validates this observation. Further increasing the salinity to 10000 ppm (Figure 6-11, M13), the microemulsion remains intact during the whole simulation (0-50 ns), except for a few liberated solvent molecules. This observation is reinforced by Figure 6-12c. It should be noted that I continue to run both M12 and M13 for another 50 ns to assess the stability of the microemulsion and the results do not change.

At the highest salinity of 100000 ppm (Figure 6-11, M14), the microemulsion

remains spherical and this observation is confirmed in Figure 6-12d.

I, therefore, indicate that the stability of microemulsions is *unstable* in M11-12, *moderately stable* in M13, and *highly stable* in M14. This is a rather surprising result indicating that the microemulsion stability in P-H clay-hosted pores increases with increasing salinity.

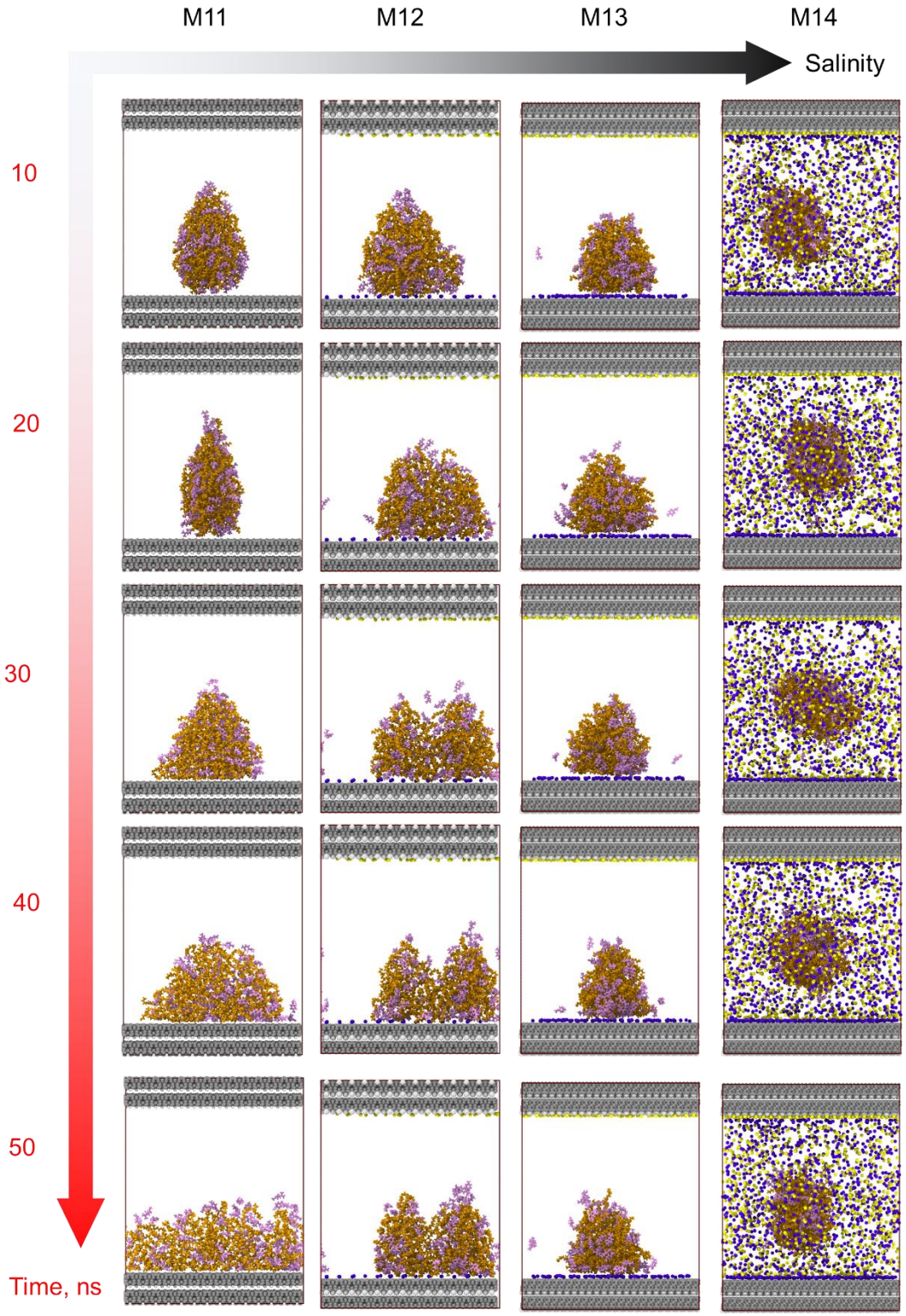

Figure 6-11 Fluid distribution in P-H clay-hosted nanopores as the function of simulation time (in the vertical direction) and salinity (in the horizontal direction). Remembered that the salinities of M11-M14 are 0, 3000, 10000, and 100000 ppm, respectively. Water molecules are not shown for clarity. It indicates the behavior of the microemulsion is a function of salinity and increasing the salinity to a certain value (i.e., 10000 ppm) can enhance the stability of the microemulsion in P-H clay-hosted nanopores.

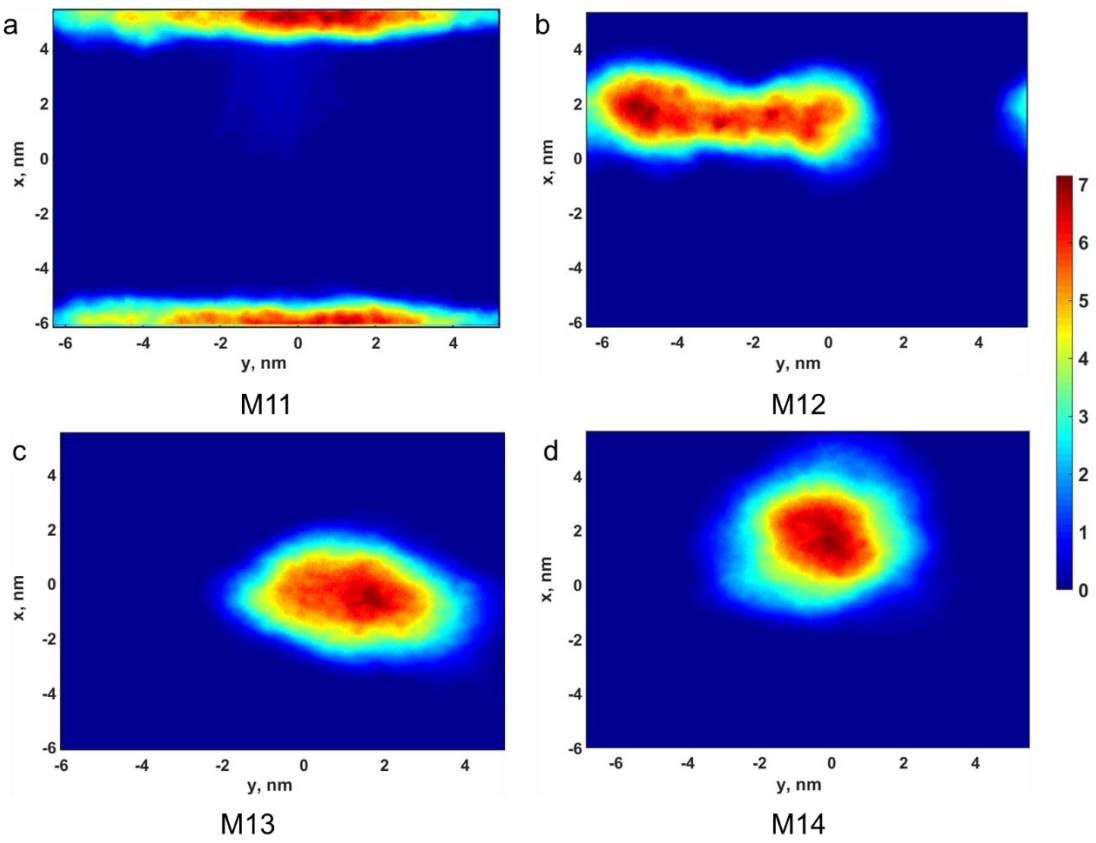

Figure 6-12 Density plot of M11-M14 in *xy*- projection at the simulation time of 50 ns in P-H clay-hosted nanopores. High-density numbers correspond to red colors and low-density numbers to blue colors. The calculated method follows the same process described in Section 6.3.1.

Figure 6-13 (upper four panels) shows the fluid distribution in H-H clay-hosted nanopores as the function of salinity where water molecules are not shown for clarity. I also plot them individually in the bottom four panels of Figure 6-13. Simulation time is 50 ns. The salinities of M15-M18 are 0, 3000, 10000, and 100000 ppm, respectively. Figure 6-14 shows the density plot of M15-M18 in *xy*- projection at the simulation time of 50 ns.

Figure 6-13 indicates that irrespective of the salinity, the microemulsions are *highly stable* with a spherical shape in H-H clay-hosted nanopores. The calculated density plot in Figure 6-14 also validates this conclusion.

Therefore, we can conclude that the behavior of the microemulsion is the function of salinity (in Figure 6-11) and surface chemistry (comparing Figure 6-11 and Figure 6-13). In the next section, I investigate these observations further.

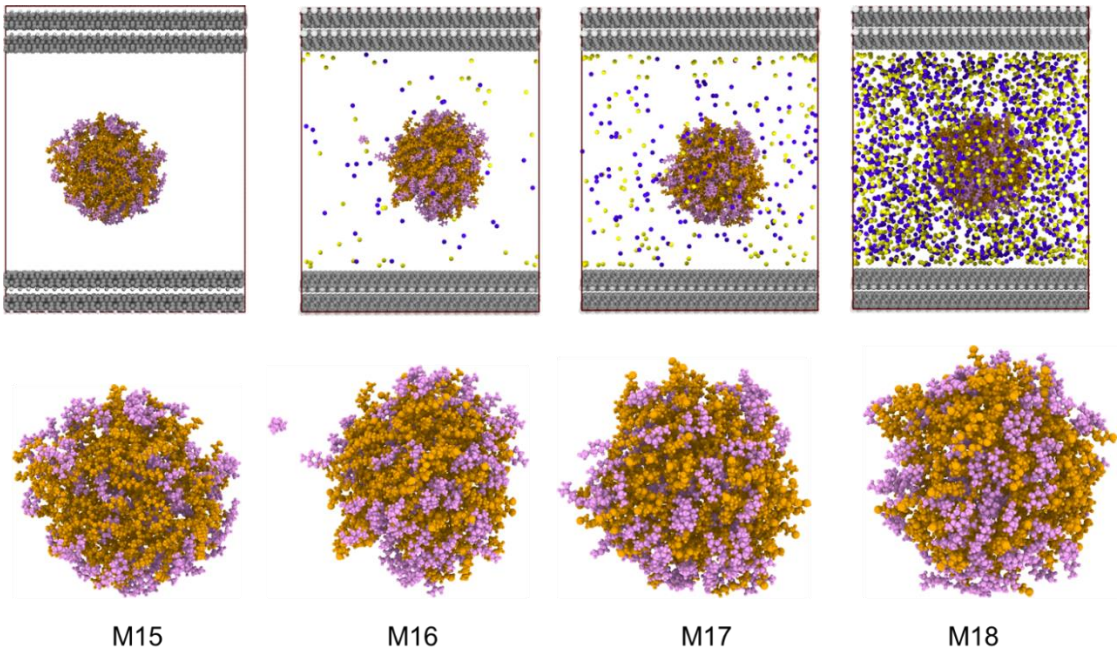

Figure 6-13 (Upper four panels) Fluid distribution in H-H clay-hosted nanopores as the function of salinity where water molecules are not shown for clarity. (Bottom four panels) Extracted microemulsions from the corresponding models. It indicates that irrespective of the salinity, the microemulsions are stable keeping the shape as a sphere in H-H clay-hosted nanopores.

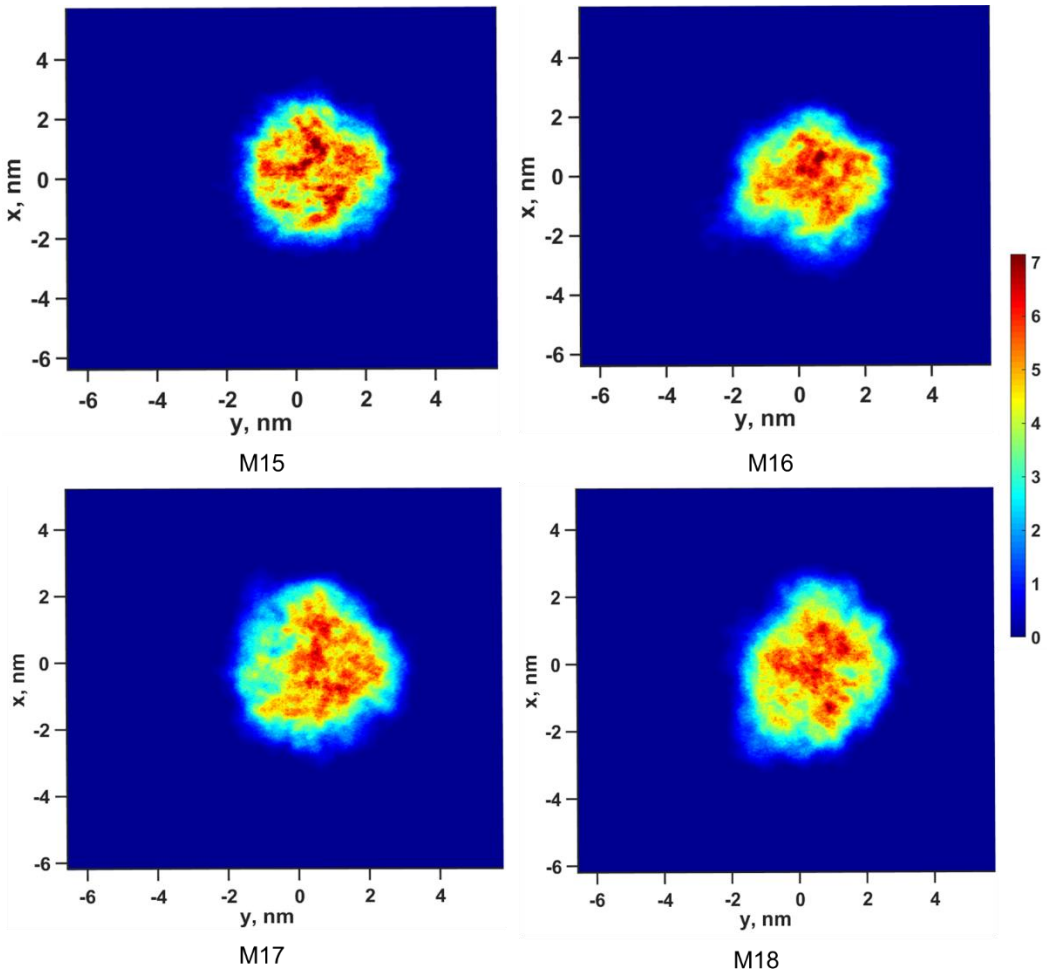

Figure 6-14 Density plot of M15-M18 in *xy*- projection at the simulation time of 50 ns in H-H clay-hosted nanopores. High-density numbers correspond to red colors and low-density numbers to blue colors. The calculated method follows the same process described in Section 6.3.1.

6.3.3 Surface Chemistry

In Chapter 3, I document the presence of local electric fields in the P-H nanopore. Therefore, following the same process in Chapter 3, I insert one charge inside the nanopores and calculate the electric fields in models M11-M18 (M11-M14 is P-H and M15-M18 H-H). The results are shown in Figure 6-15. The average electric fields are 7.77 (in M11), 4.94 (in M12), 1.13 (in M13), 0.41 (in M14), 0.51 (in M15), 0.39 (in M16), 0.35 (in M17) and 0.26 V/nm (in M18). Figure 6-15 reaffirms the conclusions of

Chapter 3. It should be noted that despite the presence of a strong electric field in M11, the clay surfaces do not move when allowed to do so as shown in Appendix B.

Figure 6-15 also demonstrates that increasing the salinity impairs the strength of the electric field as discussed in previous chapters. Since we observe *highly* or *moderately stable* microemulsions in M13-M18 but not in M11-M12, the presence of strong electric fields is likely one of the reasons to break down the microemulsion. Salinity tempers the strength of the field and renders the microemulsion stable.

However, there is also the surface effect to consider where the microemulsion coats the clay surface as seen in Figure 6-11 for a few values of salinity. Thus, I build another two models to test the effects of electric field and clay surface on microemulsion stability separately.

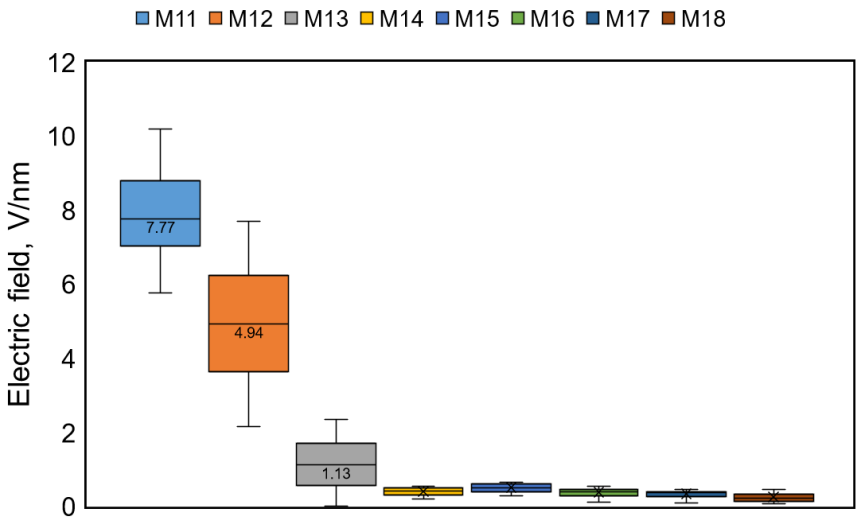

Figure 6-15 Calculated electric fields as the function of salinity and surface chemistry. Remembered that the surface chemistry of M11-M14 is P-H and M15-M18 H-H. The average electric fields in M11-M18 are 7.77, 4.94, 1.13. 0.41, 0.51, 0.39, 0.35 and 0.26 V/nm respectively.

Figure 6-16 shows the behavior of microemulsion in the presence of an electric field as the function of simulation time. With no salinity and an imposed external

electric field of 9.83 V/nm (same strength in M11, Figure 6-15) in the *z*-direction, I observe elongation of the microemulsion at a simulation time of 10 ns (Figure 6-16b); however, it continues to remain intact even at the end of 50ns of simulation time. So, the electric field alone perhaps is not sufficient to compromise microemulsion stability.

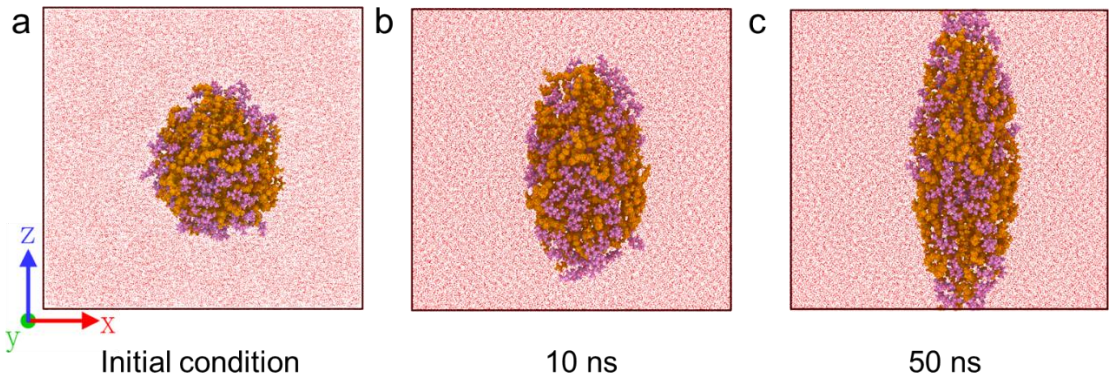

Figure 6-16 Behavior of microemulsion at the only presence of electric field as the function of simulation time. Color code refers to Figure 6-3.

In Figure 6-17, to eliminate the effect of the electric field, I only use the H-H nanopore with no salinity to test the effect of clay surfaces on microemulsion. Water molecules are not shown for clarity. I perform the simulations with an initial distance of 0.4 nm between the wall and the microemulsion (Figure 6-17a) and observe results similar to Akkutlu et al.(2014) showing adsorption can occur Figure 6-17b.

The microemulsion is *highly stable* when touching the clay surface as shown in Figure 6-17b. Figure 6-17c and Figure 6-17d are the density plots on *xz* and *xy* projections respectively. The contact angle in Figure 6-17c is about 130° which is between 90° and 180°, confirming that the microemulsion has low wettability on the clay surface but is still stable indicating that the clay surface alone, in the absence of a strong electric field cannot break the microemulsion.

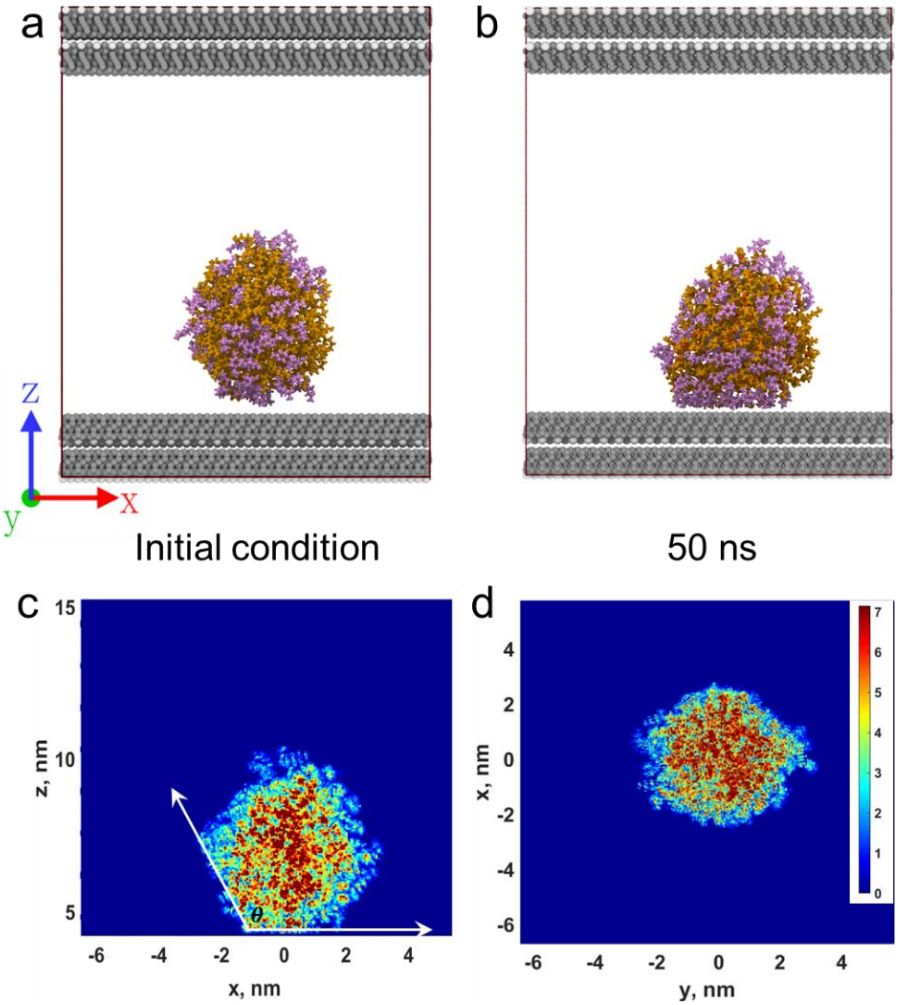

Figure 6-17 (a-b) Behavior of microemulsion at the only presence of clay surface as the function of simulation time. (c-d) Density plots on *xz* and *xy* projections respectively. High-density numbers correspond to red colors and low-density numbers to blue colors. The calculated method follows the same process described in Section 6.3.1.

6.3.4 Self-diffusion

Figure 6-18 shows the calculated self-diffusion coefficients of water, solvent, and surfactant in M1-M18. Self-diffusion is calculated using the standard relationship between the diffusion coefficient and the slope of the mean square displacement (MSD), following the process described in Section 2.4.3. Remember that M1-M10 are in bulk condition (Figure 6-18a), M11-M14 in P-H nanopore (Figure 6-18b), and M15-M18 in

H-H nanopore (Figure 6-18c). Red, pink, and brown represent the water, solvent, and surfactant molecules respectively.

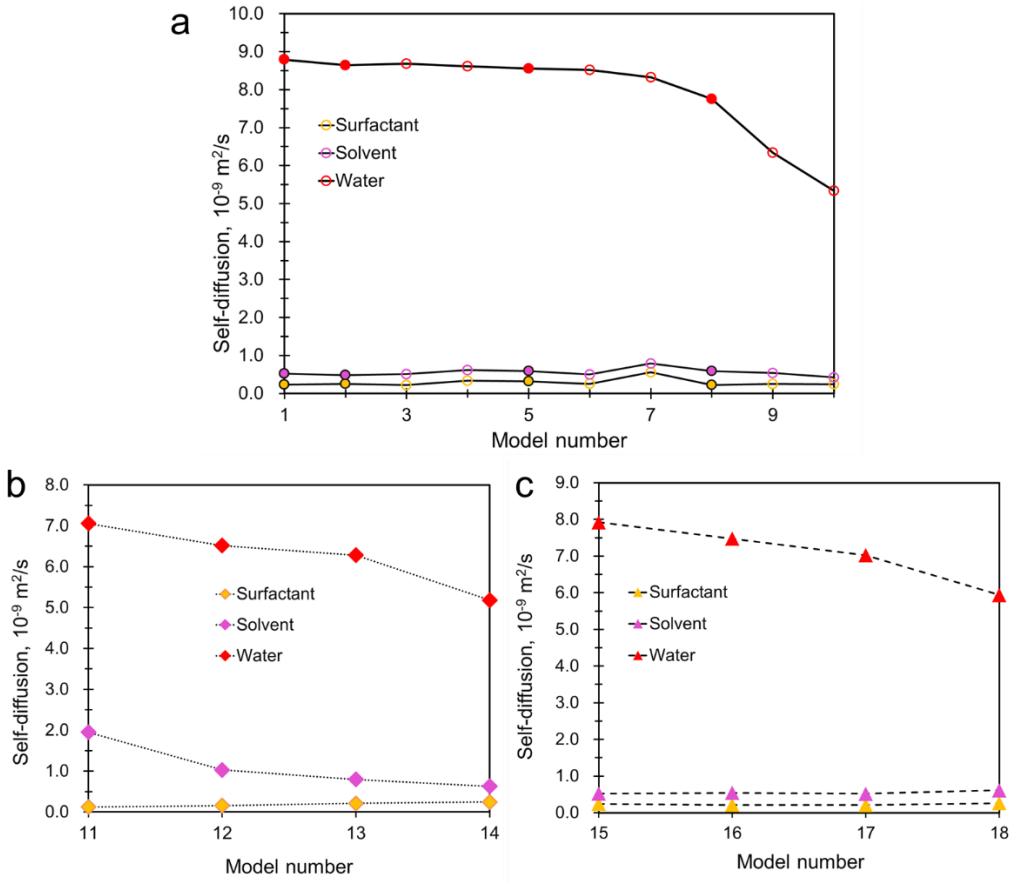

Figure 6-18 Calculated self-diffusions of water, solvent, and surfactant in M1-M18.

In M1 (no salinity), the self-diffusion of water is 8.79×10^{-9} m^2/s. Holz et al. (2000) fitted the experimental data and obtained the self-diffusion coefficients of water as the function of temperature, as shown in Equation (6-1):

$$D = D_0 \left[\left({}^{T}/_{T_S} \right) - 1 \right]^{\gamma} \tag{6-1}$$

Where D is the self-diffusion of water as the function of temperature, T_S is a singular temperature, T is the target temperature, D_0 and γ are fitting parameters. According to Holz et al. (2000),

$$D_0 = (1.635 \times 10^{-8} \pm 2.242 \times 10^{-11}) m^2 s^{-1} \tag{6-2}$$

$$T_S = (215.05 \pm 1.20)K \quad (6\text{-}3)$$

$$\gamma = 2.063 \pm 0.051 \quad (6\text{-}4)$$

Therefore, combining Equations (6-1), (6-2), (6-3), and (6-4), the self-diffusion of water at the temperature of 380 K is 9.47×10^{-9} m^2/s and my calculated value (8.79×10^{-9} m^2/s) shows a small deviation (7%) from the Holz's et al. (2000) result.

Irrespective of bulk condition and confinement (P-H and H-H), increasing the salinity (NaCl) leads to the decrease of self-diffusion of water. This trend agrees with observations in Kim et al. (2012), Ghaffari et al. (2013), and Ding et al. (2014). This is because the hydration of the ions causes a decrease in the self-diffusion of water (Kim et al. 2012). Furthermore, Ding et al. (2014) using ab initio molecular dynamics conclude that the ions can cause electronic heterogeneity of water molecules, which in turn results in significant variability in the ability of water to polarize its surroundings which eventually impacts the self-diffusion of water (In NaCl environments, it is a decrease of self-diffusion).

Meanwhile, the self-diffusion of water in the bulk is higher than that in confinement, which is consistent with our previous results (Xiong et al. 2020a). This is because the confinement (i.e., clay surface) will influence the behavior of water. A detailed discussion is presented in Chapter 3. Moreover, the self-diffusion of water in the H-H nanopore is also higher than in the P-H nanopore (i.e., M11 and M15) where the presence of an electric field promotes H-bond formation, decreasing the mobility of water.

The self-diffusions of solvent and surfactant are similar in both the bulk as well as in H-H nanopores where the microemulsion remains centered in the pore with little influence of clay surface. However, in the P-H nanopore, a large gap is observed, especially in M11 (zero salinity), where the microemulsion is not stable (Figure 6-11) causing the solvent and surfactant to diffuse separately. With increasing salinity in the P-H nanopore, the microemulsions become stable so the gap is narrows.

6.4 Further Discussion

Referring back to the question mentioned in Section 6.1 (Introduction) as to whether these microemulsions can be delivered deeper into the matrix via inorganic pores, the work in this chapter shows that the stability of microemulsion is the function of salinity and clay surface chemistry. This necessitates selecting an optimal salinity that does not lower the stability of the microemulsion and that does not promote the formation of ionic aggregates. In this work for the pore sizes considered, the optimal salinity is ~11,000 ppm. Figure 6-19a and Figure 6-19b show the equilibrium configuration of the model at the salinity of 11000 ppm in different projections. The simulation time is 50 ns. During the whole process, the microemulsion is *highly stable* and distributed at the pore center in which the calculated electric field (0.75 V/nm) is not strong enough to drag the microemulsion to the clay surface. It should be noted that the pore sizes considered in this work are limited and therefore the salinity recommendations, which will vary with pore size, should not be generalized to other pore widths.

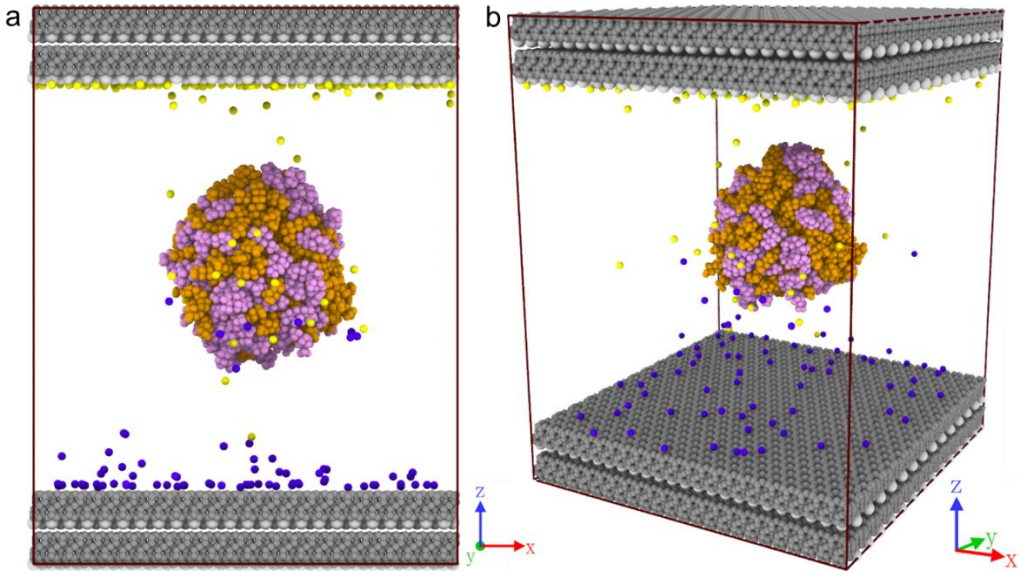

Figure 6-19 Equilibrium configuration of the model at the salinity of 11000 ppm in different projections. The simulation time is 50 ns. The color code refers to Figure 6-5.

6.5 Final Remarks

Effective delivery of microemulsions to the target kerogen is essential for chemical EOR. This chapter extends our understanding of the effects of salinity variations on microemulsions in clay-hosted nanopores. Different clay surface chemistries are considered in this work. In the bulk, I show that the microemulsions are stable across a wide range of salinities. In H-H nanopores, the microemulsions remain stable. In the P-H nanopore, the fluids are subject to the induced local electric fields. In these cases, both the electric field and the clay surface compromise the stability of the microemulsion.

Chapter 7 What Have We Learned?

7.1 Conclusions

This dissertation has been a study into the fluid behavior inside clay-hosted nanopores. Interactions between clay mineral surfaces and fluids (i.e., water, oil, solvent, or brine solutions) have been successfully modeled using classical atomistic molecular dynamics.

The following conclusions can be drawn from this work:

1. Oil swelling, diffusion, and viscosity reduction are a few of the dominant pore-scale mechanisms governing EOR. However, my findings also demonstrate that bulk fluid properties can cause overly optimistic predictions of the efficacy of EOR when dealing with inorganic, clay pore systems.

2. Confinement in illite is shown to negatively impact miscibility for methane-rich solvents. Secondly, the self-diffusion of fluids under illite confinement is only 30% of their values in the bulk. Most significantly, oil-solvent mixture viscosities under illite confinement are about two orders of magnitude higher compared to their bulk values. The presence of water exacerbates all of these effects and compromises the solubility of the injected solvent.

3. Charge imbalances on adjacent clay surfaces as in P-H nanopores can induce local electric fields, favoring the formation of water bridges. In P-H nanopores, water

bridges occur at a relatively low water concentration and are primarily driven by the electric field governing the structure of water. However, in H-H nanopores water bridges only form at high water concentrations due to capillary condensation.

4. In P-H nanopores, water bridges persist under acceleration due to the formation of hydrogen bonds under the influence of the electric field. However, in H-H pores, water bridges can form at high water saturations but dissipate during flow.

5. At high salinity (above 16000ppm) Na^+ and Cl^- ions primarily adsorb on the clay surface due to the charge screening effect. The unabsorbed Na^+ and Cl^- ions appear as aggregates that impede oil flow. At low salinity (below 8100ppm), water bridges across the pore due to a strong surface potential that is not neutralized by the low salt concentration. These water bridges severely hamper the flow of any free water and oil.

6. At intermediate values of salinity (8500-12400ppm), ionic aggregates are largely absent and water molecules merely adsorb on the surface of the pore. At these intermediate values of salinity, the mobility of the oil phase is the highest and constitutes the best range of salinity for the pore surface chemistry that I consider.

7. The microemulsions considered in this work are highly stable in solution across a wide range of (0-500,000 ppm) in the bulk. In the P-H nanopores, strong electric fields

(discussed in Chapter 3) can attract the microemulsion toward the clay surface, and finally, the microemulsion becomes unstable (i.e., broken or divided into two parts). However, in the H-H nanopore with a negligible electric field, the microemulsions remain stable for all values of salinity.

7.2 Limitations

1. Throughout this dissertation, atomistic molecular simulations have been used to help understand the behavior of fluids in clay-hosted nanopore from a molecular level. The primary aim of this study is to examine the interfaces between charged clay surfaces and fluids and to provide a more complete picture of fluid transport in unconventional reservoirs. However, in this context, the study still suffers from a few limitations beyond the traditional limitation of MD simulations: Since this work focuses on the impact of clay surfaces on fluid distribution, a more realistic representation of a fluid mixture is warranted. However, I chose dodecane as a starting point for further studies in this area.

2. The brine used in this work only contains NaCl. In general, brines contain several other dissolved salts, such as KCl, $CaCl_2$, and $CaCO_3$, and their presence needs to be considered especially when dealing with clays. Moreover, more complicated minerals should be investigated on further (or mixed) minerals, kaolinite or montmorillonite with various salts.

3. In Chapters 5 and 6 which focus on optimal salinity ranges, I want to highlight that my work is limited in terms of the pore widths and fluid saturations considered.

The recommendations should be viewed in the light of these limitations. The main purpose of my study was to show that there exists an optimal value of salinity that is neither too high nor too low. For specific clays, pore widths and saturations, these still need to be determined.

Reference

Accelrys. 2016. "Materials Studio." https://doi.org/http://accelrys.com/products/collaborative-science/biovia-materials-studio/.

Adeyeri, J. B. 2019. "Clay Mineralogy and Soil Structure." *Technology and Practice in Geotechnical Engineering. IGI Global* 2015 (11): 41–115. https://doi.org/doi:10.4018/978-1-4666-6505-7.ch002.

Ahmed, A. A., Saaid, I. M., Akhir, N., and Rashedi, M. 2016. "Influence of Various Cation Valence, Salinity, PH and Temperature on Bentonite Swelling Behaviour." *AIP Conference Proceedings* 1774 (October 2016). https://doi.org/10.1063/1.4965087.

Akkutlu, I. Y., Bui, K., Silas, J. A., Zelenev, A., and Saboowala, H.. 2014. "Molecular Dynamics Simulation of Adsorption from Microemulsions and Surfactant Micellar Solutions at Solid-Liquid and Liquid-Liquid Interfaces." *Technical Proceedings of the 2014 NSTI Nanotechnology Conference and Expo, NSTI-Nanotech 2014* 3: 517–20.

Allahyarov, E., and Gompper, G.. 2002. "Mesoscopic Solvent Simulations: Multiparticle-Collision Dynamics of Three-Dimensional Flows." *Physical Review E - Statistical Physics, Plasmas, Fluids, and Related Interdisciplinary Topics* 66 (3): 1–9. https://doi.org/10.1103/PhysRevE.66.036702.

Alotaibi, M. B., Nasralla, R. A., and Nasr-El-Din, H. A.. 2011. "Wettability Studies Using Low-Salinity Water in Sandstone Reservoirs." *SPE Reservoir Evaluation and Engineering* 14 (6): 713–25. https://doi.org/10.2118/149942-PA.

Autumn, K., Sitti, M., Liang, Y. A. et al. 2002. "Evidence for van Der Waals Adhesion in Gecko Setae." *Proceedings of the National Academy of Sciences of the United States of America* 99 (19): 12252–56. https://doi.org/10.1073/pnas.192252799.

Baran, J. R. 2001. "Winsor I⇔III⇔II Microemulsion Phase Behavior of Hydrofluoroethers and Fluorocarbon/Hydrocarbon Catanionic Surfactants." *Journal of Colloid and Interface Science* 234 (1): 117–21. https://doi.org/10.1006/jcis.2000.7284.

Barrachin, B., and Lara, E.. 1986. "Determination of the Electric Field in Zeolites NaA, NaCaA and Ca6A." *J. Chem. Soc., Faraday Trans. 2* 82: 1953–66.

Bennett, P. 2015. "Surface Chemistry and Ion Exchange," 1–5. http://www.geo.utexas.edu/courses/376m/LectureNotes/Surface.pdf%0Ahttps://www.google.com/url?sa=t&rct=j&q=&esrc=s&source=web&cd=5&cad=rja&uact=8&ved=0CDkQFjAEahUKEwj01MPdserGAhUGjpIKHWcQBDk&url=http://www.geo.utexas.edu/courses/376m/LectureNotes/Surface.p.

Bennion, D. B., Bennion, D. W., Thomas, F. B. et al. 1998. "Injection Water Quality - A Key Factor to Successful Waterflooding." *Journal of Canadian Petroleum Technology* 37 (6): 53–62. https://doi.org/10.2118/94-60.

Bera, A,, and Mandal, A. 2015. "Microemulsions: A Novel Approach to Enhanced Oil

Recovery: A Review." *Journal of Petroleum Exploration and Production Technology* 5 (3): 255–68. https://doi.org/10.1007/s13202-014-0139-5.

Berendsen, H. J. C., Grigera, J. R., and Straatsma, T. P.. 1987. "The Missing Term in Effective Pair Potentials." *Journal of Physical Chemistry* 91 (24): 6269–71. https://doi.org/10.1021/j100308a038.

Berendsen, H. J. C., Postma, J. .P M., Gunsteren, W. F. et al. 1981. "Interaction Models for Water in Relation to Protein Hydration BT - Intermolecular Forces: Proceedings of the Fourteenth Jerusalem Symposium on Quantum Chemistry and Biochemistry Held in Jerusalem, Israel, April 13–16, 1981." In , edited by Bernard Pullman, 331–42. Dordrecht: Springer Netherlands. https://doi.org/10.1007/978-94-015-7658-1_21.

Bourg, I. C., and Steefel, C. I.. 2012. "Molecular Dynamics Simulations of Water Structure and Diffusion in Silica Nanopores." *Journal of Physical Chemistry C* 116 (21): 11556–64. https://doi.org/10.1021/jp301299a.

Bousige, C., Ghimbeu, C. M., Guterl, C. V. et al. 2016. "Realistic Molecular Model of Kerogen's Nanostructure." *Nature Materials* 15 (5): 576–82. https://doi.org/10.1038/nmat4541.

Bueno, J. M., Peñuelas, C. S., and Izquierdo, S. C. 2011. "Capacitance Evaluation on Non-Parallel Thick-Plate Capacitors by Means of Finite Element Analysis." *Journal of Energy and Power Engineering* 5: 373–78.

Bui, K.;, and Akkutlu, I. Y.. 2018. "Microemulsion Effects on Oil Recovery from Kerogen Using Molecular Dynamics Simulation." *SPE Journal*.

Bui, K., and Akkutlu, I. Y. 2015a. "Nanopore Wall Effect on Surface Tension of Methane." *Molecular Physics* 113 (22): 3506–13. https://doi.org/10.1080/00268976.2015.1037369.

Bui, K., and Akkutlu, I. Y. 2015b. "Nanopore Wall Effect on Surface Tension of Methane." *Molecular Physics* 113 (22): 3506–13. https://doi.org/10.1080/00268976.2015.1037369.

Bui, K., Akkutlu, I. Y., Zelenev, A. S.et al. 2017. "Understanding Penetration Behavior of Microemulsions Into Shale Nanopores." *SPE Europec Featured at 79th EAGE Conference and Exhibition*. https://doi.org/10.2118/185787-MS.

Bui, K., Akkutlu I Y., and Hill, W. A. 2018. "Kerogen Maturation Effects on Pore Morphology and Enhanced Shale Oil Recovery."

Bui, K., Akkutlu, I Y., Zelenev, A. S. et al. 2018. "Microemulsion Effects on Oil Recovery from Kerogen Using Molecular Dynamics Simulation." *SPE Annual Technical Conference and Exhibition*. Dallas, Texas, USA: Society of Petroleum Engineers. https://doi.org/10.2118/191719-MS.

Bui, K., Akkutlu, I Y,, Zelenev, A. S. et al. 2019. "Microemulsion Effects on Oil Recovery From Kerogen Using Molecular-Dynamics Simulation." *SPE Journal* 24 (06): 2541–54. https://doi.org/10.2118/191719-PA.

Bui, K., Akkutlu, I Y., Zelenev, A.et al. 2016. "Insights into Mobilization of Shale Oil Using Microemulsion." *SPE Conference*, no. April: 1–12.

https://doi.org/10.15530/urtec-2015-2154925.

Carroll, D. 1959. *Ioon Exchange in Clays and Other Minerals*. *Bulletin of the Geological Society of America*. Vol. 70. https://doi.org/10.1130/0016-7606(1959)70[749:IEICAO]2.0.CO;2.

Champagne, L. M., Zelenev, A. S., Penny, G. S. et al. 2011. "Critical Assessment of Microemulsion Technology for Enhancing Fluid Recovery from Tight Gas Formations and Propped Fractures." *Society of Petroleum Engineers - 9th European Formation Damage Conference 2011* 2: 862–71. https://doi.org/10.2118/144095-ms.

Chen, C.l., Wang, S., Harwell, J. H. et al. 2021. "Polymer-Free Viscoelastic Fluid for Improved Oil Recovery." *Fuel* 292 (January): 120331. https://doi.org/10.1016/j.fuel.2021.120331.

Chen, D., and Savidge, T. 2015. "Comment on 'Extreme Electric Fields Power Catalysis in the Active Site of Ketosteroid Isomerase.'" *Science* 349 (6251): 936b. https://doi.org/10.1126/science.aab0095.

Chen, G., Lu, S., Zhang, J. et al. 2016. "Research of CO 2 and N 2 Adsorption Behavior in K-Illite Slit Pores by GCMC Method." *Scientific Reports* 6 (November): 1–10. https://doi.org/10.1038/srep37579.

Chen, J., Wang, C., Wei, N. et al. 2016. "3D Flexible Water Channel: Stretchability of Nanoscale Water Bridge." *Nanoscale* 8 (10): 5676–81. https://doi.org/10.1039/c5nr08072j.

Coasne, B., Galarneau, A., Renzo, F. D. et al. 2010. "Molecular Simulation of Nitrogen Adsorption in Nanoporous Silica." *Langmuir* 26 (13): 10872–81. https://doi.org/10.1021/la100757b.

Collell, J., Galliero, G., Vermorel, R. et al. 2015. "Transport of Multicomponent Hydrocarbon Mixtures in Shale Organic Matter by Molecular Simulations." *The Journal of Physical Chemistry C* 119 (39): 22587–95. https://doi.org/10.1021/acs.jpcc.5b07242.

Cramer, T., Zerbetto, F., and García, R. 2008. "Molecular Mechanism of Water Bridge Buildup: Field-Induced Formation of Nanoscale Menisci." *Langmuir* 24 (12): 6116–20. https://doi.org/10.1021/la800220r.

Cui, S. T., Cummings, P. T., and Cochran, H. D. 2001. "Molecular Simulation of the Transition from Liquidlike to Solidlike Behavior in Complex Fluids Confined to Nanoscale Gaps." *Journal of Chemical Physics* 114 (16): 7189–95. https://doi.org/10.1063/1.1359736.

Cui, S. T., McCabe, C., Cummings, P. T. et al. 2003. "Molecular Dynamics Study of the Nano-Rheology of n-Dodecane Confined between Planar Surfaces." *Journal of Chemical Physics* 118 (19): 8941–44. https://doi.org/10.1063/1.1568084.

Curtis, M. E., Ambrose, R.J., Sondergeld, C.H. et al. 2011. "Transmission and Scanning Electron Microscopy Investigation of Pore Connectivity of Gas Shales on the Nanoscale." *Society of Petroleum Engineers - SPE Americas Unconventional Gas Conference 2011, UGC 2011*, 835–44. https://doi.org/10.2118/144391-ms.

Curtis, M. E., Ambrose, R. J., and Sondergeld, C. H. 2010. “Structural Characterization of Gas Shales on the Micro- and Nano-Scales.” *Canadian Unconventional Resources and International Petroleum Conference*. https://doi.org/10.2118/137693-MS.

Cygan, R. T., Liang, J., and Kalinichev, A. G. 2004. “Molecular Models of Hydroxide, Oxyhydroxide, and Clay Phases and the Development of a General Force Field.” *The Journal of Physical Chemistry B* 108 (4): 1255–66. https://doi.org/10.1021/jp0363287.

Czyż, E. A., and Dexter, A. R. 2015. “Mechanical Dispersion of Clay from Soil into Water: Readily-Dispersed and Spontaneously-Dispersed Clay.” *International Agrophysics* 29 (1): 31–37. https://doi.org/10.1515/intag-2015-0007.

Danov, K. D., Georgiev, M. T., Kralchevsky, P. A. et al. 2018. “Hardening of Particle/Oil/Water Suspensions Due to Capillary Bridges: Experimental Yield Stress and Theoretical Interpretation.” *Advances in Colloid and Interface Science* 251 (December): 80–96. https://doi.org/10.1016/j.cis.2017.11.004.

Denney, D. 2009. “Low-Salinity Waterflooding Improves Oil Recovery— Historical Field Evidence.” *Journal of Petroleum Technology* 61 (January): 47–49. https://doi.org/https://doi.org/10.2118/0109-0047-JPT.

Deshpande, S., Shiau, B. J., Wade, D. et al. 1999. “Surfactant Selection for Enhancing Ex Situ Soil Washing.” *Water Research* 33 (2): 351–60. https://doi.org/10.1016/S0043-1354(98)00234-6.

Diaz, C., Akkutlu, I Y., and Sigal, R. F. 2009. “A Molecular Dynamics Study on Natural Gas Solubility Enhancement in Water Confined to Small Pores.” *SPE Annual Technical Conference and Exhibition*. New Orleans, Louisiana: Society of Petroleum Engineers. https://doi.org/10.2118/124491-MS.

Ding, Y., Hassanali, A. A., and Parrinello, M. 2014. “Anomalous Water Diffusion in Salt Solutions.” *Proceedings of the National Academy of Sciences of the United States of America* 111 (9): 3310–15. https://doi.org/10.1073/pnas.1400675111.

Dörmann, M., and Schmid, H. 2015. “Simulation of Capillary Bridges between Particles.” *Procedia Engineering* 102: 14–23. https://doi.org/10.1016/j.proeng.2015.01.102.

Drits, F.W., Salyn, A.L., Tsipursky, S.I. 1993. “X-Ray Identification of One-Layer Illite Varieties: Application to the Study of Illites around Unranium Deposits of Canada.” *Clays and Clay Minerals* 41 (3): 389–98. https://doi.org/10.1346/CCMN.1993.0410316.

Drits, V. A., McCarty, D. K., and Zviagina, B. B. 2006. “Crystal-Chemical Factors Responsible for the Distribution of Octahedral Cations over Trans- and Cis-Sites in Dioctahedral 2:1 Layer Silicates.” *Clays and Clay Minerals* 54 (2): 131–52. https://doi.org/10.1346/CCMN.2006.0540201.

Drits, V. A., and Zviagina, B. B. 2009. “Trans-Vacant and Cis-Vacant 2:1 Layer Silicates: Structural Features, Identification, and Occurrence.” *Clays and Clay Minerals* 57 (4): 405–15. https://doi.org/10.1346/CCMN.2009.0570401.

Eastoe, J., Robinson, B. H., and Steytler, D. C.. 1990. “Influence of Pressure and Temperature on Microemulsion Stability.” *J. CHEM. SOC. FARADAY TRANS.* 86 (3): 511–17.

Eastwood, J.W., Hockney, R.W., and Lawrence, D.N. 1984. “P3M3DP-the Three-Dimensional Periodic Particle-Particle/Particle-Mesh Program.” *Computer Physics Communications* 35 (January): C–618. https://doi.org/10.1016/S0010-4655(84)82783-6.

EIA. 2019. “International Energy Outlook.” *Outlook* 0484 (July): 70–99. https://doi.org/https://www.eia.gov/outlooks/ieo/pdf/ieo2019.pdf.

Evans, D. J. and Morriss, G. P. 1984. “Nonlinear-Response Theory for Steady Planar Couette Flow.” *Physical Review* 30 (3): 1528–30. https://doi.org/10.1103/PhysRevA.30.1528.

Eveline, V. F, Akkutlu, I Y., and Texas, A. 2018. “SPE-191599-MS Osmosis and Clay Swelling Effects in Gas Shale Formations under Stress,” no. September: 24–26.

Falk, K., Sedlmeier, F., Joly, L. et al. 2012. “Ultralow Liquid/Solid Friction in Carbon Nanotubes: Comprehensive Theory for Alcohols, Alkanes, OMCTS, and Water.” *Langmuir* 28 (40): 14261–72. https://doi.org/10.1021/la3029403.

Fan, B., Bhattacharya, A., and Bandaru, P. R. 2018. “Enhanced Voltage Generation through Electrolyte Flow on Liquid-Filled Surfaces.” *Nature Communications* 9 (1): 1–7. https://doi.org/10.1038/s41467-018-06297-9.

Fang, T., Zhang, Y., Yan, Y. et al. 2020. “Molecular Insight into the Aggregation and Dispersion Behavior of Modified Nanoparticles.” *Journal of Petroleum Science and Engineering* 191: 107193. https://doi.org/https://doi.org/10.1016/j.petrol.2020.107193.

Ferrari, L., Kaufmann, J., Winnefeld, F. et al. 2010. “Interaction of Cement Model Systems with Superplasticizers Investigated by Atomic Force Microscopy, Zeta Potential, and Adsorption Measurements.” *Journal of Colloid and Interface Science* 347 (1): 15–24. https://doi.org/10.1016/j.jcis.2010.03.005.

Frenkel, D., and Smit, B. 2002. “Chapter 4 - Molecular Dynamics Simulations.” In , edited by Daan Frenkel and Berend B T - Understanding Molecular Simulation (Second Edition) Smit, 63–107. San Diego: Academic Press. https://doi.org/https://doi.org/10.1016/B978-012267351-1/50006-7.

Fuchs, E. C., Gatterer, K., Holler, G. et al. 2008. “Dynamics of the Floating Water Bridge.” *Journal of Physics D: Applied Physics* 41 (18): 2–7. https://doi.org/10.1088/0022-3727/41/18/185502.

Fuchs, E. C., Woisetschläger, J., Gatterer, K. et al. 2007. “The Floating Water Bridge.” *Journal of Physics D: Applied Physics* 40 (19): 6112–14. https://doi.org/10.1088/0022-3727/40/19/052.

Galán, E., and Ferrell, R.E.. 2013. “Genesis of Clay Minerals.” *Developments in Clay Science* 5 (January): 83–126. https://doi.org/10.1016/B978-0-08-098258-8.00003-1.

Galliano, G., Federici, M., and Cavallaro, A. 2000. “Formation Damage Control:

Selecting Optimum Salinity in a Waterflooding Pilot." *Canadian International Petroleum Conference 2000, CIPC 2000* 41 (2): 55–61. https://doi.org/10.2118/2000-054.

Gamadi, T.D., Sheng, J.J., and Soliman, M.Y. 2013. "An Experimental Study of Cyclic Gas Injection to Improve Shale Oil Recovery." *SPE Annual Technical Conference and Exhibition*, 1–9. https://doi.org/10.2118/166334-MS.

Geramian, M., Osacky, M., Ivey, D. G. et al. 2016. "Effect of Swelling Clay Minerals (Montmorillonite and Illite-Smectite) on Nonaqueous Bitumen Extraction from Alberta Oil Sands." *Energy and Fuels* 30 (10): 8083–90. https://doi.org/10.1021/acs.energyfuels.6b01026.

Ghaffari, A., and Kelishami, A. R. 2013. "MD Simulation and Evaluation of the Self-Diffusion Coefficients in Aqueous NaCl Solutions at Different Temperatures and Concentrations." *Journal of Molecular Liquids* 187: 238–45. https://doi.org/https://doi.org/10.1016/j.molliq.2013.08.004.

Giner, I., Torun, B., Han, Y. et al. 2019. "Water Adsorption and Capillary Bridge Formation on Silica Micro-Particle Layers Modified with Perfluorinated Organosilane Monolayers." *Applied Surface Science* 475 (December 2018): 873–79. https://doi.org/10.1016/j.apsusc.2018.12.221.

Gouth, F., Collell, J., Galliero, G. et al. 2013. "Molecular Simulation To Determine Key Shale Gas Parameters, And Their Use In A Commercial Simulator For Production Forecasting." *EAGE Annual Conference & Exhibition Incorporating SPE Europec*. London, UK: Society of Petroleum Engineers. https://doi.org/10.2118/164790-MS.

Gray, A. 1895. "Clausius' Virial Theorem." *Nature* 52: 568. https://doi.org/https://doi.org/10.1038/052568a0.

Green, M. S. 1954. "Markoff Random Processes and the Statistical Mechanics of Time-Dependent Phenomena. II. Irreversible Processes in Fluids." *The Journal of Chemical Physics* 22 (3): 398–413. https://doi.org/10.1063/1.1740082.

Gualtieri, A. F., Ferrari, S., Leoni, M. et al. 2008. "Structural Characterization of the Clay Mineral Illite-1M." *Journal of Applied Crystallography* 41 (2): 402–15. https://doi.org/10.1107/S0021889808004202.

Guichet, X., Fleury, M., and Kohler, E. 2008. "Effect of Clay Aggregation on Water Diffusivity Using Low Field NMR." *Journal of Colloid and Interface Science* 327 (1): 84–93. https://doi.org/10.1016/j.jcis.2008.08.013.

Hamidian, R., Lashkarbolooki, M., and Amani, H. 2019. "Ion Type Adjustment with Emphasize on the Presence of NaCl Existence; Measuring Interfacial Tension, Wettability and Spreading of Crude Oil in the Carbonate Reservoir." *Journal of Petroleum Science and Engineering* 182: 106266. https://doi.org/https://doi.org/10.1016/j.petrol.2019.106266.

Hans-J., Karlheinz, B., and Kappl, G. M. 2003. "Physics and Chemistry of Interfaces." In *Wiley-VCH Verlag GmbH & Co. KGaA*, 42–56.

Hansen, J. S., Todd, B. D., and Daivis, P. J. 2011. "Prediction of Fluid Velocity Slip at Solid Surfaces." *Physical Review E - Statistical, Nonlinear, and Soft Matter*

Physics 84 (1): 1–8. https://doi.org/10.1103/PhysRevE.84.016313.

Hao, Y., Jia, X., Lu, Z. et al. 2019a. "Water Film or Water Bridge ? In Fl Uence of Self-Generated Electric Field on Coexisting Patterns of Water and Methane in Clay Nanopores." *Journal of Physical Chemistry C*. https://doi.org/10.1021/acs.jpcc.9b06519.

Hao, Y., Jia, X., Lu, Z. et al.. 2019b. "Water Film or Water Bridge? Influence of Self-Generated Electric Field on Coexisting Patterns of Water and Methane in Clay Nanopores." Research-article. *Journal of Physical Chemistry C* 123 (36): 22656–64. https://doi.org/10.1021/acs.jpcc.9b06519.

Hao, Y., Yuan, L., Li, P. et al. 2018. "Molecular Simulations of Methane Adsorption Behavior in Illite Nanopores Considering Basal and Edge Surfaces." *Energy and Fuels* 32 (4): 4783–96. https://doi.org/10.1021/acs.energyfuels.8b00070.

Harder, E., Eaves, J. D., Tokmakoff, A. et al. 2005. "Polarizable Molecules in the Vibrational Spectroscopy of Water." *Proceedings of the National Academy of Sciences of the United States of America* 102 (33): 11611–16. https://doi.org/10.1073/pnas.0505206102.

He, Y., Yang, B., Cheng, G. et al. 2004. "Influence of the Thermodynamic Stability of Microemulsion on the Size of Nanoparticles Prepared by a Coupling Route of Microemulsion with Homogeneous Precipitation." *Materials Letters* 58 (14): 2019–22. https://doi.org/10.1016/j.matlet.2003.12.033.

Heidari, Z., Verdín, C. T., and Preeg, W. E. 2011. "Quantitative Method for Estimating Total Organic Carbon and Porosity , and for Diagnosing Mineral Constituents From Well Logs in Shale-Gas Formations." *SPWLA 52nd Annual Logging Symposium*, 1–15.

Hensen, E. J.M., and Smit, B. 2002. "Why Clays Swell." *Journal of Physical Chemistry B* 106 (49): 12664–67. https://doi.org/10.1021/jp0264883.

Ho, T. A., and Striolo, A. 2015. "Water and Methane in Shale Rocks: Flow Pattern Effects on Fluid Transport and Pore Structure." *AIChE Journal* 61 (9): 2993–99. https://doi.org/10.1002/aic.14869.

Hoffman, B. T. 2013. "Comparison of Various Gases for Enhanced Recovery from Shale Oil Reservoirs." *SPE Conference*, no. 1: 1–8. https://doi.org/10.2118/154329-MS.

Hoffman, B. T, and Evans, J. G. 2016. "Improved Oil Recovery IOR Pilot Projects in the Bakken Formation." *SPE Low Perm Symposium*, no. May: 5–6. https://doi.org/10.2118/180270-MS.

Holz, M., Heil, S. R., and Sacco, A.. 2000. "Temperature-Dependent Self-Diffusion Coefficients of Water and Six Selected Molecular Liquids for Calibration in Accurate 1H NMR PFG Measurements." *Physical Chemistry Chemical Physics* 2 (20): 4740–42. https://doi.org/10.1039/b005319h.

Howard, J. J., Perkyns, J. S., and Pettitt, B. M. 2010. "The Behavior of Ions near a Charged Wall-Dependence on Ion Size, Concentration, and Surface Charge." *Journal of Physical Chemistry B* 114 (18): 6074–83.

https://doi.org/10.1021/jp9108865.

Hu, Y., Devegowda, D., and Sigal, R. 2016. "A Microscopic Characterization of Wettability in Shale Kerogen with Varying Maturity Levels." *Journal of Natural Gas Science and Engineering* 33 (July): 1078–86. https://doi.org/10.1016/J.JNGSE.2016.06.014.

Hu, Y., Devegowda, D., Striolo, A. et al. 2015. "Microscopic Dynamics of Water and Hydrocarbon in Shale-Kerogen Pores of Potentially Mixed Wettability." *SPE Journal* 20 (1): 112–24. https://doi.org/10.2118/167234-pa.

Huang, L., Ning, Z., Wang, Q. et al. 2018. "Effect of Organic Type and Moisture on CO2/CH4 Competitive Adsorption in Kerogen with Implications for CO2 Sequestration and Enhanced CH4 Recovery." *Applied Energy* 210 (July 2017): 28–43. https://doi.org/10.1016/j.apenergy.2017.10.122.

Huang, S., Xiong, H., Wei, S.et al. 2016. "Physical Simulation of the Interlayer Effect on SAGD Production in Mackay River Oil Sands." *Fuel* 183 (November): 373–85. https://doi.org/10.1016/J.FUEL.2016.06.104.

Huber, F., Berwanger, J., Polesya, S. et al. 2019. "Chemical Bond Formation Showing a Transition from Physisorption to Chemisorption." *Science* 3444 (September): eaay3444. https://doi.org/10.1126/science.aay3444.

Humphrey, W., Dalke, A., and Schulten, K. 1996. "VMD: Visual Molecular Dynamics." *Journal of Molecular Graphics* 14 (1): 33–38. https://doi.org/10.1016/0263-7855(96)00018-5.

Hwang, J., Joss, L., and Pini, R. 2019. "Measuring and Modelling Supercritical Adsorption of CO2 and CH4 on Montmorillonite Source Clay." *Microporous and Mesoporous Materials* 273 (January): 107–21. https://doi.org/10.1016/J.MICROMESO.2018.06.050.

Jin, Z., and Firoozabadi, A. 2013. "Methane and Carbon Dioxide Adsorption in Clay-like Slit Pores by Monte Carlo Simulations." *Fluid Phase Equilibria* 360: 456–65. https://doi.org/10.1016/j.fluid.2013.09.047.

Jin, Z., and Firoozabadi, A. 2014. "Effect of Water on Methane and Carbon Dioxide Sorption in Clay Minerals by Monte Carlo Simulations." *Fluid Phase Equilibria* 382: 10–20. https://doi.org/10.1016/j.fluid.2014.07.035.

Jin, Z., and Firoozabadi, A. 2016. "Fluid Phase Equilibria Phase Behavior and Fl Ow in Shale Nanopores from Molecular Simulations." *Fluid Phase Equilibria* 430: 156–68. https://doi.org/10.1016/j.fluid.2016.09.011.

Jorgensen, W. L., Maxwell, D. S., and Rives, J. 1996. "Development and Testing of the OPLS All-Atom Force Field on Conformational Energetics and Properties of Organic Liquids." *Journal of the American Chemical Society* 118 (45): 11225–36. https://doi.org/10.1021/ja9621760.

Kadoura, A., Kumar, A., and Sun, S. 2016. "Molecular Dynamics Simulations of Carbon Dioxide, Methane, and Their Mixture in Montmorillonite Clay Hydrates." *Journal of Physical Chemistry C* 120 (23): 12517–29. https://doi.org/10.1021/acs.jpcc.6b02748.

Kahl, H., and Enders, S. 2002. “Thermodynamics of Carbohydrate Surfactant Containing Systems.” *Fluid Phase Equilibria* 194–197: 739–53. https://doi.org/https://doi.org/10.1016/S0378-3812(01)00701-4.

Kalra, A., Garde, S., and Hummer, G. 2003. “Osmotic Water Transport through Carbon Nanotube Membranes.” *Proceedings of the National Academy of Sciences of the United States of America* 100 (18): 10175–80. https://doi.org/10.1073/pnas.1633354100.

Katti, D. R., Thapa, K. B., and Katti, K. S.. 2017. “Modeling Molecular Interactions of Sodium Montmorillonite Clay with 3D Kerogen Models.” *Fuel* 199 (July): 641–52. https://doi.org/10.1016/J.FUEL.2017.03.021.

Kazemi, M., and Borujeni, A. 2016. “Multiscale Modeling of Gas Transport in Organic-Rich Shale: From Molecular Scale to Core Plug Scale.” *SPE/AAPG/SEG Unconventional Resources Technology Conference*. San Antonio, Texas, USA: Unconventional Resources Technology Conference. https://doi.org/10.15530/URTEC-2016-2460802.

Kazemi, M., and Borujeni, A.. 2019. “Enhanced Oil Recovery of Shale Oil: A Molecular Simulation Study.” *SPE/AAPG/SEG Unconventional Resources Technology Conference*. Denver, Colorado, USA: Unconventional Resources Technology Conference. https://doi.org/10.15530/urtec-2019-937.

Keffer, D. 2001. “The Working Man’s Guide to Obtaining Self Diffusion Coefficients from Molecular Dynamics Simulations.” *Course Website*. https://doi.org/http://www.cs.unc.edu/Research/nbody/pubs/external/Keffer/self D.pdf.

Keffer, D. J., and Adhangale, P. 2004. “The Composition Dependence of Self and Transport Diffusivities from Molecular Dynamics Simulations.” *Chemical Engineering Journal* 100 (1–3): 51–69. https://doi.org/10.1016/j.cej.2003.11.028.

Kim, C. 2020. “A MOLECULAR DYNAMICS STUDY OF SPATIAL FLUID DISTRIBUTION IN MIXED- WET SHALE NANOPORES.” *Master Thesis*.

Kim, J. S., Wu, Z., Morrow, A. R. et al. 2012. “Self-Diffusion and Viscosity in Electrolyte Solutions.” *Journal of Physical Chemistry B* 116 (39): 12007–13. https://doi.org/10.1021/jp306847t.

Klein, J., and Kumacheva, E. 1998. “Simple Liquids Confined to Molecularly Thin Layers. I. Confinement-Induced Liquid-to-Solid Phase Transitions.” *Journal of Chemical Physics* 108 (16): 6996–7009. https://doi.org/10.1063/1.476114.

Klier, J, Tucker, C. J., Kalantar, T. H. et al. 2000. “Properties and Applications of Microemulsions.” *Advanced Materials* 12 (23): 1751–57. https://doi.org/10.1002/1521-4095(200012)12:23<1751::AID-ADMA1751>3.0.CO;2-I.

Koleini, M. M., Badizad, M. H., Kargozarfard, Z. et al. 2019a. “Interactions between Rock/Brine and Oil/Brine Interfaces within Thin Brine Film Wetting Carbonates: A Molecular Dynamics Simulation Study.” Research-article. *Energy & Fuels* 33: 7983–92. https://doi.org/10.1021/acs.energyfuels.9b00496.

Koleini, M. M., Badizad, M. H., Kargozarfard, Z. et al.. 2019b. “Interactions between Rock/Brine and Oil/Brine Interfaces within Thin Brine Film Wetting Carbonates: A Molecular Dynamics Simulation Study.” *Energy and Fuels* 33 (9): 7983–92. https://doi.org/10.1021/acs.energyfuels.9b00496.

Krapf, D., and Metzler, R. 2019. “Strange Interfacial Molecular Dynamics.” *Physics Today* 72 (9): 49–54. https://doi.org/10.1063/PT.3.4294.

Kubiak-Ossowska, K., Burley, G., Patwardhan, S. V. et al. 2013. “Spontaneous Membrane-Translocating Peptide Adsorption at Silica Surfaces: A Molecular Dynamics Study.” *Journal of Physical Chemistry B* 117 (47): 14666–75. https://doi.org/10.1021/jp409130s.

Kuila, U., and Prasad, M. 2013. “Specific Surface Area and Pore-Size Distribution in Clays and Shales.” *Geophysical Prospecting* 61 (2): 341–62. https://doi.org/10.1111/1365-2478.12028.

Kumar, N., Andersson, M. P., Ende , D. et al. 2017. “Probing the Surface Charge on the Basal Planes of Kaolinite Particles with High-Resolution Atomic Force Microscopy.” *Langmuir* 33 (50): 14226–37. https://doi.org/10.1021/acs.langmuir.7b03153.

Lager, A., Webb, K. J., Black, C. J.J. et al. 2008. “Low Salinity Oil Recovery - An Experimental Investigation.” *Petrophysics* 49 (1): 28–35.

Lamura, A., Gompper, G., Ihle, T. et al. 2001. “Multi-Particle Collision Dynamics : Flow around a Circular.” *Europhysics Letters* 56 (3): 319–25.

Lara, L. S., Rigo, V. A., and Miranda, C. R. 2017. “Controlling Clay Swelling-Shrinkage with Inorganic Nanoparticles: A Molecular Dynamics Study.” *Journal of Physical Chemistry C* 121 (37): 20266–71. https://doi.org/10.1021/acs.jpcc.7b05130.

Lee, J., and Babadagli, T. 2018. “Improvement of Microemulsion Generation and Stability Using New Generation Chemicals and Nano Materials during Waterflooding as a Cost-Efficient Heavy-Oil Recovery Method.” *Society of Petroleum Engineers - SPE Trinidad and Tobago Section Energy Resources Conference 2018*. https://doi.org/10.2118/191171-ms.

Leike, A. 2002. “Demonstration of the Exponential Decay Law Using Beer Froth.” *European Journal of Physics* 23 (1): 21–26. https://doi.org/10.1088/0143-0807/23/1/304.

Lennard-Jones, J. E. 1924. “On the Determination o f Molecular Fields. — II. From the Equation o f State o f a Gas.” *Proc. R. Soc. Lond.* 4 (71). https://doi.org/10.1098/rspa.1924.0082.

Leroch, S., and Wendland, M.. 2013. “Influence of Capillary Bridge Formation onto the Silica Nanoparticle Interaction Studied by Grand Canonical Monte Carlo Simulations.” *Langmuir* 29 (40): 12410–20. https://doi.org/10.1021/la402002f.

Li, J., Li, X., Wu, K. et al. 2016. “Water Sorption and Distribution Characteristics in Clay and Shale: Effect of Surface Force.” *Energy and Fuels* 30 (11): 8863–74. https://doi.org/10.1021/acs.energyfuels.6b00927.

Li, W., and Jin, Z. 2019. “Molecular Dynamics Simulations of Natural Gas-Water Interfacial Tensions over Wide Range of Pressures.” *Fuel* 236: 480–92. https://doi.org/https://doi.org/10.1016/j.fuel.2018.09.040.

Li, X., Li, H., and Yang, D. 2013. “Determination of Multiphase Boundaries and Swelling Factors of Solvent(s)-CO2-Heavy Oil Systems at High Pressures and Elevated Temperatures.” *Energy and Fuels* 27 (3): 1293–1306. https://doi.org/10.1021/ef301866e.

Liu, B., Qi, C., Zhao, X. et al. 2018. “Nanoscale Two-Phase Flow of Methane and Water in Shale Inorganic Matrix.” Research-article. *Journal of Physical Chemistry C* 122: 26671–79. https://doi.org/10.1021/acs.jpcc.8b06780.

Liu, B., Wang, C., Zhang, J. et al. 2017. “Displacement Mechanism of Oil in Shale Inorganic Nanopores by Supercritical Carbon Dioxide from Molecular Dynamics Simulations.” *Energy and Fuels* 31 (1): 738–46. https://doi.org/10.1021/acs.energyfuels.6b02377.

Liu, B., Wu, R., Baimova, J. A. et al. 2016. “Molecular Dynamics Study of Pressure-Driven Water Transport through Graphene Bilayers.” *Physical Chemistry Chemical Physics* 18 (3): 1886–96. https://doi.org/10.1039/c5cp04976h.

Liu, N., Zhang, R., Li, Y. et al. 2014. “Local Electric Field Effect of TMI (Fe, Co, Cu)-BEA on N2O Direct Dissociation.” *Journal of Physical Chemistry C* 118 (20): 10944–56. https://doi.org/10.1021/jp5023949.

Liu, Y., Jin, Z., and Li, H. 2018. “Comparison of Peng-Robinson Equation of State With Capillary Pressure Model With Engineering Density-Functional Theory in Describing the Phase Behavior of Confined Hydrocarbons.” *SPE Journal*, no. October 2017: 9–11. https://doi.org/10.2118/187405-PA.

Lockhart, N.C. 1980. “Electrical Properties and the Surface Characteristics and Structure of Clays.” *Journal of Colloid and Interface Science* 74 (2): 520–29.

Loewenstein, W. 1954. “The Distribution of Aluminum in the Tetrahedra of Silicates and Aluminates.” *American Mineralogist* 39: 92–96. https://doi.org/10.1002/anie.201004007.

Loring, J. S., Schaef, H. T., Thompson, C. J. et al. 2013. “Clay Hydration/Dehydration in Dry to Water-Saturated Supercritical CO 2: Implications for Caprock Integrity.” *Energy Procedia* 37: 5443–48. https://doi.org/10.1016/j.egypro.2013.06.463.

Low, P. F. 1961. “Physical Chemistry of Clay-Water Interaction.” *Advances in Agronomy* 13 (C): 269–327. https://doi.org/10.1016/S0065-2113(08)60962-1.

Ma, J., Song, X., Luo, J. et al. 2019. “Molecular Dynamics Simulation Insight into Interfacial Stability and Fluidity Properties of Microemulsions.” *Langmuir* 35 (42): 13636–45. https://doi.org/10.1021/acs.langmuir.9b02325.

Malevanets, A. 1999. “Mesoscopic Model for Solvent Dynamics.” *Journal of Chemical Physics* 110 (17): 8605–13. https://doi.org/10.1063/1.478857.

Malevanets, A., and Kapral, R. 2000. “Solute Molecular Dynamics in a Mesoscale Solvent.” *Journal of Chemical Physics* 112 (16): 7260–69. https://doi.org/10.1063/1.481289.

Malmberg, C.G., and Maryott, A.A. 1956. “Dielectric Constant of Water from 0 to 100 C.” *Journal of Research of the National Bureau of Standards* 56 (1): 1. https://doi.org/10.6028/jres.056.001.

Mamoudou, S., Perez, F., Tinni, A. et al. 2020. “Evaluation of Huff-n-Puff in Shale Using Experiments and Molecular Simulations.” *SPE/AAPG/SEG Unconventional Resources Technology Conference*. Virtual: Unconventional Resources Technology Conference. https://doi.org/10.15530/urtec-2020-2923.

Martínez, J. M., and Martínez, L. 2003. “Packing Optimization for Automated Generation of Complex System’s Initial Configurations for Molecular Dynamics and Docking.” *Journal of Computational Chemistry* 24 (7): 819–25. https://doi.org/10.1002/jcc.10216.

Martins Costa, M. T.C. 2005. “QM/MM Simulations of Polyols in Aqueous Solution.” *Journal of Molecular Structure: THEOCHEM* 729 (1-2 SPEC. ISS.): 47–52. https://doi.org/10.1016/j.theochem.2005.03.016.

Méring, J., and Brindley, G. W. 1967. “X-Ray Diffraction Band Profiles of Montmorillonite—Influence of Hydration and of the Exchangeable Cations.” *Clays and Clay Minerals* 15 (1): 51–60. https://doi.org/10.1346/CCMN.1967.0150107.

Mondal, A., and Balasubramanian, S. 2014. “A Molecular Dynamics Study of Collective Transport Properties of Imidazolium-Based Room-Temperature Ionic Liquids.” *Journal of Chemical and Engineering Data* 59 (10): 3061–68. https://doi.org/10.1021/je500132u.

Monson, P. A. 2012. “Understanding Adsorption/Desorption Hysteresis for Fluids in Mesoporous Materials Using Simple Molecular Models and Classical Density Functional Theory.” *Microporous and Mesoporous Materials* 160: 47–66. https://doi.org/10.1016/j.micromeso.2012.04.043.

Montazeri, R., Lindi, S. A., Amjadi, A. et al. 2013. “Experimental Investigation of the Stability of the Floating Water Bridge.” *Physical Review E - Statistical, Nonlinear, and Soft Matter Physics* 88 (3): 1–6. https://doi.org/10.1103/PhysRevE.88.033019.

Morrow, N., and Buckley, J. 2011. “Improved Oil Recovery by Low-Salinity Waterflooding.” *Journal of Petroleum Technology* 63 (05): 106–12. https://doi.org/10.2118/129421-jpt.

Mosher, K., He, J., Liu, Y. et al. 2013. “Molecular Simulation of Methane Adsorption in Micro- and Mesoporous Carbons with Applications to Coal and Gas Shale Systems.” *International Journal of Coal Geology* 109–110: 36–44. https://doi.org/10.1016/j.coal.2013.01.001.

Mouas, M., Gasser, J. G., Hellal, S. et al. 2012. “Diffusion and Viscosity of Liquid Tin: Green-Kubo Relationship-Based Calculations from Molecular Dynamics Simulations.” *Journal of Chemical Physics* 136 (9). https://doi.org/10.1063/1.3687243.

Moučka, F., Svoboda, M., and Lísal, M. 2017. “Modelling Aqueous Solubility of Sodium Chloride in Clays at Thermodynamic Conditions of Hydraulic Fracturing

by Molecular Simulations." *Physical Chemistry Chemical Physics* 19 (25): 16586–99. https://doi.org/10.1039/c7cp02121f.

Mueller, K. T., Sanders, R. L., and Washton, N. M. 2014. "Clay Minerals." *EMagRes* 3 (1): 13–28. https://doi.org/10.1002/9780470034590.emrstm1332.

Müller, F.. 1997. "A Simple Nonequilibrium Molecular Dynamics Method for Calculating the Thermal Conductivity." *The Journal of Chemical Physics* 106 (14): 6082–85. https://doi.org/10.1063/1.473271.

Nelson, P. H. 2009. "Pore-Throat Sizes in Sandstones, Tight Sandstones, and Shales." *AAPG Bulletin* 93 (3): 329–40. https://doi.org/10.1306/10240808059.

Nguyen, M. N., Dultz, S., Kasbohm, J. et al. 2009. "Clay Dispersion and Its Relation to Surface Charge in a Paddy Soil of the Red River Delta, Vietnam." *Journal of Plant Nutrition and Soil Science* 172 (4): 477–86. https://doi.org/10.1002/jpln.200700217.

Nikoubashman, A., and Likos, C. N. 2010. "Flow-Induced Polymer Translocation through Narrow and Patterned Channels." *Journal of Chemical Physics* 133 (7). https://doi.org/10.1063/1.3466918.

Nikoubashman, A., and Likos, C. N. 2013. "Computer Simulations of Colloidal Particles under Flow in Microfluidic Channels." *Soft Matter* 9 (9): 2603–13. https://doi.org/10.1039/c2sm26727f.

Noé, F. 2018. "Machine Learning for Molecular Dynamics on Long Timescales," 1–27. http://arxiv.org/abs/1812.07669.

Nosé, S. 1984. "A Unified Formulation of the Constant Temperature Molecular Dynamics Methods." *The Journal of Chemical Physics* 81 (1): 511–19. https://doi.org/10.1063/1.447334.

Orton, E., Kern, K. F., Maegdefrau, E et al. 1906. "FUNDAMENTAL STUDY OF CLAY: II MECHANISM OF DEFLOCCULATION IN THE CLAY-WATER SYSTEM." *Journal of the American Ceramic Society* 11 (1891).

Osipov, V. I. 2012. "Nanofilms of Adsorbed Water in Clay: Mechanism of Formation and Properties." *Water Resources* 39 (7): 709–21. https://doi.org/10.1134/s009780781207010x.

P. Allen, M, and Tildesley, D J.. 1988. *Computer Simulation of Liquids / M.P. Allen, D.J. Tildesley.*

Parrinello, M., and Rahman, A.. 1981. "Polymorphic Transitions in Single Crystals: A New Molecular Dynamics Method." *Journal of Applied Physics* 52 (12): 7182–90. https://doi.org/10.1063/1.328693.

Peng, D., and Robinson, D. B.. 1976. "Two and Three Phase Equilibrium Calculations for Systems Containing Water." *The Canadian Journal of Chemical Engineering* 54 (5): 595–99. https://doi.org/10.1002/cjce.5450540541.

Penny, G., Zelenev, A., Lett, N. et al. 2012. "SPE 154308 Nanofluid System Improves Post Frac Oil and Gas Recovery in Hydrocarbon Rich Gas Reservoirs Alcohol Ethoxylates Can Be Used Independently or in Combination with Demulsifier Bases C10-12 with 4 to 9 Moles EO."

Perez, F. 2020. “Production of Hydrocarbons from Organic Nanopores : A Comprehensive Study Using Molecular Dynamics.” *Phd Thesis*.

Perez, F., and Devegowda, D. 2020a. “A Molecular Dynamics Study of Primary Production from Shale Organic Pores.” *SPE Journal* Preprint (Preprint): 13. https://doi.org/10.2118/201198-PA.

Perez, F., and Devegowda, D.. 2020b. “A Molecular Dynamics Study of Soaking During Enhanced Oil Recovery in Shale Organic Pores.” *SPE Journal* 25 (02): 832–41. https://doi.org/10.2118/199879-PA.

Perez, F., and Devegowda, D.. 2020c. “A Molecular Dynamics Study of Soaking During Enhanced Oil Recovery in Shale Organic Pores.” *SPE Journal*, no. May 2019: 832–41. https://doi.org/10.2118/201198-pa.

Pevear, D. R. 1999. “Illite and Hydrocarbon Exploration.” *Proceedings of the National Academy of Sciences* 96 (7): 3440–46. https://doi.org/10.1073/pnas.96.7.3440.

Phan, A., Ho, T. A., Cole, D. R. et al. 2012. “Molecular Structure and Dynamics in Thin Water Films at Metal Oxide Surfaces: Magnesium, Aluminum, and Silicon Oxide Surfaces.” *Journal of Physical Chemistry C* 116 (30): 15962–73. https://doi.org/10.1021/jp300679v.

Plimpton, S. 1995. “Fast Parallel Algorithms for Short-Range Molecular Dynamics.” *Journal of Computational Physics* 117 (1): 1–19. https://doi.org/https://doi.org/10.1006/jcph.1995.1039.

Ponterio, R. C., Pochylski , M., Vasi, F. A. et al. 2010. “Raman Scattering Measurements on a Floating Water Bridge.” *Journal of Physics D: Applied Physics* 43 (17). https://doi.org/10.1088/0022-3727/43/17/175405.

Prakash, S., Zambrano, H. A., Fuest, M. et al. 2015. “Electrokinetic Transport in Silica Nanochannels with Asymmetric Surface Charge.” *Microfluidics and Nanofluidics* 19 (6): 1455–64. https://doi.org/10.1007/s10404-015-1659-0.

Price, M. L.P., Ostrovsky, D., and Jorgensen, W. L. 2001. “Gas-Phase and Liquid-State Properties of Esters, Nitriles, and Nitro Compounds with the OPLS-AA Force Field.” *Journal of Computational Chemistry* 22 (13): 1340–52. https://doi.org/10.1002/jcc.1092.

Rareem, K. 2016. “Nano Geochemistry of Low Salinity Enhanced Oil Recovery.” *PhD Thesis, Durham University*.

Rahromostaqim, M., and Sahimi, M. 2018. “Molecular Dynamics Simulation of Hydration and Swelling of Mixed-Layer Clays.” Research-article. *Journal of Physical Chemistry C* 122 (26): 14631–39. https://doi.org/10.1021/acs.jpcc.8b03693.

Rao, Q., Xiang, Y., and Leng, Y. 2013. “Molecular Simulations on the Structure and Dynamics of Water-Methane Fluids between Na-Montmorillonite Clay Surfaces at Elevated Temperature and Pressure.” *Journal of Physical Chemistry C* 117 (27): 14061–69. https://doi.org/10.1021/jp403349p.

Richard, D., and Rendtorff, N. M. 2019. “First Principles Study of Structural Properties and Electric Field Gradients in Kaolinite.” *Applied Clay Science* 169 (November

2018): 67–73. https://doi.org/10.1016/j.clay.2018.12.013.

Rigo, E., Dong, Z., Park, J. H. et al. 2019. “Measurements of the Size and Correlations between Ions Using an Electrolytic Point Contact.” *Nature Communications* 10 (1): 2382. https://doi.org/10.1038/s41467-019-10265-2.

Ryckaert, J. P., Ciccotti, G., and Berendsen, H. J.C. 1977. “Numerical Integration of the Cartesian Equations of Motion of a System with Constraints: Molecular Dynamics of n-Alkanes.” *Journal of Computational Physics* 23 (3): 327–41. https://doi.org/10.1016/0021-9991(77)90098-5.

Saarenketo, T. 1998. “Electrical Properties of Water in Clay and Silty Soils.” *Journal of Applied Geophysics* 40 (1–3): 73–88. https://doi.org/10.1016/S0926-9851(98)00017-2.

Sakhawoth, Y., Michot, L. J., Levitz, P.et al. 2017. “Flocculation of Clay Colloids Induced by Model Polyelectrolytes: Effects of Relative Charge Density and Size.” *ChemPhysChem* 18 (19): 2756–65. https://doi.org/10.1002/cphc.201700430.

Salahshoor, S., Fahes, M., and Teodoriu, C. 2018. “A Review on the Effect of Confinement on Phase Behavior in Tight Formations.” *Journal of Natural Gas Science and Engineering* 51 (March): 89–103. https://doi.org/10.1016/J.JNGSE.2017.12.011.

Sameni, A., Pourafshary, P., Ghanbarzadeh, M. et al. 2015. “Effect of Nanoparticles on Clay Swelling and Migration.” *Egyptian Journal of Petroleum* 24 (4): 429–37. https://doi.org/10.1016/j.ejpe.2015.10.006.

Schramm, L. L, and Novosad, J. J. 1992. “The Destabilization of Foams for Improved Oil Recovery by Crude Oils: Effect of the Nature of the Oil.” *Journal of Petroleum Science and Engineering* 7 (1): 77–90. https://doi.org/https://doi.org/10.1016/0920-4105(92)90010-X.

Shakeel, A., Safar, Z., Ibanez, M. et al. 2020. “Flocculation of Clay Suspensions by Anionic and Cationic Polyelectrolytes: A Systematic Analysis.” *Minerals* 10 (11): 1–24. https://doi.org/10.3390/min10110999.

Sharma, S., and Sheng, J. J. 2017. “A Comparative Study of Huff-n-Puff Gas and Solvent Injection in a Shale Gas Condensate Core.” *Journal of Natural Gas Science and Engineering* 38 (February): 549–65. https://doi.org/10.1016/J.JNGSE.2017.01.012.

Sheng, J. J. 2014. “Critical Review of Low-Salinity Waterflooding.” *Journal of Petroleum Science and Engineering* 120: 216–24. https://doi.org/10.1016/j.petrol.2014.05.026.

Sheng, J. J. 2015a. “Enhanced Oil Recovery in Shale Reservoirs by Gas Injection.” *Journal of Natural Gas Science and Engineering* 22: 252–59. https://doi.org/10.1016/j.jngse.2014.12.002.

Sheng, J. J. 2015b. “Increase Liquid Oil Production by Huff-n-Puff of Produced Gas in Shale Gas Condensate Reservoirs.” *Journal of Unconventional Oil and Gas Resources* 11 (September): 19–26. https://doi.org/10.1016/J.JUOGR.2015.04.004.

Sheng, J. J. 2017. “Critical Review of Field EOR Projects in Shale and Tight

Reservoirs." *Journal of Petroleum Science and Engineering* 159 (November): 654–65. https://doi.org/10.1016/J.PETROL.2017.09.022.

Sheng, J. J. 2018. "Performance Analysis of Chemical Flooding in Fractured Shale and Tight Reservoirs." *Asia-Pacific Journal of Chemical Engineering* 13 (1): 1–16. https://doi.org/10.1002/apj.2147.

Sheng, J. J., and Chen, K. 2014. "Evaluation of the EOR Potential of Gas and Water Injection in Shale Oil Reservoirs." *Journal of Unconventional Oil and Gas Resources* 5 (March): 1–9. https://doi.org/10.1016/J.JUOGR.2013.12.001.

Singh, M. B., Harmalkar, A. U., Prabhu, S. S. et al. 2018. "Molecular Dynamics Simulation for Desulphurization of Hydrocarbon Fuel Using Ionic Liquids." *Journal of Molecular Liquids* 264: 490–98. https://doi.org/https://doi.org/10.1016/j.molliq.2018.05.088.

Singh, S., Sinha, A., Deo, G. et al. 2009. "Vapor-Liquid Phase Coexistence, Critical Properties, and Surface Tension of Confined Alkanes." *Journal of Physical Chemistry C* 113 (17): 7170–80. https://doi.org/10.1021/jp8073915.

Skinner, L. B., Benmore, C. J., Shyam, B. et al. 2012. "Structure of the Floating Water Bridge and Water in an Electric Field." *Proceedings of the National Academy of Sciences of the United States of America* 109 (41): 16463–68. https://doi.org/10.1073/pnas.1210732109.

Smalley, M. V. 1994. "Electrical Theory of Clay Swelling." *Langmuir* 10 (9): 2884–91. https://doi.org/10.1021/la00021a009.

Snosy, M. F., Ela, M., Banbi, A. et al. 2020. "Comprehensive Investigation of Low-Salinity Waterflooding in Sandstone Reservoirs." *Journal of Petroleum Exploration and Production Technology* 10 (5): 2019–34. https://doi.org/10.1007/s13202-020-00862-z.

Son, D. 2019. "Understanding the Fundamental Drive Mechanisms for Huff-n-Puff Enhanced Oil Recovery in Tight Formations." *Phd Thesis*. https://doi.org/10.13440/j.slxy.1674-0033.2018.05.002.

Sondergeld, C. H., Newsham, K. E., Comisky, J. T. et al. 2010. "Petrophysical Considerations in Evaluating and Producing Shale Gas Resources." *SPE Unconventional Gas Conference*. https://doi.org/10.2118/131768-MS.

Sposito, G. 2006. "Equilibrium Theory of the Kaolinite-Water System at Low Moisture Contents, with Some Remarks Concerning Adsorption Hysteresis." *Clays and Clay Minerals* 14 (1): 133–47. https://doi.org/10.1346/ccmn.1966.0140112.

Sposito, G, Skipper, N. T., Sutton, R. et al. 1999. "Surface Geochemistry of the Clay Minerals." *Proceedings of the National Academy of Sciences of the United States of America* 96 (7): 3358–64. https://doi.org/10.1073/pnas.96.7.3358.

Stone, J. E.. 1998. "An Efficient Library for Parallel." *Master's Thesis, University of Missouri, Rolla, Missouri, USA*.

Striolo A., Ho, T. A. 2015. "Water and Methane in Shale Rocks: Flow Pattern Effects on Fluid Transport and Pore Structure." *AIChE Journal* 60 (9): 2993–99. https://doi.org/10.1002/aic.

Stukowski, A. 2010. “Visualization and Analysis of Atomistic Simulation Data with OVITO-the Open Visualization Tool.” *Modelling and Simulation in Materials Science and Engineering* 18 (1). https://doi.org/10.1088/0965-0393/18/1/015012.

Sun, L., Hirvi, J. T., Schatz, T. et al. 2015. “Estimation of Montmorillonite Swelling Pressure: A Molecular Dynamics Approach.” *Journal of Physical Chemistry C* 119 (34): 19863–68. https://doi.org/10.1021/acs.jpcc.5b04972.

Sun, Z., Shi, J., Wu, K. et al. 2018. “Gas Flow Behavior through Inorganic Nanopores in Shale Considering Confinement Effect and Moisture Content.” *Industrial and Engineering Chemistry Research* 57 (9): 3430–40. https://doi.org/10.1021/acs.iecr.8b00271.

Svoboda, M., Moučka, F., and Lísal, M. 2018. “Saturated Aqueous NaCl Solution and Pure Water in Na-Montmorillonite Clay at Thermodynamic Conditions of Hydraulic Fracturing: Thermodynamics, Structure and Diffusion from Molecular Simulations.” *Journal of Molecular Liquids* 271: 490–500. https://doi.org/https://doi.org/10.1016/j.molliq.2018.08.144.

Szczerba, M., McCarty, D. K., Derkowski, A. et al. 2020. “Molecular Dynamics Simulations of Interactions of Organic Molecules Found in Oil with Smectite: Influence of Brine Chemistry on Oil Recovery.” *Journal of Petroleum Science and Engineering* 191: 107148. https://doi.org/https://doi.org/10.1016/j.petrol.2020.107148.

Tan, S. P., and Piri, M. 2015. “Equation-of-State Modeling of Associating-Fluids Phase Equilibria in Nanopores.” *Fluid Phase Equilibria* 405: 157–66. https://doi.org/10.1016/j.fluid.2015.07.044.

Tang, G. Q., and Morrow, N. R.. 1997. “Salinity, Temperature, Oil Composition, and Oil Recovery by Waterflooding.” *SPE Reservoir Engineering (Society of Petroleum Engineers)* 12 (4): 269–76. https://doi.org/10.2118/36680-PA.

Thomas, J. A., and McGaughey, A. 2009. “Water Flow in Carbon Nanotubes: Transition to Subcontinuum Transport.” *Physical Review Letters* 102 (18): 1–4. https://doi.org/10.1103/PhysRevLett.102.184502.

Tombácz, E., Nyilas, T., Libor, Z., and Csanaki, C. 2004. “Surface Charge Heterogeneity and Aggregation of Clay Lamellae in Aqueous Suspensions.” *Progress in Colloid and Polymer Science* 125: 206–15. https://doi.org/10.1007/b14303.

Tombácz, E., and Szekeres, M. 2006. “Surface Charge Heterogeneity of Kaolinite in Aqueous Suspension in Comparison with Montmorillonite.” *Applied Clay Science* 34 (1): 105–24. https://doi.org/https://doi.org/10.1016/j.clay.2006.05.009.

Torrealba, V.A., Johns, R.T., and Hoteit, H. 2019. “Curvature-Based Equation of State for Microemulsion-Phase Behavior.” *SPE Journal* 24 (2): 647–59. https://doi.org/10.2118/194022-PA.

Toukmaji, A. Y., and Board, J. A. 1996. “Ewald Summation Techniques in Perspective: A Survey.” *Computer Physics Communications* 95 (2–3): 73–92. https://doi.org/10.1016/0010-4655(96)00016-1.

Tovar, F. D., Eide, O., Graue, A. et al. 2014. “Experimental Investigation of Enhanced Recovery in Unconventional Liquid Reservoirs Using CO2: A Look Ahead to the Future of Unconventional EOR.” *SPE Unconventional Resources Conference* 1986: 1–3. https://doi.org/10.2118/169022-MS.

Umeda, K., Zivanovic, L., Kobayashi, K. et al. 2017. “Atomic-Resolution Three-Dimensional Hydration Structures on a Heterogeneously Charged Surface.” *Nature Communications* 8 (1): 1–9. https://doi.org/10.1038/s41467-017-01896-4.

Underwood, T., Erastova, V., Cubillas, P. et al. 2015. “Molecular Dynamic Simulations of Montmorillonite Organic Interactions under Varying Salinity: An Insight into Enhanced Oil Recovery.” *Journal of Physical Chemistry C* 119 (13): 7282–94. https://doi.org/10.1021/acs.jpcc.5b00555.

Underwood, T., Erastova, V., and Greenwell, H. C. 2016. “Wetting Effects and Molecular Adsorption at Hydrated Kaolinite Clay Mineral Surfaces.” *Journal of Physical Chemistry C* 120 (21): 11433–49. https://doi.org/10.1021/acs.jpcc.6b00187.

Underwood, T., and Greenwell, H. C. 2018. “The Water-Alkane Interface at Various NaCl Salt Concentrations: A Molecular Dynamics Study of the Readily Available Force Fields.” *Scientific Reports* 8 (1): 1–11. https://doi.org/10.1038/s41598-017-18633-y.

Ungerer, P., Collell, J., and Yiannourakou, M. 2015. “Molecular Modeling of the Volumetric and Thermodynamic Properties of Kerogen: Influence of Organic Type and Maturity.” *Energy and Fuels* 29 (1): 91–105. https://doi.org/10.1021/ef502154k.

Vlachy, V. 2001. “Ion-Partitioning between Charged Capillaries and Bulk Electrolyte Solution: An Example of Negative ‘Rejection.’” *Langmuir* 17 (2): 399–402. https://doi.org/10.1021/la000826e.

Wang, S., Feng, Q., Javadpour, F. et al. 2016. “Breakdown of Fast Mass Transport of Methane through Calcite Nanopores.” *Journal of Physical Chemistry C* 120 (26): 14260–69. https://doi.org/10.1021/acs.jpcc.6b05511.

Wang, S., Javadpour, F., and Feng, Q. 2016a. “Fast Mass Transport of Oil and Supercritical Carbon Dioxide through Organic Nanopores in Shale.” *Fuel* 181: 741–58. https://doi.org/10.1016/j.fuel.2016.05.057.

Wang, S., Javadpour, F., and Feng, Q.. 2016b. “Molecular Dynamics Simulations of Oil Transport through Inorganic Nanopores in Shale.” *Fuel* 171: 74–86. https://doi.org/10.1016/j.fuel.2015.12.071.

Wang, X., Luo, P., Er, V., et al. 2010. “Assessment of CO2 Flooding Potential for Bakken Formation , Saskatchewan.” *Society of Petroleum Engineers*, no. October: 1–14. https://doi.org/10.1016/j.tetlet.2003.08.106.

Wongkoblap, A., and Do, D. 2008. “Adsorption of Polar and Nonpolar Fluids in Finite-Length Carbon Slit Pore: A Monte Carlo Simulation Study.” *Chemical Engineering Communications* 195 (11): 1382–95. https://doi.org/10.1080/00986440801963733.

Xiong, H., Devegowda, D., and Huang, L. 2020. “Oil-Water Transport in Clay-Hosted Nanopores: Effects of Long-Range Electrostatic Forces.” *AIChE Journal* 16 (03): 129. https://doi.org/https://doi.org/10.1002/aic.16276.

Xiong, H., Devegowda, D., and Huang, L. 2019a. “EOR Solvent-Oil Interaction in Clay-Hosted Pores: Insights from Molecular Dynamics Simulations.” *Fuel* 249: 233–51. https://doi.org/https://doi.org/10.1016/j.fuel.2019.03.104.

Xiong, H., Devegowda, D., and Huang, L. 2019b. “EOR Solvent-Oil Interaction in Clay-Hosted Pores: Insights from Molecular Dynamics Simulations.” *Fuel* 249 (August): 233–51. https://doi.org/10.1016/j.fuel.2019.03.104.

Xiong, H., Devegowda, D., and Huang, L.2020a. “Water Bridges in Clay Nanopores: Mechanisms of Formation and Impact on Hydrocarbon Transport.” *Langmuir* 0 (ja). https://doi.org/10.1021/acs.langmuir.9b03244.

Xiong, H., Devegowda, D., and Huang, L. 2020b. “Water Bridges in Clay Nanopores: Mechanisms of Formation and Impact on Hydrocarbon Transport.” *Langmuir* 0 (0). https://doi.org/10.1021/acs.langmuir.9b03244.

Xiong, H, Huang, S., Devegowda, D. et al. 2019. “Influence of Pressure Difference Between Reservoir and Production Well on Steam-Chamber Propagation and Reservoir-Production Performance.” *SPE Journal* 24 (02): 452–76. https://doi.org/https://doi.org/10.2118/190107-PA.

Yamashita, K., and Daiguji, Y. 2013. “Molecular Simulations of Water Adsorbed on Mesoporous Silica Thin Films.” *Journal of Physical Chemistry C* 117 (5): 2084–95. https://doi.org/10.1021/jp312804c.

Yamashita, K., and Daiguji, Y.. 2015. “Molecular Dynamics Simulations of Water Uptake into a Silica Nanopore.” *Journal of Physical Chemistry C* 119 (6): 3012–23. https://doi.org/10.1021/jp5088493.

Yanagihara, H., Yamashita, K., Endo, A. et al. 2013. “Adsorption-Desorption and Transport of Water in Two-Dimensional Hexagonal Mesoporous Silica.” *Journal of Physical Chemistry C* 117 (42): 21795–802. https://doi.org/10.1021/jp405623p.

Yang, F., Ning, Z., Wang, Q. et al. 2016. “Pore Structure Characteristics of Lower Silurian Shales in the Southern Sichuan Basin, China: Insights to Pore Development and Gas Storage Mechanism.” *International Journal of Coal Geology* 156 (February): 12–24. https://doi.org/10.1016/J.COAL.2015.12.015.

Yang, Y., Huang, S., Liu, Y. et al. 2017. “A Multistage Theoretical Model To Characterize the Liquid Level During Steam-Assisted-Gravity-Drainage Process.” *SPE Journal* 22 (01): 327–38. https://doi.org/10.2118/183630-PA.

Ye, X., Cui, S., Almeida, V. et al. 2013. “Effect of Varying the 1-4 Intramolecular Scaling Factor in Atomistic Simulations of Long-Chain N-Alkanes with the OPLS-AA Model.” *Journal of Molecular Modeling* 19 (3): 1251–58. https://doi.org/10.1007/s00894-012-1651-5.

Yi, H., Jia, F., Zhao, Y. et al. 2018. “Surface Wettability of Montmorillonite (0 0 1) Surface as Affected by Surface Charge and Exchangeable Cations: A Molecular Dynamic Study.” *Applied Surface Science* 459: 148–54.

https://doi.org/https://doi.org/10.1016/j.apsusc.2018.07.216.

Yuan, N. 2018. “Improved Surfactant Performances in Porous Media: Effects of Hydrotropes and Bio-cosolvents..” *Master Thesis*.

Zen, A., Roch, L. M., Cox, S. J. et al. 2016. “Toward Accurate Adsorption Energetics on Clay Surfaces.” *Journal of Physical Chemistry C* 120 (46): 26402–13. https://doi.org/10.1021/acs.jpcc.6b09559.

Zhai, Z., Wang, X., Jin, X. et al. 2014. “Adsorption and Diffusion of Shale Gas Reservoirs in Modeled Clay Minerals at Different Geological Depths.” *Energy and Fuels* 28 (12): 7467–73. https://doi.org/10.1021/ef5023434.

Zhang, C., Hutter, J., and Sprik, M. 2019. “ Coupling of Surface Chemistry and Electric Double Layer at TiO 2 Electrochemical Interfaces .” *The Journal of Physical Chemistry Letters* 10 (14): 3871–76. https://doi.org/10.1021/acs.jpclett.9b01355.

Zhang, J., Clennell, M. B., Liu, K. et al. 2016a. “Methane and Carbon Dioxide Adsorption on Illite.” *Energy and Fuels* 30 (12): 10643–52. https://doi.org/10.1021/acs.energyfuels.6b01776.

Zhang, J., Clennell, M. B., Liu, K. et al.. 2016b. “Methane and Carbon Dioxide Adsorption on Illite.” *Energy & Fuels* 30 (12): 10643–52. https://doi.org/10.1021/acs.energyfuels.6b01776.

Zhang, L., Wu, P., Wei, Q. et al. 2016. “The Effect of Spacer on the Structure of Surfactant at Liquid/Air Interface: A Molecular Dynamics Simulation Study.” *Journal of Molecular Liquids* 222: 988–94. https://doi.org/https://doi.org/10.1016/j.molliq.2016.07.142.

Zhang, Y., Otani, A., and Maginn, E. J. 2015. “Reliable Viscosity Calculation from Equilibrium Molecular Dynamics Simulations: A Time Decomposition Method.” *Journal of Chemical Theory and Computation* 11 (8): 3537–46. https://doi.org/10.1021/acs.jctc.5b00351.

Zhao, J., Yao, G., Ramisetti, S. B., Hammond, R. B. et al. 2018. “Molecular Dynamics Simulation of the Salinity Effect on the N-Decane/Water/Vapor Interfacial Equilibrium.” *Energy and Fuels* 32 (11): 11080–92. https://doi.org/10.1021/acs.energyfuels.8b00706.

Zhao, P., Ma, H., Rasouli, V. et al. 2017. “An Improved Model for Estimating the TOC in Shale Formations.” *Marine and Petroleum Geology* 83 (May): 174–83. https://doi.org/10.1016/J.MARPETGEO.2017.03.018.

Zheng, S., Li, H., Sun, H. et al. 2016. “Determination of Diffusion Coefficient for Alkane Solvent-CO2Mixtures in Heavy Oil with Consideration of Swelling Effect.” *Industrial and Engineering Chemistry Research* 55 (6): 1533–49. https://doi.org/10.1021/acs.iecr.5b03929.

Zhu, Z., Coskuner, Y., Yin, X. et al. 2020. “Experimental and Molecular Studies of the Effect of CO2 on Hindered Flows of Oil through Niobrara Shale.” *SPE/AAPG/SEG Unconventional Resources Technology Conference*. Virtual: Unconventional Resources Technology Conference. https://doi.org/10.15530/urtec-2020-3088.

Appendix A

A-1 Temperature

In LAMMPS, the temperature is calculated by the kinetic energy (KE) based on the equation (A-1) as shown below:

$$KE = \sum_{i=1}^{N} \frac{1}{2} m_i v_i^2 = \frac{dim}{2} N k_B T \quad \text{(A1)}$$

Where KE is the total kinetic energy of the group of atoms, m_i is the mass of i particle, v_i is the velocity of i particle, dim is the dimensionality of the simulation, N is the number of atoms in the group, T is the temperature and k_B is the Boltzmann constant number.

Derivation

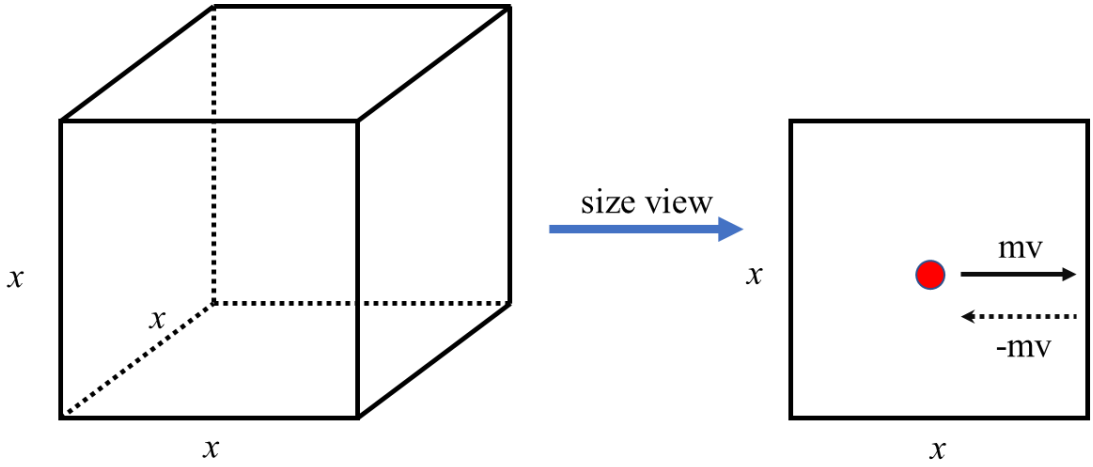

Figure A-1 Schematic of a cubic box

There is a cubic box with a length of x in all directions (Figure A-1**left**), which is saturated by N particles. We make some assumptions: (1) all the particles are monatomic; (2) there is no energy loss when they hit the wall (boundary); (3) along with each axis, the same number particles are hitting the wall. Here we take a side view

(Figure A-1**right**) and study only one particle with a mass of *m* and velocity of *v*.

According to Newton's second law:

$$F = ma = m\frac{\Delta v}{\Delta t} = \frac{\Delta(mv)}{\Delta t} = \frac{\Delta p}{\Delta t} \tag{A2}$$

Where p is the momentum, the change of momentum: $\Delta p = 2mv$ and the particle traveling through the cubic box is: $\Delta t = \frac{2x}{v}$. Putting the Δt and Δp into equation A2 gives:

$$F = \frac{2mv}{\frac{2x}{v}} = \frac{mv^2}{x} \tag{A3}$$

Then the pressure is:

$$P = \frac{F}{A} = \frac{F}{x^2} = \frac{mv^2}{x^3} = \frac{mv^2}{V} \tag{A4}$$

Where V is the volume of the simulation box.

This is just pressure from one particle, so the total pressure in one direction is:

$$P_{Tot} = \frac{mv^2}{V} \cdot \frac{N}{3} \tag{A5}$$

We can arrange the equation (A5):

$$3P_{Tot}V = mv^2N \tag{A6}$$

$$\frac{3P_{Tot}V}{2} = \frac{mv^2}{2}N = KE \tag{A7}$$

$$KE = \frac{3}{2}Nk_BT \tag{A8}$$

Where KE is the total energy of the group. And $\mathrm{PV} = Nk_BT$

Note: in this derivation, the dimensionality is 3.

A-2 Pressure

In LAMMPS, the pressure is computed by equation (A9):

$$P = \frac{Nk_BT}{V} + \frac{\sum_i^N \boldsymbol{r_i} \cdot \boldsymbol{F_i}}{dim \cdot V} \tag{A9}$$

Where $\boldsymbol{r_i}$ and $\boldsymbol{F_i}$ are the position and force vector of i particle.

Derivation

Let us consider the system of N particles in a finite space. According to Clausius virial function(GRAY et al. 1895):

$$W^{Tot} = \sum_{i=1}^{N} \boldsymbol{r_i} \cdot \boldsymbol{F_i}^{Tot} \tag{A10}$$

Where $\boldsymbol{F_i}^{Tot}$ is the total force acting on *i* particle.

Assuming the total simulation is τ. Averaging over the MD trajectory is shown below:

$$\langle W^{Tot} \rangle = \lim_{\tau \to \infty} \frac{1}{\tau} \int_0^{\tau} \sum_{i=1}^{N} \boldsymbol{r_i}(\tau) \cdot \boldsymbol{F_i}^{Tot}(\boldsymbol{t})\, dt \tag{A11}$$

$$\langle W^{Tot} \rangle = \lim_{\tau \to \infty} \frac{1}{\tau} \int_0^{\tau} \sum_{i=1}^{N} \boldsymbol{r_i}(\tau) \cdot m_i \cdot \ddot{\boldsymbol{r_i}}(\tau)\, dt \tag{A12}$$

$$\langle W^{Tot} \rangle = \lim_{\tau \to \infty} \frac{1}{\tau} \int_0^{\tau} \sum_{i=1}^{N} \boldsymbol{r_i}(\tau) \cdot m_i\, d\dot{\boldsymbol{r_i}}(\tau) \tag{A13}$$

$$\begin{aligned} \langle W^{Tot} \rangle = \lim_{\tau \to \infty} m_i \sum_{i}^{N} \frac{\boldsymbol{r_i}(\tau) \cdot \dot{\boldsymbol{r_i}}(\boldsymbol{\tau}) - \boldsymbol{r_i}(\boldsymbol{0}) \cdot \dot{\boldsymbol{r_i}}(\boldsymbol{0})}{\tau} \\ - \lim_{\tau \to \infty} \frac{1}{\tau} \int_0^{\tau} \sum_{i=1}^{N} m_i \cdot |\dot{\boldsymbol{r_i}}(\tau)|^2\, d\tau \end{aligned} \tag{A14}$$

If the system is in a finite region and particles are not accelerating to infinity. The numerator of the first term in Equation A14 is finite, but the denominator (time) is infinity. Therefore, the first term of Equation A14 is zero. Combing equation A8 gives:

$$\langle W^{Tot} \rangle = -\lim_{\tau \to \infty} \frac{1}{\tau} \int_0^{\tau} \sum_{i=1}^{N} m_i \cdot |\dot{\boldsymbol{r_i}}(\tau)|^2\, d\tau = -2\langle KE \rangle = -3Nk_BT \tag{A15}$$

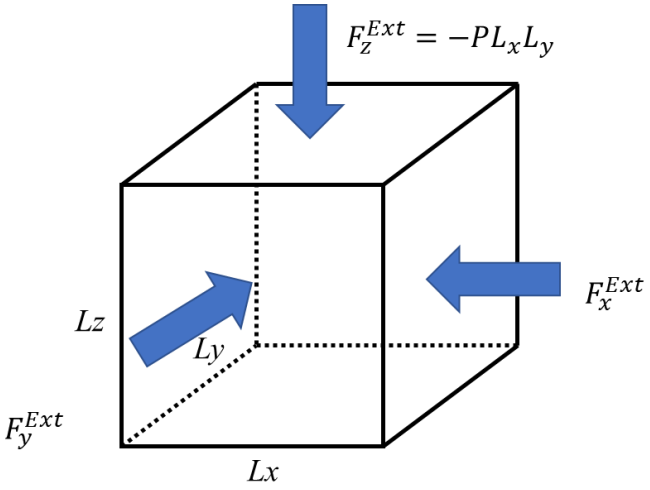

Figure A- 2 Schematic of external pressure

Pressure P is defined by considering a system enclosed in a parallelepiped container as shown in Figure A- 2. The total force acting on *i* particle is composed of internal force and external force.

$$\boldsymbol{F}_i^{Tot} = \boldsymbol{F}_i^{Int} + \boldsymbol{F}_i^{Ext} \tag{A16}$$

The total viral function can also be written as the sum of internal and external virials:

$$\langle W^{Tot} \rangle = \langle W^{Int} \rangle + \langle W^{Ext} \rangle = -3Nk_BT \tag{A17}$$

The external virial part of the container with coordinate origin on one of its corners is:

$$\langle W^{Ext} \rangle = L_x\left(-PL_zL_y\right) + L_y(-PL_zL_x) + L_z\left(-PL_xL_y\right) = -3PV \tag{A18}$$

Combing Equations A10, A17, and A18:

$$3PV = 3Nk_BT + \langle W^{Int} \rangle = 3Nk_BT + \langle \sum_{i=1}^{N} \boldsymbol{r_i} \cdot \boldsymbol{F_i}^{Int} \rangle \tag{A19}$$

$$P = \frac{Nk_BT}{V} + \frac{\langle \sum_{i=1}^{N} \boldsymbol{r_i} \cdot \boldsymbol{F_i}^{Int} \rangle}{3 \cdot V} \tag{A20}$$

From Equation A20, we know that the pressure is determined by temperature (first term) and internal force (second term) such as pair, bond, angle, dihedral, improper and electrostatic force. For the second term (pairwise interaction), we can calculate from

potential energy.

The total internal force $\boldsymbol{F_i}^{Int}$ on particle *i* is the sum of all the forces from other particles *j* in the system:

$$\boldsymbol{F_i}^{Int} = \sum_{\boldsymbol{j=1}}^{\boldsymbol{N}} \boldsymbol{F_{ji}}^{Int} \tag{A21}$$

Therefore,

$$\sum_{i=1}^{N} \boldsymbol{r_i} \cdot \boldsymbol{F_i}^{Int} = \sum_{i=1}^{N} \sum_{j=1}^{N} \boldsymbol{F_{ji}}^{Int} \cdot \boldsymbol{r_i} \tag{A22}$$

Given that no particle can act on itself, therefore $\boldsymbol{F_{ii}}^{Int} = 0$. Therefore, we split the Equation A22 into two parts:

$$\sum_{i=1}^{N} \boldsymbol{r_i} \cdot \boldsymbol{F_i}^{Int} = \sum_{i=1}^{N} \sum_{j<i} \boldsymbol{F_{ji}}^{Int} \cdot \boldsymbol{r_i} + \sum_{i=1}^{N} \sum_{j>i} \boldsymbol{F_{ji}}^{Int} \cdot \boldsymbol{r_i} \tag{A23}$$

Using Newton's third law where $\boldsymbol{F_{ij}}^{Int} = -\boldsymbol{F_{ji}}^{Int}$ and rearranging Equation A23, we can get:

$$\sum_{i=1}^{N} \boldsymbol{r_i} \cdot \boldsymbol{F_i}^{Int} = \sum_{i=1}^{N} \sum_{j<i} \boldsymbol{F_{ji}}^{Int} \cdot \boldsymbol{r_i} - \sum_{i=1}^{N} \sum_{j>i} \boldsymbol{F_{ij}}^{Int} \cdot \boldsymbol{r_i} \tag{A24}$$

Here, we can arrange the last term in Equation A24:

$$\begin{aligned} \sum_{i=1}^{N} \sum_{j>i} \boldsymbol{F_{ij}}^{Int} \cdot \boldsymbol{r_i} = {} & \boldsymbol{F_{12}^{Int}} \cdot \boldsymbol{r_1} + \boldsymbol{F_{13}^{Int}} \cdot \boldsymbol{r_1} + \boldsymbol{F_{14}^{Int}} \cdot \boldsymbol{r_1} + \cdots + \boldsymbol{F_{1N}^{Int}} \cdot \boldsymbol{r_1} + \\ & \boldsymbol{F_{23}^{Int}} \cdot \boldsymbol{r_2} + \boldsymbol{F_{24}^{Int}} \cdot \boldsymbol{r_2} + \boldsymbol{F_{25}^{Int}} \cdot \boldsymbol{r_2} + \cdots + \boldsymbol{F_{2N}^{Int}} \cdot \boldsymbol{r_2} + \\ & \cdots\cdots\cdots\cdots \\ & \boldsymbol{F_{N-1N}^{Int}} \cdot \boldsymbol{r_{N-1}} \end{aligned} \tag{A25}$$

Rearrange Equation (A25):

$$\sum_{i=1}^{N}\sum_{j>i}\boldsymbol{F_{ij}}^{Int}\cdot\boldsymbol{r_i}=\boldsymbol{F_{12}^{Int}}\cdot\boldsymbol{r_1}+$$

$$\boldsymbol{F_{13}^{Int}}\cdot\boldsymbol{r_1}+\boldsymbol{F_{23}^{Int}}\cdot\boldsymbol{r_2}$$

$$\boldsymbol{F_{14}^{Int}}\cdot\boldsymbol{r_1}++\boldsymbol{F_{24}^{Int}}\cdot\boldsymbol{r_2}+\boldsymbol{F_{34}^{Int}}\cdot\boldsymbol{r_3}+$$

$$\cdots\cdots\cdots\cdots \tag{A26}$$

$$\boldsymbol{F_{1N}^{Int}}\cdot\boldsymbol{r_1}+\boldsymbol{F_{2N}^{Int}}\cdot\boldsymbol{r_2}+\boldsymbol{F_{3N}^{Int}}\cdot\boldsymbol{r_3}+\cdots+\boldsymbol{F_{N-1N}^{Int}}\cdot\boldsymbol{r_{N-1}}$$

$$=\sum_{i=1}^{N}\sum_{j<i}\boldsymbol{F_{ji}}^{Int}\cdot\boldsymbol{r_j}$$

Combing Equations A23 and A26:

$$\begin{aligned}\sum_{i=1}^{N}\boldsymbol{r_i}\cdot\boldsymbol{F_i}^{Int}&=\sum_{i=1}^{N}\sum_{j<i}\boldsymbol{F_{ji}}^{Int}\cdot\boldsymbol{r_i}-\sum_{i=1}^{N}\sum_{j<i}\boldsymbol{F_{ji}}^{Int}\cdot\boldsymbol{r_j}\\&=\sum_{i=1}^{N}\sum_{j<i}\boldsymbol{F_{ji}}^{Int}\cdot(\boldsymbol{r_i}-\boldsymbol{r_j})\end{aligned} \tag{A27}$$

Usually, the force can be derived from potential energy V that is a function only of the distance $\boldsymbol{r_{ji}}$ between particle j and i.

$$\boldsymbol{F_{ji}^{Int}}=-\nabla_{r_i}V=-\frac{dV}{dr}\left(\frac{\boldsymbol{r_i}-\boldsymbol{r_j}}{r_{ji}}\right) \tag{A28}$$

Combing Equations A27 and A28:

$$\sum_{i=1}^{N}\boldsymbol{r_i}\cdot\boldsymbol{F_i}^{Int}=-\sum_{i=1}^{N}\sum_{j<i}\frac{dV}{dr}\left(\frac{\boldsymbol{r_i}-\boldsymbol{r_i}}{r_{ji}}\right)\cdot(\boldsymbol{r_i}-\boldsymbol{r_j})=-\sum_{i=1}^{N}\sum_{j<i}\frac{dV}{dr}\cdot r_{ji} \tag{A29}$$

Put Equation A28 into Equation A19:

$$P=\frac{Nk_BT}{V}-\frac{1}{3\cdot V}\left\langle\sum_{i=1}^{N}\sum_{j<i}\frac{dV}{dr}\cdot r_{ji}\right\rangle \tag{A30}$$

Note: the dimensionality is 3.

Appendix B-Supplementary Data

MD Simulation with Ions Randomly Distributed in Clay Nanopore

We build one model with potassium ions randomly distributed in clay nanopores following the way as Jin et al. (2014), as shown in Figure B-1a. The color code follows in Chapter 3. Water saturation is 38%. Figure B-1b shows the initial ion distribution without showing water and oil where the total number of ions is 40. The purpose of this model is to characterize ion distribution when oil and water are present in clay-hosted nanopores and to quantify its impact on the distribution of water-oil mixture. We start our simulation from the same model but with different initial velocities. The equilibrium results after 20 ns are shown in Figure B-1c to Figure B-1g where oil is not shown for clarity. Figure B-1c to Figure B-1g indicate that although starting from the same model, the distribution of ions is the function of initial velocities. The numbers in Figure B-1c to Figure B-1g are the number of potassium ions corresponding to upper and bottom surfaces. Meanwhile, the distribution of water molecules is strongly determined by the adsorption of potassium ions. When the clay surfaces are charge-balanced or with moderate imbalance (Figure B-1c and e), a familiar sandwich structure of water film-hydrocarbon-water film is formed which is also similar to the silica-based nanopores. With a strong charge imbalance (Figure B-1d, f, and g), however, water bridges instead of water adsorption films are observed due to the electric field induced by a strong unbalanced charged surface (discussed in detail in Chapter 3).

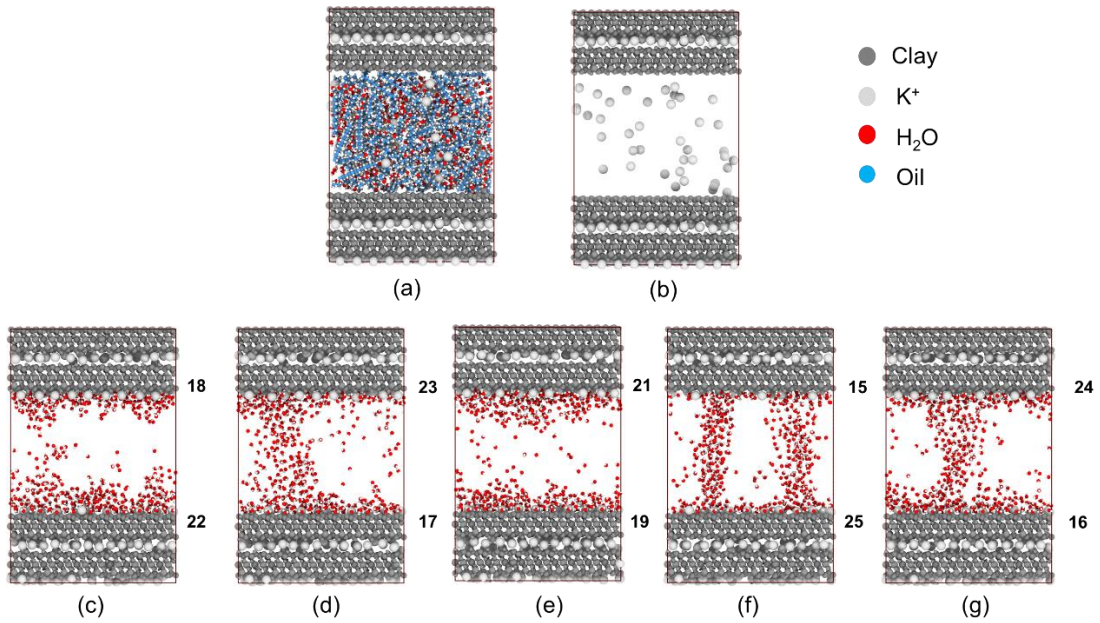

Figure B-1 (a) Initial model where potassium ions are randomly distributed in clay nanopore, the pore width is 5 nm and water saturation 38%. (b) An initial model where oil and water are not shown. (c-g) Equilibrium results after 20 ns starting from the same model but with 5 different initial velocities. The numbers in panels c to g are the number of potassium ions corresponding to upper and bottom surfaces. Color codes: clay, grey; potassium, light grey; water, red; and oil, blue.

Although recently some experiments proved the existence of heterogeneous surface charge in clay and our simulations are also consistent with their results, the phenomenon of water bridge is still interesting. If the ion distribution in clay nanopore is unbalanced which can produce instant electric field (discussed in detail in Chapter 3), a naturally subsequent question arises: *can the produced electric field drag the ions to the other side and make a balanced ion distribution*? Carried with this question, we build another 3 models with different pore widths (1, 2, and 5 nm), as shown in Figure B-2 where oil and water are not shown. The models in Figure B-2 are P-H structures with the highest unbalanced ion distribution which can produce the largest electric field (discussed in detail in Chapter 3) compared with the rest of the structures (H-H, P-P, and the one between H-H and P-H). Therefore, in these models, we want to test whether

the strongest electric field can drag the ions to other side and reach a balanced ion distribution. Results are shown in Figure B-2a to Figure B-2c where potassium ions are handled by a transparent process and green lines are the trajectories of potassium ions.

Figure B-2a indicates when the pore width is 1 nm, there is a strong interaction between clay upper and bottom surfaces. After 20 ns, 14 potassium ions move to the bottom surface. When we increase the pore width to 2 nm (Figure B-2b), after 20 ns, only 5 potassium ions move to the bottom surface and an impaired interaction between clay upper and bottom surfaces is observed. Further increasing the pore width to 5 nm (Figure B-2c), after 20 ns, no potassium ions move to the bottom surface and all of them are firmly adsorbed on the upper clay surface with a small move. Therefore, we can conclude that potassium ions are almost located firmly on the clay surface at a pore width larger than 2 nm, consistent with Hao's et al. (2019b) work.

That is, at a large pore width (i.e., 5 nm in Figure B-1), the produced electric field due to unbalanced ion distribution cannot drag the ions to the other side, demonstrating that the existence of electric fields in clay nanopore can persist without other perturbations such as salinity which is discussed in detail in Chapter 5.

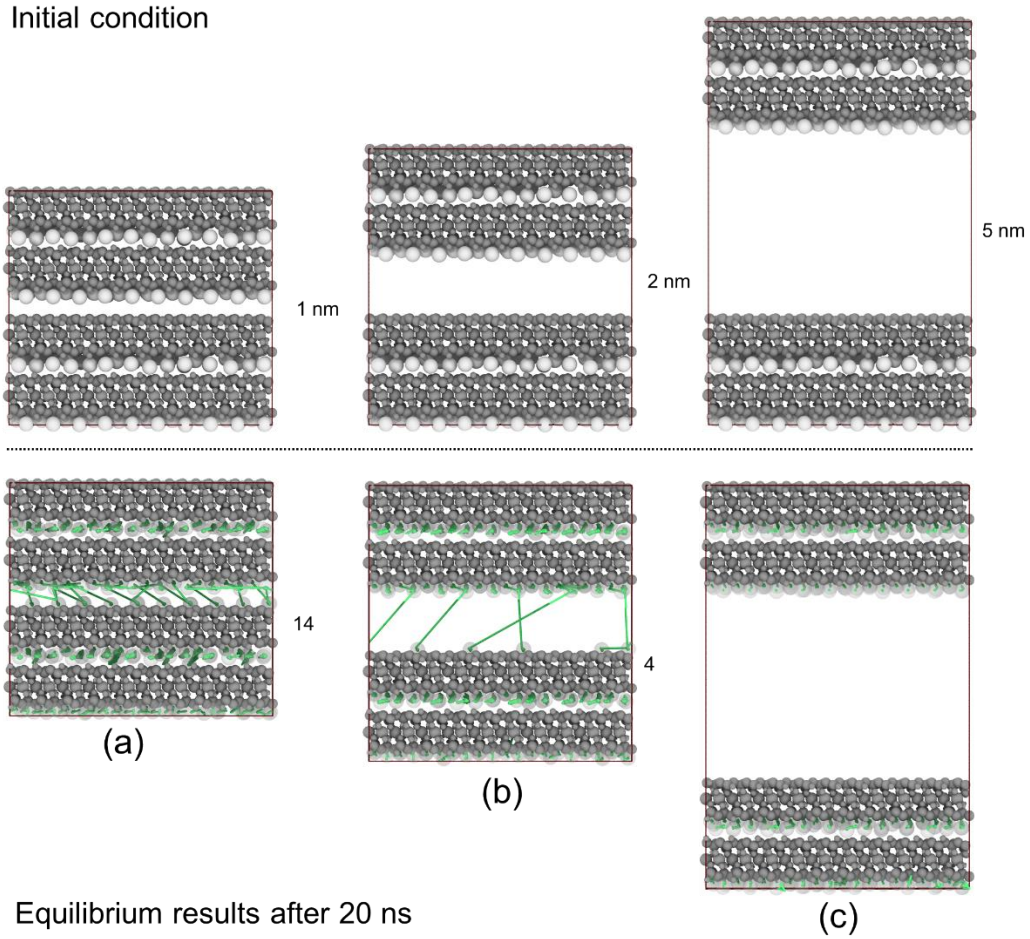

Figure B-2 (Upper three figures) initial configuration of models with different pore widths (1, 2, and 5 nm). (a-c) Equilibrium results after 20 ns where potassium ions are handled by a transparent process (transparency is 0.8) and green lines are the trajectories of potassium ions. Color codes refer to Figure B-1.

Results of NEMD Simulation

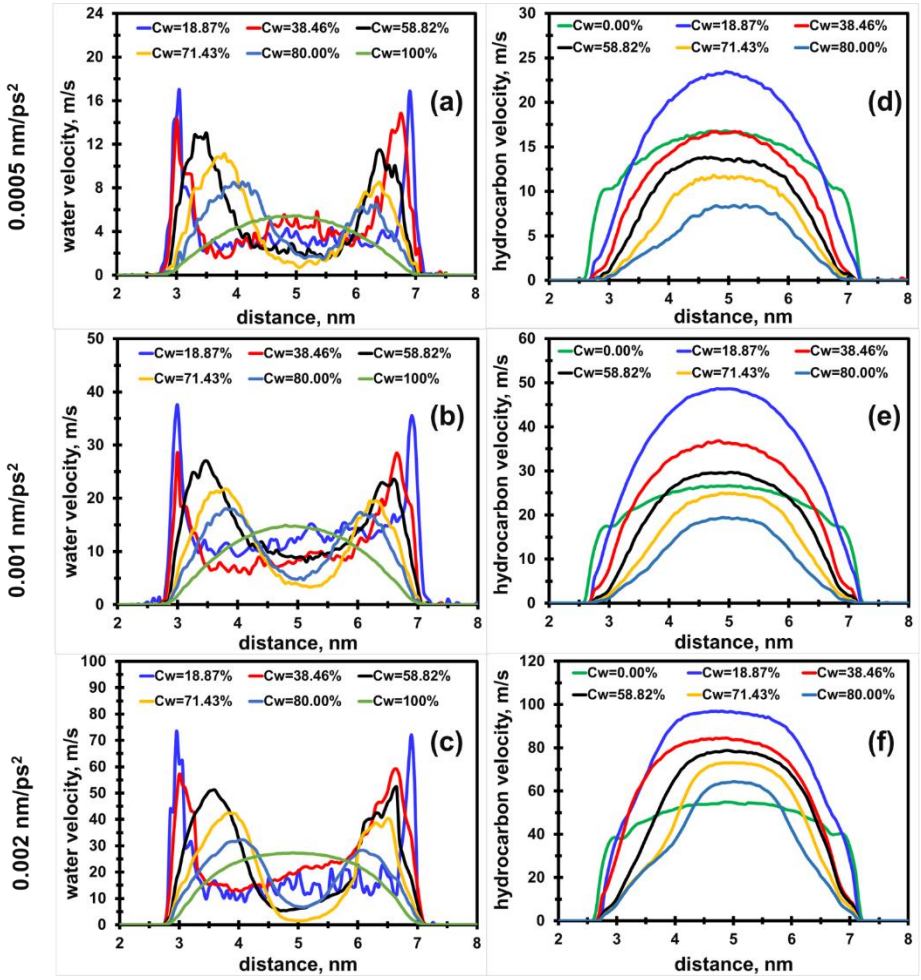

Figure B-3 Water and hydrocarbon velocity profiles at the acceleration of 0.0005 nm/ps^2 ,0.001 nm/ps^{2,} and 0.002 nm/ps^2 in a 5 nm H-H nanopore. Cw stands for water concentration. Water concentration is seen to strongly impact both water and hydrocarbon velocities.

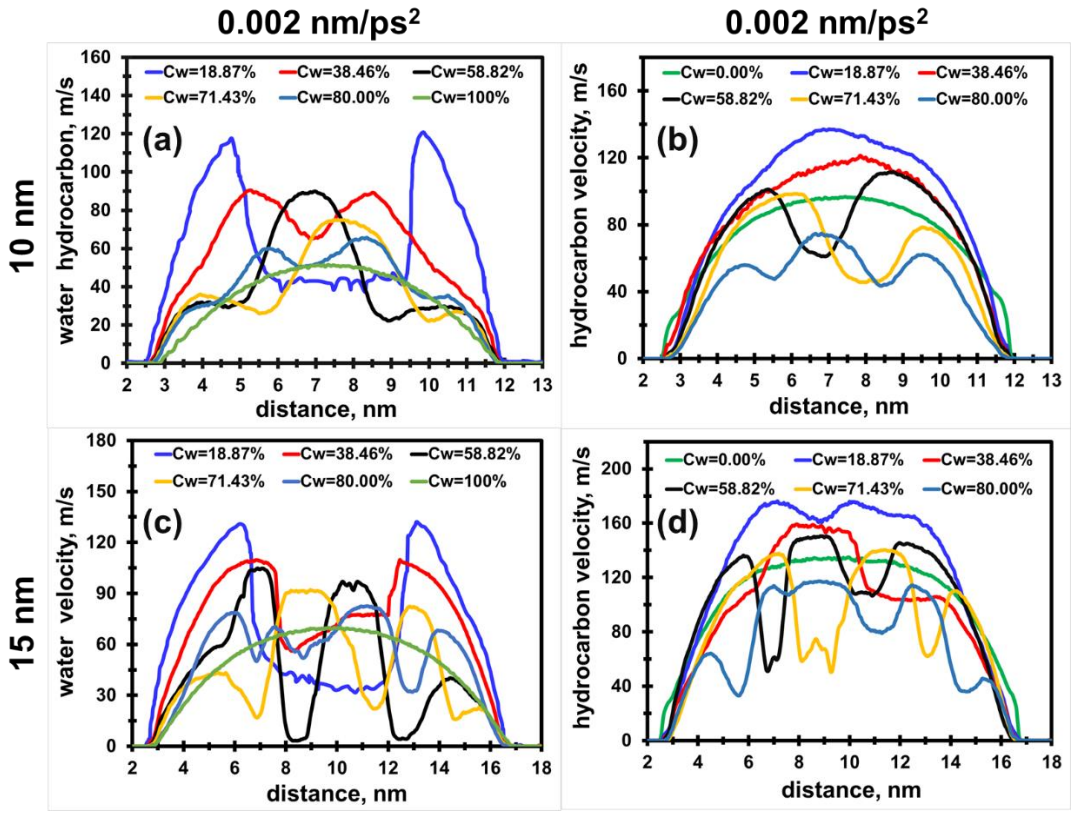

Figure B-4 Water and hydrocarbon velocity profiles at the acceleration of 0.002 nm/ps^2 in 10 nm and 15 nm H-H nanopores. Increasing the pore width causes a more complex and disturbed flow pattern. The peaks and troughs in the velocity profiles correspond to local phase density variations.

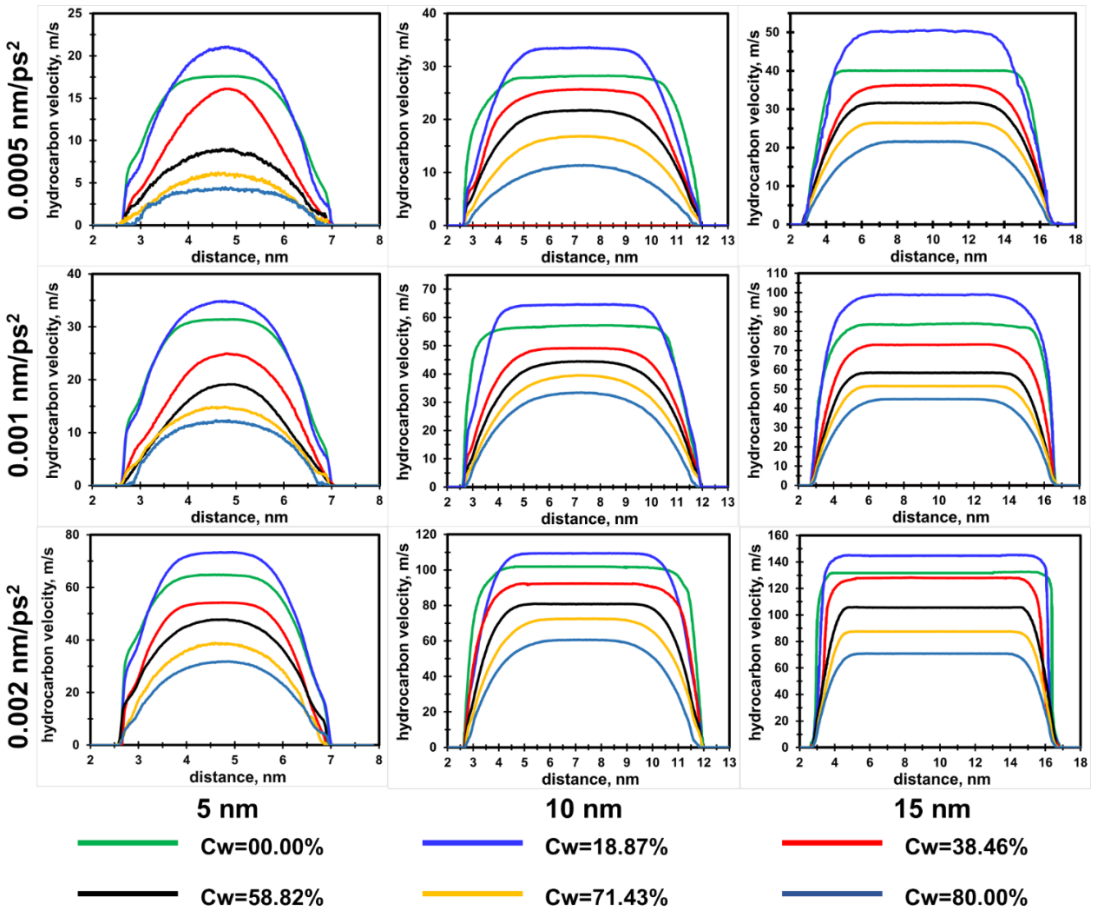

Figure B-5 Hydrocarbon velocity profiles from all 54 NEMD simulations for P-H pores, where the effects of acceleration, pore width, and water concentration are analyzed. The results indicate that at increasing water concentrations, hydrocarbon velocity decreases. An increase in pore width and acceleration also increases the velocities. The flat velocity profile is more pronounced at larger pore widths because of the decreasing interaction between hydrocarbon molecules and clay surface.

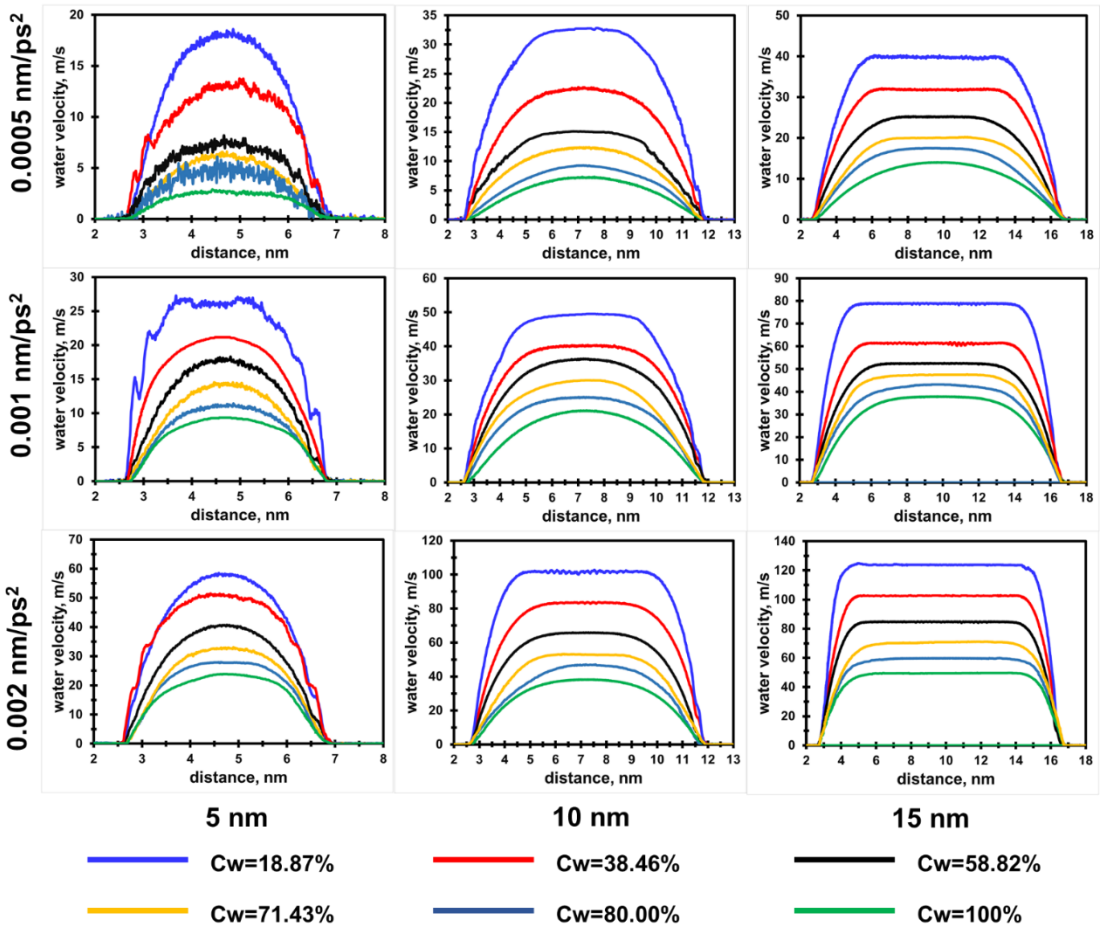

Figure B-6 Water velocity profiles for 54 NEMD simulations in P-H nanopore. The results indicate that increasing water concentrations will decrease water velocity. An increase in pore width and acceleration also increases the velocities. The flat velocity profile is more pronounced at larger pore widths because of the decreasing interaction between water molecules and the clay surface.

Effect of Acceleration

Figure B-7 shows the water velocity profiles at different values of acceleration and 100% water concentration in a 15 nm P-H nanopore. It indicates that water velocity increases with acceleration due to the larger kinetic energy of water molecules with the higher acceleration. At the acceleration of 0.0005 nm/ps^2, the water velocity profile is parabolic. However, increasing the acceleration to 0.001 nm/ps^2 or 0.002 nm/ps^2, the velocity profiles for water acquire a flat profile at the pore center. This happens when

pore wall effects play a smaller role than the imposed acceleration.

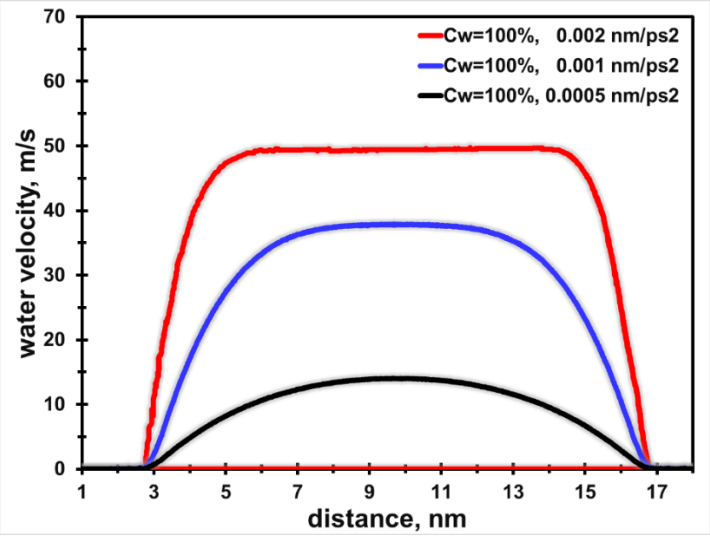

Figure B-7 Water velocity profiles at different accelerations and 100% water concentration in 15 nm P-H nanopore. The result indicates that a flatter velocity profile is observed when the acceleration is dominant and any other wall effects are less significant'.

Equilibrium Result with Flexible Clay Structure

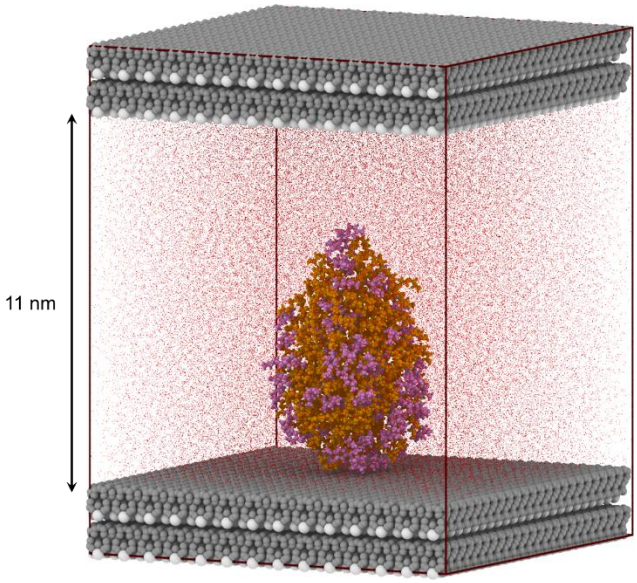

Figure B- 8 Equilibrium Result with a flexible clay structure. In the presence of a strong electric field, even when I allow the clay structure to move, the distance between upper and lower surfaces is still not changed.

Unit Conversion of Electrostatic Force

Because the electrostatic force, *F* is the product of the electric field, *E* and the charge, *e*:

$$F = Ee$$

Where $F = k_e \frac{|q_1 q_2|}{r^2}$. In SI units, k_e is Coulomb's constant ($\approx 8.988 \times 10^9\ N \cdot m^2 \cdot C^{-2}$). q_1 and q_2 are the signed magnitudes of the charges in Coulombs (C), and the scalar *r* is the distance between the charges in meter (m).

Theoretically, when the distance *r* is near zero, the electrostatic force can reach infinity. In my work, the distance *r* is in the range of nanometer. Therefore, in this small distance, it is possible to have a high magnitude electric field. Here, I will give a simple example. We have two electrons ($1\ e = 1.6 \times 10^{-19} C$) and the distance between them is 10 nm. Therefore, the electrostatic force is:

$$\begin{aligned} F &= 8.988 \times 10^9\ N \cdot m^2 \cdot C^{-2} \cdot \frac{e \cdot e}{(10\ nm)^2} \\ &= 8.988 \times 10^9\ N \cdot m^2 \cdot C^{-2} \cdot \frac{e \cdot e}{(10\ \times 10^{-9} m)^2} \\ &= 8.988 \times 10^9 \times 10^{16} N \cdot C^{-2} \cdot e \cdot e \\ &= 8.988 \times 10^{27} N \cdot C^{-2} \cdot 1.6 \times 10^{-19} C \cdot e = 1.438 \times 10^7 \frac{N}{C} \cdot e \\ &= 1.438 \times 10^7 \frac{V}{m} \cdot e = 1.438 \times 10^{-2} \frac{V}{nm} \cdot e \end{aligned}$$

The electric field is $1.438 \times 10^{-2} \frac{V}{nm}$. Overall, due to the complexity of the clay structure and the small distance (< 10 nm), it is possible to have a such high electric field.

Appendix C-LAMMPS Scripts

Solvent pdb File

CRYST1	0	0	0	90	90	90	P	1	1		
ATOM	1	C1	LIG	X	1	1.031	0.952	0.018	1	0	Cd
ATOM	2	C2	LIG	X	1	-0.496	0.939	0.06	1	0	Cd
ATOM	3	C1	LIG	X	1	-0.93	0.925	1.525	1	0	Cd
ATOM	4	C4	LIG	X	1	-0.295	2.078	2.273	1	0	Cd
ATOM	5	C5	LIG	X	1	0.841	2.7	1.893	1	0	Cd
ATOM	6	C1	LIG	X	1	1.591	2.235	0.649	1	0	Cd
ATOM	7	C5	LIG	X	1	-1.054	-0.26	-0.689	1	0	Cd
ATOM	8	C3	LIG	X	1	1.299	3.893	2.707	1	0	Cd
ATOM	9	C3	LIG	X	1	-0.723	-1.699	-0.335	1	0	Cd
ATOM	10	C6	LIG	X	1	-1.881	-0.035	-1.724	1	0	Cd
ATOM	11	HR	LIG	X	1	1.419	0.089	0.56	1	0	Hd
ATOM	12	HR	LIG	X	1	1.387	0.859	-1.009	1	0	Hd
ATOM	13	HR	LIG	X	1	-0.862	1.858	-0.402	1	0	Hd
ATOM	14	HR	LIG	X	1	-2.015	1.019	1.584	1	0	Hd
ATOM	15	HR	LIG	X	1	-0.66	-0.006	2.024	1	0	Hd
ATOM	16	HX	LIG	X	1	-0.864	2.501	3.088	1	0	Hd
ATOM	17	HR	LIG	X	1	2.644	2.093	0.892	1	0	Hd
ATOM	18	HR	LIG	X	1	1.548	3.042	-0.083	1	0	Hd
ATOM	19	HR	LIG	X	1	0.645	4.093	3.557	1	0	Hd
ATOM	20	HR	LIG	X	1	2.304	3.72	3.092	1	0	Hd
ATOM	21	HR	LIG	X	1	1.323	4.787	2.083	1	0	Hd
ATOM	22	HR	LIG	X	1	-1.042	-1.926	0.682	1	0	Hd
ATOM	23	HR	LIG	X	1	-1.214	-2.407	-1.002	1	0	Hd
ATOM	24	HR	LIG	X	1	0.351	-1.871	-0.401	1	0	Hd
ATOM	25	HX	LIG	X	1	-2.308	-0.845	-2.298	1	0	Hd
ATOM	26	HX	LIG	X	1	-2.153	0.966	-2.027	1	0	Hd
END											

Surfactant pdb File

CRYST1	0	0	0	90	90	90	P	1	1		
ATOM	1	Cb	MOL	X	1	-19.23	1.695	3.246	1	0	C
ATOM	2	Cs	MOL	X	1	-18.75	0.856	4.445	1	0	C
ATOM	3	Cs	MOL	X	1	-18.192	1.789	5.535	1	0	C
ATOM	4	Cs	MOL	X	1	-17.711	0.949	6.733	1	0	C
ATOM	5	Cs	MOL	X	1	-17.174	1.882	7.834	1	0	C
ATOM	6	Cs	MOL	X	1	-16.689	1.039	9.029	1	0	C
ATOM	7	Cs	MOL	X	1	-16.169	1.97	10.14	1	0	C
ATOM	8	Cs	MOL	X	1	-15.676	1.125	11.33	1	0	C
ATOM	9	Cs	MOL	X	1	-15.163	2.053	12.446	1	0	C
ATOM	10	Cs	MOL	X	1	-14.659	1.206	13.63	1	0	C
ATOM	11	Cs	MOL	X	1	-14.149	2.133	14.749	1	0	C
ATOM	12	Co	MOL	X	1	-13.638	1.284	15.929	1	0	C
ATOM	13	Os	MOL	X	1	-13.137	2.19	17.028	1	0	O
ATOM	14	Co	MOL	X	1	-12.629	1.355	18.18	1	0	C
ATOM	15	Co	MOL	X	1	-12.118	2.277	19.304	1	0	C
ATOM	16	Os	MOL	X	1	-11.607	1.442	20.454	1	0	O
ATOM	17	Co	MOL	X	1	-11.107	2.346	21.556	1	0	C
ATOM	18	Co	MOL	X	1	-10.582	1.495	22.727	1	0	C
ATOM	19	Os	MOL	X	1	-10.082	2.399	23.829	1	0	O
ATOM	20	Co	MOL	X	1	-9.563	1.561	24.975	1	0	C
ATOM	21	Co	MOL	X	1	-9.056	2.481	26.102	1	0	C
ATOM	22	Os	MOL	X	1	-8.535	1.644	27.246	1	0	O
ATOM	23	Co	MOL	X	1	-8.043	2.548	28.351	1	0	C
ATOM	24	Co	MOL	X	1	-7.508	1.696	29.518	1	0	C
ATOM	25	Os	MOL	X	1	-7.019	2.6	30.624	1	0	O
ATOM	26	Co	MOL	X	1	-6.488	1.763	31.764	1	0	C
ATOM	27	Co	MOL	X	1	-5.993	2.684	32.894	1	0	C
ATOM	28	Os	MOL	X	1	-5.456	1.849	34.032	1	0	O
ATOM	29	Co	MOL	X	1	-4.975	2.756	35.139	1	0	C
ATOM	30	Co	MOL	X	1	-4.42	1.906	36.297	1	0	C
ATOM	31	Os	MOL	X	1	-3.952	2.812	37.411	1	0	O
ATOM	32	Co	MOL	X	1	-3.426	1.972	38.55	1	0	C
ATOM	33	CH	MOL	X	1	-2.995	2.888	39.711	1	0	C
ATOM	34	OH	MOL	X	1	-2.482	2.044	40.853	1	0	O
ATOM	35	Hs	MOL	X	1	-19.642	1.005	2.439	1	0	H
ATOM	36	Hs	MOL	X	1	-18.354	2.293	2.825	1	0	H
ATOM	37	Hs	MOL	X	1	-20.048	2.411	3.59	1	0	H
ATOM	38	Hs	MOL	X	1	-17.935	0.135	4.105	1	0	H
ATOM	39	Hs	MOL	X	1	-19.627	0.264	4.869	1	0	H

ATOM	40	Hs	MOL	X	1	-19.015	2.5	5.878	1	0	H
ATOM	41	Hs	MOL	X	1	-17.319	2.392	5.117	1	0	H
ATOM	42	Hs	MOL	X	1	-16.883	0.242	6.394	1	0	H
ATOM	43	Hs	MOL	X	1	-18.585	0.342	7.144	1	0	H
ATOM	44	Hs	MOL	X	1	-18.005	2.583	8.175	1	0	H
ATOM	45	Hs	MOL	X	1	-16.304	2.495	7.425	1	0	H
ATOM	46	Hs	MOL	X	1	-15.851	0.345	8.689	1	0	H
ATOM	47	Hs	MOL	X	1	-17.556	0.418	9.432	1	0	H
ATOM	48	Hs	MOL	X	1	-17.012	2.657	10.483	1	0	H
ATOM	49	Hs	MOL	X	1	-15.307	2.598	9.738	1	0	H
ATOM	50	Hs	MOL	X	1	-14.83	0.443	10.984	1	0	H
ATOM	51	Hs	MOL	X	1	-16.535	0.491	11.729	1	0	H
ATOM	52	Hs	MOL	X	1	-16.011	2.73	12.797	1	0	H
ATOM	53	Hs	MOL	X	1	-14.308	2.692	12.046	1	0	H
ATOM	54	Hs	MOL	X	1	-13.81	0.532	13.278	1	0	H
ATOM	55	Hs	MOL	X	1	-15.513	0.564	14.029	1	0	H
ATOM	56	Hs	MOL	X	1	-14.999	2.805	15.103	1	0	H
ATOM	57	Hs	MOL	X	1	-13.297	2.777	14.349	1	0	H
ATOM	58	Hm	MOL	X	1	-12.787	0.614	15.572	1	0	H
ATOM	59	Hm	MOL	X	1	-14.488	0.638	16.328	1	0	H
ATOM	60	Hm	MOL	X	1	-11.777	0.69	17.818	1	0	H
ATOM	61	Hm	MOL	X	1	-13.475	0.704	18.579	1	0	H
ATOM	62	Hm	MOL	X	1	-12.97	2.942	19.667	1	0	H
ATOM	63	Hm	MOL	X	1	-11.272	2.929	18.904	1	0	H
ATOM	64	Hm	MOL	X	1	-11.961	3.007	21.92	1	0	H
ATOM	65	Hm	MOL	X	1	-10.265	3.002	21.155	1	0	H
ATOM	66	Hm	MOL	X	1	-9.727	0.834	22.362	1	0	H
ATOM	67	Hm	MOL	X	1	-11.423	0.838	23.127	1	0	H
ATOM	68	Hm	MOL	X	1	-8.706	0.906	24.606	1	0	H
ATOM	69	Hm	MOL	X	1	-10.402	0.901	25.373	1	0	H
ATOM	70	Hm	MOL	X	1	-9.913	3.136	26.471	1	0	H
ATOM	71	Hm	MOL	X	1	-8.217	3.143	25.703	1	0	H
ATOM	72	Hm	MOL	X	1	-8.904	3.198	28.72	1	0	H
ATOM	73	Hm	MOL	X	1	-7.208	3.215	27.954	1	0	H
ATOM	74	Hm	MOL	X	1	-6.646	1.047	29.149	1	0	H
ATOM	75	Hm	MOL	X	1	-8.343	1.028	29.915	1	0	H
ATOM	76	Hm	MOL	X	1	-5.624	1.12	31.391	1	0	H
ATOM	77	Hm	MOL	X	1	-7.319	1.09	32.159	1	0	H
ATOM	78	Hm	MOL	X	1	-6.858	3.325	33.268	1	0	H
ATOM	79	Hm	MOL	X	1	-5.164	3.36	32.497	1	0	H
ATOM	80	Hm	MOL	X	1	-5.846	3.388	35.516	1	0	H
ATOM	81	Hm	MOL	X	1	-4.155	3.44	34.741	1	0	H

ATOM	82	Hm	MOL	X	1	-3.546	1.277	35.924	1	0	H
ATOM	83	Hm	MOL	X	1	-5.241	1.22	36.689	1	0	H
ATOM	84	Hm	MOL	X	1	-2.534	1.359	38.191	1	0	H
ATOM	85	Hm	MOL	X	1	-4.248	1.271	38.912	1	0	H
ATOM	86	Hs	MOL	X	1	-3.892	3.496	40.064	1	0	H
ATOM	87	Hs	MOL	X	1	-2.172	3.594	39.358	1	0	H
ATOM	88	HO	MOL	X	1	-2.176	2.706	41.69	1	0	H
END											

Water pdb File

HEADER	water							
COMPND								
SOURCE								
HETATM	1	HW	HOH		1	9.626	6.787	12.673
HETATM	2	HW	HOH		1	9.626	8.42	12.673
HETATM	3	OW	HOH		1	10.203	7.604	12.673
CONECT	1	3						
CONECT	2	3						
CONECT	3	1	2					
END								

Salt pdb File

CRYST1	0.32	1.013	1.37	90	90	90	P		1	1
ATOM	1	rN	X	-2	-2.727	0.648	1.924		0	0
ATOM	2	rC	X	-2	-2.407	1.661	3.294		0	0
END										

Input File

```
#    LAMMPS input script for Microemulsion
########################################################################
variable            dump_rate           equal 20000
variable            thermo_rate         equal 100
# relaxation time (timesteps)
variable            relax               equal 400000
# timestep
variable            ts                  equal 1 # fs
```

```
# temperature
variable        T               equal 380. # K
# thermostat damping constant
variable        Tdamp           equal 100 # fs
# pressure
variable        p               equal 400. # atm
# barostat damping constant
variable        pdamp           equal 1000 # fs
# random seed
variable        seed            equal 102180844
# cutoff
variable        rc              equal 10. # A
variable    V equal vol
variable    p equal 400     # correlation length
variable    s equal 5       # sample interval
variable    d equal $p*$s   # dump interval
# convert from LAMMPS real units to SI
variable    kB equal 1.3806504e-23      # [J/K/** Boltzmann
variable    atm2Pa equal 101325.0
variable    A2m equal 1.0e-10
variable    fs2s equal 1.0e-15
variable    convert equal
${atm2Pa}*${atm2Pa}*${fs2s}*${A2m}*${A2m}*${A2m}
###########################################################################
# ----------------------- INITIALIZATION ----------------------------
units                       real
dimension           3
boundary            p   p   p
atom_style              full
read_data           R3.data


pair_style          lj/cut/coul/long ${rc}
pair_coeff      1       1       0.066   3.5     #C1
pair_coeff      2       2       0.066   3.5     #C2
pair_coeff      3       3       0.066   3.5     #C3
pair_coeff      4       4       0.076   3.55    #C4
pair_coeff      5       5       0.076   3.55    #C5
pair_coeff      6       6       0.076   3.55    #C6
pair_coeff      7       7       0.066   3.5     #CH
pair_coeff      8       8       0.066   3.5     #Cb
pair_coeff      9       9       0.066   3.5     #Co
```

```
pair_coeff      10      10      0.066   3.5     #Cs
pair_coeff      11      11      0       0       #HO
pair_coeff      12      12      0.03    2.5     #HR
pair_coeff      13      13      0       0       #HW
pair_coeff      14      14      0.03    2.42    #HX
pair_coeff      15      15      0.03    2.5     #Hm
pair_coeff      16      16      0.03    2.5     #Hs
pair_coeff      17      17      0.17    3.12    #OH
pair_coeff      18      18      0.1553  3.166 # O-O (SPC Refined)
pair_coeff      19      19      0.14    2.9     #Os
pair_coeff      20      20      0.1001  4.9388
pair_coeff      21      21      0.155416412     3.5532

bond_style              harmonic
bond_coeff      1       268     1.529   #C-C
bond_coeff      2       317     1.51    #=C-C
bond_coeff      4       340     1.08    #=C-H2
bond_coeff      3       340     1.09    #C-H
bond_coeff      5       367     1.08    #=C-H
bond_coeff      6       549     1.34    #C=C
bond_coeff      7       268     1.529   #C-C
bond_coeff      8       320     1.41    #C-O
bond_coeff      9       340     1.09    #C-H
bond_coeff      10      553     0.945   #O-H
bond_coeff      11      554.1349 1      #H2O


angle_style             harmonic
angle_coeff     1       33      107.8   #H-C-H
angle_coeff     2       35      109.5   #=C-C-H
angle_coeff     3       37.5    110.7   #C-C-H
angle_coeff     4       63      111.1   #C-C-C=
angle_coeff     5       58.35   112.7   #C-C-C
angle_coeff     6       35      117     #H-C=H
angle_coeff     7       60.43   118.76  #C-C=H
angle_coeff     8       35      120     #C-C=H2
angle_coeff     9       70      124     #C-C=C
angle_coeff     10      70      130     #C-C(=)-C
angle_coeff     11      33      107.8   #H-C-H
angle_coeff     12      35      109.5   #O-C-H
angle_coeff     13      37.5    110.7   #C-C-H
angle_coeff     14      50      109.5   #C-C-O
```

```
angle_coeff     15      55      108.5   #C-O-H
angle_coeff     16      58.35   112.7   #C-C-C
angle_coeff     17      60      109.5   #C-O-C
angle_coeff     18      45.7696 109.47  #H2O


dihedral_style      opls
dihedral_coeff  1       0.346   0.405   -0.904  0       #C=C-C-C
dihedral_coeff  2       0       0       -0.372  0       #C=C-C-H
dihedral_coeff  3       0       14      0       0       #C-C=C-H
dihedral_coeff  4       0       -8      0       0       #C-C-C(=)-H
dihedral_coeff  5       1.3     -0.2    0.2     0       #C-C-C-C=
dihedral_coeff  6       0       0       0.3     0       #C-C(=)-C-H
dihedral_coeff  7       0       0       0.318   0       #H-C(=)-C-H
dihedral_coeff  8       0       0       0.366   0       #H-C-C-C=
dihedral_coeff  9       2.817   -0.169  0.543   0       #C-C(=)-C-C
dihedral_coeff  10      -0.55   0       0       0       #O-C-C-O
dihedral_coeff  11      4.319   0       0       0       #O-C-C-OH
dihedral_coeff  12      1.3     -0.2    0.2     0       #C-C-C-C
dihedral_coeff  13      0       0       0.3     0       #C-C-C-H
dihedral_coeff  14      0       0       0.352   0       #H-O-C-H
dihedral_coeff  15      0       0       0.468   0       #O-C-C-H
dihedral_coeff  16      -0.356  -0.174  0.492   0       #C-C-O-H
dihedral_coeff  17      1.711   -0.5    0.663   0       #C-C-C-O
dihedral_coeff  18      0.65    -0.25   0.67    0       #C-C-O-C
dihedral_coeff  19      0       0       0.76    0       #C-O-C-H


pair_modify         mix arithmetic tail yes
special_bonds       lj/coul 0.0 0.0 0.3
kspace_style        pppm 1.0e-6
comm_modify         vel yes


group               solvent type 1 2 3 4 5 6 12 14
group               surfactant type 7 8 9 10 11 15 16 17 19
group               all type 1 2 3 4 5 6 7 8 9 10 11 12 13 14 15 16 17 18 19
group               water type 13 18
group               Na type 21
group               Cl type 20

#---------------------Run NPT-ISO-------------------------
```

```
reset_timestep 0
velocity                all create $T ${seed} mom yes rot yes dist gaussian

neighbor                2.0 bin
neigh_modify            every 1 delay 10 check yes
timestep ${ts}
#fix 1 all nvt temp $T $T ${Tdamp}
fix                             1       water shake 0.0001 100 0 b    11 a 18
fix                             2       all npt temp $T $T ${Tdamp} iso ${p} ${p}
${pdamp}    pchain 3 mtk yes nreset 100
thermo 100
thermo_style            custom step temp press pe etotal vol density
dump                            1 all atom ${dump_rate} npt1.lammpstrj
dump_modify                     1 sort id scale no
run                             210000
write_data              R4.data
run                             100000
write_data              R5.data
```